Old Dominion University

ODU Digital Commons

Civil & Environmental Engineering Theses & Dissertations

Civil & Environmental Engineering

Fall 2019

Catalytic Transfer Hydrogenation Reactions of Lipids

Alexander Asiedu
Old Dominion University, asiealexnana@gmail.com

Follow this and additional works at: https://digitalcommons.odu.edu/cee_etds

Part of the Chemical Engineering Commons, Environmental Engineering Commons, and the Oil, Gas, and Energy Commons

Recommended Citation

Asiedu, Alexander. "Catalytic Transfer Hydrogenation Reactions of Lipids" (2019). Doctor of Philosophy (PhD), Dissertation, Civil & Environmental Engineering, Old Dominion University, DOI: 10.25777/nyqd-a964
https://digitalcommons.odu.edu/cee_etds/104

This Dissertation is brought to you for free and open access by the Civil & Environmental Engineering at ODU Digital Commons. It has been accepted for inclusion in Civil & Environmental Engineering Theses & Dissertations by an authorized administrator of ODU Digital Commons. For more information, please contact digitalcommons@odu.edu.

CATALYTIC TRANSFER HYDROGENATION REACTIONS OF LIPIDS

by

Alexander N. Asiedu

B.S. March 2003, Kwame Nkrumah University of Science & Technology, Ghana

M.S. June 2008, Kwame Nkrumah University of Science & Technology, Ghana

M.S. December 2015, Old Dominion University, Virginia, USA

A Dissertation Submitted to the Faculty of Old Dominion University in Partial Fulfillment of the Requirements for the Degree of

DOCTOR OF PHILOSOPHY

CIVIL AND ENVIRONMENTAL ENGINEERING

OLD DOMINION UNIVERSITY

DECEMBER 2019

Approved by:

Sandeep Kumar (Director)

Ben Stuart (Member)

Mujde Erten-Unal (Member)

James W. Lee (Member)

ABSTRACT

CATALYTIC TRANSFER HYDROGENATION REACTIONS OF LIPIDS

Catalytic transfer hydrogenation (CTH) of lipids was investigated using 2-propanol as hydrogen donor for producing liquid hydrocarbons, e.g. jet fuels. The main sources of lipids selected in this study were waste cooking oil (WCO) and oil-laden algae-derived biofuel intermediate (BI). Two different catalysts were employed in this study, namely activated carbon and trimetallic-doped zeolite.

The CTH reaction was between WCO and 2-propanol in a continuous flow reactor over a packed-bed activated carbon at near atmospheric pressure. Results revealed a high level of alkenes and aromatics compounds, which are not stable and are not environmentally unfriendly. To reduce these compounds in the liquid fuel, trimetallic catalyst was prepared and the reaction was by optimizing the reaction variables (temperature, pressure, weight hourly space velocity, and oil-2-propanol ratio). Results from the second study were better than that of the first, as the level of aromatics and alkenes was lower in the second study. However, the amount of branched and cyclo-alkanes (high octane rating compounds) was insignificant.

Lipids from algae-derived oil-laden BI were extracted by 2-propanol and without evaporation of alcohol; the pregnant 2-propanol was subjected to CTH over the prepared trimetallic catalyst in a batch reactor. The liquid fuel product from this third study produced significant branched and cyclo-alkanes (serendipity).

Finally, technoeconomic analysis (TEA) and life cycle assessment (LCA) of CTH reaction were conducted. The results were compared, with a conventional hydroprocessed renewable jet fuels (HRJ) process. Results showed that the economic performance of CTH was lower than that of

HRJ, due to the large volume of 2-propanol employed in the CTH. However, the environmental performance of CTH was very impressive, compared to that of HRJ.

Chapter 1 of this study describes the rationale for selecting WCO and 2-propanol as the potential hydrogen donor.

In Chapter 2, 2-propanol was used the react with waste cooking oil by considering four reaction parameters: temperature, oil flow rate, WHSV, and pressure. Finally, the kinetics of the reaction were ascertained, in order to estimate reaction order, activation energy, and kinetic rate constant.

Chapter 3 employed commercial catalyst doped with transition metals which catalyzed the reaction between waste cooking oil and 2-propanol. Optimization of the reaction was studied by varying temperature, WHSV, pressure, and oil-2-propanol ratio. The percent of transition metal employed remained constant.

Chapter 4, on the other hand, explored the possibility of using oil-laden biofuel intermediate from flash hydrolyzed algae. The purpose was to utilize 2-propanol as oil extract and hydrogen donor in CTH reaction of the oil.

Finally, Chapter 5 thoroughly discussed the technoeconomic and environmental performance of the CTH reaction of waste cooking oil and 2-propanol.

Copyright, 2019, by Alexander N. Asiedu, All Rights Reserved

This dissertation is dedicated to my dear wife, Abigail.

Editing formats of this dissertation are based on American Chemical Society (Chapters 3); the Elsevier publishing company (Chapter 4 and 5); and Wiley online library (Chapter 2).

ACKNOWLEDGEMENTS

I wish to express my sincere appreciation and gratitude to my principal advisor, Dr. Sandeep Kumar, for his untiring guidance, advice, and discussions, and for his support for my dissertation research; to my committee members Dr. Mujde Erten-Unal, Dr. Ben Stuart, and Dr. James W. Lee for their valuable comments and suggestions; to the Department of Civil and Environmental Engineering for providing all of the facilities and equipment required for my research over the last four years; to the current and former members of the Biomass Research Laboratory, who helped me along the way with their friendship, help, advice, discussions, and time spent solving problems together; and to the Department of Chemistry and Biochemistry and Applied Research Center for their help with sample analysis and collaborative research. I recognize the prayers, love, and support of my wife Abigail.

NOMENCLATURE

Abbreviations

ACF	Annualized cash flow
BET	Brunauer-Emmett-Teller
CEPCI	Engineering plant cost index
COM	Cost of manufacturing
COM_d	Cost of manufacturing without depreciation
CTH	Catalytic transfer hydrogenation
DCO	Decarbonylation
DCO_2	Decarboxylation
DMC	Direct Manufacturing
DOE	Design of experiment
DPBP	Discounted payback period
DTA	Differential thermal analysis
EDS	Energy dispersive spectroscopy
EIA	Energy Information Administration
FAME	Fatty acid methyl esters
FCI	Fixed capital investment
FMC	Fixed Manufacturing Cost
FTIR	Fourier transform infrared spectroscopy
GCMS	Gas chromatography mass spectroscopy
GE	General Expenses
GP	Gross Profit HRJ Hyroprocessing Renewable Jet
HDO	Hydrodeoxygenation
HPLC	High performance liquid chromatography

IRR	Internal rate of return
LC	Long chain
LCALK	Long chain alkanes
LHC	Liquid hydrocarbon
MACRS	Modified accelerated capital recovery system
NPV	Net Present Value
PVR	Present value ratio
RM	Raw materials
SAPO	Silicoaluminophosphate
SC	Short chain
SCALK	Short chain alkanes
SEM	Scanning electron microscope
TCD	Thermal conductivity detector
TGA	Thermogravimetric analysis
USY	Ultra-stable zeolite
UT	Utilities
WC	Working capital cost
WCO	Waste cooking oil
WHSV	Weight hourly space velocity (h^{-1})
XRD	X-ray diffraction

Symbols

C_A	Concentration of product species (mol/L)
C_{GT}	Hydrogen concentration of WCO at any time (mol/m^3)
C_{H2}	Hydrogen concentration (mol/m^3)
C_{TG0}	Inlet concentration of WCO (mol/m^3)
C_{bm}	Equipment bare module cost
C_{exp}	Experimental value of concentration of product species (mol/m^3)
$C_{i=1......9}$	Concentration of product species (mol/m^3)
C_p	Purchase cost
C_{pred}	Predicted value of concentration of product species (mol/m^3)
C_{p-ref}	Reference purchase cost
E_a	Activation energy (kJ/mol)
E_a	Activation energy (kJ/mol)
F_{GTO}	Flow rate of WCO (mol/s)
N_{eq}	Number of equipment
N_{op}	Number of operators of equipment
R_{H2O}	Molar ratio of H_2 over WCO at the inlet
X_{cal}	Calculated value for the conversion of WCO
X_{cal}	Predicted value of conversion of fatty acid
X_{exp}	Experimental value for the conversion of WCO

$\frac{dC}{dt}$	Rate of disappearance of fatty acid or rate of formation of product species (mol/L.s)
$\frac{dC}{d\tau}$	Rate of disappearance of WCO or rate of formation of product species (mol/m^3.s)
d_k	Value of depreciation at year *k*
r_{TG}	Rate of disappearance of WCO (mol/g catalyst.s)
v_{H2}, v_{TG}	Hydrogen and WCO stoichiometric coefficients
ε_{gas}	Void fraction (%)
ρ_{cat}	Density of catalyst (kg/m^3)
$°API$	Specific gravity [1] of petroleum product used by American Petroleum institute
A	Pre-exponential factor (s^{-1})
S	Cross-sectional area (m^2)
T	Temperature (K)
W	Weight of catalyst (g)
X	Conversion of WCO (%)
β	Model coefficients
k	Kinetic rate constant (s^{-1})
n	Reaction order
t	Reaction time (s),
γ	Cost exponent
ε	Expansion coefficient of the reaction (dimensionless)
τ	Space time (s),

TABLE OF CONTENTS

ABSTRACT iii

NOMENCLATURE viii

TABLE OF CONTENTS xii

LIST OF TABLES xvi

LIST OF FIGURES xix

CHAPTER 1 1

1.0. INTRODUCTION 1

CHAPTER 2 6

WASTE COOKING OIL TO JET-DIESEL FUEL RANGE USING 6

2-PROPANOL VIA CATALYTIC TRANSFER HYDROGENATION REACTIONS 6

2.0. INTRODUCTION 8

2.1. MATERIAL AND METHODS 14

2.2. RESULTS AND DISCUSSIONS 19

2.3. CONCLUSIONS 37

2.4. ACKNOWLEDGEMENT 38

CHAPTER 3 39

KINETICS AND OPTIMIZATION OF CATALYTIC TRANSFER HYDROGENATION OF WCO USING 2-PROPANOL AS H-DONOR OVER NIO_X-MOO_X-COO_X/ZEOLITE 39

3.0. INTRODUCTION 40

3.1. MATERIALS AND METHODS 44

3.2. RESULTS AND DISCUSSIONS 49

3. 3. CONCLUSIONS 75

3.4. ACKNOWLEDGEMENT 76

CHAPTER 4 77

CATALYTIC TRANSFER HYDROGENATION AND CHARACTERIZATION OF FLASH HYDROLYZED MICROALGAE INTO HYDROCARBON FUELS PRODUCTION (JET FUEL) 77

4.0 INTRODUCTION 78

4.1. MATERIALS AND METHODS 84

4.2. RESULTS AND DISCUSSIONS 91

4.3. CONCLUSIONS 116

4.4. ACKNOWLEDGEMENTS 117

CHAPTER 5 118

TECHNO-ECONOMIC ANALYSIS AND LIFE-CYCLE ASSESSMENT OF JET FUELS PRODUCTION FROM WASTE COOKING OIL VIA CATALYTIC TRANSFER HYDROGENATION 118

5.0. INTRODUCTION 119

5.1. MATERIALS AND METHODS 122

5.2. RESULTS AND DISCUSSIONS 145

5.3. CONCLUSIONS 169

5.4. ACKNOWLEDGEMENTS 169

CHAPTER 6 170

RECOMMENDATION FOR FUTURE WORK 170

REFERENCES 172

APPPENDIX A 189

WASTE COOKING OIL TO JET-DIESEL FUEL RANGE USING 2-PROPANOL VIA CATALYTIC TRANSFER HYDROGENATION REACTIONS: SUPPLEMENTARY DOCUMENTS 189

APPENDIX B 203

KINETICS AND OPTIMIZATION OF CATALYTIC TRANSFER HYDROGENATION OF WCO USING 2-PROPANOL AS H-DONOR OVER NIO_X-MOO_X-COO_X/ZEOLITE 203

APPENDIX C 211

CATALYTIC TRANSFER HYDROGENATION AND CHARACTERIZATION OF FLASH HYDROLYZED MICROALGAE INTO HYDROCARBON FUELS PRODUCTION (JET FUEL, & DIESEL): SUPPLEMENTARY DOCUMENTS 211

APPENDIX D 222

TECHNO-ECONOMIC ANALYSIS AND LIFE-CYCLE ASSESSMENT OF JET FUELS PRODUCTION FROM WASTE COOKING OIL VIA CATALYTIC TRANSFER HYDROGENATION: SUPPLEMENTARY DOCUMENTS......... 222

FIXED CAPITAL INVESTMENT (FCI) 230

APPENDIX E 245

ANALYTICAL METHODS EMPLOYED IN THIS STUDY 245

VITA 252

LIST OF TABLES

Table Page

TABLE 1.1. THE FAA’S APPROVED BIOJET FUELS PATHWAYS ……………………….…3

TABLE 2.1. CONDITIONS FOR CONTROL EXPERIMENTS……...……………………….17

TABLE 2.2. CTH EXPERIMENTAL CONDITIONS…………………………………………18

TABLE 2.3. FATTY ACID COMPOSITION OF WCO…………………………………….20

TABLE 2.4. PHYSICAL PROPERTIES OF THE LIQUID HYDROCARBON COMPARED TO THAT OF ASTM STANDARDS……………………………………………………...25

TABLE 2.5. STOICHIOMETRIC REACTIONS OF CONVERSION OF WCO TO C12H26, C8H16 AND C17H36………………………………………………………………….29

TABLE 2.6. SURFACE AREA DETERMINATION OF USED CATALYST AT DIFFERENT REACTION TEMPERATURES…………………………………………………………..33

TABLE 2.7. WEIGHT LOSS OF USED CATALYST USING TGA………………………….36

TABLE 3.1. DESIGN OF EXPERIMENT (34)…………………………………………...…48

TABLE 3.2. EDS OF ZEOLITE, FRESH NI-CO-MO-ZEOLITE AND USED NI-CO-MO-ZEOLITE AT THE OPTIMUM CTH CONDITIONS (380 ^{O}C & 14 BAR)…………………..54

TABLE 3.3. KINETIC RATE CONSTANT, ACTIVATION ENERGY AND PRE-EXPONENTIAL FACTORS CALCULATED AT DIFFERENT TEMPERATURES…………65

TABLE 3.4. PHYSICAL PROPERTIES OF THE LIQUID HYDROCARBON COMPARED TO THAT OF ASTM STANDARDS……………………………………………………...74

TABLE 4.1. LIPID CONTENTS OF DIFFERENT SPECIES OF MICROALGAE……..……78

TABLE 4.2. FACTORS CONSIDERED IN OPTIMIZING THE OIL EXTRACTION PROCESS BY 33 FRACTIONAL FACTORIAL DESIGN…………………………………….86

TABLE 4.3. EXPERIMENTAL RUNS OF CTH OF ALGAE OIL USING 2-PROPANOL AS H2 DONOR……………………..……………………………………………………....89

TABLE 4.4. EXPERIMENTAL OIL YIELD, YEXP, AND CALCULATED OIL YIELD, YCAL……………………………………………………………………………………97

TABLE 4.5. ANOVA MODEL FOR BI OIL EXTRACTION………………………………...99

TABLE 4.6. EVALUATION OF LIQUID PRODUCT FROM CTH AT 390 ^{O}C……………110

TABLE 4.7. ESTIMATED KINETIC PARAMETERS………………………………………113

TABLE 5.1. FATTY ACIDS COMPOSITION OF WASTE COOKING OIL FEEDSTOCK…………………………………………………………………………122

TABLE 5.2. MASS-, ENERGY-, AND MARKET-BASED EQUIVALENCY (IMPACT) FACTORS USED IN THE IMPACT ASSESSMENT PHASE OF HRJ AND CTH LIFE CYCLE…………………………………………………………………………………..140

TABLE 5.3. EQUIVALENCY FACTORS USED IN MODELING HRJ AND CTH PROCESSES……………………………………………………………………………142

TABLE 5.4. GLOBAL LCI FOR HRJ AND CTH DETAILING ENERGY/MATERIALS INPUTS/OUTPUTS TO AND FROM THE TECHNOSPHERE/ENVIRONMENT BASED ON TABLE D36. ENERGY AND HEAT ARE IN MJ/DAY AND MATERIALS AND CHEMICALS ARE IN TONS/DAY……………………………………………………….143

TABLE 5.5. PROCESS PERFORMANCES OF HRJ AND CTH SYSTEMS. ALL SPECIFIC ENERGY CONSUMPTION OF UTILITIES IS SCALED TO THE MASS OF WCO FEED……………………………………………………………………………………..145

TABLE 5.6. TOTAL BARE MODULE COST IN HRJ AND CTH JET FUEL PRODUCTION PROCESSES. FOR HRJ THE COST AT ATMOSPHERIC PRESSURE (BASE) IS REPORTED IN ADDITION TO THE FINAL ONE……………………………………….147

TABLE 5.7. FIXED CAPITAL INVESTMENT IN HRJ AND CTH JET FUEL PRODUCTION PROCESSES……………………………………………………………………………..147

TABLE 5.8. SUMMARY OF DIRECT MANUFACTURING COSTS…………………….148

TABLE 5.9. TOTAL COST OF MANUFACTURING IN HRJ JET FUEL PRODUCTION PROCESS…………………………………………………………………………………….148

TABLE 5.10. TOTAL COST OF MANUFACTURING IN CTH JET FUEL PRODUCTION PROCESS……………………………………………………………………………………..149

TABLE 5.11. PRODUCT INCOMES AND GROSS PROFITS IN HRJ AND CTH JET FUEL PRODUCTION PROCESSES…………………………………………………………..151

TABLE 5.12. CHARACTERIZATION RESULTS OF FIGURE 5.7. CUMULATIVE FOSSIL ENERGY DEMAND (CED) AND OUTPUT FUEL ENERGY (OUT) ARE EXPRESSED AS × 106 MJ/1,000 TONS WCO AND GLOBAL WARMING POTENTIAL (GWP) IS EXPRESSED AS 106 KG CO2-EQUIVALENTS/1,000 TONS WCO……………………………………158

LIST OF FIGURES

Figure Page

FIGURE 2.1. EXPERIMENTAL SET-UP FOR A CONTINUOUS-FLOW FIXED BED FOR DEOXYGENATION OF WASTE COOKING OIL. PG-PRESSURE GAUGE; TG-DIGITAL TEMPERATURE GAUGE……………………………………………………………..16

FIGURE 2.2. THERMAL GRAVIMETRIC ANALYSIS OF WCO……………………………………………………………………………………..21

FIGURE 2.3. CONVERSION OF WCO BY CTH AT DIFFERENT REACTION TEMPERATURES…………………………………………………………………………22

FIGURE 2.4. OVERALL LIQUID FUEL YIELD FROM CTH OF WCO AT DIFFERENT REACTION TEMPERATURES……………………………………………………...…23

FIGURE 2.5. LIQUID FUEL COMPOSITION AT DIFFERENT TEMPERATURES………..24

FIGURE 2.6. PRODUCTS: (A) RAW PRODUCT FUEL OBTAINED AT 2 BAR; (B) FUEL DISTILLATE FROM RAW PRODUCT DISTILLED UNDER VACUUM (0.2 BAR) AT 90 ^{O}C; (C) TAR OBTAINED AFTER VACUUM DISTILLATION OF RAW PRODUCT FUEL……………………………………………………………………………………….25

FIGURE 2.7. SIMULATED DISTILLATION OF THE LIQUID FUEL PRODUCT OBTAINED AT 380 ^{O}C………..……………………………………………………….26

FIGURE 2.8. LIQUID FUEL FRACTIONS AT DIFFERENT TEMPERATURES…..………27

FIGURE 2.9. POSSIBLE WCO DEOXYGENATION ROUTES USING 2-PROPANOL AND FORMIC ACID AS H-DONORS. THE RED DASH LINES REPRESENT C-O CLEAVAGE ROUTE WHILE THE VIOLET LINES DEPICT THE C-C CLEAVAGE ROUTES………….28

FIGURE 2.10. REGRESSION OF THE KINETIC EQUATION USING LEAST SQUARE METHOD……………………………………………………………………………………32

FIGURE 2.11. PORE SIZE DISTRIBUTION OF FRESH AND USED CATALYST AT 380 ^{O}C………………………………………………………………………………………33

FIGURE 2.12. NITROGEN ADSORPTION/DESORPTION 77.35 K OF FRESH AND USED CATALYST AT 380 ^{O}C………………………………………………………………………34

FIGURE 2.13. FIRST DERIVATIVE OF TGA OF USED CATALYST AT DIFFERENT REACTION TEMPERATURES……………………………………………………………35

FIGURE 2.14. TOTAL COKE FORMED FROM RUNNING AFTER 10 HOURS OF REACTION…………………………………………………………………………………36

FIGURE 2.15. EFFECT OF COKE FORMATION ON WCO CONVERSION AT 380 OC AFTER 10 HOURS (3 CYCLES) USE OF THE CATALYST……………………………….37

FIGURE 3.1. CHARACTERIZATION OF WCO: (A) TGA ANALYSIS AT DIFFERENT HEATING RATES (HR); (B) DTA SHOWING DIFFERENT MAXIMUM RATES OF THERMAL DECOMPOSITION AT DIFFERENT TEMPERATURES; (C) KINETICS OF TGA TO DETERMINE THE ORDER OF THERMAL DECOMPOSITION OF WCO; (D) ACTIVATION ENERGY PROFILE AT DIFFERENT REACTION ORDERS………………50

FIGURE 3.2. WHICH HIGHLIGHTS TGA PROFILES FOR THE FRESH CATALYST, THE USED CATALYST, AND THE ZEOLITE (SUPPORT), ELUCIDATES THREE STAGES OF WEIGHT LOSS. THE FIRST STAGE (BELOW 200 ^{O}C) SHOWED APPROXIMATELY 13%, 16%, AND 10% WEIGHT LOSS FOR ZEOLITE, FRESH CATALYST, AND THE USED

CATALYST, RESPECTIVELY. FIGURE 3.0.2. TGA OF FRESH CATALYST AND USED CATALYST AT OPTIMUM REACTION CONDITION……………………………………52

FIGURE 3.3. SEM (WITH ACCELERATING VOLTAGE: 15.0 KV, MAGNIFICATION: 2000) AND EDS ANALYSIS FOR FRESH AND USED CATALYST (A) FRESH NI-CO-MO-ZEOLITE, (B) USED NI-CO-MO-ZEOLITE AT THE OPTIMUM CTH REACTION CONDITION…………………………………………………………………………………….53

FIGURE 3.4. XRD PATTERN FOR THE ZEOLITE, THE FRESH AND THE USED NI-CO-MO-ZEOLITE CATALYSTS WITH INTENSITY MEASURED IN ARBITRARY UNIT (A.U.), AND X-RAY INCIDENT ANGLE IN DEGREES……………………………………55

FIGURE 3.5. FTIR FOR THE ZEOLITE, THE FRESH NI-CO-MO-ZEOLITE, AND THE USED NI-CO-MO-ZEOLITE CATALYSTS AT 380 OC AND AT 14 BAR CTH…………56

FIGURE 3.6. BET FOR THE RAW AND THE USED CATALYST AT 380 OC AND AT 14 BAR CTH…………………………………………………………………………………..58

FIGURE 3.7. POSSIBLE REACTION PATHWAY FOR CATALYTIC TRANSFER HYDROGENATION OF WCO. SC= SHORT-CHAIN (C6-C14); LC= LONG-CHAIN (C15-C18)……………………………………………………………………………………59

FIGURE 3.8. KINETIC FIT OF THE EXPERIMENTAL DATA FROM CTH AT 360 OC AND 14 BAR; DASHED AND CONTINUOUS LINES REPRESENT THE ESTIMATED VALUES WHILE DOTS REPRESENT THE EXPERIMENTAL VALUES………………..63

FIGURE 3.9. KINETIC FIT OF THE EXPERIMENTAL DATA FROM CTH AT 390 OC AND 14 BAR; DASHED AND CONTINUOUS LINES REPRESENT THE ESTIMATED VALUES WHILE DOTS REPRESENT THE EXPERIMENTAL VALUES……….……..….65

FIGURE 3.10. KINETIC FIT OF THE EXPERIMENTAL DATA FROM CTH AT 420 ^{O}C AND 14 BAR; DASHED AND CONTINUOUS LINES REPRESENT THE ESTIMATED VALUES WHILE DOTS REPRESENT THE EXPERIMENTAL VALUES………………….65

FIGURE 3.11. DIAGNOSTIC PLOTS OF THE REGRESSION MODEL: (A) RESIDUALS OF FITTED VALUES; (B) RESIDUALS AND LAGGED RESIDUALS; (C) NORMAL PROBABILITY; (D) HISTOGRAM OF RESIDUALS………………………………………..68

FIGURE 3.12. THREE-DIMENSIONAL RESPONSE SURFACE SHOWING THE EXPECTED ALKANES YIELD AS A FUNCTION OF TEMPERATURE, PRESSURE, OIL-2-PROPANOL RATIO, AND WHSV…………………………………………………………..69

FIGURE 3.13. CONTOUR PLOT OF THE YIELD OF ALKANE RESPONSE SURFACE IN……………………………………………………………………………………….72

FIGURE 3.14. VALIDATION OF EXPERIMENTAL MODEL WITH PRODUCTS DISTRIBUTION AT OPTIMUM CONDITION (383.7 OC, 14.8 BAR, 1.57 WCO/2-PROPANOL, AND 6.7 H-1)……………………………………………………………….72

FIGURE 3.15. SIMULATED DISTILLATION OF LIQUID FUEL PRODUCT FROM OPTIMUM CONDITION……………………………………………………………….73

FIGURE 4.1. FLASH HYDROLYSIS OF CHLORELLA VULGARIS WITH THE RESULTING BIOPRODUCTS AND BIOFUEL INTERMEDIATE…………………………..80

FIGURE 4.2. CHARACTERIZATION OF BI USING PYROLYSIS TO GENERATE GASEOUS PRODUCT AND ANALYZE IT BY GAS CHROMATOGRAPHY MASS SPECTRUM (GCMS)……………………………………………………………………..85

FIGURE 4.3. PREPARATION OF NIOX-COOX-MOOX-ZEOLITE CATALYST…………87

FIGURE 4.4. OIL EXTRACTION AND CTH REACTION PROCEDURE……………..….89

FIGURE 4.5. WEIGHT LOSS OF OIL-LADEN BI AS IT WAS SUBJECTED TO TGA AT DIFFERENT HEATING RATES (HR) OF 5-30 OC/MIN WITH N2 FLOW RATE OF 20 ML/MIN………………………………………………………………………………………90

FIGURE 4.6. RATE OF THERMAL DECOMPOSITION OF OIL-LADEN BI AT DIFFERENT HEATING RATES WITH N2 FLOW RATE OF 20 ML/MIN…………………91

FIGURE 4.7. FTIR PROFILE FOR OIL-LADEN AND DEPLETED BI RECORDED AT ROOM TEMPERATURE. THE LIGHT BLUE AND RED PROFILES REPRESENT THE DEPLETED BI AND OIL-LADEN BI, RESPECTIVELY…………………………………….92

FIGURE 4.8. GASEOUS PRODUCT FROM THE PYROLYSIS OF BI……………………..94

FIGURE 4.9. HEATING VALUE, O/C, AND H/C OF THE GASEOUS PRODUCTS FROM THE PYRO-GCMS……………………………………………………………………….95

FIGURE 4.10. FRACTIONAL CONVERSION EFFECT ON ACTIVATION ENERGY OF BI THERMAL DECOMPOSITION……………………………………………………………….96

FIGURE 4.11. DIAGNOSTIC PLOT OF SURFACE RESPONSE OF ALGAE OIL YIELD…………………………………………………………………………………………99

FIGURE 4.12. SURFACE RESPONSE OF OIL YIELD FROM BI WITH OPTIMUM OIL EXTRACTION CONDITION: TEMPERATURE (49.7 OC), BI MASS-2-PROPANOL RATIO (0.133 G/G), TIME OF EXTRACTION (101 MIN (1.68 H)), AND MAXIMUM OIL YIELD (62.7 WT%)……………………………………………………………………………………100

FIGURE 4.13. DETERMINATION COKE DEPOSITION ON THE CATALYST DURING VIA TGA DURING THE 3 HOURS OF CTH REACTION OF ALGAE OIL………………..101

FIGURE 4.14. SEM (WITH ACCELERATING VOLTAGE: 15.0 KV, MAGNIFICATION: 4000) AND EDS ANALYSIS FOR ZEOLITE, FRESH AND USED CATALYSTS AT THE 3 HOURS OF CTH REACTION……………………………………………………………103

FIGURE 4.15. XRD PATTERN FOR THE ZEOLITE, THE FRESH AND USED NIOX-COOX-MOOX-ZEOLITE CATALYSTS WITH INTENSITY MEASURED IN ARBITRARY UNIT (A.U.), AND X-RAY INCIDENT ANGLES IN DEGREES…………………………..104

FIGURE 4.16. FTIR PROFILE FOR ZEOLITE (SUPPORT) AND THE FRESH AND USED CATALYSTS. THE CATALYST USED 3 H FOR THE CTH REACTION WAS REFERENCED………………………………………………………………………………106

FIGURE 4.17. SURFACE AREA ANALYSIS OF FRESH AND USED NIOX-COOX-MOOX-ZEOLITE CATALYST AFTER 3 HOURS OF CTH REACTION……………………………107

FIGURE 4.18. CTH CONVERSION OF ALGAE OIL AT DIFFERENT TEMPERATURES…………………………………………………………………………..109

FIGURE 4.19. CARBON NUMBER DISTRIBUTION IN THE LIQUID PRODUCTS AT 390 ^{O}C……………………………………………………………………………………110

FIGURE 4.20. MATERIAL BALANCE FOR SCALE UP CTH REACTION AT 390 OC FOR 1.0 TON OF BI TREATMENT…………………………………………………………..114

FIGURE 5.1. BLOCK-FLOW DIAGRAM OF HRJ (A) AND CTH (B) PROCESSES FOR THE CONVERSION OF TRIGLYCERIDE INTO BIOJET FUELS…………………………121

FIGURE 5.2. PROCESS FLOWSHEET FOR THE HRJ PROCESS. BLACK SOLID LINES INDICATE MATERIAL FLOWS WHILE GRAY DASHED LINES INDICATE NERGY/HEAT FLOWS……………………………………………………………………….123

FIGURE 5.3. PROCESS FLOWSHEET FOR THE CTH PROCESS. BLACK SOLID LINES INDICATE MATERIAL FLOWS WHILE GRAY DASHED LINES INDICATE ENERGY/HEAT FLOWS……………………………………………………………………..127

FIGURE 5.4. CAPITAL EXPENSES OF HRJ (ABOVE LEFT) AND CTH (ABOVE RIGHT) SYSTEMS. OPERATING EXPENSES FOR RAW MATERIALS AND UTILITIES OF HRJ (BELOW LEFT) AND CTH (B) SYSTEMS………………………………………………….152

FIGURE 5.5. CUMULATIVE NPV PROFILES FOR CTH (LEFT) AND HRJ (RIGHT) SYSTEMS AT VARIOUS DEBT FINANCING TERMS SHOWING CORRESPONDING BREAK-EVEN POINTS (5, 10, 15, 20, AND 25 YEARS)………………………………….153

FIGURE 5.6. IRR PROFILES FOR CTH AND HRJ SYSTEMS UNDER 10-YEAR DEBT FINANCING TERM……………………………………………………………………….155

FIGURE 5.7. RESULTS OF CHARACTERIZATION IN THE PRODUCTION OF CTH- AND HRJ-BASED BIOJET FUEL FROM 1,000 TONS WCO. LEFT PANE CORRESPONDS TO ENVIRONMENTAL ENDPOINTS (CED AND GWP) AND RIGHT PANE CORRESPONDS

TO DISTRIBUTION OF OUTPUT ENERGY. ENERGY-RETURN-ON-INVESTMENT (EROI) IS INCLUDED IN THE RIGHT PANE……………………………………………….152

FIGURE 5.8. ELECTRICITY AND HEAT USE BREAKDOWN AMONG SUB-PROCESSES IN THE PRODUCTION OF CTH- AND HRJ-BASED BIOJET FUEL FROM 1,000 TONS WCO………………………………………………………………………………………161

FIGURE 5.9. GWP BREAKDOWN AMONG SUB-PROCESSES IN THE PRODUCTION OF CTH- AND HRJ-BASED BIOJET FUEL FROM 1,000 TONS WCO………………………..161

FIGURE 5.10. ANALYSIS OF CED AND GWP IN THE PRODUCTION OF CTH- AND HRJ-BASED BIOJET FUEL FROM 1,000 TONS WCO USING MASS RATE (MRA), ENERGY RATE (ERA), AND MARKET VALUE (MVA) ALLOCATIONS……………….163

FIGURE 5.11. TORNADO PLOTS DEPICTING DRIVERS IN CED AND GWP OF CTH. DOTTED BARS INDICATE +5-10% CHANGE IN ASSUMPTION FROM BASE CASE AND LINED BARS INDICATE -5-10% CHANGE IN ASSUMPTION FROM BASE CASE. BAR LABELS SHOW THE TEST RANGE FOR EACH INPUT VARIABLE. TORNADO METHOD USED IS PERCENTILES OF THE VARIABLES AND TEST RANGE IS BETWEEN 10% TO 90%. EXPLAINED VARIATION IN FORECAST IS CUMULATIVE…………………………………………………………………………...165

FIGURE 5.12. TREND CHART SHOWCASING THE SHIFT IN EROI FROM HRJ TO EROI AT MEDIAN EROI VALUES (HRJ-EROI=10.5, CTH-EROI=18.6………………………….167

CHAPTER 1

INTRODUCTION

1.0. Introduction

The US annual energy consumption was estimated at 99.3 quadrillion Btu in the year 2018, comprising 37% petroleum, 31% natural gas, 13% coal, 8% nuclear, 7% renewable, 3% hydroelectric, and 1% biofuels [2]. With an increase in primary energy consumption, and its attendant environmental concerns due to the use of fossil fuels, a lot of effort is being made to develop renewable and sustainable biofuels using organic feedstock, such as non-food biomass, oil seeds, municipal solid waste, algae, cyanobacteria, fats, grease, and waste cooking oils (WCOs). The organic matter that is being considered for biofuels primarily contains four major components: carbohydrates, proteins, lignin, and lipids. The last category, i.e. lipids or lipid-based feedstock, is of primary interest in this chapter. Biofuels derived from non-food lipid-rich biomass such as microalgae, fats, and oils are considered as one of the important options of producing drop-in liquid fuels.

There is a large quantity of triglycerides available that can be used for biofuel production. The world production of plant oil rose to 175 million tonnes in 2014. Despite this rise, production of "first generation" biofuel (e.g. biodiesel) from crude plant oil is hindered by the fact that most of these oils are edible. However, waste lipids, such as waste cooking oil (WCO), waste fish oil, and acid oil from soap stock are important renewable feedstocks. These feedstocks have no competition from human consumption or agriculture, and their use can also solve environmental issues associated with disposal of waste organic materials. As of June 2016, there were 95 biodiesel producers across the United States, with a total annual production capacity of 2.1 billion gallons per year. These are from an increasingly diverse mix of resources, such as recycled cooking oil, soybean oil and animal fats. Biodiesel is the first and the only commercial-scale fuel produced across the US to meet the Environmental Protection Agency's (EPA's) definition of an Advanced Biofuel, i.e. it reduces greenhouse gas emissions (GHGs) by more than 50 percent, compared with petroleum diesel. The successful commercial-scale production of biodiesel indicates that the feedstock logistics is reasonably well established.

The aviation sector faces fuel cost and environmental and energy security challenges that arise from the use of petroleum-based jet fuels. Sustainable alternative jet fuels (biojet fuels) from renewable resources can play a key role in addressing these challenges. The development of biojet fuels could reduce emissions that impact surface air quality and global climate, while expanding domestic energy sources that diversify fuel supplies, stabilizing price and supply and generating economic development in rural communities. The strategies for reducing CO_2 emission from land or water transportation include an array of options, ranging from improving engine efficiency and blending bioethanol/biodiesel with gasoline/diesel to using plug-in electric vehicles [3]. Aviation fuels pose a unique problem, because of stringent specifications that require oxygen-free compounds, and they are often characterized as a pure hydrocarbon with an aggregate composition of $C_{12}H_{23}$. Aircraft engines are designed to burn only a narrow range of fuels; therefore, using fuels with characteristics that fall outside this range will detract from safety, efficiency, and/or operability [4]. Bioethanol and biodiesel blending components have dominated consideration as alternative transportation fuels for ground vehicles, but these fuels are not suitable for aviation. In view of these issues, the Federal Aviation Administration's

(FAA) Environment and Energy Division has undertaken several initiatives, including the Continuous Lower Energy, Emissions, and Noise (CLEEN) program that provides leadership in this evolving field of biojet fuels.

The fuels derived from non-food-based lipid biomass, such as waste fats, oils, greases, and non-food plant-derived oils grown on marginal lands, are being viewed as cost-competitive options for producing drop-in sustainable alternative jet fuel(s), SAJF. As of April 2016, the FAA has approved five (Table 1.1) biojet fuels under ASTM D7566 for blending with conventional petroleum-based jet fuels. Each of the five approved pathways for biojet fuels uses one of the following renewable feedstocks: sugar, agricultural/forest residues, municipal solid wastes, fats, oils and greases. For biojet fuels, depending upon the feedstock and conversion processes, reductions in CO_2 emissions, relative to conventional jet fuel, range from 41 to 89 percent [5].

Table 1.1. The FAA’s approved biojet fuels pathways [5]

Process	**Brief Description**	**Qualification Date**	**Blend Limit (%)**
FT-SPK	Fischer-Tropsch conversion of syngas to synthetic paraffinic kerosene	September 2009	50
HEPA-SPK	Hydroprocessed esters and fatty acids (lipids from plant and animal sources) to synthetic paraffinic kerosene	July 2011	50
HES-SIP	Hydroprocessed fermented sugars to synthesized isoparaffins	June 2014	10
FT-SPK/A	Fischer-Tropsch conversion of syngas to synthetic paraffinic kerosene and aromatics	November 2015	50
ATJ-SPK	Thermochemical conversion of alcohols (isobutanol only initially) to paraffinic kerosene	April 2016	30

However, due to the low hydrogen-to-carbon ratio of all the biomass/lipid feedstocks, hydrogen gas, a key input, is needed for almost all biojet fuels production pathways; this represents a significant portion of operating cost. Most of these pathways to produce biojet fuel require a considerable amount of hydrogen gas for the conversion; this leads to the tremendous cost of hydrogen gas handling. Hydrogen gas, being immiscible with fatty acid, is forced to react with oil by applying significant amount of pressures. The most viable option to avoid handling of H_2 gas is to employ catalytic transfer hydrogenation (CTH), which is the reduction and hydrogenation of the oil by using a solvent as *in situ* hydrogen donor.

In this work, the application of 2-propanol as the hydrogen donor over selected catalysts was extensively explored. Chapter 2 reports the CTH of WCO over activated carbon in a continuous flow reactor near atmospheric pressure and temperature range of 360-400 ^{o}C. The kinetics of the reaction were studied, in order to measure the reaction rate equation, activation energy, and order of reaction. Because of high level of oxygenated compounds and aromatics in obtained in Chapter 2, Chapter 3 reduces these parameters by conducting the CTH over commercially available trimetallic catalyst, which was significantly active, compared to the activated carbon. The kinetics of the reaction were studied to estimate the reaction rate equation, rate constant, energy of activation, and order of reaction. Optimization of the CTH was studied by design of experiment (DOE) to determine the optimum parameters that lead to maximum yield and conversion.

The most essential components of jet fuel are branched, and cyclo-alkanes, which are less significant in the Chapter 2 and 3, are explored in Chapter 4. In this case, oil-laden biofuel intermediate from flash hydrolyzed microalgae was used to produced liquid branched and cyclo-alkanes, which could be blended with the fuel obtained from the WCO. Optimization of oil extraction from the BI was conducted using 2-propanol and, without evaporation, the pregnant 2-propanol was subjected to CTH. CTH reaction kinetics were explored to ascertain the rate equation, rate constant, activation energy, and reaction order.

Chapter 5 deals with the economic and environmental performance of CTH. The results were compared to that of hydroprocessed renewable jet (HRJ), which used gaseous hydrogen to hydrogenate the oil and produced biojet fuel. Economic indicators, such as net present value (NPV), the internal rate of return (IRR), and the payback period (PBB) were used to assess the viability of the two processes. Evidently, the fixed capital investment for CTH was 3% that of HRJ. The environmental performance of CTH was assessed by life cycle assessment (LCA) that considered the cradle-to-use conditions. Monte Carlo simulation was employed to evaluate the total greenhouse gas emissions, which was connected to the thermal energy consumption of the two processes.

Recommendations and suggestions for future work for this study are highlighted in Chapter 6.

CHAPTER 2

WASTE COOKING OIL TO JET-DIESEL FUEL RANGE USING 2-PROPANOL VIA CATALYTIC TRANSFER HYDROGENATION REACTIONS

Note: The contents of this chapter were published in the Biofuels Journal.

Asiedu, A.; Barbera, E.; Naurzaliyev, R.; Bertucco, A.; Kumar, S., Waste cooking oil to jet-diesel fuel range using 2-propanol via catalytic transfer hydrogenation reactions. Biofuels ***2019****, 1-14.*
https://doi.org/10.1080/17597269.2018.1532754

2-propanol (99.9 wt%) was used as a H-donor to produce jet/diesel fuel range from waste cooking oil (WCO) over a fixed bed of granular activated carbon in a continuous flow reactor. The reactions were carried out at 2 bar and at a temperature range of 300-400 ^{o}C with weight hourly space velocity (WHSV) of 6.7 h^{-1}. An optimum yield of 72% liquid hydrocarbon (LHC) at 380 ^{o}C was observed. The LHC contained 32% alkanes, 16% aromatics, and 37% alkenes at the optimum temperature. Using 2-propanol as an *in-situ* hydrogen source will potentially reduce volume ratio of hydrogen source to oil (0.4 liter 2-propanol per liter WCO), compared to what is reported in literature for conventional use of hydrogen gas at high pressures. Kinetics evaluation revealed that the rate of catalytic transfer hydrogenation of WCO is second order, with an activation energy of 53 kJ/mol. With 10 hours of continuous catalytic transfer hydrogenation (CTH) of WCO, the catalyst still maintained its catalytic activity, despite the inherent coke formation.

Keywords: Waste cooking oil, catalytic transfer hydrogenation, Hydrocarbon, jet fuel, Kinetics, coke formation.

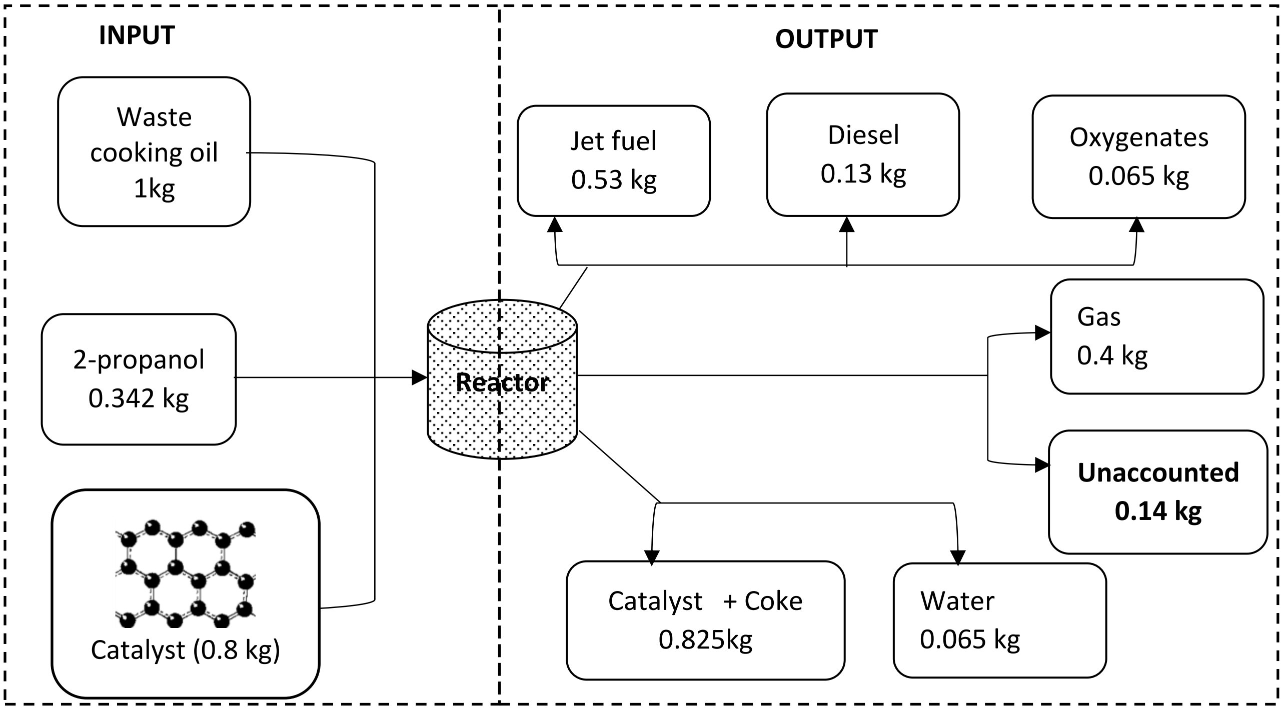
INPUT
OUTPUT
Waste cooking oil 1kg
2-propanol 0.342 kg
Catalyst (0.8 kg)
Reactor
Jet fuel 0.53 kg
Diesel 0.13 kg
Oxygenates 0.065 kg
Gas 0.4 kg
Unaccounted 0.14 kg
Catalyst + Coke 0.825kg
Water 0.065 kg

Catalytic Transfer Hydrogenation of waste cooking oil (70% C18:2 & C18:1) using 2-propanol at 2 bars and 380 °C over activated carbon

2.0. Introduction

The dwindling fossil fuels and their attendant environmental impacts in our time have given impetus to researchers in the energy sector to delve into different sustainable energy sources. These attendant problems are driven by the fact that the world population has been forecast to grow by 0.9% per year, from 7.3 billion in 2014 to 9.2 billion in 2040. Population growth will evidently trigger an increase in global energy consumption by approximately 29% in 2040. Its attendant CO_2 emission will increase as well, from 32381-36673 million tonnes [6]. In USA alone, 103 trillion MJ (transportation provides 29%) were consumed in 2016. According to U.S. Energy Information Administration (EIA), energy consumption will increase by 5% in US from 2016 to 2040. One of the energy consuming industries is the aviation sector, which the EIA predicts approximately a 45% increase (2.5-3.6 trillion MJ) in jet fuel consumption between 2016 and 2040 [7]. Furthermore, in its report in 2016, the Air Transport Action Group claimed that 278 billion liters of jet fuel were consumed by commercial operators; this led to 781 million tonnes of CO_2 emission [8].

Typical commercial or military jet fuel constitutes alkanes, cycloparafins, and aromatics (with carbon atom range: C_8-C_{16}), while road transportation constitutes diesel alkanes, cycloparafins, aromatics, and some oxygenates (with carbon atoms >C_{16}) [9]. This range of carbon atoms can be obtained from the conversion of waste triglyceride (renewable and sustainable), as the aviation industry has targeted 50% reduction in carbon emission by 2050. There are almost 300 types of fatty acid sources (mainly from animal fat or plant lipids) that can be harnessed for the production of jet/diesel fuel range [10]. However, some researchers have raised concerns about a potential interference with nutritional consumption if virgin fatty acids were employed in the jet/diesel fuel production [11, 12]. In view of this, there is continuous research for non-edible oil as a feedstock for jet/diesel fuel. A few of the proven non-edible oils as jet/diesel feedstock are jatropha [13]; bio-oil [14]; fatty acid distillates [15]; and microalgae [16].

In the quest for non-edible oil as jet/diesel fuel range feedstock, waste cooking oil (WCO) is no exception. WCO is produced by continuous oxidation reaction of virgin cooking oil via a typical free radical mechanism after an open-air frying process. The main oxidation product is hydroperoxide, which may further oxidize to toxic products, such as 4-hydroxy-2-alkenal, thereby rendering WCO a hazardous waste [17]. Moreover, it has been reported that WCO is considered non-edible, as it poses harmful diseases, such as dyspepsia, diarrhea, stomachache, and gastric cancer [18].

There are a few reasons why WCO oil should be considered as jet/diesel fuel feedstock. First, it is in large quantity around the globe, with an annual global generation of 29 million tons [19]. As consumption of edible oil will increase from 145 million to 660 million tons by 2050, its disposal will pose enormous challenges [20]. Second, a liter of WCO, when discharged to waterways, can pollute approximately 500,000 liters of water by obstructing sunlight penetration and oxygen exchange between the aquatic living things and the atmosphere [21]. Third, WCO is three times cheaper than virgin cooking oil, i.e. WCO costs 224 US dollar/ton compared to 771 US dollar/ton of virgin soybean oil [22]. Fourth, reusing WCO saves the environment and reduces the cost of wastewater treatment [23]. Lastly, the fatty acids composition of WCO contains approximately 14-22 carbon atoms. In addition, the carboxylic acid is the only functional group in the waste triglycerides, as compared to other biomass. With reference to these properties, it is easy to upgrade triglycerides into hydrocarbon fuels [24]. In view of these factors, WCO has been a feedstock for the commercial production of biodiesel with well-established processing facilities in the USA. This implies that there is a viable feedstock logistics and that there is the possibility of tailoring the current infrastructure to produce fuel for the aviation industry [22, 25]. In order to convert WCO into liquid hydrocarbon (LHC), whose cold properties are similar to that of the convention jet/diesel fuel, the WCO must be subjected to deoxygenation (oxygen removal from the triglyceride structure in the presence of hydrogen gas) via hydrodeoxygenation (HDO) and decarbonylation (DCO), and without hydrogen gas via decarboxylation (DCO_2) [26]. Thus, oxygen is removed from the oil in the form of water and carbon monoxide, and carbon dioxide, respectively. Conventionally, oxygen is removed from triglycerides using large volumes of gaseous hydrogen. Much research has been done to produce jet/diesel fuel range with hydrogen gas. Nearly 300-400 m^3 H_2/m^3 of vegetable oil is required to obtain a desirable LHC fuel (aromatic, alkanes, iso-alkanes, and cycloalkanes) [15]. A batch deoxygenation of soybean oil was performed at 300°C using 1 wt% Pd-supported on montmorillonite at an optimum time of 6 hours and H_2 gas pressure of 30 bars [27]. Mordechay et al. treated vegetable and animal oil in a batch reactor using Pt/SAPO-11. In addition, 800-1200 liters of H_2 gas per liter of oil was used [15]. Moti et al. also used 550 liters of H_2 gas to convert one liter of vegetable oil over Pt/SAPO-11 in a batch reactor at a reaction time of 150 hours and a temperature range of 375-380 °C [28]. Kim et al. reported the deoxygenation of soybean oil over Ni and $CoMoS_x$ catalyst by employing a H_2/oil molar ratio of 30-46 at a reaction temperature range of 300-400 °C and at a pressure range of 2.5-15 MPa (25-150 bar) [29]. Lu Li et al. cracked WCO over an ultra-stable zeolite (USY) catalyst in a pyrolytic reactor at a reaction time of 100 minutes and a temperature of 430 °C, and produced alkanes and alkenes with no aromatics [30]. A batch process of WCO to produce jet biofuel range using three different types of zeolite catalysts (Meso-Y, SAPO-34, and HY) loaded with nickel, and deoxygenation was achieved by H_2 gas at 30 bar in eight hours [31].

Based on the preceding laboratory hydrogenation work, many oil companies have scaled up the results of these studies to commercial levels. Among these companies are UOP/Eni (Ecofining process), Haldor Topsøe, The Neste Oil. (NExBTL process), Tyson Foods Inc. and Syntroleum Corporation, Valero Energy Corporation, ConocoPhillips, Toyota Motor Corporation, Hino Motors, and Nippon Oil Corporation. These companies employ a two-step process: hydrodeoxygenation to produce long-chain paraffins followed by hydroisomerization-hydrocracking, in order to improve the cold properties of the fuel in a different reactor. These two steps utilize large volumes of gaseous hydrogen at an inordinate pressure of 150 bar [32]. All of the above-mentioned processes require a long reaction time, high pressure, and most of all a very large amount of hydrogen gas. Although hydrogen is produced at the refinery industries and is considered to be the best raw material for hydrotreating conventional fuel, it is in short supply and it is of fossil-fuel base [33]. This means that relying on gaseous hydrogen from the refining industry to hydrogenate and deoxygenate triglycerides will be unsustainable. Additionally, employing a large volume of hydrogen gas in the deoxygenation process poses handling problems that require a potentially huge fixed capital investment. Besides, gaseous hydrogen (nonpolar) is not all that soluble in triglyceride at near atmosphere. Hence, there is an inherent problem of mass transfer and diffusion of hydrogen during deoxygenation. To overcome the problem of diffusion and mass transfer, some researchers have carried out the deoxygenation reaction at the high pressure range of 25-100 bar [34], [35], [36], [37]. Running deoxygenation at such a high-pressure range may pose probable safety concerns with high energy input, and may put significant stress on the deoxygenation reactors and their ancillary equipment that could lead to considerable maintenance cost and an attendant short project life span. Lastly, one of the major problems with gaseous hydrogen is its ability to diffuse through stainless steel to decrease its plasticity and toughness, which leads to a phenomenon known as hydrogen embrittlement, leading to cracks and unpredictable fractures in the walls of reactors [38], [39]. Consequently, all of these factors may increase the unit cost and price of the fuel, and may finally render the process unsustainable.

Most of these potential problems can be solved or reduced by the application of CTH, which is a reduction of unsaturated organics (such as oleic acid), using hydrogen-donating compounds, that catalytically produces hydrogen *in situ*. As opposed to hydrotreating, that uses gaseous hydrogen to remove sulfur, nitrogen, and aromatics from organics [40], CTH uses a hydrogen-donating solvent as a reducing agent by producing hydrogen *in situ* in the presence of a catalyst. CTH is advantageous over hydrogenation using gaseous hydrogen, since CTH can address most of the above-mentioned disadvantages of hydrogenating triglyceride with gaseous hydrogen [41]. In addition to reducing inconvenient transportation and high cost of hydrogen storage [42], CTH addresses most of the above-mentioned potential problems associated with gaseous hydrogen.

With exception of WCO, a large amount of biomass was subjected to CTH by using different solvents: dehydrogenation of lignin with decalin and tetralin [43]; stearic acid was hydrotreated with tetralin [44]; heavy crude oil was upgraded with tetralin, decalin and naphthalene [45]; oil palm fruit bunch was liquefied with sub- and supercritical tetralin and n-dodecane [46]; crude Jatropha oil [13], levulinic acid [47], and furfural [48] were deoxygenated with formic acid; the effect of cyclohexane as hydrogen donor has been reported [49]; atmospheric residue was treated with tetrahydronaphthalene [50]; sunflower [51], allylic alcohol [52]; carbonyl compounds, alkenes, and nitrobenzene [53] were deoxygenated with glycerol; coal was liquefied by 9,10-dihydroanthracene, 9,10-dihydrophenanthrene, 1,2,3,4-tetrahydroquinoline, 1,2,3,4-tetrahydro-6-naphthol and 1,2,3,4,5,6,7,8-octahydroanthracene [54]. One of the advantages of using hydrocarbons as *in situ* hydrogen donors lies in the fact that the bond energy of C-H is lower than that of the H-H bond in H_2 [55]. However, most of these hydrogen donors are costly, toxic, and volatile. The most available, less toxic, and less costly are the common alcohols (methanol, ethanol, n-propanol and 2-propanol), which have been reported to be effective hydrogen donors. Methanol has been used to hydrogenate styrene and nitrobenzene [41]. Ethanol and 2-propanol were used to deoxygenate levulinic acid over 5% Pd/C [56]. Among these common alcohols, the primary alcohols are generally less active than the secondary alcohols, due to the smaller electron-releasing inductive effect of one alkyl group as against two [41]. For example, the two methyl groups in 2-propanol donate more electrons to weaken the O-H bond, compared to the lower electron-donating ability of one methyl group and one ethyl group in methanol and ethanol respectively. This premise makes 2-propanol a better CTH solvent than the other common alcohols. 2-propanol is inexpensive ($1.80/kg [57]) compared to gaseous hydrogen ($3-12.85/kg [58] [59, 60]); it is non-toxic, and it possesses good solvent properties [61] (e.g. miscible with triglycerides). Lastly, 2-propanol can be produced from renewable feedstocks: acetone that can be hydrogenated to 2-propanol [62-64]; glycerol that can be converted catalytically to propylene that, in turn, undergoes hydration to produce 2-propanol [65, 66]. Since no work has been done on the reaction between 2-propanol and waste cooking oil, we take advantage of CTH by employing the hydrogen-donating capacity of 2-propanol, which produces acetone and hydrogen upon decomposition, as reported in literature Eq.(2.1-2.2) [67].

$$C_3H_7OH \longrightarrow CH_3C(O)CH_3 + H_2 \tag{2.1}$$

$$C_3H_7OH \longrightarrow CH_2C(OH)CH_3 + H_2 \tag{2.2}$$

To the best of our knowledge, 2-propanol has not been used for the hydrogenation and deoxygenation of WCO. Hence, in this study, catalytic transfer hydrogenation of WCO to produce LHC fuels was performed, using 2-propanol as a H-donor in a continuous flow reactor over a fixed bed of activated carbon. The selected catalyst in this study is relatively inexpensive and is renewable [68], [34]. The kinetics of CTH, comprising a lump reaction order for WCO conversion, was elucidated. The lump reaction rate equation was assumed to be controlled by hydrogen produced by 2-propanol. The catalyst in this study was characterized using thermogravimetric and surface area analysis. This work addresses the problems of high-pressure hydrogenation, the high volume of gaseous H_2 handling, and the inherently low mass transfer of gaseous H_2 in a conventional hydrogenation. It should be noted that a rigorous proof of the occurrence of CTH, which requires isotope labeling, and the rate of mass transfer of H_2 produced by 2-propanol is beyond the scope of this work. Summarily, the novelty of this work lies in the fact that catalytic transfer hydrogenation of WCO was carried out near an atmospheric pressure that is impossible by using gaseous hydrogen. Besides, CTH was executed by using non-toxic and non-acidic 2-propanol as an *in-situ* hydrogen donor.

2.1. Material and Methods

2.1.1. Materials

The granular activated carbon (8-20 mesh), 2-propanol (99.5 wt%) and dichloromethane, diethyl ether, and anhydrous sodium sulfate were purchased from Fisher Scientific Company. The WCO was obtained from a local restaurant in Norfolk, Virginia.

2.1.2. Characterization of WCO

Determination of fatty acid composition of WCO

1 mL of WCO was measured into a 20-mL test tube. The tube and its contents were placed in a water bath and allowed to heat to the required 60 ^{o}C. Then, 1.2 wt.% catalyst (NaOH) (1.2% of WCO) was dissolved in 0.397 mL of methanol to obtain approximate molar ratio of methanol to oil of 10 [69]. The basic methanol was added to the oil in the test tube. The test tube was then

capped, and the transesterification reaction was allowed to proceed. The test tube and its contents were agitated intermittently with a vortex mixer to enhance the reaction. The reaction was stopped in one hour and was allowed to cool to room temperature. The FAME and the glycerol were separated by centrifugation. The FAME was pipetted into a separating funnel, and 2 mL of diethyl ether was added to the FAME, followed by several washings, using distilled water to remove excess base. The solvent was then dried over anhydrous sodium sulfate. The ether was separated from the oil by vacuum (0.1 bars) evaporation. The oil was poured into small aluminum can and was dried for two hours at 60 ^{o}C in an oven. The FAME was then poured into a vial and was refrigerated prior to FAME analysis by gas chromatography mass spectroscopy (GCMS). The experiment was conducted in triplicate.

Thermogravimetric-Differential Analysis (TGA-DTA) of WCO

TGA-DTA analysis was carried out using Shimadzu TGA 50-50H. Approximately 0.1 mL of WCO was placed into a Pt sample pan. The experiment was conducted in a nitrogen atmosphere at a flow rate of 10 mL/min. The sample was heated from 20 to 900 ^{o}C at a heating rate of 10 ^{o}C/min, and was held at 900 ^{o}C for 5 min. The experiment was repeated in triplicate.

2.1.3. Characterization of Catalyst

To assess the stability of the catalyst, the surface area, the pore volume, and the pore size of the new and used catalyst were measured by using Quantachrome NOVA 200e surface area analyzer. Catalyst samples were cleaned in hexane, dried, and degassed at 300 ^{o}C for three hours. Samples were cooled to room temperature after which nitrogen adsorption-desorption isotherms at -196 ^{o}C were measured. The surface area was evaluated using the multi-point Brunauer-Emmett-Teller (BET) model, as it considers both monolayer and multilayer adsorption, which gives better results, as opposed to monolayer adsorption models, which give a lower surface area than the actual value [70]. The pore size distribution was obtained from the desorption isotherm using the Barret-Joyner-Halenda (BJH) model, while the total pore volume was calculated at relative pressure range of 0.0-1.0. All of these models were embedded in the NovaWin Software. The amount of coke formation was determined using TGA-DTA, by measuring the percent mass loss of the catalyst. The procedure is the same as the one described in the section above. In this case, approximately 10 mg of catalyst was used in the analysis.

2.1.4. CTH Experiments

The CTH experiments were carried out in a packed bed continuous flow reactor. The stainless-steel tubular reactor of dimension 360 x 15 mm was placed inside an 8-kW heating furnace with an automatic temperature control (Figure 2.1). Flow rates of both 2-propanol and WCO were controlled by high-performance liquid chromatography (HPLC) pumps.

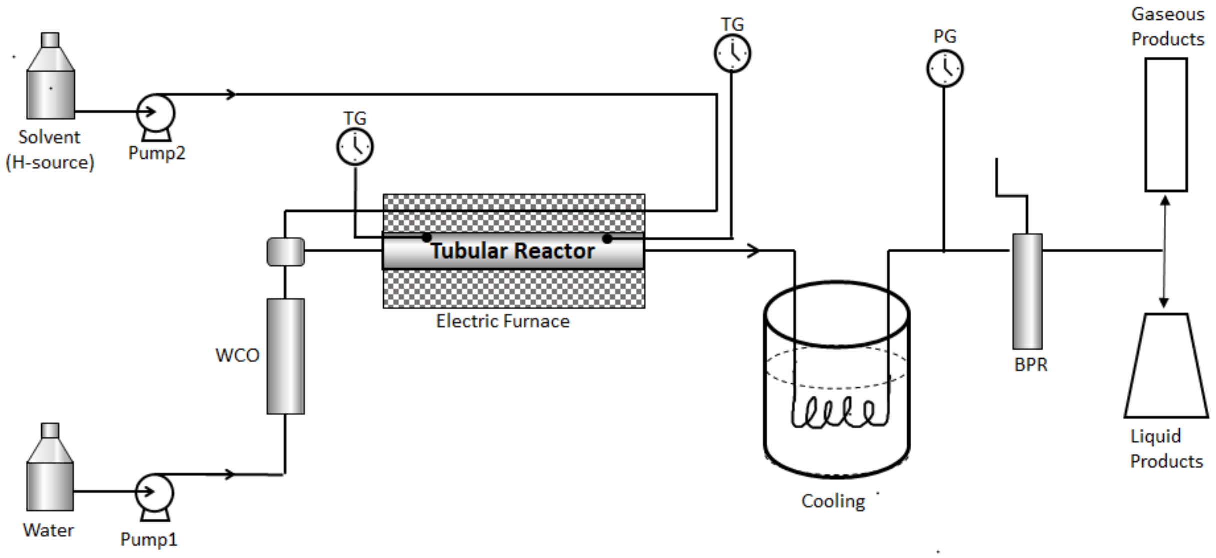
TG
PG
Gaseous Products
Solvent (H-source)
Pump2
TG
Tubular Reactor
Electric Furnace
WCO
BPR
Liquid Products
Water
Pump1
Cooling

Figure 2.1. Experimental set-up for a continuous-flow fixed bed for deoxygenation of waste cooking oil. PG-Pressure gauge; TG-Digital temperature gauge.

The CTH reaction was carried out at 2 bar, a temperature range of 300-400 ^{o}C, a weight hourly space velocity (WHSV) of 6.8 h^{-1}, and WCO:2-propanol ratio of 2.5. The WHSV, pressure, and WCO:2-propanol ratio were kept constant. To ensure low reaction pressure, the back-pressure regulator was open to the fullest, which gave a minimum pressure of 2 bar at feed flow rate of 0.7 mL/min (WCO:2-propanol = 0.5:0.2). The ratio of WCO to 2-propanol was calculated based on the amount of hydrogen required to saturate or hydrogenate the two double bonds in the C18 fatty acid. The pressure (2 bar) was maintained using a back-pressure regulator located at the outlet of the reactor. As a control experiment, 78 mL of WCO was placed in a vertical tube connected to a piston and was run through a tubular reactor at a flow rate of 0.5 mL/min without a catalyst. Pump 1 was used to pump the water, which acted as a hydraulic fluid that pushed a piston that, in turn, pushed the WCO through the reactor. Liquid products were sampled every 30 minutes for 2.5 hours per run at different temperatures (Table 2.1). The reactor was then loaded with 5.5 g of granulated activated carbon, and the procedure was repeated. Next, 2-propanol and WCO were run through the reactor without a catalyst.

Table 2.1 Conditions for Control Experiments.

Experimental Run	Temperature (°C)	Pressure (bar)	Run time (h)
1	300	2	2.5
2	340	2	2.5
3	360	2	2.5
4	380	2	2.5
5	400	2	2.5

Table 2.2. CTH Experimental Conditions

Experimental Run	Temperature (^oC)	Pressure (bar)	WHSV (h^{-1})	Run time (h)
1	300	2	6.8	2.5
2	300	2	6.8	2.5
3	340	2	6.8	2.5
4	340	2	6.8	2.5
5	360	2	6.8	2.5
6	360	2	6.8	2.5
7	380	2	6.8	2.5
8	380	2	6.8	2.5
9	400	2	6.8	2.5
10	400	2	6.8	2.5

After these runs, the CTH of WCO was run using 2-propanol (99.5 wt%) by flowing 0.5 mL/min WCO and 0.2 mL/min 2-propanol over 5.5-g catalytic fixed bed while keeping the weight hourly space velocity (WHSV) of 6.8 h^{-1}. The CTH was run at different temperatures while keeping the pressure constant (Table 2.2). The amount of liquid fuel obtained from each run was collected and measured in each case.

2.1.5. Product Analysis

Liquid fuel products were analyzed by the Shimadzu GCMS-QP2010SE and Gas chromatography GC2010 plus. The following were the settings of the instrument: inlet pressure 45 kPa; column flow 0.94 mL/min; split ratio 25; injection temperature-250 ^oC; GC-MS interface temperature 280 ^oC; ion source temperature-225 ^oC; sample ionization method: electron ionization. The column specifications were as follows: column type SH-Rxi-5Sil MS; length 30 m; internal diameter 0.25 mm; film thickness 0.25 µm. The temperature program for the column were initial temperature 40 ^oC, ramp 12 ^oC/min, and final temperature of 300 ^oC at a hold time of

8 minutes. The gaseous products were detected by SRI model 8610C gas chromatography (GC) with a TCD and dual 3 feet x 1/8-inch OD packed column. Carrier gas used was helium at a flow rate of 10 mL/min. The initial oven temperature was set at 40 °C and ramped at 20 °C/min to 250 °C. All products analyses were performed in triplicates. With the results from the GCMS, the WCO conversion X (%) was calculated as Eq. (2.3):

$$\text{Conversion} = \frac{[(Initial\ mass\ of\ WCO)-(unreacted\ \ mass\ of\ WCO)]\times 100\%}{Initial\ mass\ of\ WCO} \quad (2.3)$$

It was assumed that the fatty acids obtained in the GCMS results represented the unreacted WCO.

The liquid fuel yield was also calculated as Eq. (2.4):

$$\text{Yield} = \frac{Total\ mass\ of\ liquid\ product}{Mass\ of\ WCO} \times 100\% \quad (2.4)$$

Moreover, the total amount of coke formed was calculated as Eq. (2.5):

$$\text{Total coke formed} = (\%\ \text{mass loss}) \times (\text{total mass of catalyst}) \quad (2.5)$$

2.2. Results and Discussions

2.2.1. Characterization of WCO

The analysis of WCO showed 70.34% unsaturated (compose one or two $-C=C-$ bonds) in the carbon chain, while the rest was saturated (contained only $-C-C-$ bond) (Table 2. 3). This value of unsaturation can be compared to what is in the literature: 87.18 % [71]; 91.5% [72]; 88.3% [73]; 48.1% [74]. The discrepancy in the degree of unsaturation might be traceable to the degree of degradation of the oil during deep frying. Also, their respective virgin oils could have different fatty acid compositions. It could also be attributed to the degree of hydrolysis that the oil underwent during its use

Table 2.3. Fatty Acid Composition of WCO

Compound	wt%
9-Hexadecenoic acid-($C_{16}H_{30}O_2$)	1.36
Pentadecanoic acid ($C_{15}H_{30}O_2$)	16.96
Heptadecanoic acid($C_{17}H_{34}O_2$)	0.25
8,11 Octadecadienoic acid ($C_{18}H_{32}O_2$)	49.57
9-Octadecenoic acid ($C_{18}H_{34}O_2$)	17.8
Stearic acid ($C_{18}H_{36}O_2$)	10.68
9,11-Octadecadienoic acid ($C_{18}H_{32}O_2$)	0.69
11-eicosenoate($C_{20}H_{38}O_2$)	0.92
Nonadecanoic acid($C_{20}H_{40}O_2$)	0.76
Heneicosanoic acid ($C_{21}H_{42}O_2$)	0.10
Docosanoic acid($C_{22}H_{44}O_2$)	0.65
Tricosanoic acid($C_{23}H_{46}O_2$)	0.07
Tetracosanoic acid($C_{24}H_{48}O_2$)	0.19

The unsaturated nature, or the presence of carbon-carbon double bond of the WCO, renders it reactive when subjected to hydrogenation [75]. Table 2.3 shows that 78% of the fatty acid comprises eighteen carbon atoms (C18), and 16% contains less than eighteen carbon atoms (C15-C17), while 2.7% contains more than eighteen carbon atoms (C19-C24). This means that the average molecular weight of fatty acid in the WCO was estimated to be 280 g/mol. To further understand the possible deoxygenation temperature range of the WCO, TGA-DTA was performed. It was revealed that, at a temperature range of 300-460 ^{o}C, the chemical bonds of WCO could be broken. Within this temperature range, 98% of the mass of the WCO was vaporized (Figure 2.2). The free fatty acid of and the density of WCO were determined to be 1.41 and 0.92 g/mL, respectively. The presence of FFA in the WCO signifies that it has undergone some hydrolysis, and it is, no more, a triglyceride.

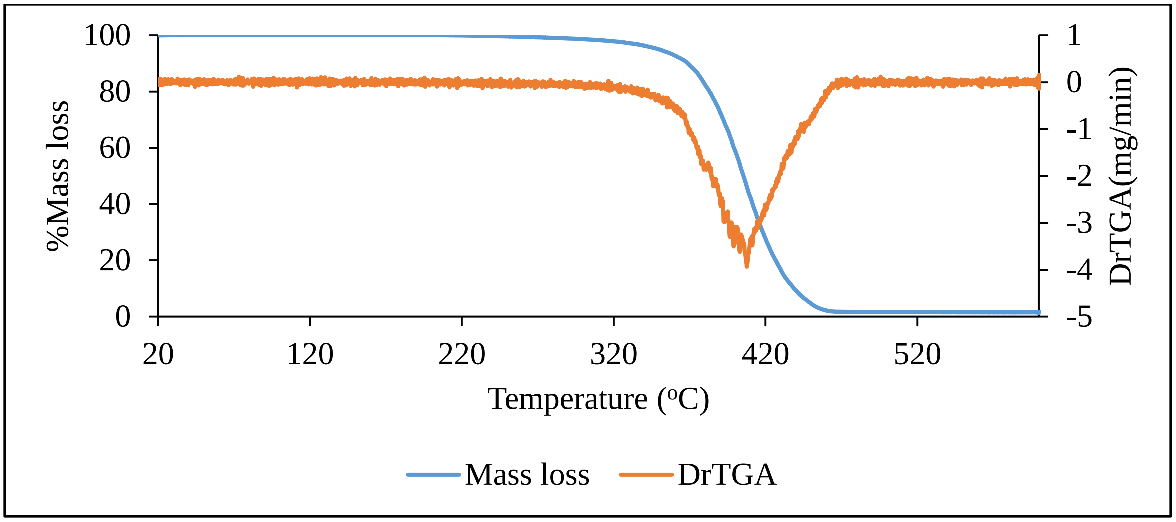

Figure 1.2. Thermal gravimetric analysis of WCO

2.2.2. CTH of WCO

Conversion

It was observed that running only WCO through the reactor at a temperature range of 300-400 ^{o}C caused some chemical changes, in the absence of a hydrogen donor. Increasing the temperature from 300-400 ^{o}C produced alkenes, oxygenates (alcohols, ketones, acetates and aldehydes), and an insignificant amount of alkanes (Figure A1). A progressive decrease in fatty acid gave rise to the production of more oxygenates, which comprise alcohols, ketones, acetates and aldehydes (Figure A2). As the temperature increased, the acetates decomposed to produce more alcohols and an insignificant amount of aldehydes and ketones. The result of this control experiment can be compared to that found in literature [20].

Also, running the reaction with WCO and catalyst without 2-propanol did not produce many alkanes (24%) and aromatics (2.5%) at 380 ^{o}C, because there was H-donor to supply hydrogen to saturate the oil (Figure A3). Notably, running the reaction (WCO and 2-propanol only) without a catalyst produced just 18% alkanes, 10% aromatics, and high level of oxygenates at 380 ^{o}C (Figure A4-A5) because there was no catalyst to facilitate the transfer of H_2 to the oil.

The catalytic transfer hydrogenation of WCO using 2-propanol as the hydrogen donor revealed different kinds of products based on the results from the GCMS analysis. The main components in the liquid fuel are aromatics (toluene, xylene and naphthalene), alkanes (n-alkanes, iso-alkanes, and cyclo-alkanes), alkenes (straight chain alkenes and cyclo-alkenes), oxygenates (alcohol, ketones and aldehydes), and unreacted fatty acids (Tables A2-A6, supplementary sheet). These results could be compared to the deoxygenation of oleic acid over activated carbon in the presence of formic acid as a hydrogen donor that resulted in cyclization and hydrogenation [76]. Gaseous products revealed in the GC analysis contained H_2, CO, CO_2 and C1-C3 gaseous products (Table A1). The material balance shows that 30% of the total material input produced gaseous products; 54% was liquid fuel, 4.8% was water, and 1.8% was coke formation at the optimum operating temperature of 380 ^{o}C (see graphical abstract). The presence of H_2O, CO and CO_2 was a clear evidence that WCO underwent hydrodeoxygenation, decarbonylation, and decarboxylation, respectively [77-79].

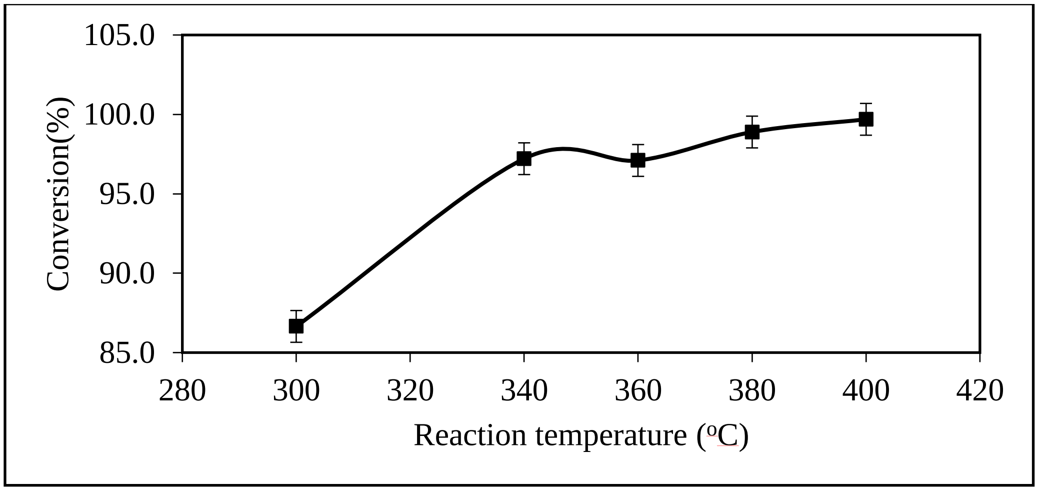

Figure 2.2. Conversion of WCO by CTH at different reaction temperatures

Evidently, the conversion of WCO did increase from 87-99.9% as the temperature increased from 300-400 °C (Figure 2.3) by keeping the pressure and the WHSV at 2 bar and 6.8 h^{-1}, respectively. Other studies obtained similar WCO conversions over a NiMo-CoMo-NiW/SiO_2-Al_2O_3 catalyst using gaseous H_2 for hydrogenation at a pressure range of 70-100 bar: 99.8% [71]; 85.7 [80]; 83% [73]. The level of conversion in the current study was comparable to the published results of work probably because of the easy mass transfer of the H_2 produced by 2-propanol due to the premixed nature of the two reactants (liquid-liquid mixture). The increase in WCO conversion was due to the increasing C-C and C-O bonds breaking as the temperature increased [81, 82]. Consequently, liquid fuel yield also increased from 58% to 72% with an increase in temperature (Figure 2.4). The liquid fuel peaked at 380 °C and dipped as temperature increased above 380 °C, as more thermal cracking led to more gaseous products.

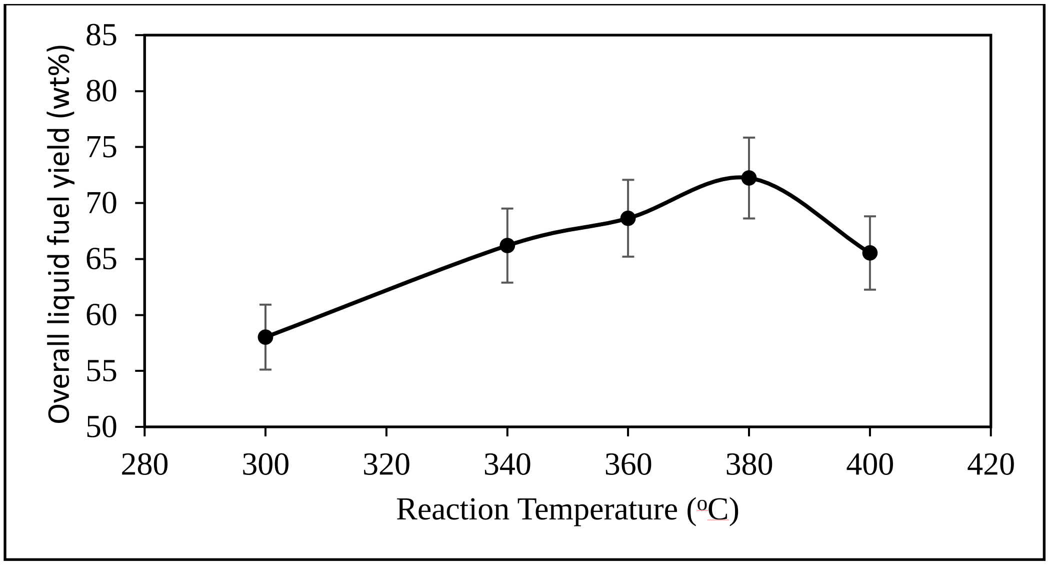

Figure 2.3. Overall liquid fuel yield from CTH of WCO at different reaction temperatures

The fuel composition obtained from hydrotreating of WCO were short-chain alkanes (C6-C14), aromatics, cyclo-alkenes, cyclo-alkanes, short-chain alkenes (C6-C14), long-chain alkenes (C15-C17), oxygenates, long-chain alkanes (C15-C17), and iso-alkanes (Tables A2-A5 & Figures 6A-

A7). C6-C14 was classified as being short because the shortest carbon chain in the triglyceride used in this study was C15. This means that any number of carbon chain below C15 was obtained by cleavage during the reaction. From 300-340 ^{o}C, it could be inferred that most of the fuel composition remained somehow constant except for the oxygenates and short-chain (SC) alkenes; these changed sharply due to C-O and C-C-bond cleavages, respectively. As the RCOOH degraded via C-O bond scission, which gave rise to long-chain(LC) alkenes, the LC alkenes, in turn, cleaved, to produce more SC alkenes that decreased the LC alkenes from 300-340 ^{o}C[81]. It was also observed that, at higher temperatures, aromatics increased due to dehydrogenation of alkanes to form alkenes leading aromatization (Figure 2.5) since dehydrogenation is endothermic [81]. Figure 2.6 shows the distillates obtained from raw fuels at different temperatures.

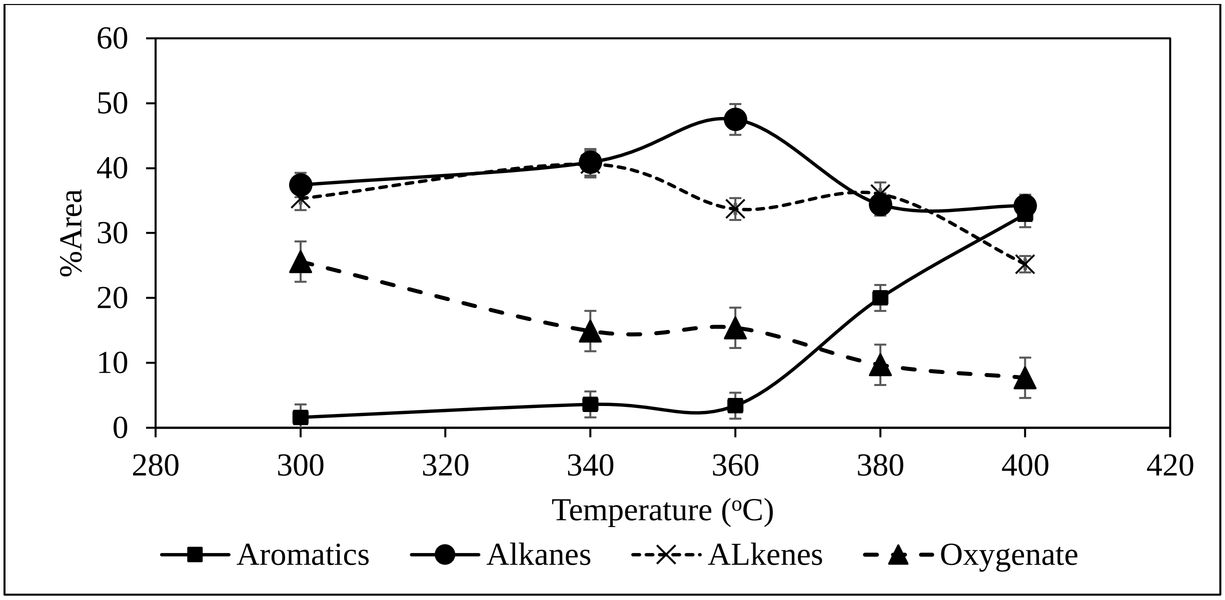

Figure 2.4. Liquid fuel composition at different temperatures

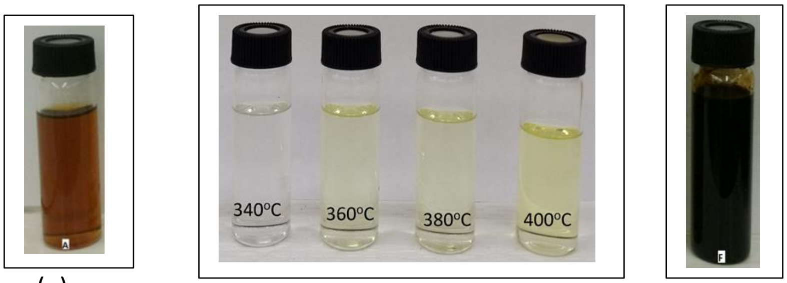

(a) (b) (c)

Figure 2.5. Products: (a) raw product fuel obtained at 2 bar; (b) fuel distillate from raw product distilled under vacuum (0.2 bar) at 90 °C; (c) tar obtained after vacuum distillation of raw product fuel.

Table 2.4 compares the physical properties of the liquid fuel to those of ASTM standard [83].

Simulated distillation (Figure 2.7) of the fuel product at 380 °C revealed that approximately 95% of the fuel is recovered below 200 °C, signifying the lightness of the fuel.

Table 2.4. Physical Properties of the Liquid Hydrocarbon Compared to that of ASTM standards

Physical properties	**Current study**		**ASTM[83]**	**Test method**
Acidity, mg KOH/g	0.11	max	0.1	D3242
Aromatics(%v/v)	20	max	25	D1319
Distillation temperature, °C				
%10 recovered	54	max	200	
%50 recovered	74		Report	
%90 recovered	172		Report	
Final boiling point °C	403	max	300	
Density @ 15 °C, kg/m^3	790-820		775-840	D1298
Freezing point (°C)	-46		-40-47	D5972
Viscosity (mm^2/s)	6.6		8	D445
Net Heat of Combustion, MJ/kg	44		42.8	D4529

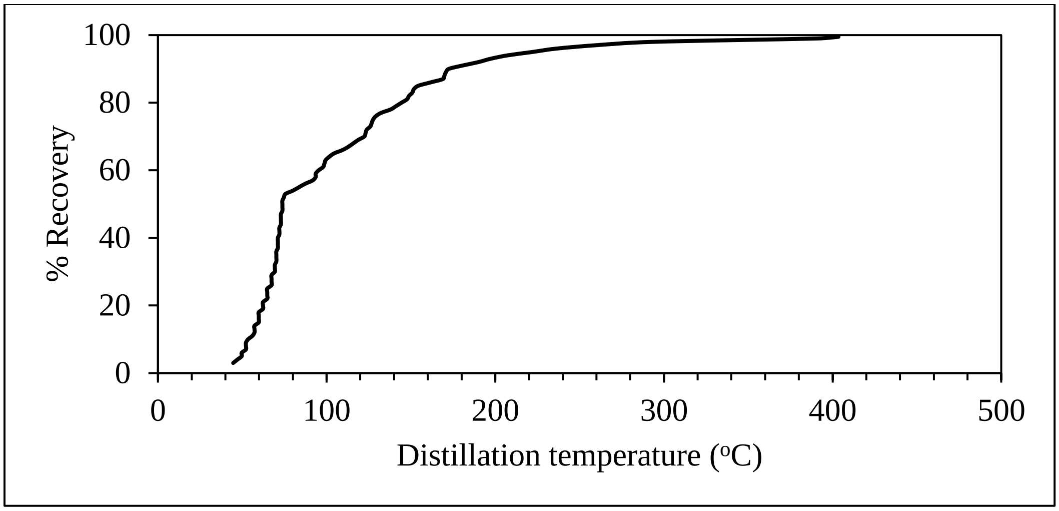

Figure 2.6. Simulated distillation of the liquid fuel product obtained at 380 ^oC.

Fuel Yield

The jet-range fuel yield increased from 22% to 52% under the CTH conditions at a high temperature. This result is comparable to that reported by Li et al. [31], who used nickel-base mesoporous zeolite catalyst under H_2 pressure of 30 bar at 390 ^oC. Diesel-range fuel (C15-C18), on the other hand, decreases from 29% to 9% (Figure 2.8). It could also be inferred from Figure 6A that C6-C14 increased due to high probability of thermal cracking of C15-C18 at high temperature. Besides, iso- and cyclo-alkanes decreased with increasing temperature, owing to dehydrogenation. This buttresses the fact that the yield for jet-fuel range increased, while that of diesel-fuel range decreased as the temperature increased.

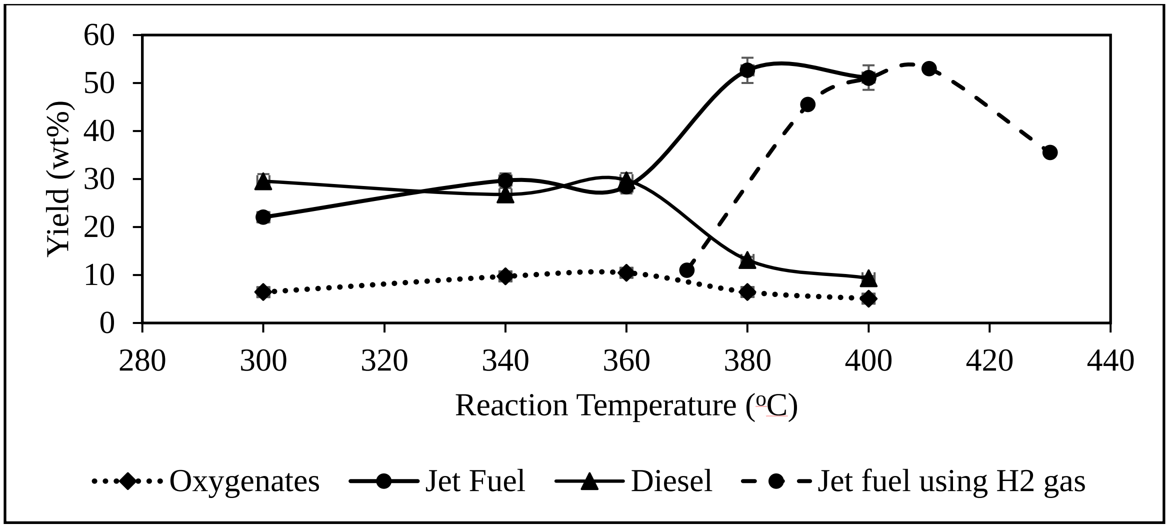

Figure 2.7. Liquid Fuel fractions at different temperatures

2.2.3. Reaction Mechanism

Based on the products obtained at different temperatures (300-400 °C), we proposed possible reaction pathways (Figure 2.9) for CTH of WCO that are in agreement with the literature [81]. The CTH could occur in two different routes: the left route (2’-7’-10’-11’ or 2’-9’-6’-9’’-10’-11’) and the right route (1-2-3-5-6-9-10-11-12-13 or 1-2-7-10-11-12-13).

On the left route, C-O bond underwent thermal cleavage, followed by a decarboxylation (CO_2 release) (7’) of carboxylic acid that resulted in long-chain alkenes. These LC alkenes underwent hydrogenolysis (C-C bond scission by H_2) (10’) and gave rise to SC alkenes. This was followed by isomerization (11’), to produce iso-alkanes.

On the right route, the WCO was subjected to hydrogenation (1’). This was followed by hydrodeoxygenation with the scission of C-O and with an addition of H_2; HDO occurred (2’), which produced fatty acid (RCOOH) and propane. The resulting carboxylic acid could suffer either decarboxylation (7) or decarbonylation (8) or hydrodeoxygenation (9) to produce long-chain alkanes. The long-chain alkanes were then subjected to hydrogenolysis (10) to produce short-chain alkanes. The short-chain alkanes also underwent cyclization (12) to produce cycloalkanes. Finally, by catalytic dehydrogenation [84] to release H_2, cyclo-alkanes produced aromatics and polyaromatics such as naphthalene.

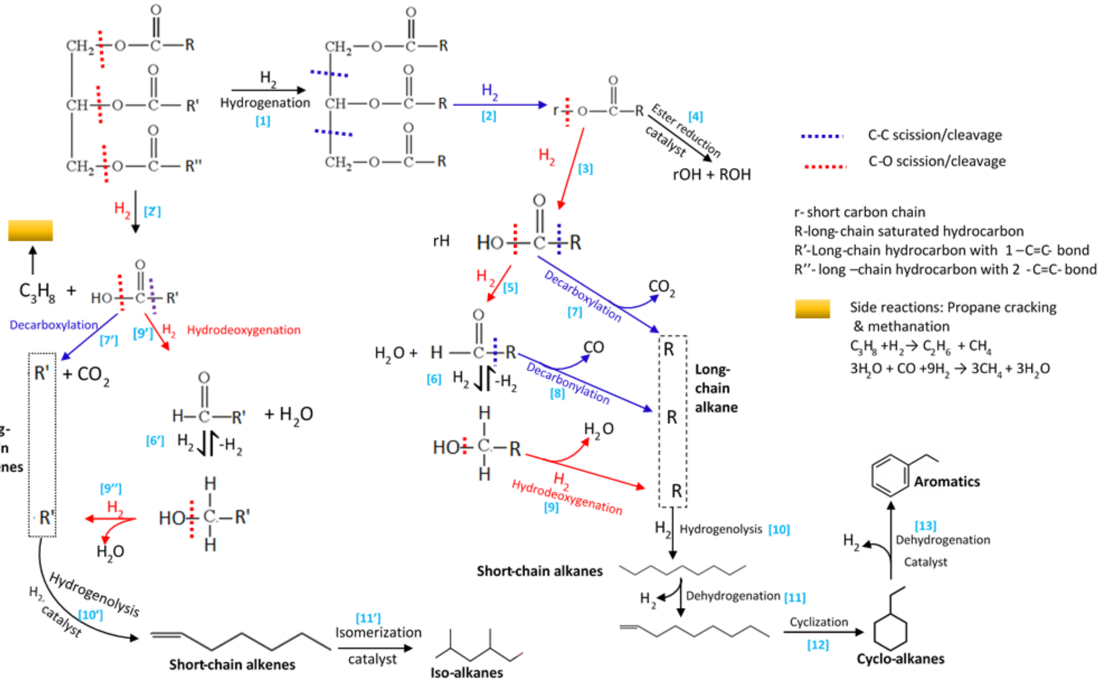
H2
Hydrogenation
[1]
H2
[2]
Ester reduction
catalyst
[4]
rOH + ROH
H2
[3]
H2
[2']
C3H8 +
Decarboxylation
[7']
[9']
H2
Hydrodeoxygenation
R' + CO2
Long-chain alkenes
rH
H2
[5]
Decarboxylation
[7]
CO2
H2O + H
CO
[6]
Decarbonylation
[8]
Long-chain alkane
H2O
H2
Hydrodeoxygenation
[9]
+ H2O
[6']
[9'']
H2
H2O
Hydrogenolysis
[10']
H2, catalyst
H2
Hydrogenolysis [10]
Short-chain alkanes
H2
Dehydrogenation [11]
Cyclization
[12]
Cyclo-alkanes
H2
[13]
Dehydrogenation
Catalyst
Aromatics
Short-chain alkenes
[11']
Isomerization
catalyst
Iso-alkanes
C-C scission/cleavage
C-O scission/cleavage
r- short carbon chain
R-long-chain saturated hydrocarbon
R'-Long-chain hydrocarbon with 1 –C=C- bond
R''- long –chain hydrocarbon with 2 -C=C- bond
Side reactions: Propane cracking & methanation
C3H8 +H2→ C2H6 + CH4
3H2O + CO +9H2 → 3CH4 + 3H2O

Figure 2.8. Possible WCO deoxygenation routes using 2-propanol and formic acid as H-donors. The red dash lines represent the C-O cleavage route, while the violet lines depict the C-C cleavage routes.

2.2.4. Reaction Kinetics.

The CTH rate was assessed by lumping the complex reaction into a single reaction as shown in Eq. (2.6), which was obtained from the elementary reactions in Table 2.5. The following elementary assumptions were made: (i) one-dimensional flow; (ii) isothermal and steady state conditions; (iii) mathematical expression, which was assumed to be independent of kinetic mechanism or proposed reaction path; (iv) the gaseous phase reaction, which was assumed at such a near atmospheric pressure; (v) the lump reaction, which was assumed to composed of the elementary reactions of conventional fatty acids (Table 2.5); (vi) it was assumed that compressibility factor of species in the reactor does not change significantly; and [85] perfect plug flow and absence of temperature gradients inside the catalyst particles were assumed.

Table 2.5. Stoichiometric reactions of conversion of WCO to $C_{12}H_{26}$, C_8H_{16} and $C_{17}H_{36}$

	REACTIONS
1.a	$C_{18}H_{34}O_2+4H_2 \rightarrow C_{12}H_{26}+CO+H_2O+C_3H_8+C_2H_6$
1.b	$C_{18}H_{34}O_2+H_2 \rightarrow 2C_8H_{16}+CO_2+CH_4$
1.c	$C_{18}H_{34}O_2+2H \rightarrow C_{17}H_{36}+CO+H_2O$
1.total	**$C_{18}H_{34}O_2+(4a+b+2c)H_2 \rightarrow aC_{12}H_{26}+2bC_8H_{16}+cC_{17}H_{36}+(a+c)CO+(a+c)H_2O+bCO_2+aC_3H_8+aC_2H_6+bCH_4$**
2.a	$C_{18}H_{32}O_2+5H_2 \rightarrow C_{12}H_{26}+CO+H_2O+C_3H_8+C_2H_6$
2.b	$C_{18}H_{32}O_2+2H_2 \rightarrow 2C_8H_{16}+CO_2+CH_4$
2.c	$C_{18}H_{32}O_2+3H_2 \rightarrow C_{17}H_{36}+CO+H_2O$
2.total	**$C_{18}H_{32}O_2+(5a+2b+3c)H_2 \rightarrow aC_{12}H_{26}+2bC_8H_{16}+cC_{17}H_{36}+(a+c)CO+(a+c)H_2O+bCO_2+aC_3H_8+aC_2H_6+bCH_4$**
3.a	$C_{18}H_{36}O_2+3H_2 \rightarrow C_{12}H_{26}+CO+H_2O+C_3H_8+C_2H_6$
3.b	$C_{18}H_{36}O_2 \rightarrow 2C_8H_{16}+CO_2+CH_4$
3.c	$C_{18}H_{36}O_2+H_2 \rightarrow C_{17}H_{36}+CO+H_2O$
3.total	**$C_{18}H_{36}O_2+(3a+0b+1c)H_2 \rightarrow aC_{12}H_{26}+2bC_8H_{16}+cC_{17}H_{36}+(a+c)CO+(a+c)H_2O+bCO_2+aC_3H_8+aC_2H_6+bCH_4$**
4.a'	$C_{15}H_{30}O_2+2H_2 \rightarrow C_{12}H_{26}+CO+H_2O+C_2H_6$
4.b'	$C_{15}H_{30}O_2+2H_2 \rightarrow C_8H_{16}+CO_2+C_3H_8+C_2H_6+CH_4$
4.total	**$C_{15}H_{30}O_2+(2a'+2b')H_2 \rightarrow a'C_{12}H_{26}+b'C_3H_8+a'CO+a'H_2O+(a'+b')C_2H_6 + b'CO_2+b'CH_4$**
GLOBAL	**$4\ WCO+11\ H_2 \rightarrow 17.5$ Products**

(a = 0.56; b = 0.28; c = 0.12; a' = 0.52; b' = 0.48)

The critical temperature (no liquid exists above this) of the reactants was estimated to be 440 ^oC; this was slightly higher than reaction temperature. This was estimated from the average critical temperature of WCO (based on C15-C18) and that of 2-propanol [86]. Moreover, this critical value was based on a pure components mixture. In a real case, where the catalyst is present to enhance chemical reaction or bond disruption at 380 ^oC, there is a high possibility of a more gaseous phase than liquid phase present. Also, the reaction occurred in the gaseous phase because 40% of the pure WCO existed in the gaseous phase (Figure 2.2), meaning that the likely boiling point of WCO was 380 ^oC. In addition, the boiling point of 2-propanol was approximately 81^oC (from the material data sheet). Therefore, a mixture of 0.5 mL WCO and 0.2

mL 2-propanol would have a boiling point of 295 ^oC. Hence, gaseous reactants at 380 ^oC (and at such a low pressure (2 bar)) could be assumed.

Furthermore, it was assumed that 2-propanol thermally decomposes in the first section of the reactor to release H_2 according to Eq. (2.1), and that acetone is further degraded to give CH_4, C_2H_6 and CO (Eq. (A2)) [87] .

$$4WCO + 11H_2 \xrightarrow{Catalyst} 17.5\ Products \tag{2.6}$$

The above overall stoichiometry was determined by considering the inlet composition and the products distribution reported in the graphical abstract and in Tables A2-A7 (for liquid products). Regarding the latter, only the most representative components (having a boiling point T_b and molecular weight similar to the average ones of naphtha, diesel and kerosene) were considered. i.e. C_8H_{16}, $C_{12}H_{26}$ and $C_{17}H_{36}$, C_3H_8, C_2H_6, CH_4, CO, CO_2, H_2O.

The material balance in terms of WCO conversion in a packed bed plug-flow reactor could be written as shown in Eq. (2.7) [88].

$$r_{TG} = F_{TG0}\frac{dX}{dW} \tag{2.7}$$

where F_{TG0} is the molar flowrate of the WCO; W is the mass of the catalyst; X is the conversion of WCO. Considering a second order reaction kinetics, r_{TG} can be written as shown in Eq. (2.8).

$$r_{TG} = kC_{TG}C_{H_2} = k\ \frac{(1-X)}{(1+\varepsilon X)}\ C_{TG0}\frac{\left(R_{H20}-\frac{\upsilon_{H_2}}{\upsilon_{TG}}X\right)}{(1+\varepsilon X)}\ C_{TG0} \tag{2.8}$$

where ε is the expansion coefficient of the reaction; C_{TG0} is the inlet concentration of WCO; R_{H20} is the molar ratio of H_2 over WCO at the inlet; ν_{H2} and ν_{TG} are hydrogen and WCO stoichiometric coefficients; k is the reaction constant. Since k is dependent on temperature according to the Arrhenius equation, the rate can be written as shown in Eq. (2.9).

$$r_{TG} = Ae^{\left(-E_a/_{RT}\right)} \frac{(1-X)}{(1+\varepsilon X)} \frac{\left(R_{H20}-\frac{\upsilon_{H_2}}{\upsilon_{TG}}X\right)}{(1+\varepsilon X)} \; C_{TG0}^2 \tag{2.9}$$

where A is the pre-exponential factor; E_a is the activation energy (J/mol); R is the molar gas constant (8.314 J/mol.K). Accordingly, Eq. (2.7) can be re-written as:

$$\frac{dX}{dz} = A\, e^{\left(\frac{-Ea}{RT}\right)} \frac{S\,(1-\varepsilon_{gas})\rho_{cat}}{F_{TG0}} C_{TG0}^2 \frac{\left(R_{H20}-\frac{\upsilon_{H_2}}{\upsilon_{TG}}X\right)(1-X)}{(1+\varepsilon X)^2} \tag{2.10}$$

where *S* is the cross-sectional area of the reactor (m^2), ε_{gas} is the void fraction, and ρ_{cat} is the catalyst density. The differential equation (Eq. (2.10)) was solved by using ***ode15s*** in the MATLAB software by integrating the function (dX/dz) to obtain X_{cal} (conversion as a function of temperature). Next, the ***Fminsearch*** function in the MATLAB software was employed to minimize the error function (Eq. (2.11)) to evaluate the parameters E_a (activation energy) and *A* (frequency factor).

$$\text{SSE} = \sum (X_{calc} - Xexp)^2 \tag{2.11}$$

where X_{cal} and X_{exp} are the calculated and the experimental values, respectively, of the percent conversion of WCO.

The values of E_a and *A* were found to be 53.7 kJ/mol and 4.32 s^{-1}, respectively, by minimizing the SSE, which turned out to be $2.74 \cdot 10^{-4}$. The result of the regression was plotted with its ordinary residuals, as shown in Figure 2.10. The residuals were plotted to check the adequacy of the kinetic model. It could be inferred that the fitted results were close to experimental results since all of the points were located within a standard deviation of 0.75 (less than unity), based on standardized residuals [89].

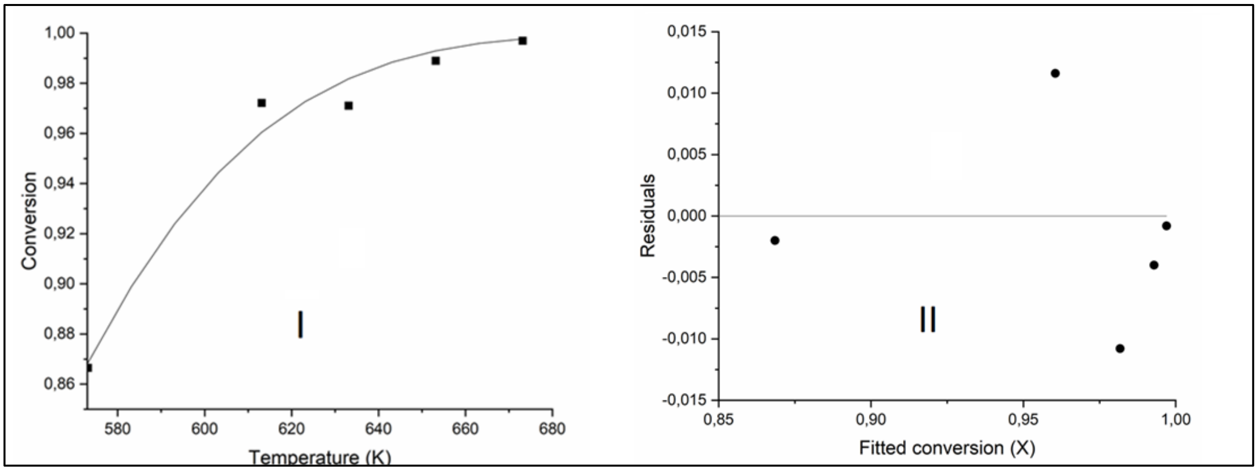

Figure 2.9. Regression of the kinetic equation using Least Square Method

The value of the activation energy obtained was comparable to that obtained from studies that used gaseous hydrogen for the conversion of different triglycerides: 26 kJ/mol [90, 91], 31 kJ/mol [92], 115 kJ/mol[93], and 57.3 kJ/mol [94].

With the knowledge of the kinetic rate constant at the optimum operating condition, the amount of catalyst required to process, for example, 60 barrels of WCO per day could be estimated. Furthermore, knowing the kinetics assisted in predicting the effect of pressure and particle size of the catalyst on the weight of catalyst required to process a given amount of WCO (Table A9 & A10). The effect of pressure and WHSV on the reaction rate was not considered in the current study. These are considered in the next chapter, which considers the optimization studies in which both normal alkanes and iso-alkanes were maximized.

2.2.5. BET Analysis of Catalyst

To assess the performance of the catalyst (activated carbon) used in this work, BET analysis was performed. The fresh catalyst, with surface area of 930 m^2/g, was reduced to a surface area of 2.1 m^2/g after three cycles of run (Table 2.6). The pore width distribution (Figure 2.11) of the fresh catalyst ranges from 18.8-70 Å, which classifies the fresh catalyst as both micropore and mesopore, with modal pore size of 18.8 Å [70].

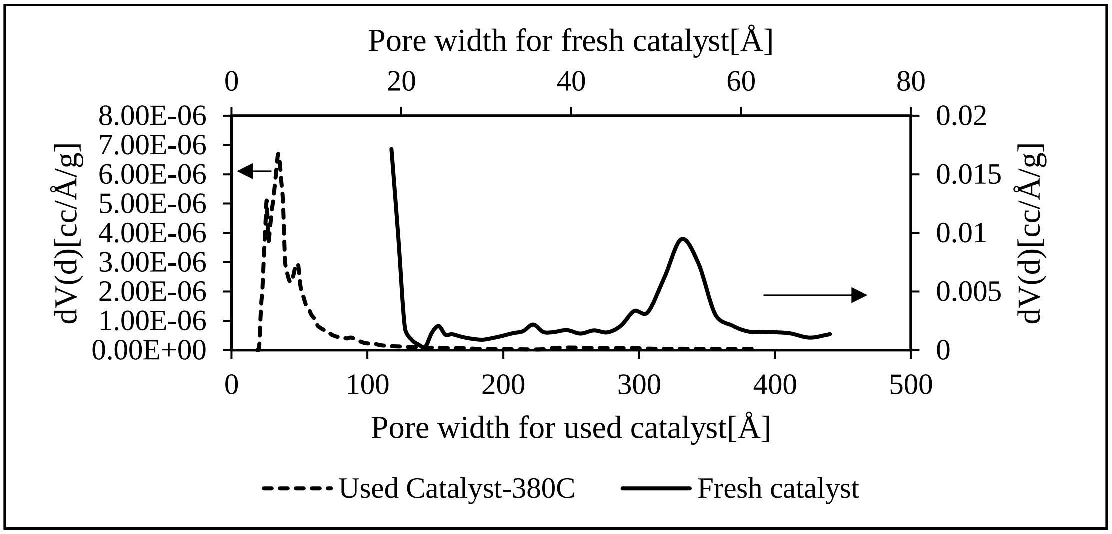

Figure 2.10. Pore size distribution of fresh and used catalyst at 380 °C.

Comparatively, the used catalyst has a somehow wider range of pore width (20-388 Å), with most of the pores clustered around 20-115 Å having a modal pore width of 34 Å. This means that the catalyst maintained its mesoporous structure during the reaction. Evidently, the used catalyst peaked at 26 Å and 49 Å. It was highlighted in Figure 2.11 that the used catalyst showed four different ranges of pore width distributions (20-27 Å, 24-44 Å, 44-116 Å, and 116-388 Å) while the fresh catalyst showed a close-range pore size distribution (19-49 Å, 49-58 Å, and 58-70 Å). Large pore size distribution of the used catalyst might be due to formation of coke on the catalyst surface, which reduced the effective surface area and, consequently, increased the average pore radius or diameter.

Table 2.6. Surface Area Determination of Used Catalyst at Different Reaction Temperatures

Temperature (°C)	**300**	**340**	**360**	**380**	**400**	**Fresh catalyst**
BET surface area (m^2/g)	0.030	0.034	0.048	0.085	2.093	930

It is widely accepted that there is a correlation between the shape of the hysteresis loop (adsorption-desorption loop) and the texture (pore size distribution, pore geometry etc.) of the mesopore catalyst. Figure 2.12 highlights the adsorption-desorption isotherms for both fresh and used catalyst at 380 ^oC. Increasing the relative pressure from 0.05-0.99 filled the pores with N_2 (adsorption) until the pores were condensed. Decreasing the pressure from 0.99-0.4 evaporated (desorption) the adsorbed N_2 that closed that loop at a pressure of 0.45 for the fresh catalyst, while that for the used catalyst closed at 0.04. This means that almost all of the adsorbed N_2 was evaporated from the mesoporous structure of the used catalyst since the large pored could not hold fluid due to low adhesive force. Conversely, there remained some amount of N_2 in the pores of the fresh catalyst after the loop closed, since small pores retained fluids due to the presence of high adhesive forces.

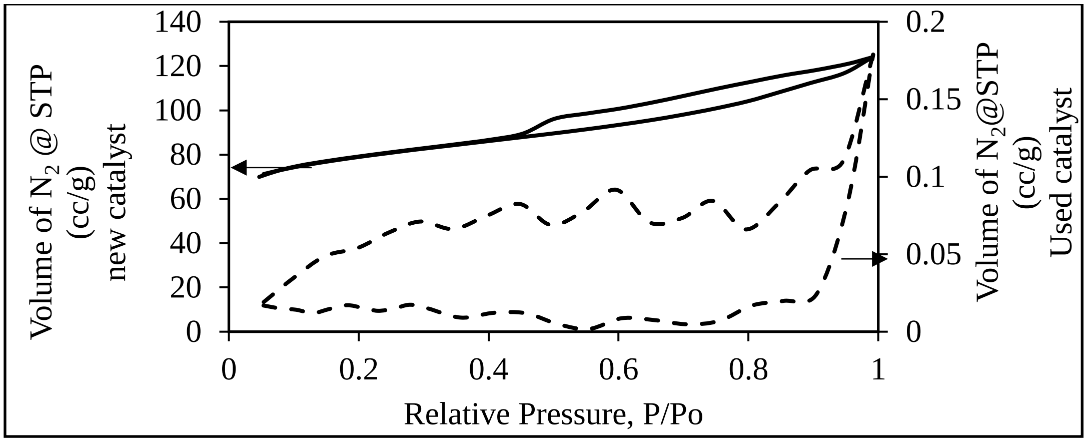

Figure 2.11. Nitrogen adsorption/desorption 77.35 K of fresh and used catalyst at 380 ^oC.

The hysteresis loop for the fresh catalyst showed type 1 and 4 isotherms, according to the International Union of Pure and Applied Chemistry [70], which buttresses the fact that there exist both micropores and mesopores in the fresh catalyst. Increasing the pressure from 0.05-0.45 enhanced the adsorption and the desorption of the micropores, whereas pressure between 0.45-0.99 aided the filling of the mesopores in the fresh catalyst. It was also observed that the total amount of N_2 adsorbed within the relative pressure range of 0.05-0.99 equaled 124 cm^3/g fresh catalyst, while the used catalyst, which depicted type 4 isotherm, adsorbed barely 0.18 cm^3/g catalyst. This implies that the catalyst suffered deactivation after the CTH of the WCO oil.

2.2.6. Coke formation

The total amount of coke formed in 10 hours of CTH of WCO was determined by TGA-DTA. Figure 2.13 and Table 2.7 showed the rate of mass loss by subjecting the used catalyst to TGA-DTA. Arguably, at low temperature, weight loss was observed, probably due to refractory volatiles, which were not cleaned by the hexane.

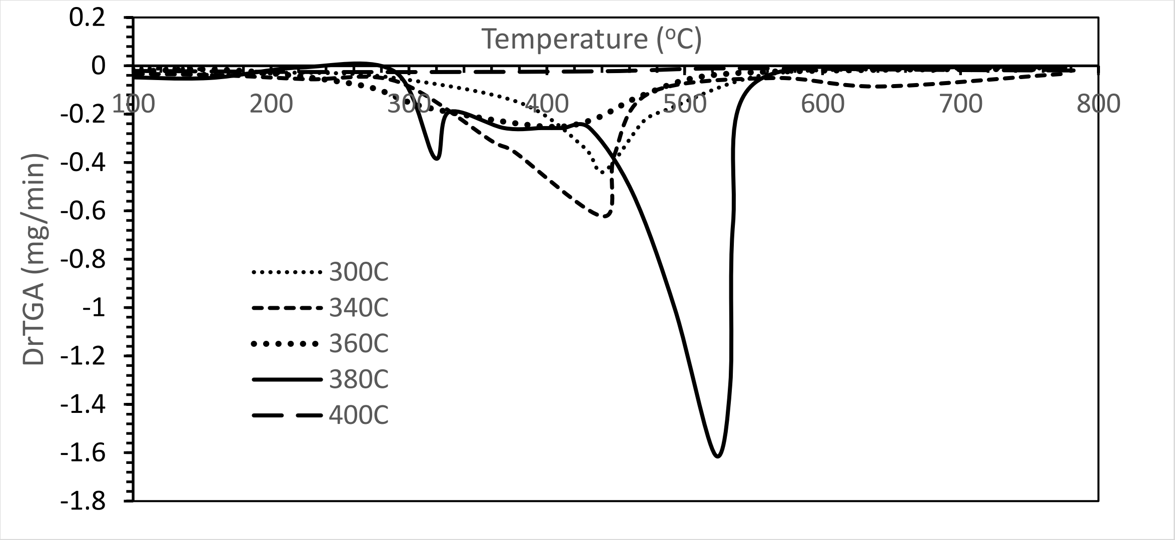

Figure 2.12. First Derivative of TGA of used catalyst at different reaction temperatures

It is evident that coke formed at 380 °C was the highest, compared to those below 380 °C. Coke formation has been attributed to poly-alkyl-aromatic [95-97]. The highest coke formation at 380 °C proves the fact that aromatization produced poly-alkyl aromatics (e.g. benzene, 1-ethyl-3-methyl and naphthalene, 2-methyl (Table A3)) at this temperature (Figure 2.5). As the temperature increased, the amount of poly-alkyl aromatics also increased (Table A2). Paradoxically, the amount of coke formed at 400 °C was lower than that at 380 °C, even though the amount of aromatics formed at 400 ^{o}C was more than the amount formed at 380 ^{o}C. This be might be traceable to the fact that the coke formed on the surface of the catalyst might have been burned off at 400 ^{o}C.

Table 2.7. Weight Loss of Used Catalyst Using TGA

	Reaction Temperature (^{o}C)	300	340	360	380	400
Using Isopropanol	% weight loss	26.3	41.3	27.7	95.1	5.8
	Temperature range (^{o}C)	249-500	224-470	230-480	210-536	Not appreciable

This might be the reason why the surface area of the used catalyst at 400^{o}C was larger than that at 380 ^{o}C and below (Table 2.6). Figure 2.14 highlights the total amount of coke formed during ten hours of running the reaction at different temperatures. The total coke formed at the optimum reaction temperature is 5.2 g per 5.5 g of catalyst used after ten hours of run. After three cycles of using the catalyst, it was observed that the conversion of WCO declined from 99 to 78% (Figure 2.15), due to the deactivation by coke deposition on the surface of the catalyst [98].

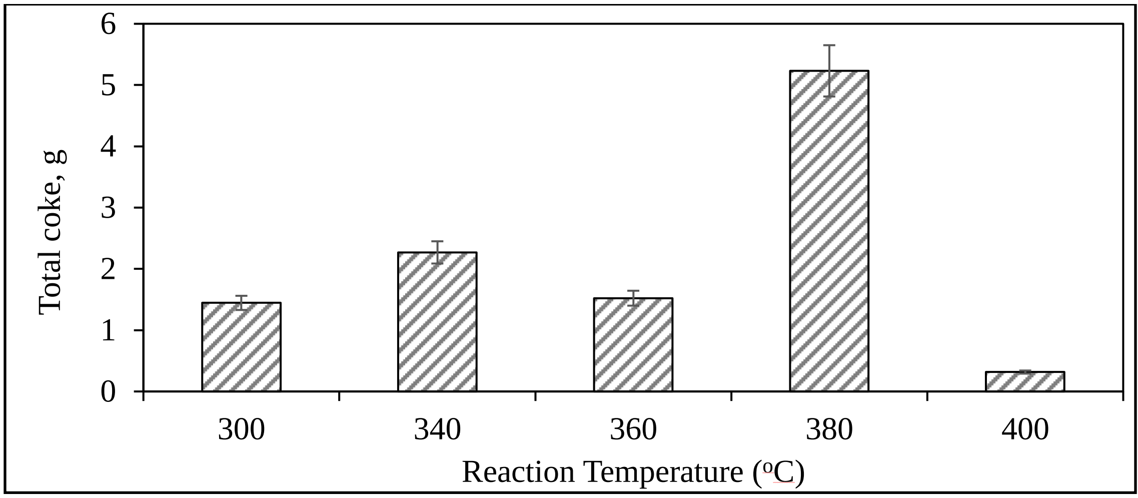

Figure 2.13. Total coke formed from running after 10 hours of reaction

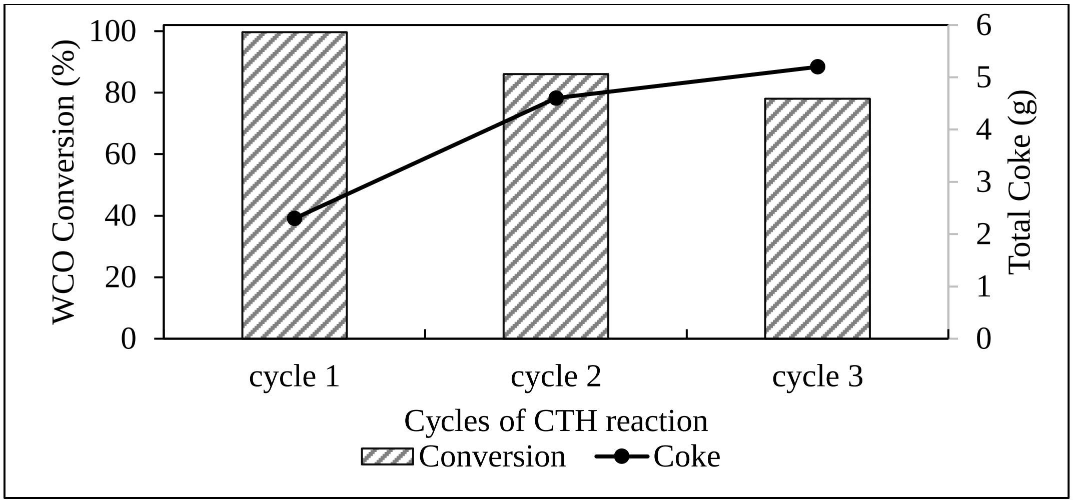

Figure 2.14. Effect of coke formation on WCO conversion at 380 ^{o}C after 10 hours' (3 cycles) use of the catalyst.

2.3. Conclusions

2-propanol (isopropanol) was used to convert waste cooking oil to jet-diesel range fuel over granular activated carbon near atmospheric pressure. The maximum liquid hydrocarbon fuel yield 72% occurred at 380^{o}C. The study shows an alternative to hydrogen gas in such processes, which can help in reducing the cost of hydrogen handling and the associated capital cost. The flow properties of the fuel are comparable to those of conventional Jet/diesel fuel. The presence of oxygenates and low levels of iso-cyclo alkanes in the liquid fuel product, compared to ASTM fuel, shows the need of continued research to minimize oxygenates and to maximize iso-cyclo alkanes.

2-propanol has proven to be a potential hydrogen donor, which hydroprocessed WCO without the use of gaseous hydrogen. On a commercial scale, there is, therefore, a potential reduction in the cost of hydrogen handling that could lead to reduction in unit cost and the price of jet-diesel fuel using 2-propanol as a hydrogen source. Based on the reported annual WCO production (29 million tons), this process could produce an annual jet-diesel fuel of approximately 20 million tons; if a more stable catalyst were employed on a commercial scale, this could provide a considerable amount of renewable transportation fuel.

The novelty and the feasibility of converting WCO to jet-diesel range by using 2-prpoanol as an *in-situ* hydrogen donor have been proven at the laboratory level. Commercialization or technoeconomic analysis (i.e. process and equipment design, capital and operational cost) and environmental performance (life cycle analysis) of this process, which requires extensive work, will be carried out in the subsequent study, so that stakeholders in the biofuel market can make an informed decision.

2.4. Acknowledgement

The authors are grateful for the financial support of the Old Dominion University Research Foundation Summer Fellowship 2016.

CHAPTER 3

KINETICS AND OPTIMIZATION OF CATALYTIC TRANSFER HYDROGENATION OF WCO USING 2-PROPANOL AS H-DONOR OVER NiO$_X$-MoO$_X$-CoO$_X$/ZEOLITE

Note: The contents of this chapter were published in the Journal of Industrial & Engineering Chemistry Research, DOI: 10.1021/acs.iecr.9b00648

Alexander Asiedu, Sandeep Kumar, Kinetics and Optimization of Catalytic Transfer Hydrogenation of WCO Using 2-propanol as H-donor over NiOx-MoOx-CoOx/Zeolite, Ind. Eng. Chem. Res. (2019)

The process optimization and the reaction kinetics of catalytic transfer hydrogenation (CTH) of waste cooking oil (WCO) into jet fuel~~s~~ using zeolite-supported Ni-Co-Mo-oxides catalyst in a packed-bed reactor were studied. Experiments were conducted at three different temperatures (360 ^{o}C, 390 ^{o}C, and 420 ^{o}C) to determine the rate constants, the order of reaction, and the activation energy. The kinetics study showed a first-order reaction, with the activation energy estimated to be 84±18.7 kJ/mol WCO, with 95% confidence. Design of Experiment (DOE) was employed to estimate the optimum reaction parameters (383.7 ^{o}C; 14.8 bar; WCO-to-2-propanol ratio = 1.57 mL/mL; and weight hourly space velocity (WHSV) = 6.7 h^{-1}) using a polynomial model. Validation of the model at the optimum operating conditions generated 80% yield of liquid products, with 77% alkanes, 3.8% alkenes, and 12.3% aromatics composition, and 6.7% gases, and 100% conversion of WCO. The catalyst was prepared by the wet impregnation method and was characterized by X-ray diffraction (XRD), Fourier transform infrared spectroscopy (FTIR), Brunaeur-Emmett-Teller (BET) adsorption and desorption, scanning electron microscope (SEM), energy dispersive spectroscopy (EDS), and thermogravimetric analysis (TGA). Characterization of the catalyst revealed a cubic structure, which was maintained after one cycle of CTH reaction. Present in both the fresh and the used

catalysts were Na_2O, K_2O, MgO, Al_2O_3, SiO_2, CaO, FeO, Fe_2O_3, which highlighted the composition of zeolite. The active sites were dominated by Co^{3+}, Ni^{2+}, and Mo^{6+} that were respectively present in the form of Co_2O_3, NiO, and MoO_3.

3.0. Introduction

In recent times, globally declining fossil fuel reserves and the concomitant challenges associated with greenhouse effects have challenged energy researchers. Because of this potential future energy deficit, researchers have focused much attention on green fuel from triglycerides, the main constituents of vegetable oils [99]. Waste cooking oil (WCO), which contains 4-hydroxy-2-alkenal (toxin and pollutant) [17] and is abundant globally (29 million tons/year) [100], has been used to produce liquid hydrocarbon fuel via decarboxylation (CO_2 release), decarbonylation (CO release), and hydrodeoxygenation (CO_2 and H_2O release), with an appropriate catalyst and hydrogen gas [101-109]. Reported processes of WCO require a large volume of hydrogen handling, with a H_2-WCO ratio in the range of 300-1200 m^3/m^3 oil, which creates potential hydrogen handling and inherent safety costs [32, 110, 111]. Although hydrogen gas is the best reagent for hydrotreating conventional fuel, it is in short supply, and it comes from fossil fuel. Since gaseous hydrogen is non-polar and immiscible with triglycerides at low pressures, there is a problem of mass transfer and diffusion during hydrogenation of triglyceride. However, the problem of mass transfer and diffusion can only be overcome by applying inordinately high pressures (25-100 bar) that require enormous energy and that task the processing equipment [35, 112].

The above-mentioned problems can be alleviated by employing catalytic transfer hydrogenation (CTH) reactions, which are a reduction of unsaturated organics (such as oleic acid) using hydrogen-donating compounds that catalytically produce hydrogen in situ. CTH is advantageous to conventional hydrogenation (use of gaseous hydrogen) because CTH reduces the high cost of transporting and storing large volumes of gaseous hydrogen [113]. Among the hydrogen-donating compounds that have been studied are tetralin, decalin, naphthalene, n-dodecane, formic acid, cyclohexane, and a whole list of hydrocarbon solvents [100]. One of the advantages of using hydrocarbons as in situ hydrogen donors is the lower bond energy of C-H in these solvents, compared to that of the H-H bond in $H_{2.}$ [114]. However, most of these hydrogen donors are costly, toxic, acidic (e.g. formic acid), and volatile. The most available, less toxic and less costly are the common alcohols (methanol, ethanol, n-propanol and 2-propanol), which have been reported to be effective hydrogen donors. Most effective hydrogen-donating among the preceding alcohols is 2-propanol, since the two methyl groups in 2-propanol donate more electrons to weaken the O-H bond compared to the lower electron-donating ability of one methyl group and one ethyl group in methanol and ethanol, respectively. 2-propanol is not only the best hydrogen-donating compound among the alcohols, but it is also less expensive ($1.8/kg) [57]. with respect to gaseous hydrogen ($3-12.85/kg) [58, 59, 115]. Since it is non-toxic with good solvent properties, 2-propanol can potentially be produced from renewable feedstocks, such as glycerol and acetone [62-66].

Our previous work was focused on CTH of WCO using 2-propanol as an in-situ hydrogen donor over activated carbon at near atmospheric pressure [100]. However, the clarity of the liquid fuel required improvement by further distillation. Moreover, there were high levels of olefins and oxygenates, signifying incomplete hydrogenation and deoxygenation respectively, due to unstable catalysts and the extremely low pressure of the process, which contributed to a large amount of gaseous products [100].

The purpose of the current study is to improve the product quality (lower unsaturated and oxygen compounds), and to optimize variables (pressure, weight hourly space velocity (WHSV), and 2-propanol-WCO ratio) that were employed in the previous work. Consequently, it was important to select a catalyst that was mechanically and hydrothermally stable in hydrotreating WCO. Numerous catalysts have been employed to hydrotreat triglycerides, with significantly successful results. Sulfided catalysts, such as $Ni–W/SiO_2–Al_2O_3$ and $Ni–Mo/Al_2O_3$, were used for hydrocracking and hydrotreating waste soya oil [116]. Sulfided $NiMo/\gamma\text{-}Al_2O_3$ and $CoMo/\gamma\text{-}Al_2O_3$ have been reported to hydrogenate methyl esters, and the effects of H_2S and CS_2 on the hydrodeoxygenation (HDO) of aliphatic esters and on the catalysts have been investigated in a fixed-bed flow reactor [117]. Olive oil has been hydrogenated with sulfided CoMo catalyst, which was biased toward hydrodeoxygenation and could not cleave C-C bond and, therefore, required constant replenishment of the sulfur via external sulfiding agents, such as H_2S, CS_2 and ammonium thiosulfate ($(NH_4)_2S_2O_3$) [118]. In addition, the use of these sulfiding agents caused sulfur residues in the final product, promoted the emission of gaseous H_2S , and engendered corrosion, due to the acidic nature of sulfur [119].

Noble metal (Palladium (Pd), Platinum (Pt), Rhodium (Rd), Ruthenium (Ru), etc.) catalysts supported on alumina, carbon, and zeolite have been used to hydrotreat vegetable oil [120-124]. Although catalytic activities of these metals have proven effective, they are costly and short-lived [125].

Surfactant-mediated mesoporous catalysts, such as SBA-1, HMS, and SBA-15 with high surface area, large pore structure, and well-ordered morphology, have been used to hydrotreat vegetable oil. However, they possess weak hydrothermal and mechanical stability, and they have reduced acidity, leading to retardation of their practical application [126, 127].

Other emerging surfactant-mediated catalysts, such as SAPO (silicoaluminophosphate), SAPO-5, SAPO-11, SAPO-31, et cetera, have also been used to hydrotreat triglyceride [111, 128-132]. These catalysts proved to be mainly effective for isomerization of linear alkanes [133-135] and seem promising. However, they are not stable in the presence of oxygen-containing compounds [28]. Their relatively low hydrothermal stability in HDO of vegetable oils is due to the water vapor produced, which results in desilication of SAPO framework and leads to the loss of acidity. This problem is offset by adding more surfactant, which renders this catalyst economically inviable. [136] In addition, SAPO has a relatively weaker acidity, which is a disadvantage to the family of bi-functional catalysts that usually need stronger acid sites for HDO of WCO [137, 138]. It has been reported that Pt-SAPO-11 and Ni-SAPO-11 have low hydrothermal stability during the hydrodeoxygenation of vegetable oils, due to the production of water, which deactivates the catalyst at temperature > 200 ^{o}C and at autogenic pressure P_{H2O} > 17 bar where the catalyst framework degrades from aluminum phosphate tridymite structure [136]. Considering the problems associated with the aforementioned catalysts, we selected commercially available non-sulfided Co-Mo-Ni-zeolite catalyst that has proven to be effective in hydroprocessing vegetable oil commercially at the refinery level by prominent refinery companies, such as ConocoPhillips (United States, Ireland), Universal Oil Products (UOP)-Eni (UK, Italy), Nippon Oil (Japan), SK Energy (Korea), and Syntroleum (United States) [125]. Apart from being economically viable and available, it is a trimetallic catalyst that is resistant to coking, compared to the mono-metallic catalyst. It is well established that catalytic activity and resistance to coke formation by HDO catalysts increases in the following order: mono-metallic < bimetallic < trimetallic [139-142]. Zeolite (being inexpensive and environmentally benign, having uniform pore structure with high attrition resistance, and recyclability) [143] has been selected as a support in this work because it has the highest acidity (which is suitable for deoxygenation) compared to other supports reported in the literature (with order of decreasing acidity:H-ZSM-5 > H-Beta >HY >Al_2O_3> TiO_2> ZrO_2> CeO_2> SiO_2) [144].

The current work focuses on the CTH reaction kinetics and optimization of process parameters via the DOE method by using commercially viable catalyst to produce high quality hydrocarbon fuel. For the first time, optimization of a CTH reaction over oxides of Co-Mo-Ni-zeolite catalyst was used to convert WCO using 2-propanol in a continuous flow reactor, in order to obtain clean liquid fuel that does not necessarily require purification or distillation.

3.1. Materials and Methods

Sodium-aluminosilicate pellets (-600 mesh), 2-propanol (99.5 wt %) and dichloromethane, nickel nitrate (II) hexahydrate (99.9%), Cobalt (II) molybdenum oxide hydrate (99% metal basis), and diethyl ether were purchased from Fisher Scientific. The WCO was collected from a local restaurant at Norfolk, Virginia.

3.1.1. Determination of Fatty Acid Composition of WCO

The object of determining the fatty acid composition of WCO was to ascertain the level of saturation, which was used to estimate the amount of 2-propanol required for the CTH reaction. The results of this section helped to elucidate the length of the carbon chain in the WCO.

1 mL of WCO was measured into a 20-mL test tube. The tube and its content were placed in a water bath and allowed to heat to 60 ^{o}C. 1.2 wt % catalyst (NaOH) (1.2% of WCO) was dissolved in 0.397 mL of methanol in order to obtain approximate molar ratio of methanol to oil of 10 [69]. The basic methanol was added to the oil in the test tube. The test tube was then capped, and a transesterification reaction was allowed to proceed. The test tube and its contents were agitated intermittently with a vortex mixer to enhance the reaction. The reaction was

stopped in one hour and was allowed to cool to room temperature. The fatty acid methyl ester (FAME) and the glycerol were separated by centrifugation. The FAME was pipetted into a separating funnel and 2 mL of diethyl ether was added to the FAME followed by several washings using distilled water to remove excess base. The solvent was then dried over anhydrous sodium sulfate. The ether was separated from the oil by vacuum (0.1 bar) evaporation. The oil was poured into an aluminum can and dried for 2 hours at 60 ^{o}C in an oven. The FAME was then poured into a vial and refrigerated prior to FAME analysis by gas chromatography mass spectroscopy (GCMS). The experiment was conducted in duplicate.

3.1.2. Thermal Analysis of WCO by TGA-DTA

This step was aimed at determining the rate of thermal decomposition of WCO without a catalyst, and consequently at ascertaining the average boiling point range of WCO that served as a guide for selecting the reaction temperature CTH. From the kinetics of the thermal decomposition of WCO, the CTH reaction order was guessed.

To study the thermal performance of the WCO, TGA-DTA was performed in a nitrogen atmosphere at a flow rate of 30 mL/min with a heating rate of 5-30 ^{o}C/min. Within this atmosphere, approximately 5 mg of WCO was placed in a platinum cup and was heated to 900 ^{o}C. From the DTA plots, the temperature at which the maximum thermal decomposition rate occurred served as a guide in choosing the CTH reaction temperature range, and from the kinetics of thermal decomposition of WCO, the order of thermal decomposition and activation energy were obtained.

3.1.3. Catalyst Preparation

NiO-MoO_x-CoO_x-zeolite was prepared by wet-impregnating the zeolite (support) with Ni-Co-Mo precursors (nickel nitrate (II) hexahydrate and cobalt (II) molybdenum oxide hydrate).

In this process, 1.9 g of $CoMoO_4.H_2O$ (5 wt % of support) was dissolved in 1000 mL of deionized water at 80 ^oC. A given amount of the support (sodium aluminosilicate) was added to the prepared solution and the content was stirred overnight. The loaded zeolite was removed by filtration and was dried in an oven at 105 ^oC. A solution of nickel nitrate (II) hexahydrate was prepared by dissolving 5.16 g of it in 1000 mL of deionized water at 80 ^oC. The dried catalyst was added to the nickel solution and was stirred overnight under a hood. The loaded catalyst was then separated from the solution and was dried. The dried catalyst was calcined in a furnace at 500 ^oC for 2 h.

3.1.4. Catalyst Characterization

The purpose of this section was to assess the stability of the catalyst by determining the surface area, the crystallinity, the chemical position of the fresh and the used catalysts, and to ascertain the level of coke formation.

The catalysts (both fresh and used) were characterized by the following technique: BET, XRD, SEM, EDS, FTIR, TGA, and differential thermal analysis (DTA). The XRD patterns were recorded on a Bruker D8 diffractometer using Cu Kα radiation ($\lambda = 0.154056$ nm) operating at 40 kV and 40 mA. Diffractograms were recorded from 5^o-80^o (2θ value in discrete mode with a step of 0.1^o). The morphologies of the catalysts were analyzed with SEM using Hitachi S-3400N operated with beam energy of 15 kV. Imbedded in the SEM was EDS, which was used to determine the elemental composition of the catalyst. The FTIR spectra of the catalysts (fresh and used) were recorded at room temperature and the wavenumber range of 480-4000 cm^{-1} by diffuse reflectance, using a ThermoNicolet Avatar 370 DTGS spectrometer.

The BET surface area, the pore volume, and the pore size of the new and used catalysts were measured by using Quantachrome NOVA 200e surface area analyzer after degassing the catalyst at 300 ^oC for three hours and adsorbing and desorbing it with N_2 at -196 ^oC. The surface area was evaluated using a multi-point BET model. The pore size distribution was obtained from the desorption isotherm using Barret-Joyner-Halenda (BJH) model, while the total pore volume was calculated at a relative pressure range of 0.0-1.0. The amount of coke formation on the surface of the catalyst was determined using TGA-DTA, by measuring the percent mass loss and the rate of thermal decomposition of the catalyst.

3.1.5. Kinetics of CTH

The kinetics of the CTH were run at 360 ^oC, 390 ^oC, and 420 ^oC by keeping the pressure and weight hourly space velocity (WHSV) at 15 bar and 6.7 h^{-1}, respectively. The WHSV (Eq. (3.1)) and the pressure were selected, based on the preliminary trials. The CTH experiments were carried out in a packed bed continuous flow reactor. A stainless-steel tubular reactor (360 mm long and 15 mm inside diameter) was placed inside an 8-kW heating furnace with an automatic temperature control (Figure 2.1). The flow rates of both 2-propanol and WCO were controlled by high performance liquid chromatography (HPLC) pumps. Pump 1 was used to pump the water, which served as hydraulic fluid. This water pushed a piston that, in turn, pushed the WCO through the reactor. Pump 2 also pumped 2-propanol to meet the water at a mixing point before both entered the reactor. The liquid products were sampled every 30 min for 2.5 h per run. The liquid products were analyzed by gas chromatography mass spectrometer (GCMS), while the gaseous products were analyzed by gas chromatography (GC). The amount of liquid fuel obtained from each run was collected and measured in each case, and the alkane yield was calculated (see Eq. (2)). The reaction mechanism, the reaction rate equations, the activation energy, the order of reaction, and the rate constants were determined, based on the results obtained from the GCMS analysis.

$$\text{WHSV} = \frac{\text{mass of feed flow rate (g/h)}}{\text{mass of catalyst in the reactor (g)}} \tag{3.1}$$

$$\text{Yield} = \frac{\text{Total mass of alkanes in liquid product}}{\text{Mass of WCO}} \times 100\% \tag{3.2}$$

3.1.6. D-optimal Design

Design of experiment method was employed to assess the effect of four independent variables on the alkanes' production (dependent variable) from CTH of WCO using the prepared NiO-MoO$_x$-CoO$_x$-zeolite catalyst. Factorial design of experiment was used in this process, as shown in Table 3.1. 3-level fractional factorial experimental design was used by considering four factors: temperature, pressure, WCO-to-2-propanol ratio, and WHSV. The effects of these factors on the alkane yield during the CTH reaction were assessed by using the MATLAB software to generate coded values and their respective real values (Table B1) by using D-optimal design syntax. 25 different runs of experiments were performed, using the same experimental set-up described above.

Table 3.1. Design of experiment (3^4).

Factors	Levels		
	Low (-1)	Medium	High (+1)
Temperature (**A**), °C	300	370	420
Pressure (**B**), bar	2	15	25
WCO/2-propanol (**C**)	0.8	1.5	3
WHSV (**D**), h^{-1}	2	6	10

Based on D-optimal design, a polynomial model was proposed (Eq. (3.3)) and then, using the analysis of variance (ANOVA) with experimental data, the coefficients, βs, were evaluated.

$$Y = \beta 0 + \beta 1A + \beta 2B + \beta 3C + \beta 4D + \beta 5AB + \beta 6AC + \beta 7AD + \beta 8BC + \beta 9BD + \beta 10CD + \beta 11A^2 + \beta 12B^2 + \beta 13C^2 + \beta 14D^2 + \beta 15ABD \tag{3.3}$$

The optimum values of the independent factors (Temperature (**A**), pressure (**B**), WCO/2-propanol(**C**), and WHSV(**D**)) were determined by both analytical and 3-dimensional surface response plots. Analytically, the partial derivative of Eq. (3.3) and application of the MS-Excel solver facility were employed. The optimum values were validated by performing the CTH reaction at these optimum values, and the percentage of alkanes was calculated. The physical properties of the liquid product were determined according to the American Standard for Testing and Materials (ASTM)[84, 145-150].

3.2. Results and discussions

3.2.1. WCO Characterization

Figure 3.1 highlights the characterization of WCO: (**a**) TGA analysis at different heating rates (HR); (**b**) DTA showing different maximum rates of thermal decomposition at different temperatures; (**c**) kinetics of TGA to determine the order of thermal decomposition of WCO; (**d**) Activation energy profile at different reaction orders.

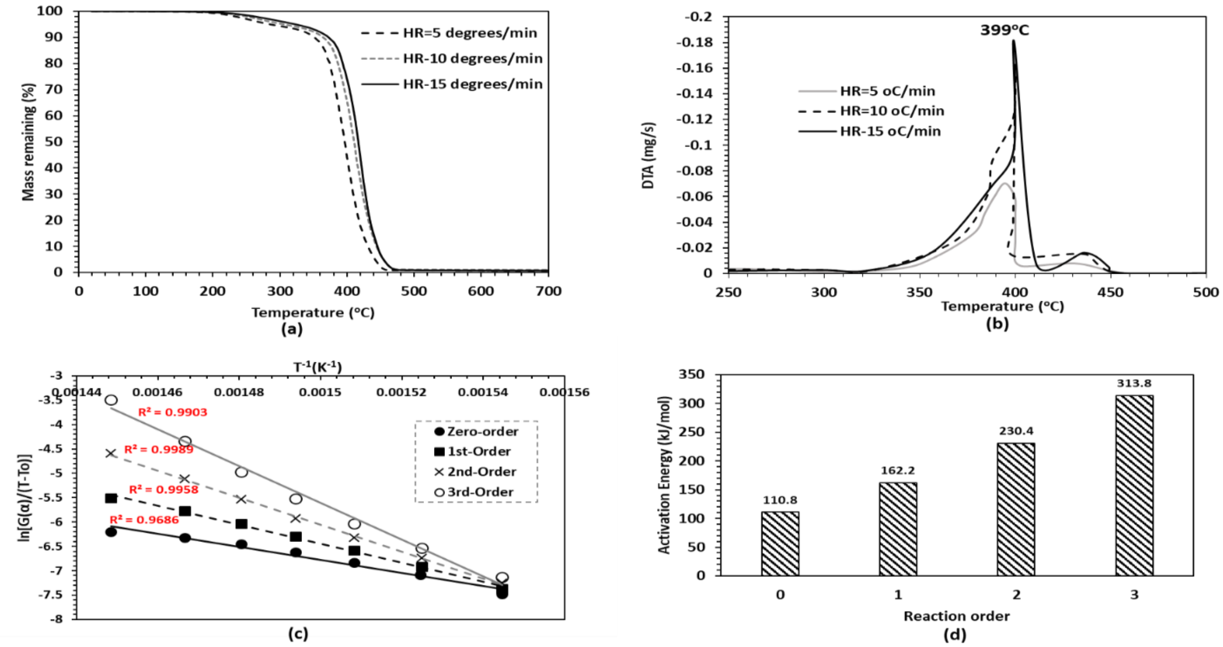

Figure 3.1. Characterization of WCO: (**a**) TGA analysis at different heating rates (HR); (**b**) DTA showing different maximum rates of thermal decomposition at different temperatures; (**c**) kinetics of TGA to determine the order of thermal decomposition of WCO; (**d**) Activation energy profile at different reaction orders.

The WCO was characterized by determining the fatty acid composition to assess the degree of saturation. It was evident that the carbon number of the oil ranged from C16 to C20, which showed an unsaturated level of approximately 72%. This information was significantly helpful in determining the amount of hydrogen required to hydrogenate and saturate the oil. In this work, based on the WCO characterization, 12 moles of 2-propanol were required to saturate the oil, on the condition that one mole of WCO (triglyceride) contained six moles of carbon-carbon double bonds (C18:2) (Figure B1) and six moles of oxygen atoms, and that every mole of 2-propanol produced one mole of hydrogen gas [100].

As an effective method in determining the thermal stability or decomposition via mass-loss monitoring and the programmed temperature process [151], TGA showed that the thermal degradation of WCO occurred in two stages: 212 °C-359 °C and 359 °C-471 °C (Figure 3.1(a)).

The first stage corresponded to a mass loss of nearly 15% that could be attributed to the degradation of C15-C16 fatty acid (approximately 15% (Figure B1)) in the WCO. The second stage could also be traceable to C17-C20 that represented approximately 85% of the fatty acid. By varying the heating rate (5 ^{o}C/min, 10 ^{o}C/min, 15 ^{o}C/min), the maximum rate of WCO decomposition occurred at 399 ^{o}C, which remained unaltered (Figure 3.1(b)). These values were comparable to those reported in the literature [151, 152]. Results from the TGA were utilized as blueprint in selecting the reaction temperatures (360 ^{o}C, 390 ^{o}C, 420 ^{o}C) in developing the kinetics of CTH. To further estimate the minimum energy required to thermally decompose the WCO, the universal integral method [153] was employed, in order to determine both activation energy and the reaction order the of thermal decomposition of WCO (Table B2 & Eq. (B1)). Using the experimental data (Table B3-B6), the thermal decomposition proved to be second order, having activation energy of 210 kJ/mol (Figure 3. 1 (d)). This could be compared to the pyrolysis of olive oil and the thermal analysis of sunflower, with the activation energy of 194.6 kJ/mol and 201 kJ/mol, respectively. [154] R-squared of 0.9989 signifies the goodness of model fit compared to the first order, with R-squared of 0.9958 (Figure 2(c) and Table B7). This information was useful in guessing the order of reaction for the CTH. It was postulated that the order of reaction for CTH could be nearly one, since a catalyst would be employed to expedite the reaction. Moreover, it was anticipated that the activation energy for CTH would be less than 230 kJ/mol, since the catalyst would lower the activation energy barrier for the reaction path. [155]

3.2.2. TGA of Catalyst

Figure 3.2, which highlights TGA profiles for the fresh catalyst, the used catalyst, and the zeolite (support), elucidates three stages of weight loss. The first stage (below 200 ^{o}C) showed approximately 13%, 16%, and 10% weight loss for zeolite, fresh catalyst, and the used catalyst, respectively.

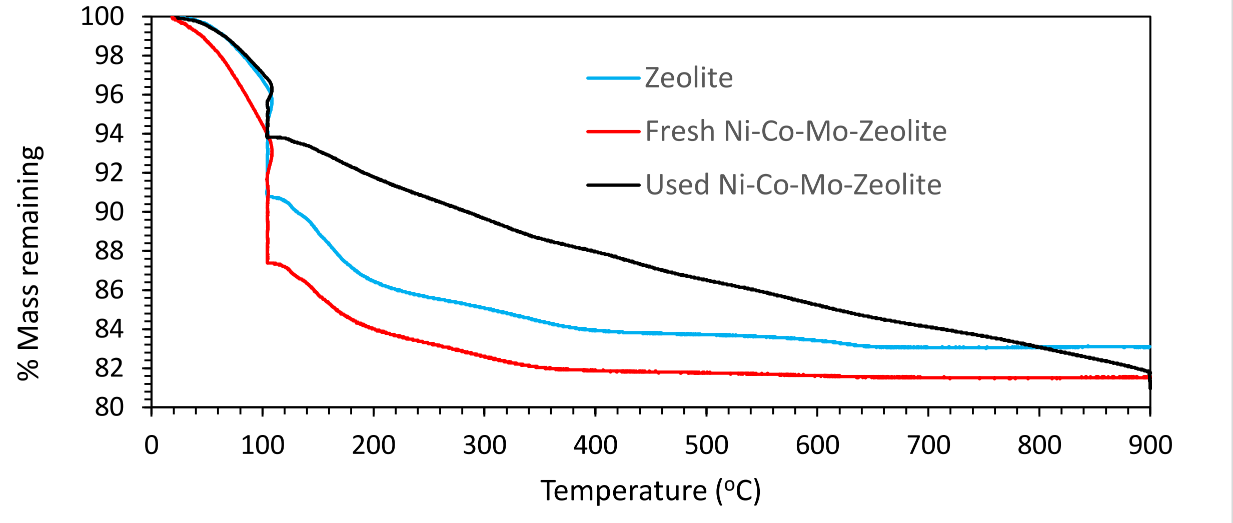

Figure 3.2. TGA of fresh catalyst and used catalyst at optimum reaction condition.

These losses could be traceable to the loss of loosely bonded water. The fresh catalyst showed the highest weight loss, probably due to adsorption of the water employed in the wet impregnation. Counterintuitively, the used catalyst showed the lowest weight loss in the first stage, presumably due to the displacement of water molecules by the fuel products that diffused to displace the water molecules in the zeolite structure during the CTH reaction. In the range of 200-400 ^{o}C, roughly 3%, 2%, and 3% weight loss for the zeolite, fresh, and used catalysts, respectively, were experienced, which could be ascribed to strongly bonded water that resides in the first coordination sphere that could not be removed under mild thermal treatment [156]. The next weight loss (1% for both zeolite and fresh catalyst, and 5% for used catalyst) occurred between 400-900 ^{o}C. This loss could be attributed to the structural hydroxyl group that condenses and dehydrates at 500 ^{o}C and above. The 5% weight loss by the used catalyst could be traceable to the coke formed from carbonized hydrocarbon or poly-alkyl aromatic hydrocarbon [96, 97], which provoked catalyst deactivation. The presence of this carbonized carbon was confirmed by the FTIR (Figure 3.5). It could be inferred that the overall weight loss from the used catalyst after thermal decomposition was estimated to be 19%, compared to what had been reported in the literature. For example, the TGA of coke-laden NiO-CaO_5/SiO_2-Al_2O_3 catalyst showed a weight loss of 15% [157], while 20Ni-6Cu-5Mo/γ-Al_2O_3 catalyst exhibited a weight loss of 22-25% [158].

3.2.3. SEM and EDS of Catalyst

Elemental composition of the zeolite and the fresh and used Ni-Co-Mo-zeolite catalysts were analyzed by the EDS, which accompanies the SEM facility. Figure 3.3 highlights the spectrum obtained from the analysis of elemental composition of the fresh and used Ni-Co-Mo-zeolite catalysts. Evidently, nine different elements were observed in the raw zeolite, while twelve elements were observed in both the fresh and used Ni-Co-Mo-Zeolite. These elements were carbon, oxygen, sodium, magnesium, aluminum, silicon, potassium, calcium, iron, cobalt, nickel, and molybdenum (Table 3.2).

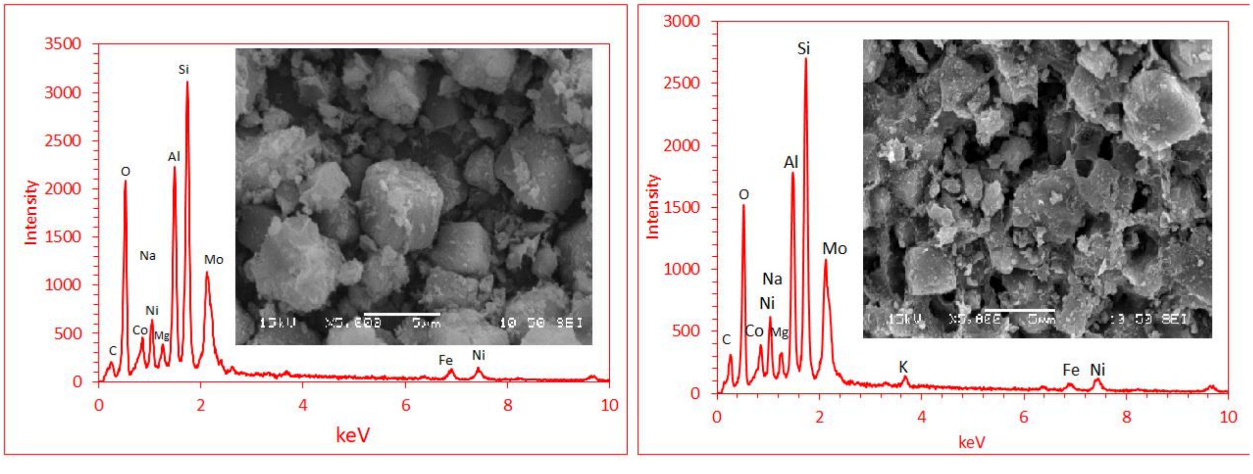

A B

Figure 3.3. SEM (with accelerating Voltage: 15.0 kV, magnification: 2000) and EDS analysis for fresh and used catalyst (A) Fresh Ni-Co-Mo-Zeolite, (B) used Ni-Co-Mo-zeolite at the optimum CTH reaction condition.

Table 3.2. EDS of zeolite, fresh Ni-Co-Mo-zeolite and used Ni-Co-Mo-zeolite at the optimum CTH conditions (380 ^{o}C & 14 bar).

Elements	C	O	Na	Mg	Al	Si	K	Ca	Fe	Co	Ni	Mo
Raw Zeolite (wt.%)	3.92	48.35	10.7	1.74	13.75	19.5	0.3	0.62	1.00	0.00	0.00	0.00
Fresh Ni-Co-Mo-zeolite (wt.%)	4.37	44.55	4.26	1.43	11.84	16.17	0.3	0.44	1.04	4.71	7.86	3.05
Used Ni-Co-Mo-zeolite (wt.%)	12.4	39.79	4.49	1.28	10.54	16.86	0.3	1.06	1.00	3.24	6.70	2.33

The presence of these nine elements in the raw zeolite announces the possible presence of the oxides of these elements (Na_2O, K_2O, MgO, Al_2O_3, SiO_2, CaO, FeO, Fe_2O_3) [159], while the presence of Ni, Co, and Mo foreshadowed the likely presence of NiO, Co_xO_y, and Mo_xO_y, respectively. The possible presence of these oxides was inevitable, as the catalyst was not reduced after calcination. These oxides were preferable to their reduced form because they offered a higher level of acidity than their metal counterparts, as reported in the literature. Besides, these oxides introduced metal support interaction for the activation of oxygen-containing compounds, and enhanced direct scission of C-O in WCO [144]. Moreover, without the reduction of the catalyst, the cost of catalyst preparation could reduce. The presence of sodium and calcium predicted the zeolite to be A-type [156] with cubic crystal structure [160], as could be observed in the SEM results. The analysis showed that the raw zeolite was weakly acidic, since Si/Al = 1.4 < 1.5 [161]. However, with Si/Al < 5 renders the zeolite hydrophobic, porous, alkaline, and more adsorbent [162]. Doping the zeolite with Ni, Co, and Mo did not impact the acidity significantly, as Si/Al = 1.36. The composition of the active metals (Ni, Co, and Mo) suffered a slight reduction after the catalyst was used for one cycle (2.5 hours of reaction at the optimum condition). This could be traceable to the rise in the carbon content (8% increase), as shown in the first column of Table 3.2.

3.2.4. X-ray Diffraction of Catalyst

X-ray diffraction patterns were observed for the zeolite, the fresh, and the used Ni-Co-Mo-zeolite catalysts, as shown in Figure 3.4, with significant characteristic peaks observed at 7.4°, 10.7°, 12.6°, 16.6°, 17.8°, 21.9°, 24.4°, 27.6°, and 30.4° for zeolite, according to the Joint Committee on Powder Diffraction Standards (JCPDS File no. 43-0142) [156].

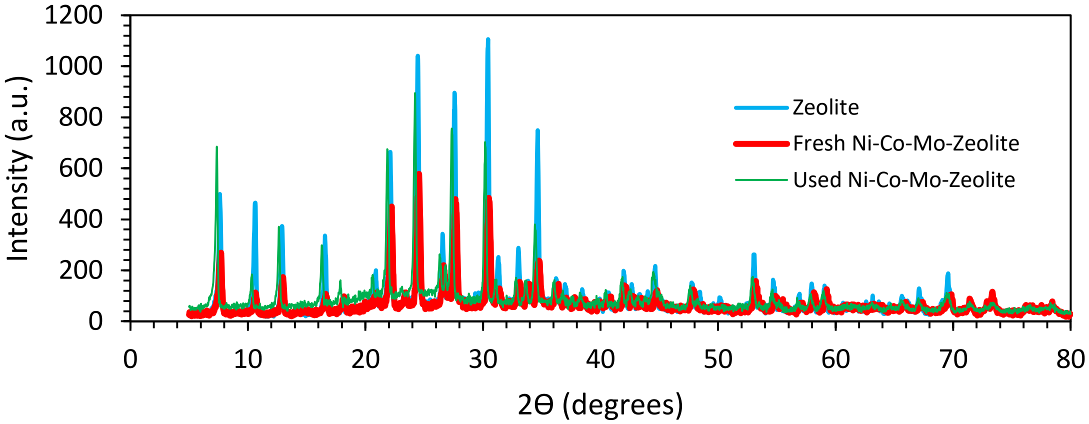

Figure 3.4. XRD pattern for the zeolite, the fresh and the used Ni-Co-Mo-zeolite catalysts with intensity measured in arbitrary units (a.u.), and X-ray incident angle in degrees.

These results were in accord with what were in the literature [163, 164]. Obviously, the zeolite had high crystallinity prior to doping it with the metal precursors. Its crystallinity diminished tremendously due to the interaction between the Si-O and Ni, Co, and Mo at 2θ =7.8°, 12.6°, 24.4°, 27.6°, and 53°. The peaks at these angles could be ascribed to the oxides of molybdenum in the following crystallographic directions: MoO_3 [100], MoO_3 [001], MoO_3 [100], MoO_3 [021], and MoO_2 [311], respectively [165-171]. Further interaction from the oxides of cobalt (Co_xO_y) found at 16.6°, 21.9°, and 41.9° decreased the crystallinity of the zeolite [172]. Lastly, the oxides of nickel (Ni_2O_3 [002], NiO [222], NiO [111]), at 30.4°, 34.7°, and 44.5° respectively, contributed to the lowering of crystallinity of the zeolite [171, 173, 174].

3.2.5. FTIR Analysis of Catalyst

FTIR spectra were recorded for zeolite (support), fresh Ni-Co-Mo-Zeolite, and used Ni-Co-Mo-zeolite in a frequency range of 400-4000 cm^{-1} (Figure 3.5).

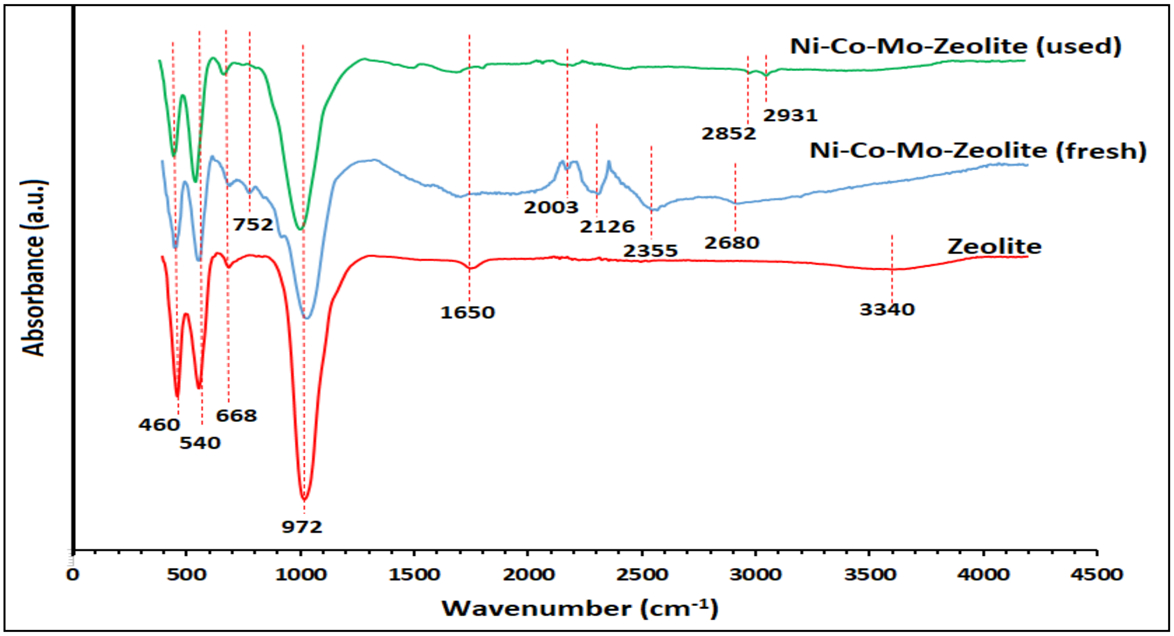

Figure 3.5. FTIR for the zeolite, the fresh Ni-Co-Mo-Zeolite, and the used Ni-Co-Mo-zeolite catalysts at 380 °C and at 14 bar CTH.

The spectrum for the zeolite exhibited frequencies of 460, 540, 668, 972, 1650, and 3340 cm^{-1}. Spectrum peaks at 460 cm^{-1} could be attributed to the bending vibration of T-O-T (T=Al, Si groups) in the zeolite structure. [175, 176] This band also depicted the bending vibration of internal tetrahedron TO_4 of the zeolite structure [177]. This also showed the presence of Al^{+3} and Si^{4+} in the zeolite. The bands around 540, 668, and 752 cm^{-1} could be attributed to internal and external linkage symmetrical stretching vibrations. The band 972 cm^{-1} highlighted the symmetrical stretching vibration and the tetrahedron vibration of the Si-O bond [177]. The peak at 1650 cm^{-1} could be attributed to the bending vibration of O-H in the adsorbed water (H_2O) on the zeolite surface [156]. 3340 cm^{-1} could be ascribed to Si-OH in the nest defects and the hydrogen bonding of loosely held water molecules [178]. Evidently, the metal-doped zeolite (fresh catalyst) exhibited the lowest intensity (absorbance) and a slight shift in frequencies due to Co^{3+}, Ni^{2+}, and Mo^{6+} interactions with O-H, Si-O, and the Al-O bond during the doping process. Spectra at 2003, 2126, and 2355 cm^{-1} could be attributed to the interaction between Ni-Co-Mo ions and TO_4 in the zeolite during the doping process. Disappearance of the wavenumber 1650 cm^{-1} in the fresh catalyst indicated sufficient calcination, which removed water molecules that caused agglomeration of active metal and consequent deactivation of the catalyst [156]. The appearance of the frequency range of 2750-3000 cm^{-1} evidenced the stretching modes of CH_x, showing the formation of hydrocarbon species on the used catalyst [179].

3.2.6. Surface Area Analysis

The performance of the catalyst was assessed by BET analysis (Figure 3.6), which highlighted the hysteresis loop for both the fresh and the spent catalyst. The catalyst surface area was reduced from 250 m^2/g to 180 m^2/g after 2.5 hours of CTH reaction. The reduction in the surface area was due to coke formation that could be corroborated by an increase in carbon (4.4-12.4 wt.%) content in the EDS analysis (Table 2). While the pore volume changed from 0.164 cm^3/g to 0.04 cm^3/g, the pore width increased from 19.6 Å to 70 Å. The surface coke formation caused an increase in the pore width of the catalyst, due to the reduction of effective surface area and, consequently, increased the average pore radius or diameter.

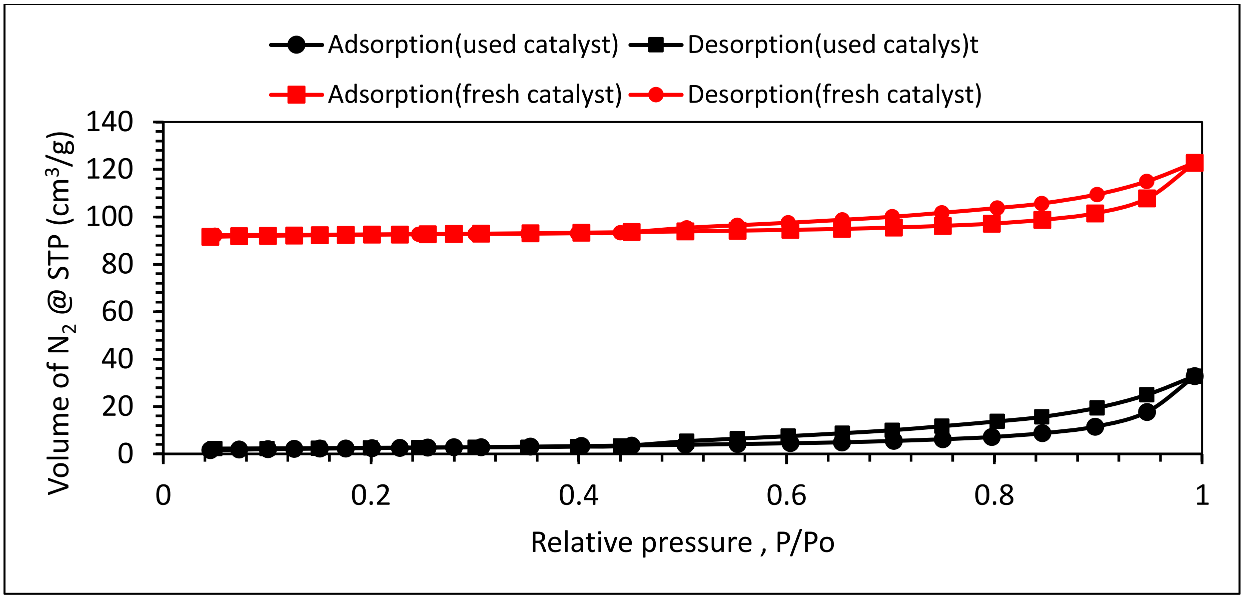

Figure 3.6. BET for the raw and the used catalyst at 380 °C and at 14 bar CTH.

The shapes of the hysteresis loop for both the used and the spent catalysts appeared parallel, which meant that there was not much change in the texture, pore size distribution, and pore geometry. Evidently, at a relative pressure of 0.44, the loop closed at a point where pore condensation and evaporation of N_2 occurred, which gave adsorption and desorption isotherm of type 1 and 4, according to the International Union of Pure and Applied Chemistry [180].

3.2.7. Kinetics

Reaction Mechanism

To render this work beneficial and of broad application to stakeholders in the biofuel community, the kinetics of CTH were performed at temperatures (360, 390, and 420 °C), since important products (e.g. iso-alkanes, cyclo-alkanes, etc.) were formed at different temperatures. Based on the products obtained from the GCMS, the reaction mechanism was proposed (Figure 3.7). C6-C14 was classified as short-chain hydrocarbon because the shortest carbon chain in the WCO used in this study was C15 (Figure B1).

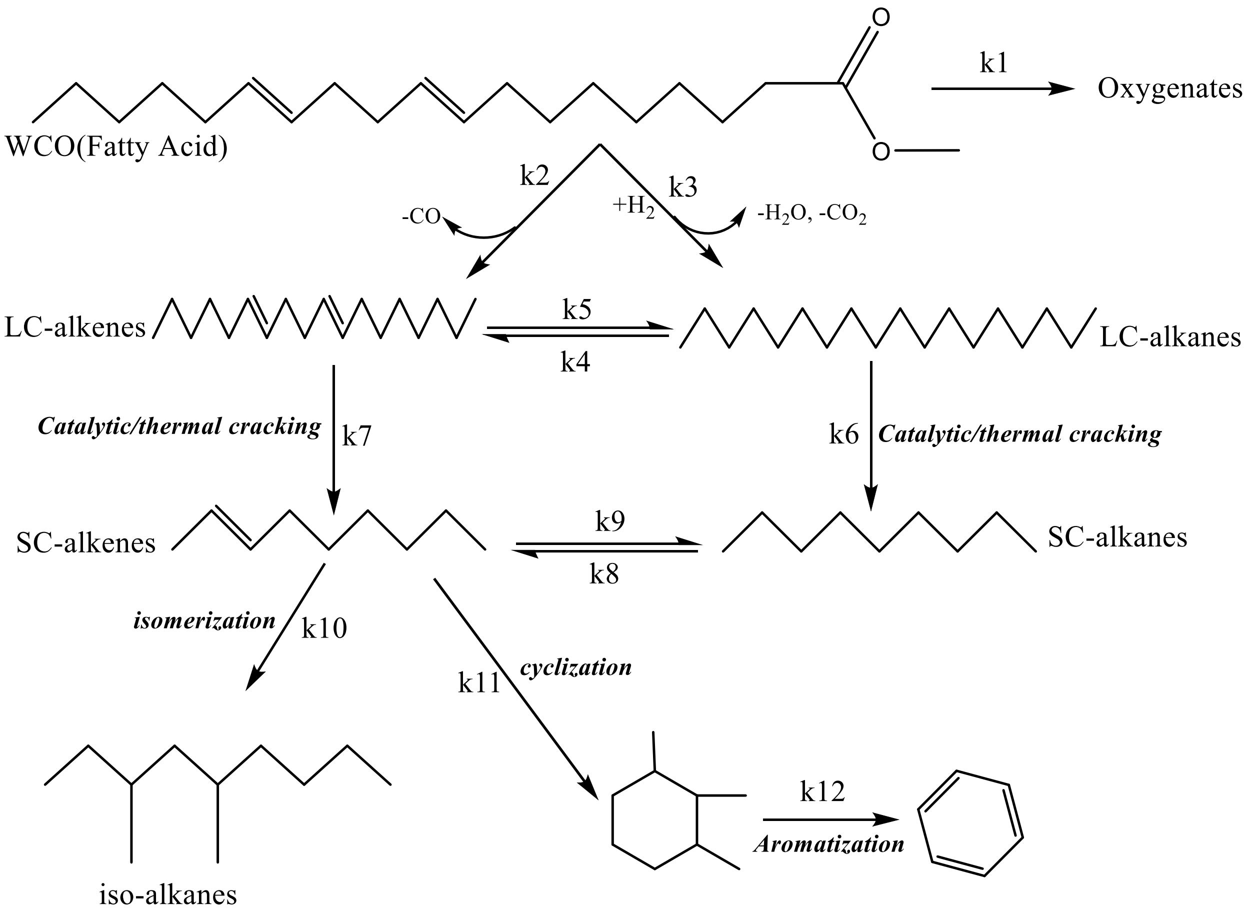

WCO(Fatty Acid)
k1
Oxygenates
k2
-CO
k3
+H2
-H2O, -CO2
LC-alkenes
k5
k4
LC-alkanes
Catalytic/thermal cracking
k7
k6
Catalytic/thermal cracking
SC-alkenes
k9
k8
SC-alkanes
isomerization
k10
k11
cyclization
iso-alkanes
k12
Aromatization

Figure 3.7. Possible reaction pathway for catalytic transfer hydrogenation of WCO. SC= short-chain (C6-C14); LC= long-chain (C15-C18)

Evidently, WCO could produce oxygenates (k1), long-chain (LC) alkane (k2) and LC alkenes (k3) via decarboxylation, hydrogenation, and dehydrogenation. There could be a reversible reaction (k4, k5) between LC-alkenes and LC-alkanes (LC alkenes could undergo hydrogenation and give rise to LC-alkanes, while LC-alkanes could undergo dehydrogenation to produce LC-alkenes). LC-alkanes could crack catalytically or thermally (k6) to produce short-chain (SC)-alkanes. LC-alkenes also cracked thermally (k7) to produce SC-alkenes. There could be a reversible reaction between SC-alkenes and SC-alkane (k8, k9) via dehydration and hydrogenation. SC-alkenes presumably underwent cyclization (k11) and isomerization (k10) to produce cyclo-alkanes and iso-alkanes, respectively. Finally, cyclo-alkanes produced aromatics via aromatization (k12).

3.2.8. Kinetic Model

The following elementary assumptions were made: (i) one-dimensional flow; (ii) isothermal and steady state conditions; (iii) perfect plug flow and absence of temperature gradients inside the catalyst particles were assumed [85]; (iv) for the sake of simplicity, possible conversion of short chains olefins and paraffins to long-chain olefins and paraffins were excluded; (v) the rate of coke and gaseous products formation were not considered, as the amounts produced were considered insignificant compared to that of the liquid products; (vi) intraparticle mass transfer resistance was assumed to be negligible as diffusion was very fast, such that the overall rate was not affected by mass transfer in any fashion [85];[181]; [85] the rate of adsorption and desorption of products and reactants were not considered.

The concentrations of the products were represented as follows: C_1 = WCO; C_2 = oxygenates; C_3 = long-chain alkanes; C_4 = long-chain alkenes; C_5 = short-chain alkenes (C6-C14); C_6 = short-chain alkanes (C6-C14); C_7 = iso-alkanes; C_8 = cyclo-alkanes, C_9 = aromatics. The rate of formation or disappearance of these products was represented by Eq. (3.4-3.12), where τ represented the space time or the mean residence time (s), which equaled the volume of the reactor divided by the volumetric flow rate. First order rate equation was assumed, since this reaction was facilitated by a catalyst and, therefore, the rate was assumed to be faster than the rate of thermal decomposition of WCO, which was second order, as observed from the previous section.

$$\frac{dC_1}{d\tau} = -(k1 + k2 + k3)C_1 \tag{3.4}$$

$$\frac{dC_2}{d\tau} = k1C_1 \tag{3.5}$$

$$\frac{dC_3}{d\tau} = k3C_1 - (k6 + k4)C_3 + k5C_4 \tag{3.6}$$

$$\frac{dC_4}{d\tau} = k2C_1 - (k5 + k7)C_4 + k4C_3 \tag{3.7}$$

$$\frac{dC_5}{d\tau} = k7C_4 - (k9 + k10 + k11)C_5 + k8C_6 \tag{3.8}$$

$$\frac{dC_6}{d\tau} = k6C_3 + k9C_5 - k8C_6 \tag{3.9}$$

$$\frac{dC_7}{d\tau} = k10C_5 \tag{3.10}$$

$$\frac{dC_8}{d\tau} = k11C_5 - (k12)C_8 \tag{3.11}$$

$$\frac{dC_9}{d\tau} = k12C_8 \tag{3.12}$$

The kinetic rate constants ($k1$-$k12$) of the developed models were estimated using the experimental data (Tables B8, B9, & B10) at three temperatures 360, 390, and 420 ^{o}C by nonlinear regression using Levenberg-Marquardt algorithm in MATLAB software [182]. The optimum values were estimated using the *least-square method* by minimizing the objective function, as shown in $Eq.$ (3.13).

$$f = \sum_{i=1}^{n} \left[\left(C_{pred}\right)_i - \left(C_{exp}\right)_i \right]^2 \tag{3.13}$$

With the known values of rate constants, the activation energy (E_a, kJ/mol) and their respective pre-exponential factors (A, s^{-1}) were evaluated using the Arrhenius equation (Eq. (3.14)). Eq. (3.14) was selected, based on the assumption that the rate constant depends on the temperature only. Besides, this equation has been verified empirically, to give the temperature behavior of most reaction rate constants within experimental accuracy over fairly large temperature ranges [181].

$$k = A\, e^{\left(\frac{-Ea}{R\,T}\right)} \qquad (3.14)$$

The activation energy, defined as the minimum energy required by reacting molecules before reaction could occur, was evaluated at 360, 390, and 420 ^{o}C by taking the natural logarithm of Eq. (3.14) that gave Eq. (3.15), and by plotting ($ln\, k$) versus (1/T) (Figure B2), which showed straight lines whose slopes were proportional to the activation energy, while the pre-exponential factors, A, were obtained from different intercepts from the ($ln\, k$)-axis.

$$ln\, k = ln\, A - \frac{E_a}{R}\left(\frac{1}{T}\right) \qquad (3.15)$$

Figure 3. 8 showed the results of the fit of the kinetic model by employing the experimental data at a temperature of 360 ^{o}C (Table B8-B10 (Supporting Information)). The main composition (80%) of the liquid products were SC alkanes (C6-C14) and LC alkanes (C15-C18), while the minor products (20%) were iso-alkanes, aromatics, and oxygenates. The kinetics depicted 98.9% conversion of WCO in approximately 1200 s (0.33 h), compared to published reports [72].

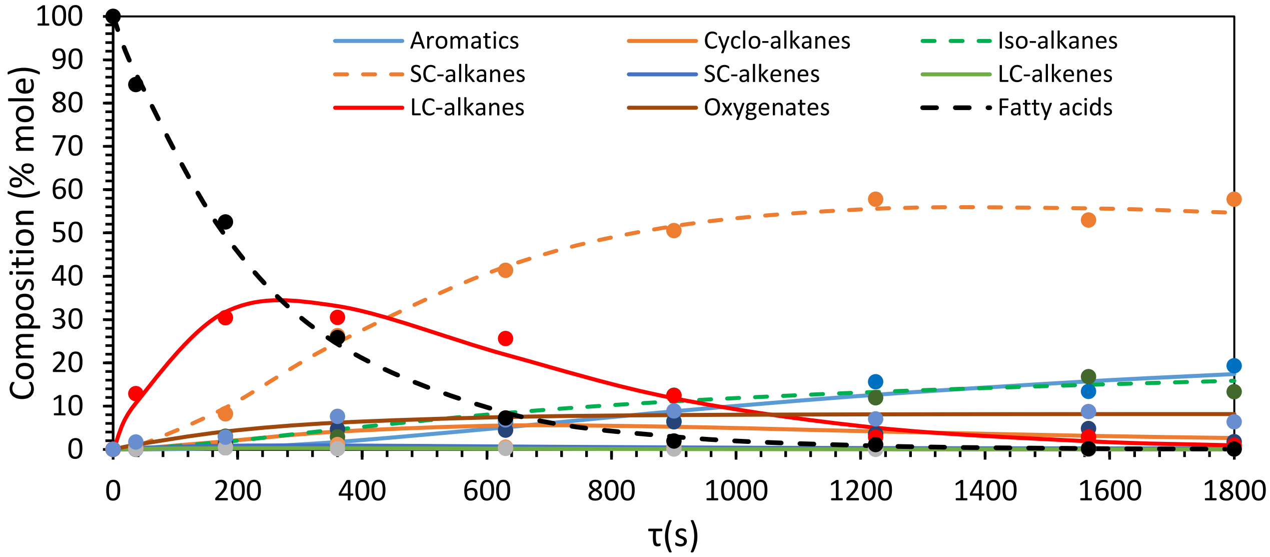

Figure 3.8. Kinetic fit of the experimental data from CTH at 360 °C and 14 bar; dashed and continuous lines represent the estimated values while dots represent the experimental values.

The long-chain alkanes (LCALK) level peaked at 320 s and gave way to short-chain alkanes (SCALK) via catalytic cracking with SCALK that plateaued at 1220 s. Iso-alkanes were insignificant, due to low temperature of operation in this work. Increasing the temperature to 390 °C (Figure 3.9) shortened the conversion time of WCO to 900 s (0.25 h), with 99.6% conversion, compared to what had been reported. [24, 71, 183-186] Evidently, LCALK started cracking catalytically and thermally at 180 s, compared to that of the reaction at 360 °C. An increase in temperature increased the production of iso-alkanes (24%) and aromatics (16%), while the SCALK dipped by 14%. Further increase in temperature to 420 °C shortened WCO conversion (99.7%) further to 360 s, while LCALK started cracking at 36 s and produced nearly 50% SCALK in 270 s.

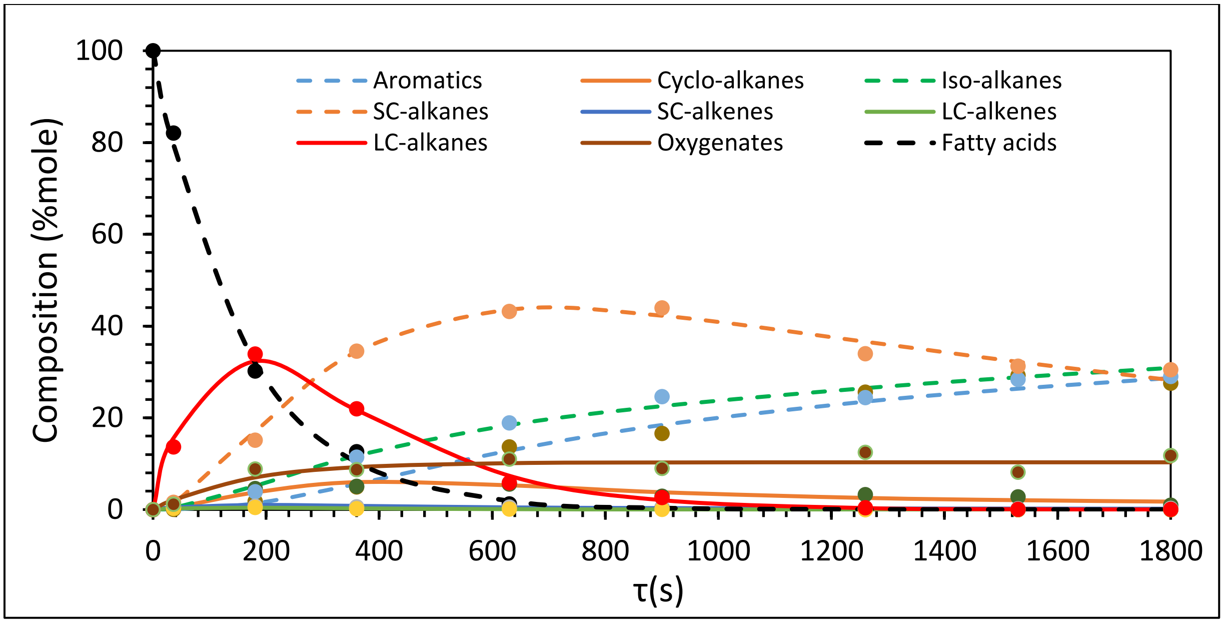

Figure 3.9. Kinetic fit of the experimental data from CTH at 390 °C and 14 bar; dashed and continuous lines represent the estimated values, while dots represent the experimental values.

Progressively, SCALK dropped and yielded to short-chain (SC)-alkenes that underwent isomerization and cyclization and produced a high level of aromatics (45%) and iso-alkanes (35%) (major products in the liquid fuel at 420 °C) (Figure 3.10). Evidently, prolonging the time could eventually convert the majority of the iso-alkanes to aromatics; this could pose environmental issues, due to the release of volatile organics during the combustion of the fuel [187, 188].

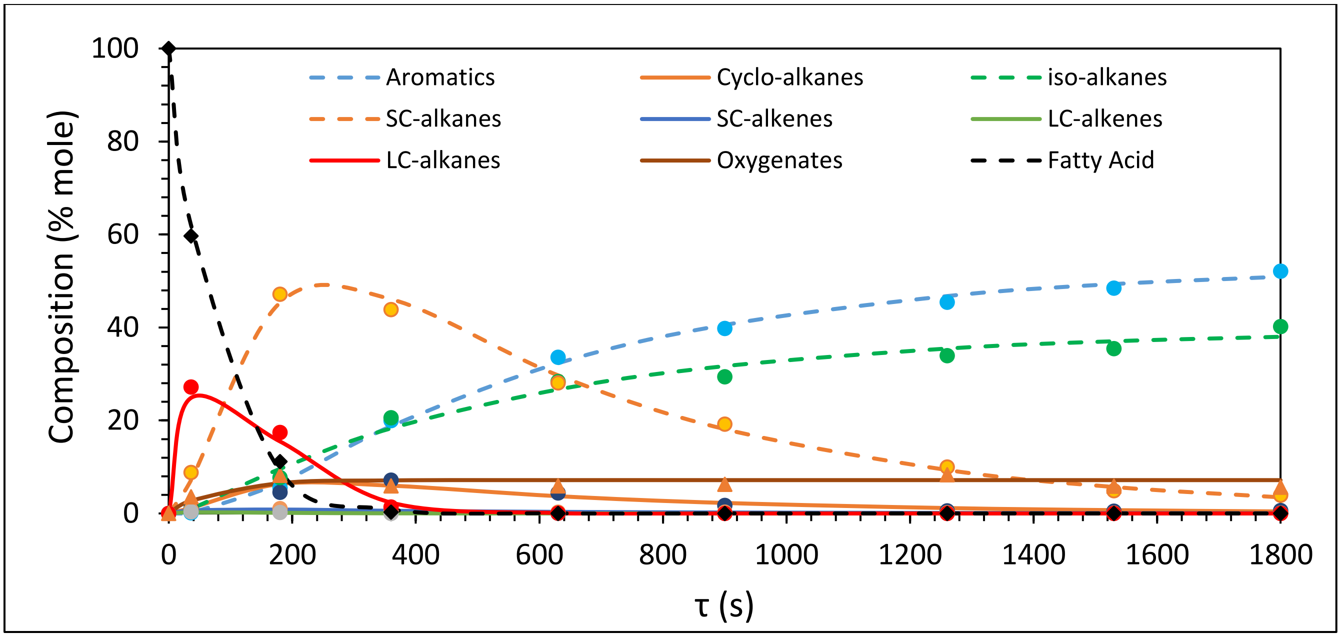

Figure 3.10. Kinetic fit of the experimental data from CTH at 420 °C and 14 bar; dashed and continuous lines represent the estimated values while dots represent the experimental values.

Table 3.3. Kinetic rate constant, activation energy and pre-exponential factors calculated at different temperatures.

Kinetic rate constants (s^{-1})				Activation energy (kJ/mol)	Pre-exponential factor (s^{-1})
Temperature (°C)	360	390	420		
k1	0.00032	0.00065	0.00095	70.37	2.03E+2
k2	0.00326	0.00410	0.00810	54.87	1.01E+2
k3	0.00094	0.00126	0.00421	90.31	2.27E+5
k4	0.04310	0.08700	0.10100	52.23	9.53E+2
k5	5.02100	7.02100	11.2100	48.67	5.07E+4
k6	0.00083	0.00121	0.00871	141.32	2.91E+8
k7	0.31200	0.40100	0.85100	60.49	2.80E+4
k8	0.00038	0.00113	0.00413	144.73	3.17E+8
k9	0.06800	0.10100	0.20100	65.57	1.65E+4
k10	0.01740	0.09961	0.10995	113.49	5.17E+7
k11	0.02200	0.03900	0.09390	87.87	3.69E+5
k12	0.00250	0.00460	0.01046	86.75	3.44E+4

Table 3.3 highlights the kinetic parameters obtained from fitting Eq. (3.4-3.12). The minimum of energy (activation energy) required to initiate the CTH was found to be 84±18.7 kJ/mol WCO,

with 95% confidence (predetermined value). The activation energy was less than that obtained from the pyrolysis of WCO (without a catalyst), as shown in the preceding section. Reported energy of activation for the hydroprocessing of jatropha oil was 115 kJ/mol [92], and that of CTH of WCO over activated carbon was 53 kJ/mol. The average activation energy in this study was (59%) higher than what had been reported in our last work, because the kinetic models employed in the current study were rigorous and exhaustive compared to the lumped model employed in the last work (Table B12) [100]. Producing LC alkanes from LC-alkenes was faster (k5 = 5.02 s^{-1}) and required the lowest energy (E_a = 48 kJ/mol). This explains why LC-alkenes were produced, in the early stages, at 360 ^{o}C. Producing SC-alkanes via LC-alkanes' route was slower (k6=0.00083-0.00871 s^{-1}) and required higher energy (E_a = 141kJ/mol) than that through the SC-alkenes' route, which was faster (k7=0.312 s^{-1}) and required lower energy (E_a = 60 kJ/mol). The reason is that the C=C bond (π--bond) in LC-alkenes can be more reactive than the C-C bond (σ -bond) in the LC-alkanes. The k-values also showed that the rate of formation of long-chain olefins and paraffins, oxygenates, and short-chain paraffins to short-chain olefins was higher than the rate of formations of other species. The assumption of first order could be justified by the R-squared value of 0.989, which took care of 98 percent of variability in the model. Figure B2 (Supporting Information) highlights the plot of $(\ln k)$ against inverse of temperature (Eq. (3.15)). The linear plots obtained buttressed the goodness of fit of the kinetic models.

3.2.9. Optimization of CTH

D-optimal Design and Regression Model

Results from the optimal design of CTH are shown in Table B11, which highlights the process variables (A, B, C, and D) and the experimental and calculated percent alkanes. The values in

Table B11 were employed in determining the coefficients in Eq. (3.3) and the interactions among the process variables. Eq. (3.16) highlights the polynomial obtained by multiple regression using MATLAB software. Eq. (3.16) represents the final and appropriate equation that best fits the experimental data, after testing other models.

$$Y = -3429.8 + 18.5\mathbf{A} - 8.4\mathbf{B} + 39.8\mathbf{C} - 5.8\mathbf{D} + 0.03\mathbf{AB} - 0.09\mathbf{AC} + 0.028\mathbf{AD} + 0.73\mathbf{BC} + 0.87\mathbf{BD} + 1.65\mathbf{CD} - 0.025\mathbf{A}^2 - 0.19\mathbf{B}^2 - 8.98\mathbf{C}^2 - 0.52\mathbf{D}^2 - 0.0024\mathbf{ABD} \quad (3.16)$$

ANOVA was used to assess the goodness of fit (Table B13) for the polynomial, using the experimental data. The goodness of fit for the regression model was determined by the R-squared value (0.999) and the R^2-adjusted value (0.986). R-squared was used to judge the adequacy of the model by measuring the variability in the data. In this case, the chosen model accounted for the 99.9% of the variability in the experimental data. The R-squared statistic proved to be somewhat problematic or deceptive as a measure of the quality of fit for multiple regression, because it never decreased when a variable was added to the model. To alleviate this problem, R^2-adjusted (0.986) was employed as a perfect index for assessing the quality of fit, as it only increased when the added variable reduced the error mean squared. The interaction of process variables and their effects on the model were determined by using the p-values. Coefficients with a p-value less than 0.05 (a rule of thumb) were considered significant. Essentially, all of the process variables had significant effects on the yield of alkanes, as their p-values were less than 5%. [89] It was also evident that the degree of these effects varied with variable p-values. For example, the effect of A (temperature) on the model was higher than that of B (pressure), since the p-value of A was lower than that of B. In addition, the effect or interaction between AB (temperature and pressure) was more significant than that between AC (temperature and WCO/2-propanol ratio). The average p-value for the polynomial model was 4.42×10^{-15}, signifying the goodness of the model.

Model Validation

The model was validated by analyzing the residuals in order to ascertain the presence of outliers in the experimental data. There was also the need to verify the assumption of normally distributed residuals. Figure 3.11 highlights the residuals of the model in different forms. Figure 3.11 (a) shows an unpattern spread or randomly scattered points of the residuals' plot of the fitted data. This showed that there were no outliers that were required to be removed from the data, as all of the points were within the standard deviation of 1. Figure 3.11 (b) showed that there was constant variance in the residuals.

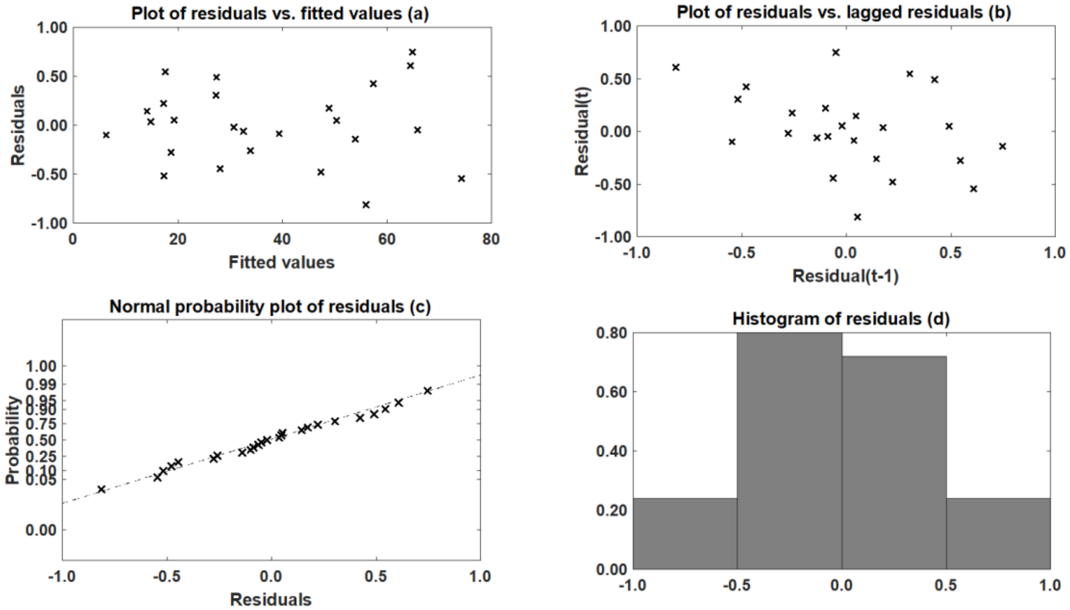

Figure 3.11. Diagnostic plots of the regression model: (a) residuals of fitted values; (b) residuals and lagged residuals; (c) normal probability; (d) histogram of residuals.

Figure 3.11 (c) showed that the residuals were normally distributed, as the points were close to the straight line of the probability plot, which was confirmed by the histogram (Figure 3.11 (d)). This showed that the error variances were homogeneous and independent of each other.

Response Surface Plot

The response surface plot assisted in determining the effect of the temperature, pressure, WCO-2-propanol ratio, and WHSV on the alkanes production. Not only did this plot show the response of alkane production to changes in the process parameters, but it also provided the optimum parameters for producing the highest percent of alkanes. Figure 3.12 highlighted the response surface plot that delineated the effect of temperature, pressure, oil-2-propanol ratio, and WHSV on alkanes produced via CTH.

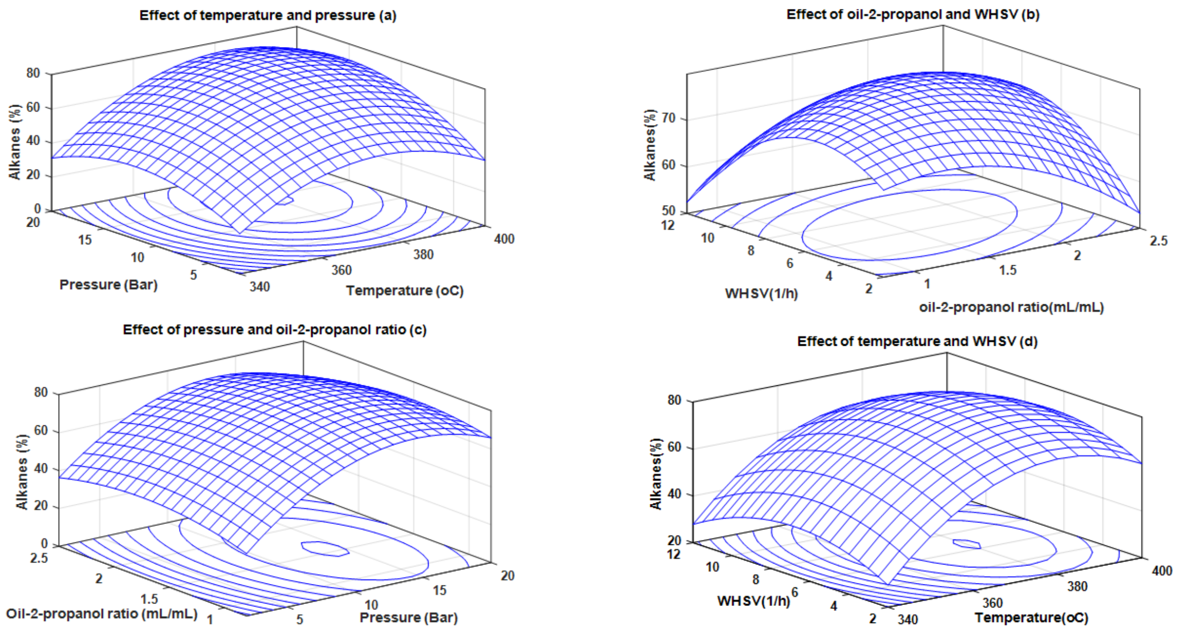

Figure 3.12. Three-dimensional response surface showing the expected alkanes yield as a function of temperature, pressure, oil-2-propanol ratio, and WHSV.

3.2.10. Effect of Process Variables

Temperature

Increasing temperature from 340 °C to 380 °C (Fig.3.13 (a & d)) enhanced the yield of alkanes, since temperature rise promoted the cracking of the heavy hydrocarbons to light hydrocarbons or SC-alkanes, as was confirmed in the preceding sections. Increasing the temperature aided the scission of the C-C and C-O bonds, leading to hydrodeoxygenation. On the contrary, beyond a temperature of 380 °C, polyaromatics and cycloalkenes predominated, due to the dehydrogenation of alkanes to alkenes, thereby decreasing production of the alkanes [82, 189].

Pressure

Figure 3.12 (a & c) highlighted the effect of pressure on alkane yield. Increasing pressure increased the partial pressure of the hydrogen produced by the 2-propanol, leading to enhanced mass transfer into the bulk of the reaction system and onto the surface of the catalyst. In addition, increasing pressure increased the residence time of the reacting species to react at the surface of the catalyst before falling into the bulk reaction domain. At inordinate pressure beyond 15 bar, reacting species did not possess the significant energy to detach from the surface of the catalyst, leading to oligomerization that decreased the percent alkanes [156].

WCO-2-propanol Ratio

Increasing the WCO-to-2-propanol ratio from 0.8 to 1.5 seems to slightly increase the alkane yield. The low WCO-2-propanol ratio enhanced the production of hydrogen for the requisite hydrogenation reaction that increased the production of the alkanes. In addition, the low ratio lowered the viscosity of the reaction mixture that facilitated the mass transfer of the reacting species. Increasing the ratio beyond 1.6 decreased the amount of 2-propanol required for producing hydrogen for hydrogenation of the WCO, and consequently reduced the yield of the alkanes, as shown in Figure 3.12(c).

WHSV

WHSV is the ratio of mass flow rate of feed (kg/h) to the mass (kg) of catalyst (Ni-Co-Mo-zeolite) loaded into the reactor. Figure 3.12 (b & d) highlights WHSV effect on the yield of the alkanes. In this work, WHSV was chosen from 2-12 h^{-1}, due to the dimensions of the reactor. It was observed at 2 h^{-1} that 70% of the liquid product was polyaromatics and cycloalkenes that were undesirable from an environmental and fuel-stability point of view. The low values of WHSV meant a long residence time of reacting species in the reactor, leading to dehydrogenation and oligomerization. The maximum percent of alkanes was obtained at 6.7 h^{-1}, due to the optimum time and the other operating parameters (pressure, temperature, and WCO/2-propanol) required for hydrodeoxygenation and cracking mechanism. As WHSV increased to 12 h^{-1}, the reactants spent a short time in the reactor, resulting in incomplete CTH reaction and, thus, the yield of alkanes dipped. High value of WHSV in this work generated oxygenates and dense liquid products.

3.2.11. Optimization and Validation

Figure 3.13 [190] delineates the contours of the response surface in Figure 3.12. To optimize the CTH reaction, the method of Steepest Ascent [89] was employed, in order to reach the optimum parameters required to achieve the highest yield of alkanes. The optimum reaction parameters were temperature (383.7 ^oC), pressure (14.8 bar), WCO/2-propanol (1.57 mL/mL), and WHSV (6.7 h^{-1}), that gave the alkanes yield of 80%. These values were verified by the analytical method, whereby the obtained polynomial (Eq. (3.14)) was solved by partial differentiation. Further experimentation was conducted at these optimum values, in order to validate the model

(Figure 3.14); this resulted in 77% alkanes, 3.8% alkenes, 12.3% aromatics, and 6.7% gaseous products. The discrepancy between the yield based on the model and the validated values could not be ascribed to the inaccuracy of the model, since it has been validated (Figure 3.11); it could, rather, be attributed to the nature of side reaction, the nature of reversible reaction, and inefficiency in product collection and handling at the laboratory, et cetera.

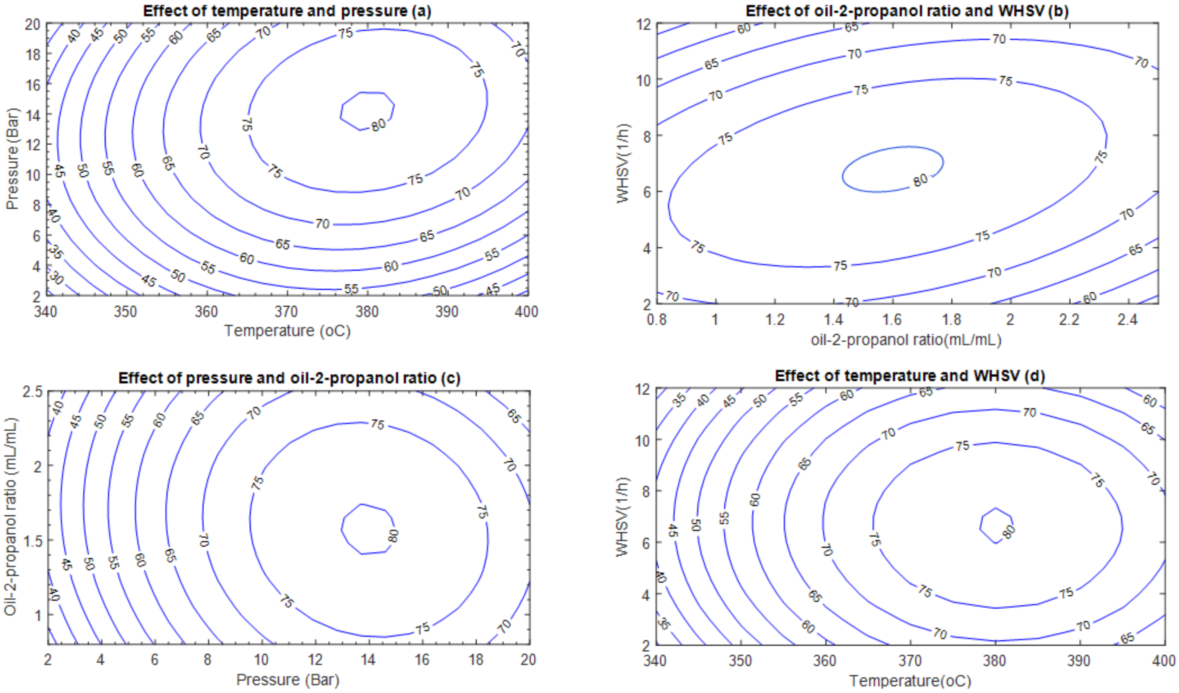

Figure 3.13. Contour plot of the yield of alkane response surface in Figure 3.12.

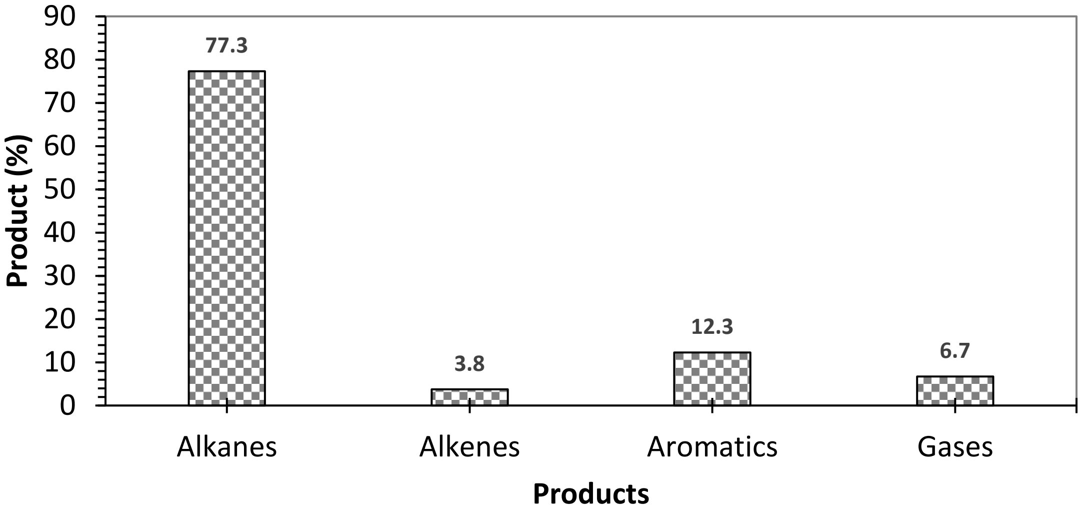

Figure 3.14. Validation of experimental model with products distribution at optimum condition (383.7 ^oC, 14.8 bar, 1.57 WCO/2-propanol, and 6.7 h^{-1}).

3.2.12. Physical Properties of Liquid Fuel

The physical properties of the liquid fuel were determined and were compared to the published work [100] and to the American Society for Testing and Material Standards (ASTM) (Table 3.4) [191]. It was observed that the final boiling point of the product obtained in this work was lower than that of the last work. Moreover, other flow properties of the fuel were better than those of the published work. Figure 3.15 highlights the results for simulated distillation of the liquid product. The results showed that 40% (gasoline) of the product was distilled below 170 ^oC, 50% (jet fuel) was distilled between 170 ^oC-230 ^oC, 8% (kerosene) was distilled between 230 ^oC- 290 ^oC, and 2% (light gas oil) between 290-335^oC [192]. The final maximum boiling point of the fuel was 332 ^oC, which is lower than that (403 ^oC) of the last work, suggesting that the Ni-Mo-Co-zeolite catalytically cracked heavy hydrocarbons, compared to the results from the last work.

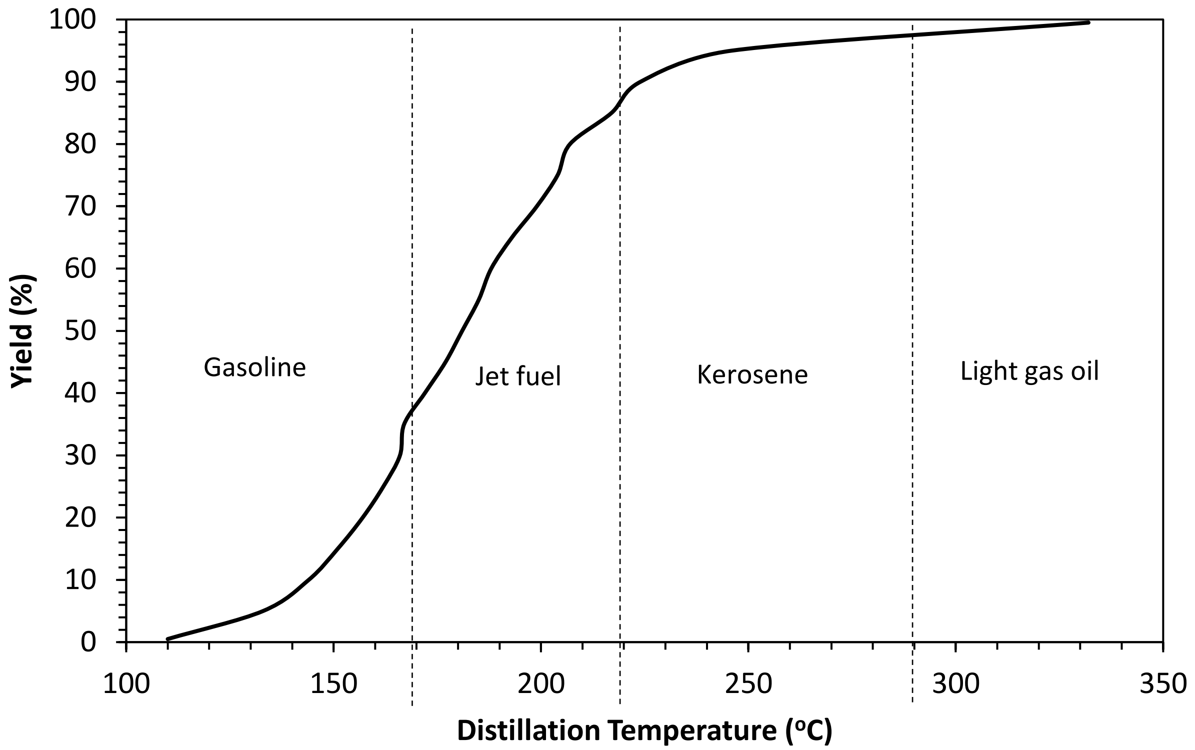

Figure 3.15. Simulated distillation of liquid fuel product from optimum condition.

Table 3.4. Physical properties of the liquid hydrocarbon compared to those of ASTM standards.

Physical properties	Current Work	Published[3] Work		ASTM	Test Method
Acidity, mg KOH/g	0.11	0.13	max	0.1	D3242
Aromatics(%v/v)	15.4	20	max	25	D1319
Distillation temperature, °C					
%10 recovered	140	54	max	200	
%50 recovered	180	74		Report	
%90 recovered	224	172		Report	
Final boiling point °C	332	403	max	300	
Density @ 15 °C, kg/m^3	776	790-820		775-840	D1298
Freezing point (°C)	-47	-46		-40-47	D5972
Viscosity (mm^2/s)	6.3	6.6		8	D445
Net Heat of Combustion, MJ/kg	45.5	44		42.8	D4529

3. 3. Conclusions

Catalytic transfer hydrogenation reactions of waste cooking oil were conducted in a continuous-flow reactor over a commercial catalyst (Co-Mo-Ni-zeolite). Characterization the catalyst revealed the cubic nature of the zeolite, which slightly lost its crystallinity after one cycle run of the CTH reaction. This trimetallic catalyst might add extra cost to the process, but this cost could be covered by the comparatively inexpensive cost of handling of 2-propanol, and by the affordable price of WCO.

The kinetic rate of formation of major composition of the fuel product was studied at different temperatures by keeping the pressure and WHSV constant. The results showed that, even at a temperature of 360 ^{o}C, short-chain alkane could be produced over the prepared catalyst. This means that stakeholders have three different temperatures to produce their preferred liquid hydrocarbon fuel products, depending on their goals. Optimization studies revealed that operating at 384 ^{o}C, 14.7 bar, WHSV of 6.7 h^{-1}, and WCO-2-propanol ratio of 1.57 produced high quality liquid products with high levels of iso-alkanes and short-chain hydrocarbons fuel, which did not necessarily require further distillation. Not only did this study produce high quality fuel, it also reduced the inherent problem of handling a large volume of hydrogen gas in the conventional hydroprocessing of vegetable oils.

Comparatively, it could be inferred from the current study that the use of trimetallic catalyst practically increased alkanes by 140%. In addition, alkenes decreased by 90%, aromatics decreased by 23%, and gaseous products decreased by 77%, due to the increase in the reaction pressure in the current work. Liquid fuel yield increased by 11% while WCO-2-propanol ratio dropped by 37%, signifying a decrease in 2-propanol used, compared to our last study. The average activation energy of the CTH reaction was (59%) higher because the kinetic models employed in the current study were rigorous and exhaustive, compared to the lumped model employed in the last work.

3.4. Acknowledgement

The financial support by Old Dominion University Research Foundation Summer Fellowship is highly acknowledged. The authors are also thankful for the support offered by Dr. Cao and his team at The Jefferson Laboratory.

CHAPTER 4

CATALYTIC TRANSFER HYDROGENATION AND CHARACTERIZATION OF FLASH HYDROLYZED MICROALGAE INTO HYDROCARBON FUELS PRODUCTION (JET FUEL)

Note: The contents of this chapter were published in the Journal of Fuel

DOI: https://doi.org/10.1016/j.fuel.2019.116440

A. Asiedu, R. Davis, S. Kumar, Catalytic transfer hydrogenation and characterization of flash hydrolyzed microalgae into hydrocarbon fuels production (jet fuel), Fuel 261 (2020) 116440.

Oil-laden biofuel intermediate (BI) from flash-hydrolyzed microalgae was characterized, pyrolyzed, and subjected to catalytic transfer hydrogenation (CTH) to produce both gaseous and liquid hydrocarbon fuels. The BI was characterized by TGA and FTIR that revealed significant triglycerides, as evidenced by the C=O bond with insignificant level of carbohydrates and proteins. Thermogravimetric analysis (TGA) indicated that the BI could be thermally decomposed at 400 ^{o}C. Pyrolysis of the BI engendered mainly gaseous hydrocarbon (alkenes) with a high heating value (HHV) of 48.5 kJ/mol at 850 ^{o}C. Energy of activation for the pyrolytic process was estimated to be 115-300 kJ/mol. Optimization of oil extraction from the BI was performed via design of experiment. The oil was subjected to CTH over NiO_x-CoO_x-MoO_x-zeolite, using 2-propanol as a hydrogen donor in a 30-ml batch reactor at a temperature range of 390-420 ^{o}C and an autogenic pressure of 24-27 bar, leading to fatty acid conversion of 99-100%. The main liquid products obtained from the CTH were iso-alkanes (41%), cyclo-alkanes (35%),

aromatics (5%), n-alkanes (14%), and alkenes (5%). Kinetics of the CTH showed first order with activation energy of 176 kJ/mol.

The catalyst was characterized by X-ray diffraction (XRD), Fourier transform infrared spectroscopy (FTIR), Brunaeur-Emmett-Teller (BET) adsorption and desorption, scanning electron microscope (SEM), energy dispersive spectroscopy (EDS), and TGA. The catalyst revealed cubic structure, which was maintained after 5 h of CTH reaction. Present in both the fresh and the used catalysts were oxides of alkali and transition metals. The active sites of the catalyst were dominated by Co^{3+}, Ni^{2+}, and Mo^{6+}.

4.0 Introduction

As the world's fossil fuel reserve continues to decrease, energy researchers resolutely investigate more sustainable energy resources. The unavoidable decrease in fossil fuel reserves will continue, as the world's population is expected to grow by 0.9% per year, from 7.3 billion in 2014 to 9.2 billion in 2040. This population growth will be attended by an increase in global energy consumption of nearly 29% by 2040. Concomitant CO_2 emissions will also increase from 32-37 giga tonnes [100]. Air transportation energy increased by 5% (24856-26030 trillion Btu) in USA from 2009-2019 [193]. The Energy Information Administration (EIA) predicts an approximately 38% increase (1.25-1.73 million barrels/day) in oil consumption between 2019 and 2050 [194]. Furthermore, global airlines' fuel consumption has been predicted to reach 97 billion gallons (367 billion liters) in 2019, with 1032 million tonnes of CO_2 emission [195]. Considering this fuel consumption and its potential environmental footprint, there is a need for alternative, sustainable liquid fuel resources. Prominent among these energy resources are microalgae that are promising biomass resources and high photosynthetic efficiency and fast growth rate [196]. Not only do microalgae possess growth advantage, but they also eliminate food-fuel competition and farmland occupation. In addition, they enhance fertilizer recycling, such as struvite (NH_4MgPO_4) [197], and act as a CO_2 sink, thereby reducing greenhouse gas emission [198-206]. Apart from their agrarian advantages, microalgae are endowed with bio-based resources, namely polysaccharides, proteins, and oil. The latter, which is of a lower percentage, has enormous level of triglycerides, which have been used to produce jet-diesel-fuel-range hydrocarbons [207-209]. Microalgae oil has a longer carbon chain than that of vegetable oil, and it can produce the carbon number (C8-C16) in jet fuel [210]. A statistical summary of lipid contents in 19 different species of microalgae is presented in Table 4.1.

Table 4.1. Lipid Contents of Different Species of Microalgae [211]

Mean (wt. %)	23.1
Standard Error (wt. %)	2.5
Median (wt. %)	18.9
Mode (wt. %)	24.0
Standard Deviation (wt. %)	11.0
Kurtosis	1.4
Skewness	1.6
Range	38.0
Minimum (wt. %)	11.0
Maximum (wt. %)	49.0
Confidence Level (95.0%)	5.3

Considering the moderate level of lipid contents microalgae, few processes in the literature have highlighted the conversion of microalgae to jet fuel. Chiefly among them are thermal and hydrocracking (time consuming); pyrolysis (uncontrollable, high level of N & O); Fischer Tropsch (costly and energy-intensive); transesterification (costly); enzymatic process (costly and immature); Centia^{TM} process (costly); plasma gasification (costly and immature) [209]. To offset the problems associated with the preceding processes, there is a need to concentrate the oil in the microalgae for sustainability. One of the most famous ways of concentrating oil is via hydrothermal liquefaction with or without a catalyst at high pressures, in order to produce biocrude that comprises high levels of nitrogen and oxygen [212]. The presence of significant levels of oxygen and nitrogen in the biocrude oil does not favor catalytic hydrogenation, as excessive hydrogen is required; this makes the process cost ineffective. In addition, the presence of nitrogen could lead to unwanted nitrogenous compounds, such as amides, in the jet fuel, leading to a low heating value in the resulting fuel [213]. Furthermore, biocrude oil possesses remarkable viscosity (high pumping cost), low pH (3.5-4.2, corrosive), and high water content that requires extra energy for evaporation [214].

Considering the problems associated with the concentrated algae oil described above, flash hydrolysis (FH) was used to concentrate the lipids content (~10 wt. %) of *Chlorella Vulgaris* [215]. FH is a chemical-free and subcritical water-based process that fractionates the components of the algae, thereby increasing the lipid content to nearly 52 wt. % (Figure 4.1) [216]. The main objective of FH was to extract the bioactive components (proteins) from the microalgae, resulting in biofuel intermediate (BI); this, having limited benefit, has not been explored to produce jet fuel. The use of BI as raw material for hydrocarbon production has the potential of cost reduction concerning raw material handling, compared to the use of raw microalgae as the raw material.

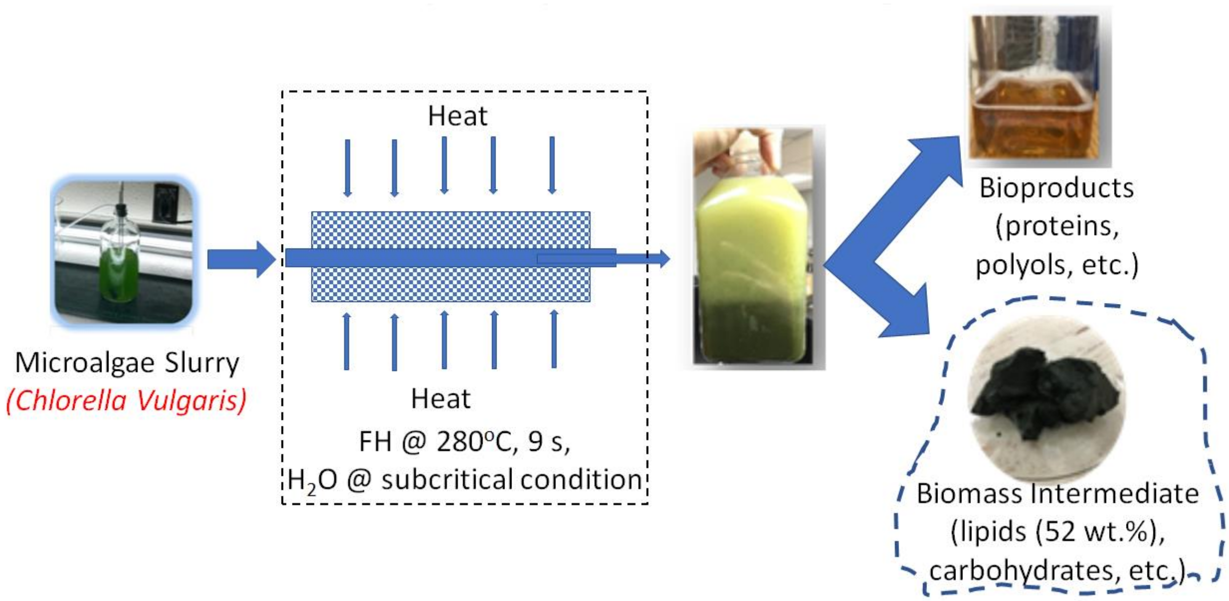
Microalgae Slurry
(Chlorella Vulgaris)
Heat
Heat
FH @ 280°C, 9 s,
H2O @ subcritical condition
Bioproducts
(proteins,
polyols, etc.)
Biomass Intermediate
(lipids (52 wt.%),
carbohydrates, etc.)

Figure 4.1. Flash hydrolysis of Chlorella Vulgaris with the resulting bioproducts and biofuel intermediate

In this study, the oil-laden BI served as raw material for the catalytic transfer hydrogenation (CTH) reaction over the NiO_x-CoO_x-MoO_x-zeolite [217] catalyst, using 2-propanol as the *in-situ* hydrogen donor.

CTH is a reduction of unsaturated organics (such as oleic acid) using hydrogen-donating compounds that catalytically produce hydrogen *in situ*. CTH is advantageous over hydrogenation using gaseous hydrogen, as CTH reduces the high cost of transporting and storing large volumes of gaseous hydrogen in the conventional process of hydrogenation, whereas CTH requires an oil-to-2-propanol ratio of approximately 1.57 mL/mL, and conventional hydrogenation uses H_2-to-oil ratio of 200-300 mL/mL [217]. Selection of 2-propanol as hydrogen donor and oil extract is due its non-toxicity and its potential renewability [62, 63, 65]. Employing 2-propanol for CTH of algae oil enhances the mass transfer and diffusion of reacting species, as 2-propanol is polar, and is significantly miscible with algae oil. On the contrary, the use of gaseous hydrogen is constrained by the mass transfer and diffusion of reacting species, except at high pressures greater than 100 bar [35, 112].

Effective CTH reaction is underpinned by a stable and commercially available catalyst. In this study, a trimetallic catalyst was employed to enhance the cracking of the long-chain algae oil. NiO_x-CoO_x-MoO_x-zeolite has excellent features, and it is commonly used in the petroleum refinery industry. Literature has shown that a mono-metallic catalyst, such as nickel, has lower activity toward the direct scission of C=O and C-O bonds due to its low electrophilicity, but has high C-C bond scission [218]. Adding more electrophilic molybdenum to nickel improves the cleavage of both C=O and C-O bonds. Mono/bimetallic sulfide catalysts (e.g. Mo_2C, MoS_2, Ni-Mo-S, and Co-Mo-S) are biased towards hydrodeoxygenation and are unable to cleave C-C bonds because sulfided catalysts lack an acid site and deactivate in the presence of water [219]. Additionally, sulfided catalysts require the constant replacement of sulfur by adding sulfiding agents such as H_2S and CS_2, which in turn produce both H_2S emission and fuel replete with sulfur [119].

Comprehensive studies have been done on the use of noble metals catalysts (Noble metals (Palladium (Pd), Platinum (Pt), Rhodium (Rd), Ruthenium (Ru), etc.) supported on alumina, activated carbon, and zeolite. Despite their catalyst effectiveness, they are expensive and short-lived [120-125]. Surfactant-mediated mesoporous catalysts, such as SBA-1, HMS, and SBA-15 with their high surface area, large pore structure, and a well-ordered morphology, have been used to hydrotreat vegetable oil. However, they possess weak hydrothermal and mechanical stability and reduced acidity, leading to retardation of their practical application [126, 127]. Silcoaluminophosphate (SAPO-5, SAPO-11, SAPO-31, et cetera) is one of the surfactant-mediated catalysts that has been employed in hydrotreating triglycerides [128-132]. Though

SAPO is micro-mesoporous and has a large surface area, it is biased towards the isomerization of short chain hydrocarbons [133-135]. It also has low hydrothermal stability during hydrogenation of triglycerides, due the production of water as a by-product [111]. This instability could be reduced by adding more surfactant, which would, consequently, render the catalyst expensive [136].

As a result of the problems associated with the preceding catalysts, we use the NiO_x-CoO_x-MoO_x-zeolite catalyst, which has been tried and tested by commercial refineries around the globe. A few of these refineries that have tailored the trimetallic catalyst to process triglycerides are ConocoPhillips (United States, Ireland), Universal Oil Products (UOP)-Eni (UK, Italy), Nippon Oil (Japan), SK Energy (Korea), and Syntroleum (United States) [125]. Not only is the NiO_x-CoO_x-MoO_x-zeolite catalyst commercially available, it is also resistant to coking as trimetallic, compared to mono-bimetallic catalysts. It has been reported that the coke resistance of catalysts ranks in the order of mono-metallic < bimetallic < trimetallic [139]. It is worth selecting zeolite as the support in this work because it is environmentally benign, recyclable, porous, acidic, and resistant to attrition [143].

There has not been exhaustive report on CTH of oil-laden BI from flashed hydrolyzed microalgae. In this study, oil-laden BI, characterized by pyro-GCMS, was employed as the raw material to produce jet-fuel range hydrocarbon. We used 2-propanol to extract the oil via design of experiment in order to obtain the maximum oil yield. Without evaporation of 2-propanol, the mixture was subject to CTH over the prepared catalyst in a batch reactor to produce iso-alkane, the major jet fuel components. Thus, 2-propanol was used as both oil extract and *in-situ* hydrogen donor and conversion of BI via CTH reaction over NiO_x-CoO_x-MoO_x-zeolite catalyst was first reported.

4.1. Materials and Methods

4.1.1. Materials

Sodium-aluminosilicate pellets (-600 mesh), 2-propanol (99.5 wt %) and dichloromethane, nickel nitrate (II) hexahydrate (99.9%), Cobalt (II) molybdenum oxide hydrate (99% metal basis), and diethyl ether were purchased from Fisher Scientific. Refrigerated BI was obtained from our last work on *Chlorella Vulgaris* [215].

4.1.2. BI Characterization

The purpose of the characterization of BI was to ascertain the chemical composition via ultimate analysis, thermogravimetric analysis (TGA), pyro-GCMS, and Fourier-transform infrared spectroscopy (FTIR). It was also necessary to determine the latent energy of the BI by determining the rate of thermal decomposition by TGA and pyro-GCMS. These techniques assisted in evaluating the heating value and the gaseous components of the pyrolysis products. The heating value obtained from this section would serve a baseline for the heating value of the liquid product from the CTH reaction.

4.1.2.1. Thermal Analysis of BI

This step was aimed at determining the rate of thermal decomposition of BI and, consequently, at ascertaining the average boiling point range of oil content that served as a guide for selecting the reaction temperature for the CTH. From the kinetics of the thermal decomposition BI, it was easy to postulate the CTH reaction order, as the catalyst was expected to lower the order of the reaction.

To study the thermal performance of the BI, TGA and differential thermal analysis (DTA) were performed in a nitrogen atmosphere at a flow rate of 30 mL/min with heating rate of 5-30

^{o}C/min. Within this atmosphere, approximately 5 mg of BI was placed in a platinum cup and was heated to 900 ^{o}C [100]. From the DTA plots, the temperature at which the maximum thermal decomposition rate occurred served as a guide in choosing the CTH reaction temperature range, and from the kinetics of the thermal decomposition of BI, the order of thermal decomposition and activation energy were obtained.

4.1.2.2. FTIR Analysis of BI

The purpose of the FTIR analysis was to determine the major components in the BI (oil, carbohydrate, and protein) by identifying the common functional groups. The FTIR spectra of the BI were recorded at room temperature and a wavenumber range of 480-4000 cm^{-1} by diffuse reflectance, using a ThermoNicolet Avatar 370 DTGS spectrometer. Each spectrum resulted from 128 scans to achieve an optimal signal-to-noise ratio.

4.1.2.3. Pyro-GCMS Analysis

To determine the nature of the gaseous products (that could not be analyzed by the TGA facility) obtained from the thermal decomposition of the BI, a pyro-GCMS (a pyrolysis unit connected to GCMS) was used to track and analyze the gaseous compounds. Figure 4.2 depicts the experimental set-up for the pyro-GCMS. 3 ± 0.03 mg of the BI sample was loaded into a platinum crucible. The crucible and its contents were placed in a 4 x 150 mm pyrolysis tube. To ensure inert condition in the pyrolysis unit, gaseous nitrogen with a flow rate of 20 mL/min was maintained. The crucible and its contents were lowered down to the pyrolysis zone by a single shot mechanism. The BI was pyrolyzed at a temperature range of 400-850 ^{o}C, and the gaseous products were analyzed by the GCMS.

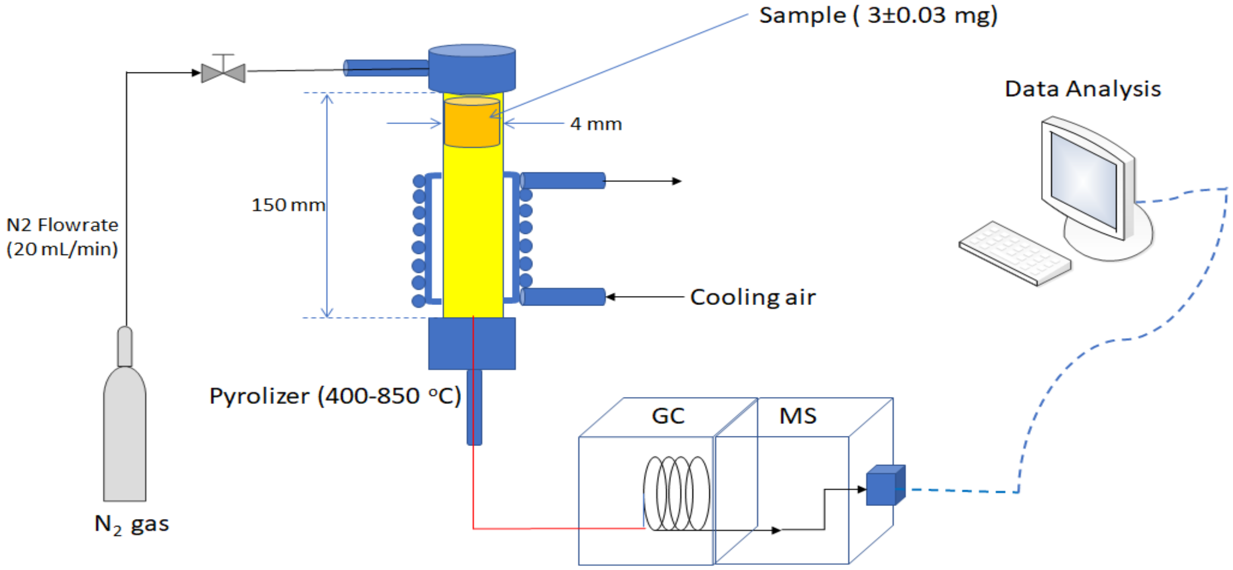

Figure 4.2. Characterization of BI using Pyrolysis to generate gaseous product and analyze it by gas chromatography mass spectrum (GCMS).

4.1.3. CTH of Algae Oil

In this section, using 2-propanol as extract, the optimum oil-extraction condition was established via design of experiment. The oil obtained at the optimum condition was characterized and, without evaporation of the propanol, the oil-2-propanol mixture was subjected to CTH over NiO_x-CoO_x-MoO_x-zeolite catalyst. The catalyst (fresh and used) for the CTH was characterized, the reaction rate equation was postulated, and the activation energy and the order of reaction were estimated.

4.1.3.1. Optimization of Oil Extraction

To convert the oil-laden to jet fuel, the oil was extracted by 2-propanol using design of experiment. Three factors were considered: temperature, BI-2-propanol ratio, and time of extraction. Table 4.2 highlights the factors considered in the 3-factor and 3-level factorial design of experiment. Using fractional factorial technique, 16 different experiments were conducted. To accomplish this, a given BI-2-propanol ratio was measured and was placed in a test tube. The content was thoroughly mixed with vortex mixer and placed in a water bath with a set temperature. The content was agitated intermittently with the vortex mixer. The pregnant 2-propanol was separated from the barren BI via centrifugation and decantation.

Table 4.2. Factors Considered in Optimizing the Oil Extraction Process by 3^3 Fractional Factorial Design.

Factor	Lower level (-1)	Middle level (0)	Upper level (+1)
Temperature (°C), A	25	45	70
BI-2-propanol ratio (g/g), B	0.1	0.3	0.5
Time (min), C	30	60	120

The yield of the oil was calculated for each experiment, as shown in Eq. (4.1).

$$Yield = \frac{Total\ mass\ of\ oil}{Mass\ of\ BI} \times 100\% \qquad (4.1)$$

Based on D-optimal design, a polynomial model was proposed (Eq. (4.2)) and, by using the analysis of variance (ANOVA) with experimental data, the coefficients, β's, were evaluated.

$$Y = \beta0 + \beta1A + \beta2B + \beta3C + \beta4AB + \beta5AC + \beta6BC + \beta7ABC + \beta8A^2 + \beta9B^2 + \beta10C^2 \qquad (4.2)$$

The optimum values for the independent factors (Temperature (**A**), BI-2-propanol ratio (**B**), and time (**C**) were determined by both analytical and a three-dimensional surface response plot. Analytically, the partial derivative of Eq. (4.2) and applying MS-Excel solver facility were employed. The optimum values were validated by running an oil extraction experiment at these optimum values, and the percent of oil yield was calculated. The barren BI obtained at the optimum run was analyzed by FTIR, whereas the pregnant 2-propanol was subject to CTH.

4.1.3.2. Catalyst Preparation

Figure 4.3 highlights the processes involved in the preparation of the catalyst. NiO_x-MoO_x-CoO_x-zeolite was prepared by wet-impregnating the zeolite (support) with Ni-Co-Mo precursors (nickel nitrate (II) hexahydrate and cobalt (II) molybdenum oxide hydrate). In this process, 1.9 g of $CoMoO_4.H_2O$ (5 wt.% of support) was dissolved in 1000 mL of deionized water at 80 ^oC. A given amount of the support (sodium aluminosilicate) was added to the prepared solution, and the content was stirred overnight. The loaded zeolite was removed from solution and was dried in an oven at 105 ^oC. A solution of nickel nitrate (II) hexahydrate was prepared by dissolving 5.16 g of it in 1000 mL of deionized water at 80 ^oC. The dried catalyst was added to the nickel solution and was stirred overnight under a hood.

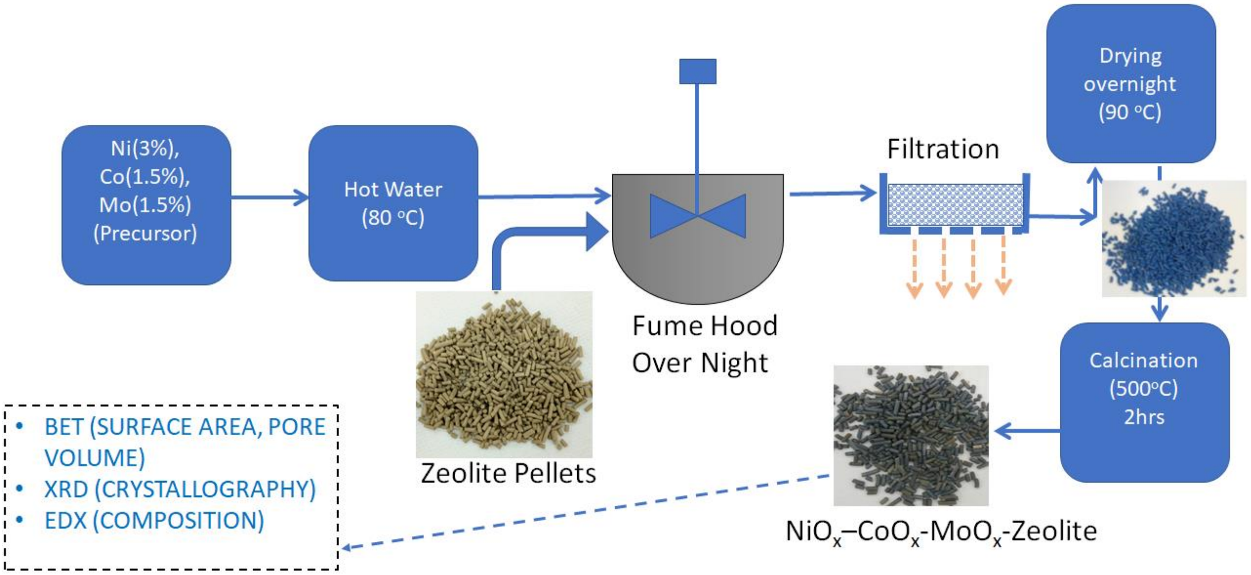
Ni(3%), Co(1.5%), Mo(1.5%) (Precursor)
Hot Water (80 °C)
Filtration
Drying overnight (90 °C)
Fume Hood Over Night
Zeolite Pellets
Calcination (500°C) 2hrs
NiO_x–CoO_x-MoO_x-Zeolite
• BET (SURFACE AREA, PORE VOLUME)
• XRD (CRYSTALLOGRAPHY)
• EDX (COMPOSITION)

Figure 4.3. Preparation of NiO_x-CoO_x-MoO_x-zeolite catalyst

The loaded catalyst was then separated from solution and was dried. The dried catalyst was calcined in a furnace at 500 ^oC for 2 h.

4.1.3.3. Catalyst Characterization

The aim of this section was to assess the stability of the catalyst by determining the surface area, the crystallinity, and the chemical position of the fresh and the used catalysts and by ascertaining the level of coke formation. Both the fresh and the used catalyst were characterized by BET, XRD, SEM, EDS, FTIR, TGA-DTA. The XRD patterns were recorded on a Bruker D8 diffractometer using Cu Kα radiation ($\lambda = 0.154056$ nm) operating at 40 kV and 40 mA. Diffractograms were recorded from 5^o-80^o (2θ values in discrete mode with a step of 0.1^o). The morphologies of the catalysts were analyzed with SEM, using Hitachi S-3400N operated with a beam energy of 15 kV. Imbedded in the SEM was EDS, which was used to determine the elemental composition of the catalysts. The FTIR spectra of the catalysts (fresh and used) were recorded at room temperature and wavenumber range of 480-4000 cm^{-1} by diffuse reflectance using a ThermoNicolet Avatar 370 DTGS spectrometer.

The BET surface area, the pore volume, and the pore size of the new and used catalysts were measured by using a Quantachrome NOVA 200e surface area analyzer after degassing the catalyst at 300 ^oC for three hours and adsorbing and desorbing it with N_2 at -196 ^oC. The surface area was evaluated, using a multi-point BET model. The pore size distribution was obtained from the desorption isotherm using Barret-Joyner-Halenda (BJH) model, while the total pore volume was calculated at a relative pressure range of 0.0-1.0. The amount of coke formation on the surface of the catalyst was determined using TGA-DTA, by measuring the percent mass loss and the rate of thermal decomposition of the catalyst.

4.1.3.4. CTH of Extracted Oil

After establishing the optimum oil yield from the BI, the oil-2-propanol mixture (0.08 g/0.8 g) was placed in a 30-mL batch reactor (Figure 4.4). 1.0 g of of NiO_x-CoO_x-MoO_x-zeolite catalyst was added to the reactor. The reactor was placed in a sand-bath furnace, and the reaction was carried out at 390, 405, and 420 ^{o}C with the respective autogenic pressures of 24.8, 26.0, and 27 bar. The reaction was stopped and was allowed to cool and, thereafter, the liquid product was separated from the catalyst and was analyzed with GCMS. The amount of water produced due to hydrodeoxygenation was separated by gravity. In all, 15 runs of experiments were conducted with different reaction times, as shown in Table 4.3. With the results from the GCMS, the algae oil conversion x (%) was calculated as Eq. (4.3). It was assumed that the fatty acids obtained in the GCMS results represented the unreacted algae oil.

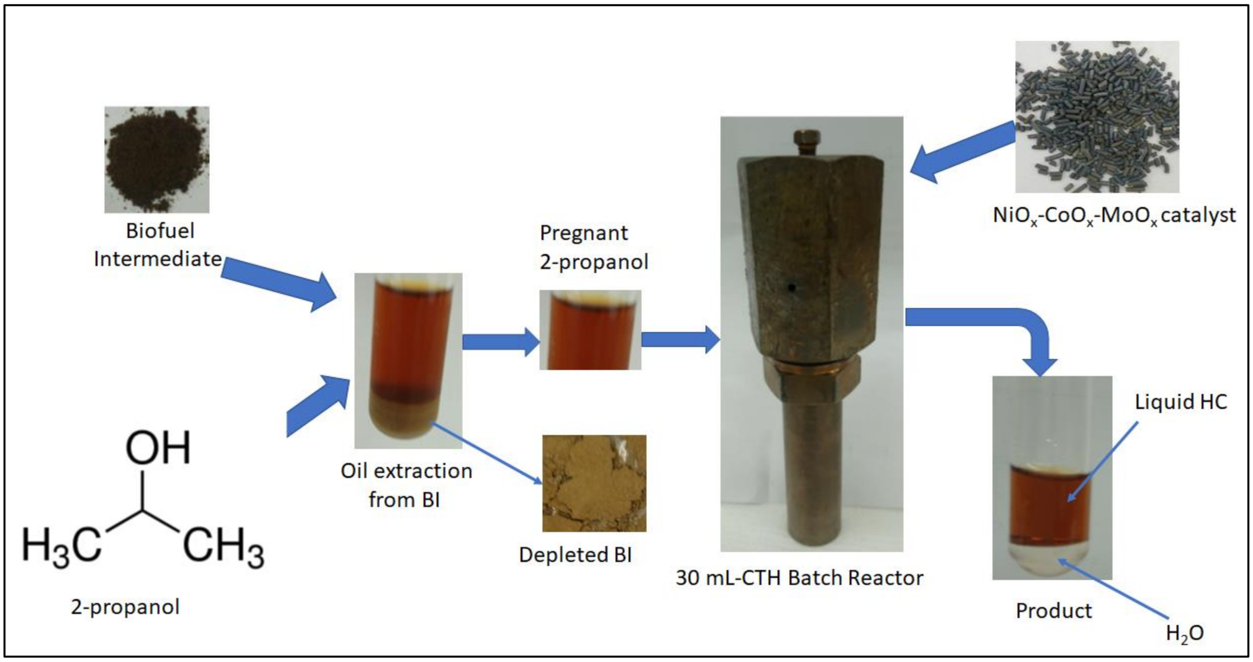
Biofuel
Intermediate
Pregnant
2-propanol
NiO_x-CoO_x-MoO_x catalyst
Liquid HC
OH
H_3C
CH_3
Oil extraction
from BI
Depleted BI
30 mL-CTH Batch Reactor
2-propanol
Product
H_2O

Figure 4.4. Oil extraction and CTH reaction procedure

Table 4.3. Experimental Runs of CTH of Algae Oil Using 2-propanol as H_2 Donor

Time (h)	T (^{o}C)	P (bar)	T (^{o}C)	P (bar)	T (^{o}C)	P (bar)
1.0	390.0	24.8	405.0	26.0	420.0	27.0
2.0	390.0	24.8	405.0	26.0	420.0	27.0
3.0	390.0	24.8	405.0	26.0	420.0	27.0
4.0	390.0	24.8	405.0	26.0	420.0	27.0
5.0	390.0	24.8	405.0	26.0	420.0	27.0

$$Conversion = \frac{[(Initial\ mass\ of\ oil)-(unreacted\ \ mass\ of\ oil)]\times 100\%}{Initial\ mass\ of\ oil} \tag{4.3}$$

4.2. Results and discussions

4.2.1. Characterization of BI

Figure 4.5 highlights the results for the mass-loss profile for the oil-laden BI when subjected to TGA analysis. It was evident that the thermal decomposition of the oil-laden BI had three different stages. The first stage showed a weight loss of 6% at 160 °C, signifying the presence of bonded water molecules during the flash hydrolysis. This loss could also be attributed to the light organic compounds present in the BI [220].

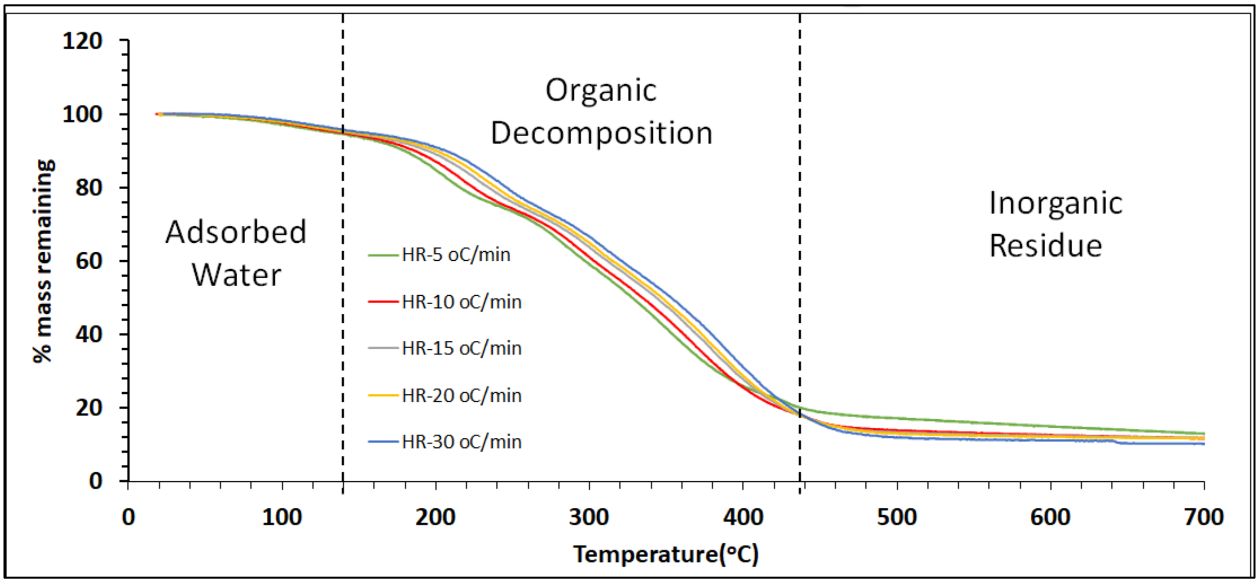

Figure 4.5. Weight loss of oil-laden BI as it was subjected to TGA at different heating rates (HR) of 5-30 °C/min with N_2 flow rate of 20 mL/min.

The second stage occurred between 160-440 °C, where the organic components (carbohydrate, protein and lipids) decomposed. Since the BI contains mainly oil, most of the weight loss (73%) at this stage could be traceable to the oil. The third stage of the weight loss occurred beyond 440 °C; that could be carbonaceous residue which decomposes slowly, giving total weight loss of approximately 10 %. Evidently, varying the heating rate (5-30 °C/min) did not affect the mass loss significantly. The total mass loss at 5 °C/min was nearly 85%, whereas that at 30 °C/min was 89%. These results could also mean that the total volatile organic compounds in the BI amounted to 83%, with roughly 10% being inorganic residue (ash content). The difference in mass loss could be because more energy was added at the latter condition than at the start of the process. It could be observed from Fig. 6 that increasing the heating rate increased the maximum rate of thermal decomposition from 0.002-0.01 mg/min. Besides, the rate of BI thermal decomposition peaked at 250 °C and 400 °C; that could represent the boiling points of the oil in the BI.

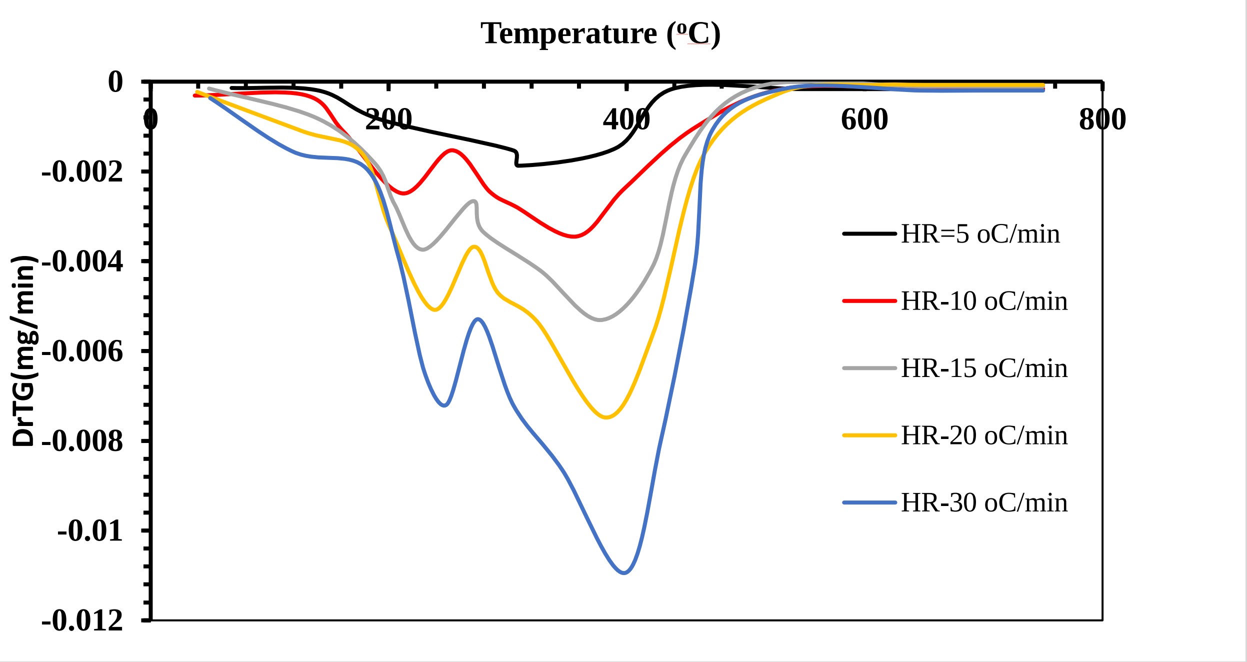

Figure 4.6. Rate of thermal decomposition of oil-laden BI at different heating rates with N_2 flow rate of 20 mL/min.

With this temperature profile obtained, the CTH reaction temperature was selected. Since there was no apparent CTH reaction below 390 °C from the experimental runs, it could be inferred that the average boiling point of the algae oil was 400 °C.

4.2.2. FTIR Analysis of BI

Figure 4.7 highlighted the FTIR profile for both the oil-laden and the depleted BI. FTIR spectra were recorded for oil-laden and depleted BI in a frequency range of 400-4000 cm^{-1}. The spectra at 3301 cm^{-1} represented O-H stretching vibration of hydroxyl or carbonyl group or polysaccharides or phenolic compounds. There was insignificant change in the peak at 3301 cm^{-1} after the oil extraction, meaning that the carbohydrate group members were not soluble in 2-propanol. Peaks at 2857 cm^{-1} and 2922 cm^{-1} represented the asymmetrical and symmetrical C-H stretching vibrations of the aliphatic methylene group, such as those in alkanes or fatty acids.

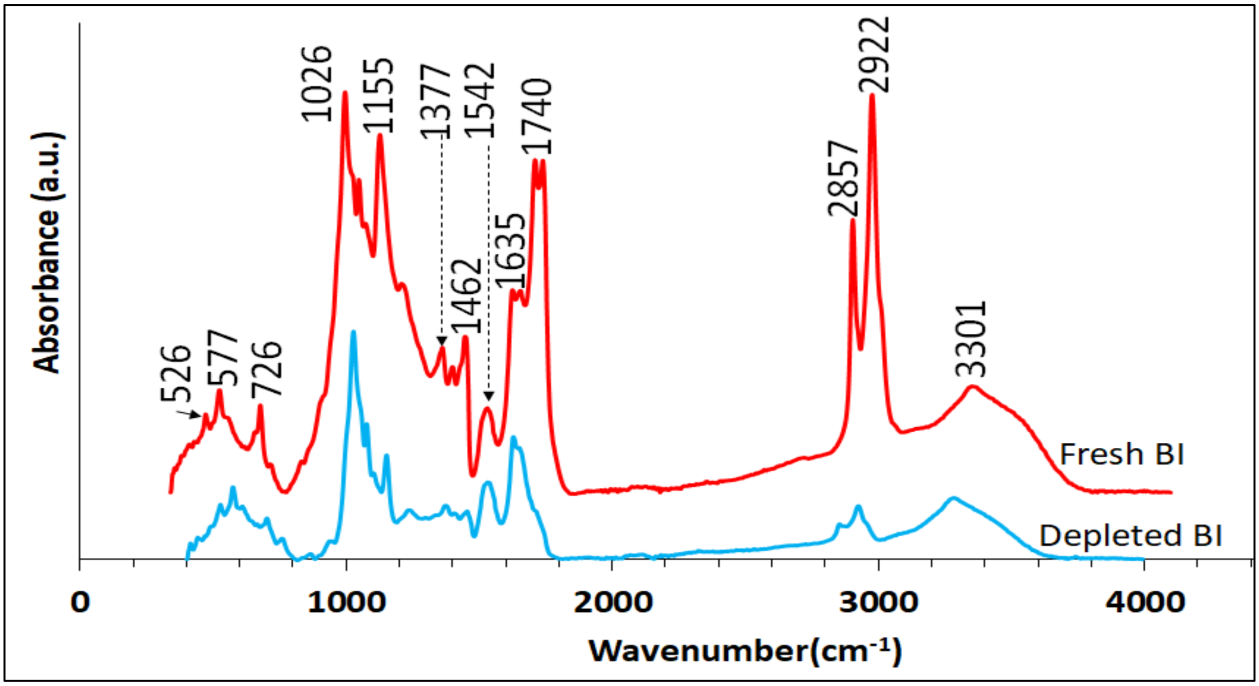

Figure 4.7. FTIR profile for oil-laden and depleted BI recorded at room temperature. The light blue and red profiles represent the depleted BI and oil-laden BI, respectively.

The depleted BI signal indicated that most of these groups vanished by dissolving in the 2-propanol. The peak registered at 1740 cm^{-1} depicted the C=O group stretching of acids and esters, which totally vanished after the oil extraction. At a frequency of 1635 cm^{-1}, there existed

C=C ring stretching, signifying the presence of aromatics and a conjugated system. At this same frequency, there existed COO- antisymmetric stretching that announced the presence of carboxylate ions [221]. The intensity at 1542 cm^{-1} represented amides (N-H and C-N) deformation vibration from protein [222], which remained insoluble in the 2-propanol. It could also be inferred that the flash hydrolysis was not able to remove all of the proteins from the algae. 1462 cm^{-1} showed the CH_2 scissoring that announced the presence of lipids, which vanished after the oil extraction. Also, 1377 cm^{-1} showed symmetric bending of the -C-H (CH_3) that emanated from lipids. Spectra at 1155 cm^{-1} and 1026 cm^{-1} highlighted C-O-C (glycosidic ether) stretching of ring and -C-O stretching, respectively. These spectra showed the presence of cellulose or polysaccharides [223], which was insoluble in 2-propanol. Finally, spectra in the range of 600-800 cm^{-1} portrayed C-H bending vibration of aromatics, which showed slight solubility in 2-propanol. It could be concluded that the fresh BI was made of lipids, polysaccharides, and insignificant protein.

4.2.3. Pyro-GCMS Analysis

Figure 4.8 highlighted the gaseous components from the BI pyrolysis. At 400-550 ^oC, it could be inferred that the percent of lipids in the BI approximated 62%, as there was no degradation of triglyceride at that temperature (Figure 4.6). The components of the BI started to degrade chemically at 650 ^oC, where the percent of fatty acid dropped by 10%. As the temperature increased, dehydration of long-chain hydrocarbon resulted and gave rise to alkenes.

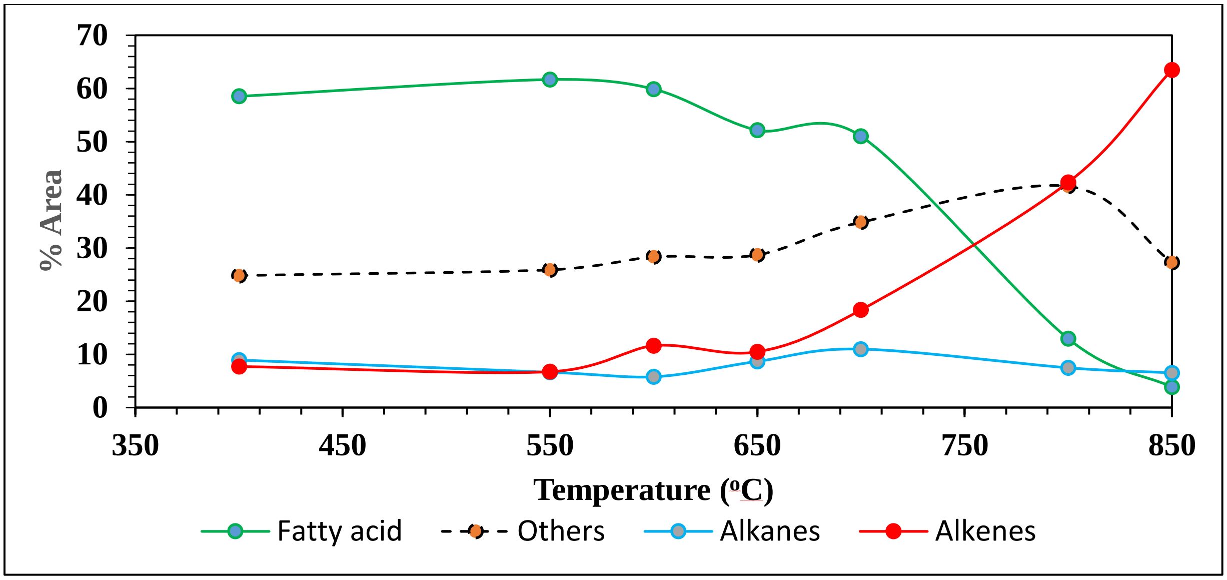

Figure 4.8. Gaseous product from the pyrolysis of BI

Other components, such as aldehydes, ketones, alcohols, amides, and aromatics, increased with increasing temperature (Figure C1). As dehydration increased at high temperatures, the O-C ratio dropped, giving rise to the high heating value of the gaseous product (Figure 4.9). The heating values of the gaseous products were estimated, based on the percent of individual compounds obtained from the GCMS analysis. The calculated calorific value was higher than that obtained from the raw BI (33.8 MJ/kg) [215]. It was observed that the H-C ratio remained unchanged, although there were some losses of hydrogen via dehydration. It could be concluded that the BI could render huge calorific value (~ 48 MJ/kg) if upgraded by pyrolysis or any other means.

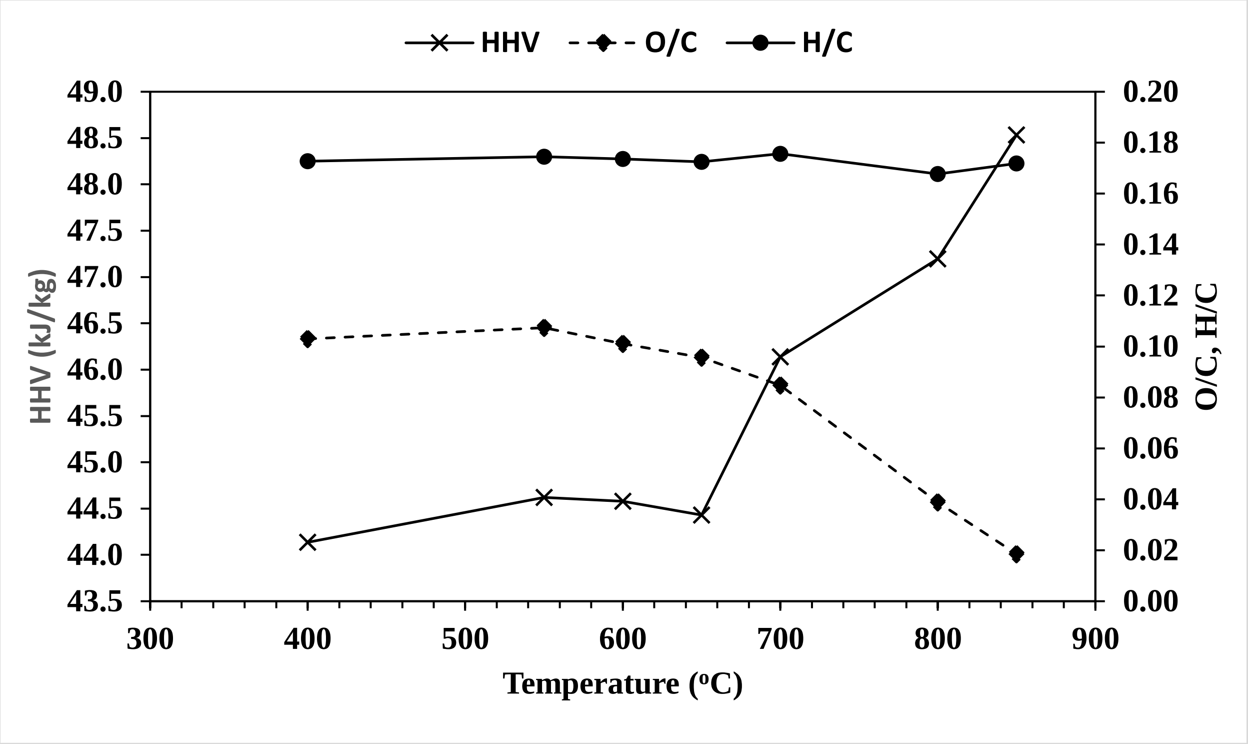

Figure 4.9. Heating value, O/C, and H/C of the gaseous products from the pyro-GCMS

4.2.4. Kinetics of Pyrolysis of BI

To determine the activation energy of the thermal decomposition of BI, two isothermal equations were employed: the Flynn-Wall-Ozawa (FWO) and the Kissinger-Akahira-Sunose (KAS), as shown in Appendix B (Eq. (B1-B3)) [224]. Given the heating rate (β), fractional conversion, and the temperature of decomposition of BI, plots of ln(β) and ln (β/T^2) against $(1/T)$ produced straight lines with R-squared values ranging from 0.94-0.99, which explained the goodness of fit (Figures B2 & B3) of these two equations (Eq. (B1-B2)). Increasing the fractional conversion increased the activation energy (Tables B1, B2, & Figure10).

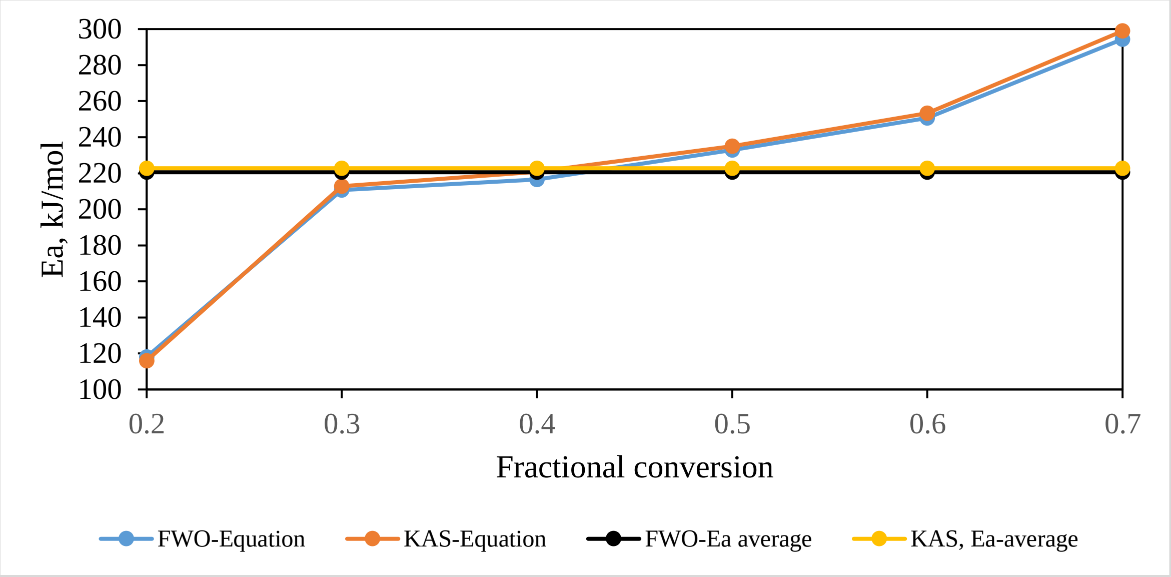

Figure 4.10. Fractional conversion effect on activation energy of BI thermal decomposition.

Since the lower boiling-point components in the BI were decomposed first, less energy was required, compared to the high boiling-point components, which required higher energy to decompose. Hence, the activation energy increased from 115-298 kJ/mol with increasing fractional conversion from 0.2-0.7. Thus, the average activation energy for thermal decomposition, based on the FWO and KAS equations, were 220 kJ/mol and 223 kJ/mol, respectively. These values could be compared to what had been reported in the literature (298-301 kJ/mol) [224]. The lower values in the current study could be attributed to the removal of proteins via flash hydrolysis, whereas the study in the literature was of fresh algae with all the three main components (lipids, proteins, and carbohydrates) present. Summarily, this characterization step has revealed the dimension of energy required to convert the BI into a high-quality fuel product.

4.2.5. Optimization of Oil Extraction

Results from the optimal design of oil extraction are shown in Table 4.4, which highlights the process variables (temperature (A), BI-2-propanol ratio (B), and time (C)) and the experimental and calculated percent oil yields. The values in Table 4.4 were employed in determining the coefficients in Eq. (4.2) and the interactions among the process variables.

Table 4.4. Experimental Oil Yield, Y_{exp}, and Calculated Oil Yield, $Y_{cal.}$

Experimental Run	Temperature (ºC) x1	BI/2-propanol (g/g) x2	Time (min) x3	Response Y_{exp}	Y_{cal}
1	45	0.1	30	43.3	43.7
2	70	0.3	120	42.6	42.7
3	70	0.1	60	38.1	37.8
4	45	0.3	60	57.6	56.9
5	25	0.5	120	27.0	26.9
6	25	0.1	120	36.0	35.8
7	70	0.1	30	25.0	24.4
8	45	0.3	120	58.4	58.4
9	70	0.3	30	28.1	29.1
10	45	0.5	30	45.4	45.0
11	25	0.5	30	18.8	19.5
12	70	0.5	120	36.0	36.1
13	45	0.1	60	55.3	55.9
14	25	0.3	30	23.6	22.5
15	25	0.3	60	31.9	32.6
16	70	0.5	60	38.8	38.4

After testing other polynomials, Eq. (4.4) highlighted the final and appropriate equation obtained by multiple regression, using the MATLAB software.

$$y = -71.2 + 3.94A + 16.8B + 0.668C + 0.556AB + 0.002AC - 0.073BC - 0.0047ABC - 0.042A^2 - 49B^2 - 0.0036C^2 \quad (4.4)$$

ANOVA was used to assess the goodness of fit (Table 4.5) for the polynomial, using the experimental data. The goodness of fit for the regression model was determined by the R-squared value (0.995) and R^2-adjusted value (0.993). R-squared was used to judge the adequacy of the model by measuring the variability in the data. In this case, the chosen model accounted for 99.5% of the variability in the experimental data. The R-squared statistic proved to be somewhat problematic or deceptive as a measure of the quality of fit for multiple regression, since it never decreased when a variable was added to the model. To alleviate this problem, R^2-adjusted (0.993) was employed as a perfect criterion for assessing the quality of fit, as it only increased when the added variable reduced the error mean squared. The interaction of process variables and their effects on the model were determined by using the p-values. Coefficients with a p-value of less than 0.05 (a rule of thumb) were considered significant. Essentially, all of the process variables had significant effects on the yield of oil, as their p-values were less than 5% [89]. It was also evident that the degree of these effects varied with variable p-values. For example, the effect of A (temperature) on the model was higher than that of B, since the p-value of A was lower than that of B (2-propanol). AB had a stronger effect on the process than did AC since the p-value of AB (temperature-BI-2-propanol ratio) is lower than that of AC (temperature-time). The average p-value was 5.52×10^{-6}, which signified the goodness of the model.

Table 4.5. ANOVA Model for BI Oil Extraction

Coefficients	Estimate	Standard error	tStat	pValue
b0	-71.1830	7.2691	-9.7926	0.0002
b1	3.9391	0.1784	22.0760	0.0000
b2	16.8310	18.7030	0.8999	0.4094
b3	0.6679	0.0871	7.6655	0.0006
b4	0.5562	0.2729	2.0374	0.0972
b5	0.0021	0.0012	1.6640	0.1570
b6	-0.0729	0.14252	-0.5113	0.6309
b7	-0.0047	0.0033	-1.4258	0.2133
b8	-0.0419	0.0012	-34.0810	0.0000
b9	-49.9840	15.2020	-3.2879	0.0218
b10	-0.0036	0.0003	-10.5650	0.0001

4.2.5.1. Model Validation

The reliability of the model used in this experiment was proved by validation, whereby data outliers in the residuals were examined and removed. The assumption that the residuals were normally distributed was verified. The residuals were plotted against the fitted values and any pattern and unpattern (random) distribution was investigated. Figure 4.11 shows the unpattern distribution of residuals, signifying an absence of outliers in the data. Moreover, the probability plot highlights how normally distributed the points are, because they lay close to the straight line.

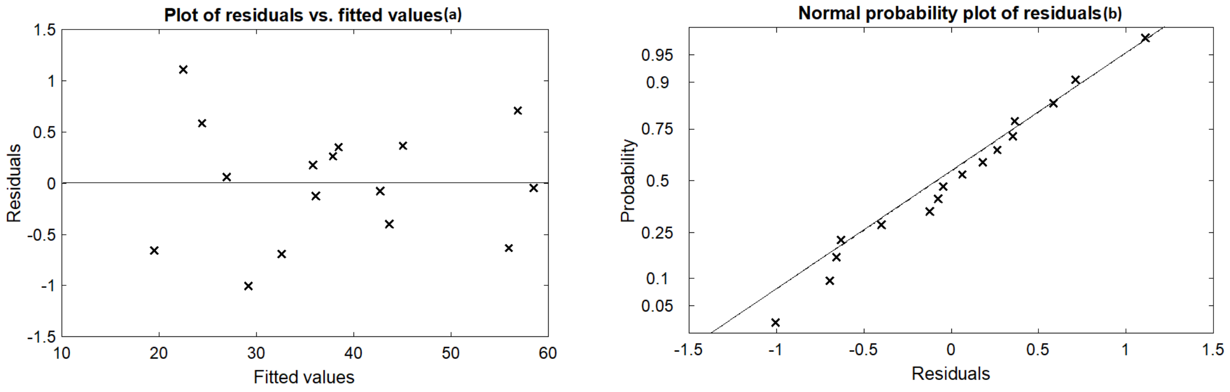

Figure 4.11. Diagnostic plot of surface response of algae oil yield

4.2.5.2. Effects of Process Variables

The effects of all the three variables were examined via response surface and contour plots. Noticeably, increasing the temperature increased the yield of oil extraction, as the oil became increasingly soluble in the 2-propanol. Beyond ~ 50 ^{o}C, the oil yield began to drop due the evaporation of 2-propanol into empty space. The BI-2-propanol ratio increased with decreasing oil yield as the required amount of 2-propanol dipped, thereby limiting the solubility of the oil. The maximum oil yield was obtained at BI-2-propanol ratio of 0.133 g/g (Figure 4.12 (1-1 & 1-2)).

Increasing the time allowed a significant amount of oil to transfer from the fibrous zone into the 2-propanol. Obviously, at infinite time, the oil yield remained unchanged, signifying that, at 1.68 h, the oil extraction process had stopped (Figure 4.12 (2-1 & 2-2) with the maximum oil yield of 62%.

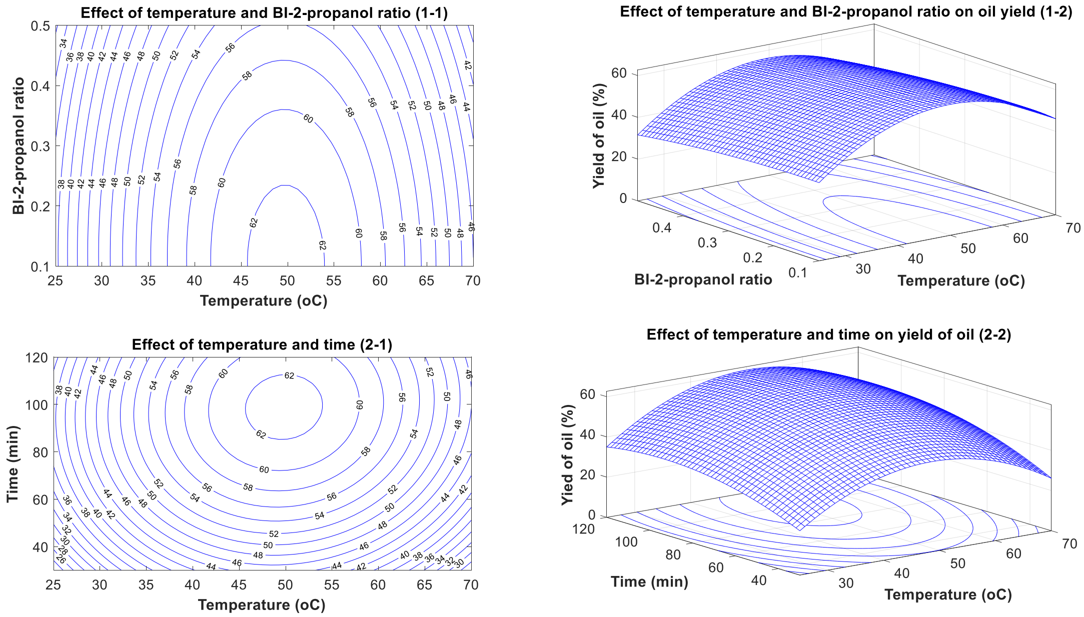

Figure 4.12. Surface response of oil yield from BI with optimum oil extraction condition: temperature (49.7 ^{o}C), BI mass-2-propanol ratio (0.133 g/g), time of extraction (101 min (1.68 h)), and maximum oil yield (62.7 wt%).

4.2.6. TGA of Catalyst

Figure 4.13 shows TGA profiles for both the fresh and the used catalysts that depicted three stages of weight losses. The first stage (below 200 °C) showed approximately 6%, and 3% weight loss for both the fresh and the used catalysts, respectively. These losses could be ascribed to the loss of loosely bonded water. The fresh catalyst showed the highest weight loss, probably due to the adsorption of water employed in the wet impregnation. Ironically, the used catalyst showed the lowest weight loss in the first stage, probably due to the displacement of water molecules by the fuel products that diffused to displace the water molecules in the zeolite structure during the CTH reaction. From 200-400 °C, approximately 6% and 13.3% weight loss for the fresh and used catalysts, respectively, were experienced. These weight losses could be linked to the strongly bonded water which resides in the first coordination sphere and could not be removed under mild thermal treatment.

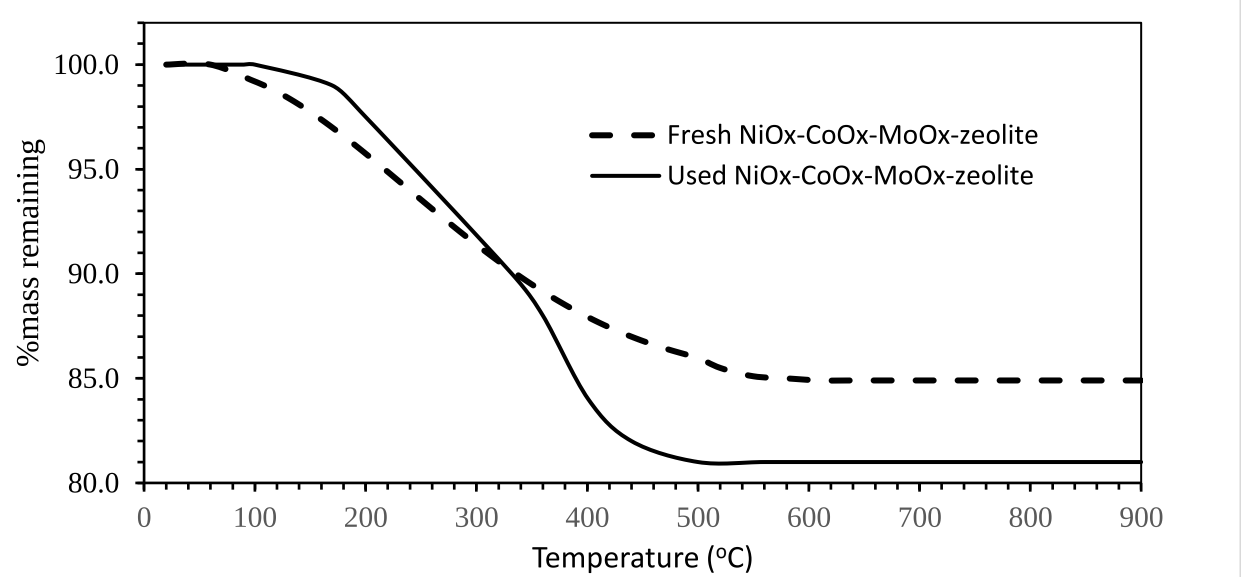

Figure 4.13. Determination coke deposition on the catalyst during via TGA during the 3 hours of CTH reaction of algae oil.

The next weight loss (3% for both fresh catalyst, and 2% for used catalyst) occurred between 400-900 ^{o}C. This loss could be attributed to the structural hydroxyl group that condenses and dehydrates at 500 ^{o}C and above. Evidently, there was 4% weight loss difference between the used and fresh catalyst within the last stage of the TGA (400-900 ^{o}C). This weight loss difference was attributable to the coke formed from the carbonized hydrocarbon or the poly-alkyl aromatic hydrocarbon that were precursors of catalyst deactivation [96, 97]. The FTIR and EDS analyses (Figure 4.16 & 4.14) confirmed the presence of this carbonized components on the used catalyst. Conclusively, the overall weight loss from the used catalyst after TGA was estimated to be 4%, compared to what was reported in literature.

Comparatively, TGA of coke-laden $NiO-CaO_5/SiO_2-Al_2O_3$ catalyst showed weight loss of 15% [157], while $20Ni-6Cu-5Mo/\gamma-Al_2O_3$ catalyst exhibited weight loss of 22-25% [158], and $NiO_x-CoO_x-MoO_x$-zeolite showed weight loss of 19% [217].

4.2.7. SEM and EDS of Catalyst

Fig. 14 highlighted the spectrum obtained from the analysis of elemental composition of the fresh and used $NiO_x-CoO_x-MoO_x$-zeolite catalysts. The analysis revealed the following elements common in zeolites: carbon, oxygen, sodium, magnesium, aluminum, silicon, potassium, calcium, and iron. These nine elements in the raw zeolite announces the possible presence of the oxides (Na_2O, K_2O, MgO, Al_2O_3, SiO_2, CaO, FeO, Fe_2O_3) [159]. The presence of cobalt, nickel, and molybdenum highlights the results of doping the zeolite that is filled with NiO, Co_xO_y, and Mo_xO_y, respectively.

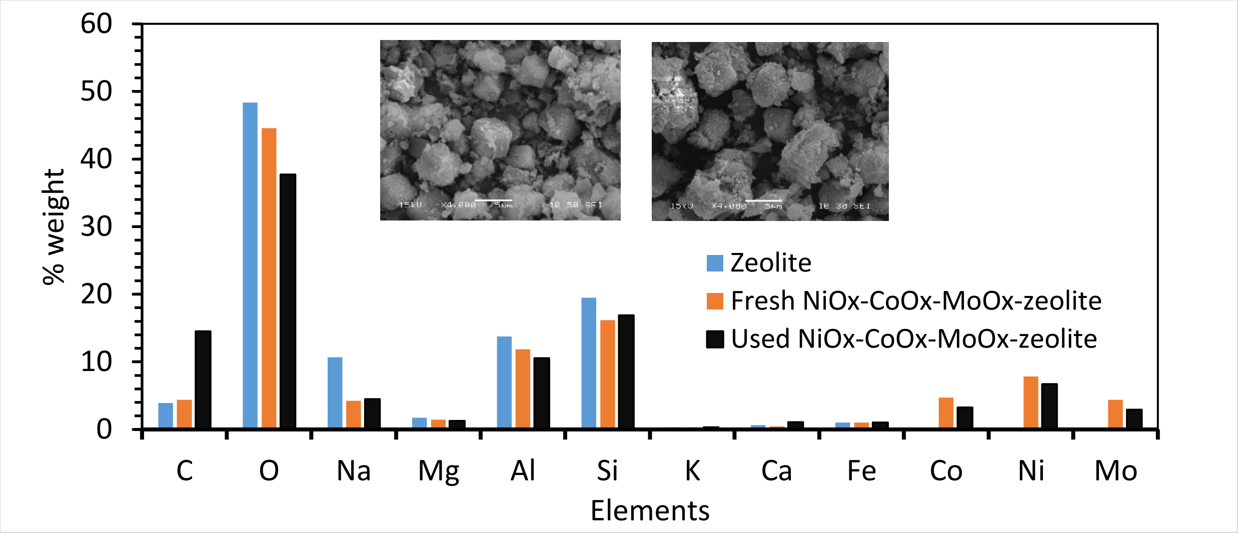

Figure 4.14. SEM (with accelerating Voltage: 15.0 kV, magnification: 4000) and EDS analysis for zeolite, fresh and used catalysts at the 3 hours of CTH reaction.

Due to the calcination of the doped zeolite, the oxides of the active metals were prominent, since reduction of the catalyst was not performed. These oxides were preferable to their reduced form because they offered higher level of acidity than their metal counterparts, as reported in the literature. Also, these oxides introduced metal support interaction for activation of oxygen-containing compounds, and improved direct cleavage of C-O in oil [144]. Moreover, without the reduction of the catalyst, the cost of catalyst preparation could reduce. The presence of sodium and calcium predicted the zeolite to be A-type [156] with cubic crystal structure [160], as could be observed in the SEM results. The analysis showed that the raw zeolite was weakly acidic, since Si/Al = 1.42 < 1.5 [161]. It was also observed that the level of acidity remained unchanged after the zeolite was impregnated with the active metals. Maintaining the Si/Al < 5 rendered the zeolite hydrophobic, porous, alkaline, and more adsorbent [162]. The percent compositions of the active metals (Ni, Co, and Mo) dropped by 15%, 31%, and 34%, respectively, after the catalyst was used for one cycle (three hours of reaction). The high reduction of cobalt and molybdenum might be attributed to weak interaction with the zeolite during the impregnation that enhanced the leaching of the metals during the CTH reaction. It could be traceable to the rise in the carbon content to 12.4%, which could occlude the active metals during the CTH reaction.

4.2.8. X-ray Diffraction of Catalyst

Figure 4.15 highlighted the X-ray diffraction patterns observed for the zeolite and the fresh and used Ni-Co-Mo-zeolite catalysts with significant characteristic peaks observed at 7.4°, 10.7°, 12.6°, 16.6°, 17.8°, 21.9°, 24.4°, 27.6°, and 30.4° for zeolite, according to the Joint Committee on Powder Diffraction Standards (JCPDS File no. 43-0142) [217]. These results were in consonance with what was found in the literature [163, 164]. Apparently, the zeolite had high crystallinity prior to doping it with the metal precursors. Its crystallinity significantly decreased due to the interaction between the Si-O and Ni, Co, and Mo at 2θ = 7.8°, 12.6°, 24.4°, 27.6°, and 53°. The peaks at these angles could be traceable to the oxides of molybdenum in the following crystallographic directions: MoO_3 [100], MoO_3 [001], MoO_3 [100], MoO_3 [021], and MoO_2 [311], respectively [165-171].

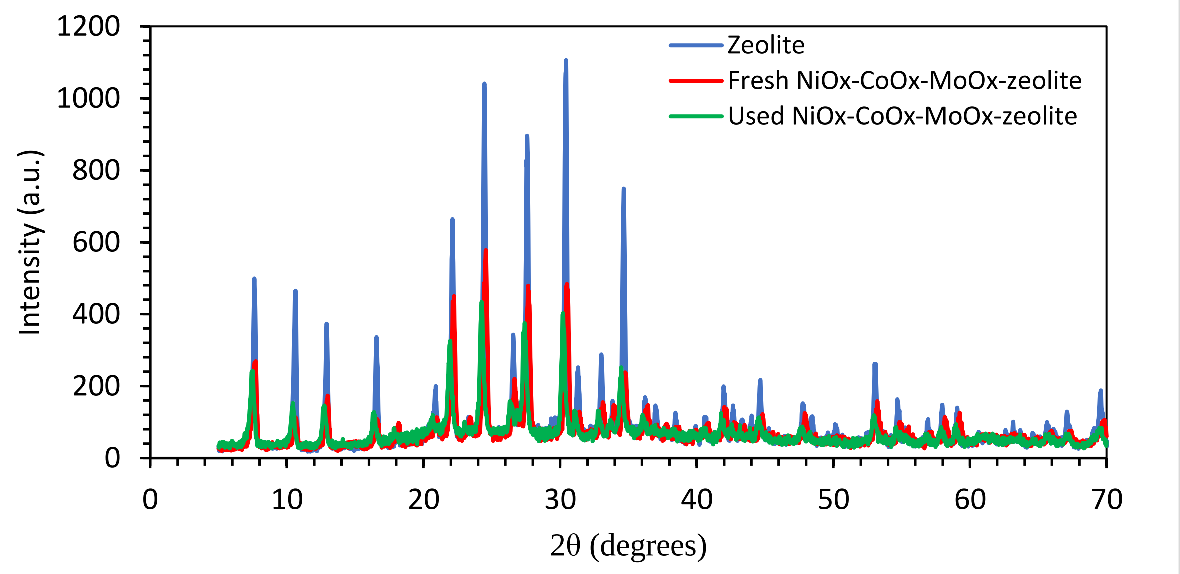

Figure 4.15. XRD pattern for the zeolite, the fresh and used NiOx-CoOx-MoOx-zeolite catalysts with intensity measured in arbitrary unit (a.u.), and X-ray incident angles in degrees.

Further interaction from oxides of cobalt (Co_xO_y), found at 16.6°, 21.9°, and 41.9°, decreased the crystallinity of the zeolite [172]. Oxides of nickel (Ni_2O_3 [002], NiO [222], NiO [111]) at 30.4°, 34.7°, and 44.5°, respectively, contributed to the lowering of crystallinity of the zeolite [171, 173, 174]. It could be observed that the stability of the catalyst was affected in this work, compared to that in the past work [217]. The intensity dropped in this work, probably, because of significant presence of ringed compounds (the forerunners of coke formation) observed in the products.

4.2.9. FTIR Analysis of Catalyst

Figure 4.16 highlights the FTIR profile for zeolite (support) and the fresh and used NiOx-CoOx-MoOx-zeolite catalyst that was recorded in a frequency range of 400-4000 cm^{-1}. The spectrum for the zeolite exhibited frequencies of 460, 540, 668, 972, 1650, and 3340 cm^{-1}. The peak at 460 cm^{-1} could be linked to bending vibration of T-O-T (T=Al, Si groups) in the zeolite structure [175, 176]. This band also depicted the bending vibration of internal tetrahedron TO_4 of the zeolite structure [177], which showed the presence of Al^{+3} and Si^{4+} in the zeolite. The bands around 540, 668, and 752 cm^{-1} could be ascribed to internal and external linkage symmetrical stretching vibrations. The band at 972 cm^{-1} highlighted the symmetrical stretching vibration and the tetrahedron vibration of Si-O bond [177]. The peak at 1650 cm^{-1} could be attributed to the bending vibration of O-H in the adsorbed water (H_2O) on the zeolite surface [156]. 3340 cm^{-1} could be ascribed to Si-OH in nest defects and to the hydrogen bonding of loosely held water molecules [178].

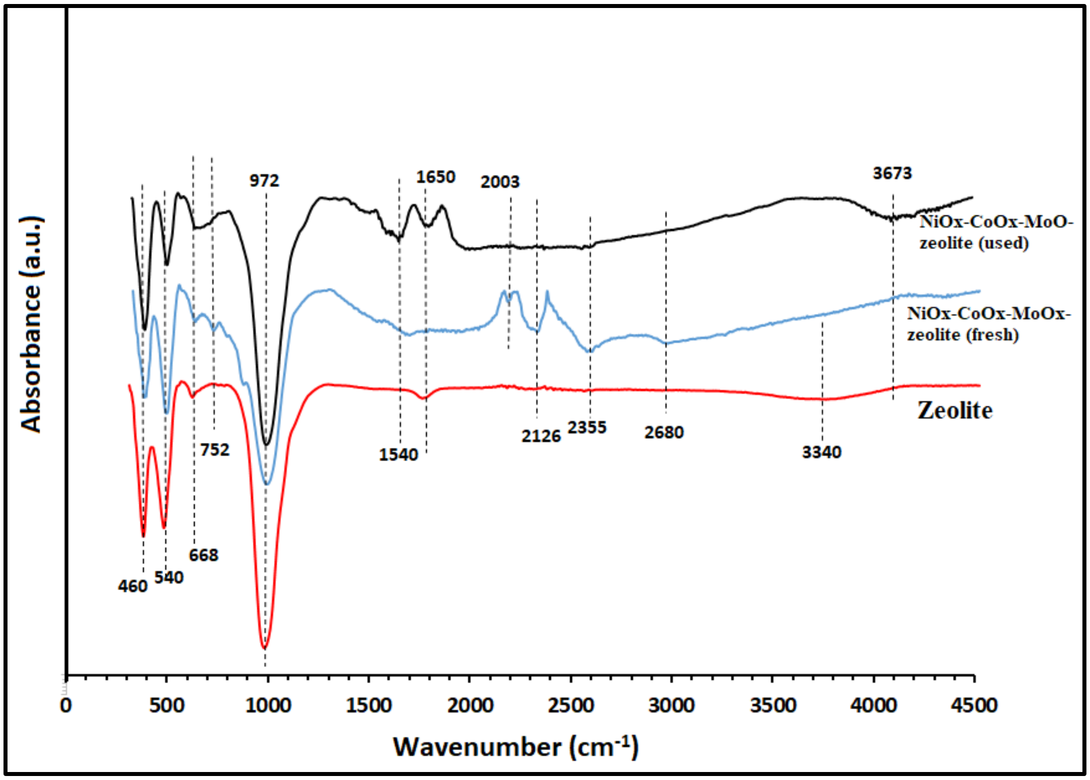

Figure 4.16. FTIR Profile for zeolite (support) and the fresh and used catalysts. The catalyst used 3 h for the CTH reaction was referenced.

Conspicuously, the metal-doped zeolite (fresh catalyst) exhibited the lowest intensity (absorbance) and a slight shift in frequencies due to Co^{3+}, Ni^{2+}, and Mo^{6+} interactions with the O-H, Si-O, and Al-O bond during the doping process. Spectra at 2003, 2126, and 2355 cm^{-1} could be attributed to the interaction between Ni-Co-Mo ions and TO_4 in the zeolite during the doping process. Conversely, the used catalyst did not exhibit peaks at 2003, 2126, and 2355 cm^{-1}, due to deactivation. It was observed that the peak at wavenumber 1650 cm^{-1} disappeared after metal doping and calcination. This indicated the thoroughness of the calcination that removed the water molecules, which could promote agglomeration and consequent deactivation [156]. In contrast, the used catalyst showed a peak at 1650 cm^{-1}, indicating the presence of water molecules that caused the catalyst deactivation during the CTH reaction. The appearance of the frequency 3673 cm^{-1} evidenced the stretching modes of CH_x, which was formed during the CTH reaction [179].

4.2.10. Surface Area Analysis of Catalyst

Figure 4.17 shows the performance of the NiO_x-CoO_x-MoO_x-zeolite via adsorption and desorption isotherm and the application of BET method. The catalyst surface area was reduced from 250 m^2/g to 150 m^2/g after three hours of CTH reaction. The reduction in the surface area was traceable to coke formation that could be corroborated by the increased in carbon (4.4-14.5 wt.%) content in the EDS analysis (Figure 4.14).

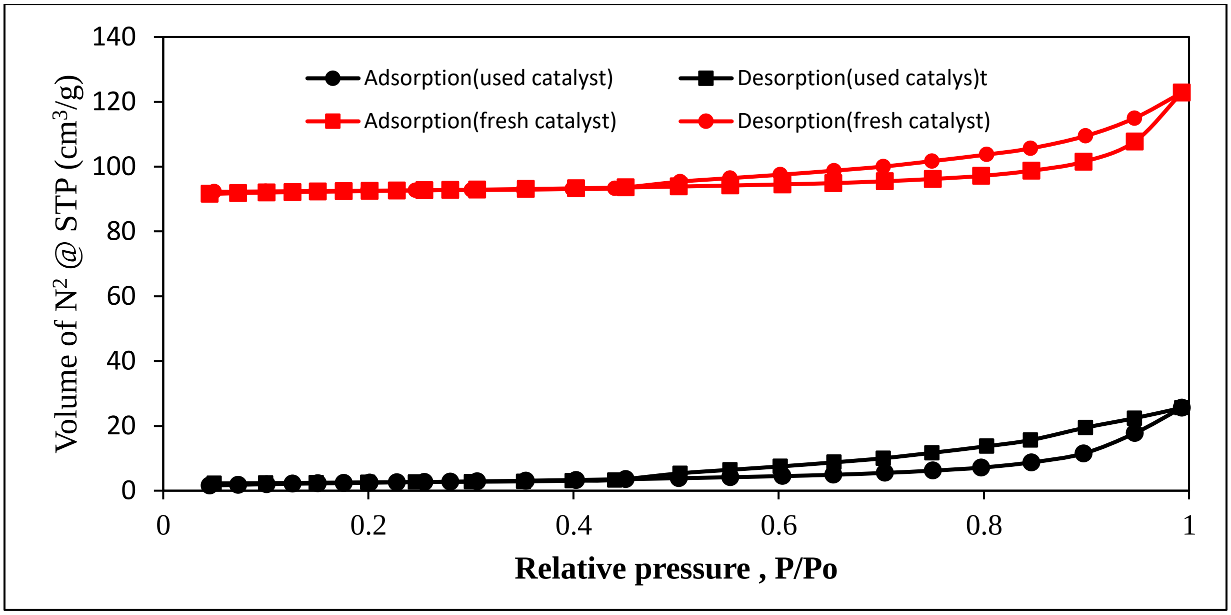

Figure 4.17. Surface area analysis of fresh and used NiO_x-CoO_x-MoO_x-zeolite catalyst after 3 hours of CTH reaction.

While the pore volume changed from 0.164 cm^3/g to 0.032 cm^3/g, the pore width increased from 19.6 Å to 86 Å. The surface coke formation caused this increase in the pore width of the catalyst due to reduction in effective surface area, and it consequently increased the average pore radius or diameter. The shapes of the hysteresis loop for both used and spent catalysts appeared parallel, which meant that there was not much change in the texture, pore size distribution, and pore geometry. Evidently, at a relative pressure of 0.44, the loop closed at a point where pore condensation and evaporation of N_2 occurred. This shape depicted adsorption and desorption isotherm of types 1 and 4, according to the International Union of Pure and Applied Chemistry [180]. These values showed how the stability of the catalyst was shaken during the CTH.

4.2.11. CTH of Algae Oil

Figure 4.18 showed the CTH conversion of algae oil conducted at different temperatures (390, 405, 420 ^{o}C). It was observed that 100% conversion was achieved at all reaction temperatures. At a temperature of 390 ^{o}C, the conversion of the oil increased as the time of reaction from 1-5 h, the percent conversion increased respectively as 50, 86, 90, 99, and 100%. Most of the hydrocarbon produced at 390 ^{o}C were cyclo-and iso-alkanes at 3-5 h (Table B5-B7), while the products at 1-2 produced both hydrocarbons and oxygenates (Table B3-B4). It was observed that the reaction at 390 ^{o}C produced branched-chain (41%) and cyclo-alkanes (35%). These cyclo-alkanes underwent dehydration and formed polyaromatics, which are not environmentally friendly during combustion. The percent of iso-cyclo alkanes produced was extraordinarily higher than what had been reported in the literature [100, 217]. As the temperature increased, the conversion increased rapidly, but the products obtained were mostly polyaromatics that caused catalyst deactivation (Figure B5). It was observed that the percents of coke formed at 390, 405, and 420 ^{o}C were 4, 15, and 25%, respectively.

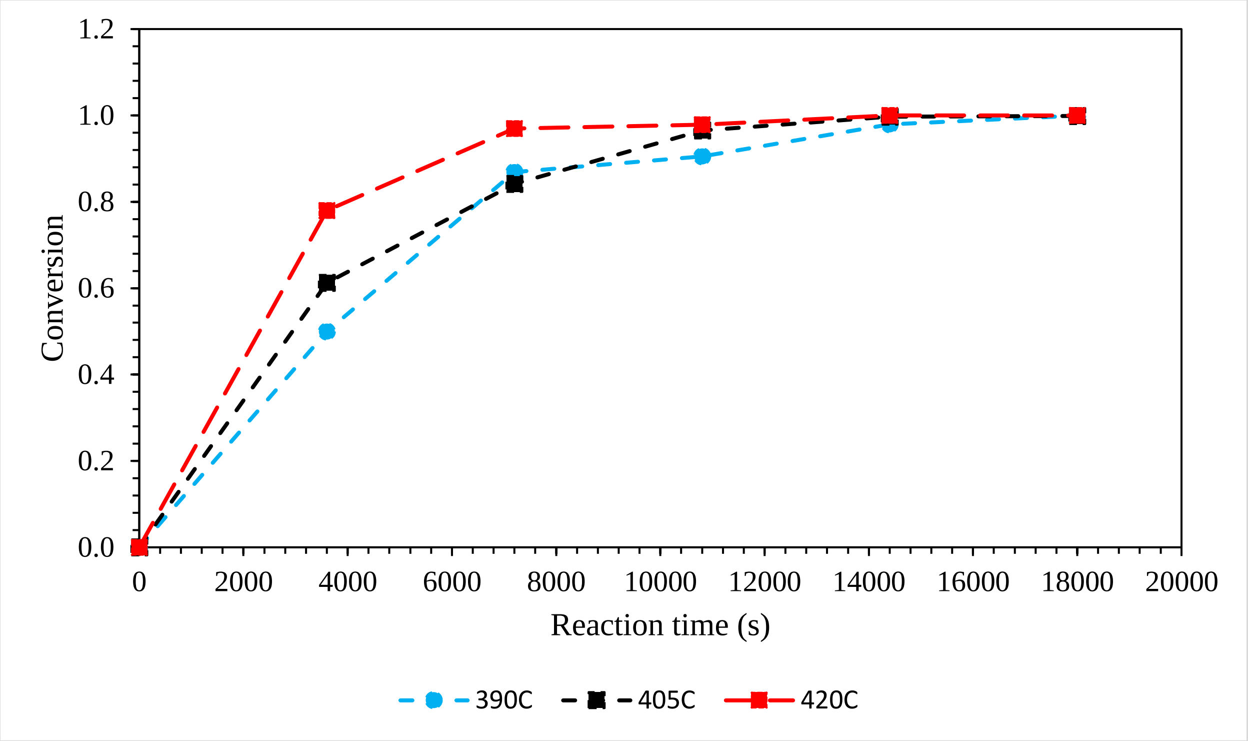

Figure 4.18. CTH conversion of algae oil at different temperatures

It was observed in one hour of the CTH reaction at 390 °C that most of the products were nitrogenous in nature (e.g. 1-Phenazinecarboxylic acid) due to the presence of little proteins left in the BI after the flash hydrolysis. As time progressed, the nitrogen vanished, probably by converting to gaseous NH_3 as the ring structure opened. It was also evident that the oxygenates disappeared via deoxygenation or hydrodeoxygenation, which gave the fuel a significant calorific value. For example, the heating value increased from 35 to 48 MJ/kg as the reaction progressed (Table 4.6). It was observed that the maximum heating value was obtained in 3 h of reaction due to the production of more branched alkanes, and this value could be compared to that observed at the pyrolysis of the BI.

Figure 4.19 highlights the number of carbon distribution in the liquid products, as CTH was conducted at the temperature range of 390-420 °C and at an autogenic pressure of 24-27 bar.

Most of the carbon were in the range of C6-C9, which depicted typical jet-fuel composition [191].

Table 4.6. Evaluation of Liquid Product from CTH at 390 °C

Time (h)	1	2	3	4	5
C (%)	68.6	77.4	84.3	81.7	83.0
H (%)	9.2	12.5	14.3	13.7	14.4
O (%)	14.3	10.2	1.4	4.5	2.6
N (%)	7.9	0.0	0.0	0.0	0.0
HHV (MJ/kg)	35.0	42.1	48.4	46.2	47.9

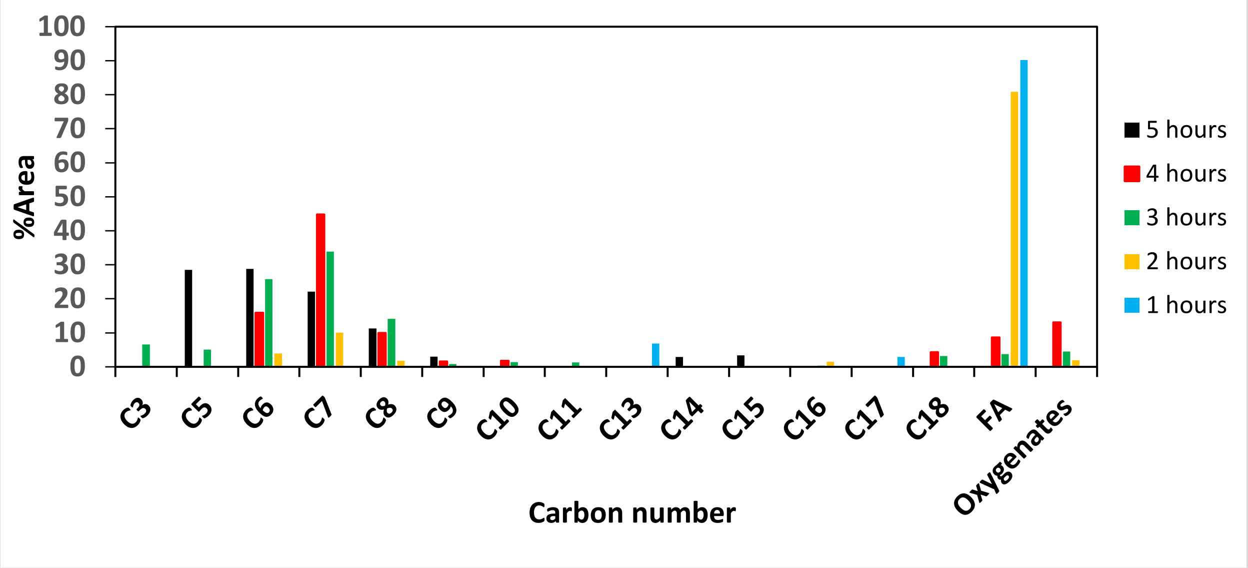

Figure 4.19. Carbon number distribution in the liquid products at 390 °C

The C3-C8 highlighted the production of cyclo-alkanes and branched hydrocarbons, such as isomers of heptane and hexane (Tables B3-B7). The liquid fuel obtained from the CTH reaction contained a carbon atom range of C3-C18, with most of the hydrocarbons within C5-C8. As the reaction proceeded from 1-5 hours at 390 °C, the percent of carbon atoms within C5-C8 increased from 7 to 94%. Since the compounds in the liquid fuel were saturated hydrocarbon, the CTH underwent either deoxygenation, catalytic cracking, or thermal cracking. Moreover, the presence of water in the liquid products signified the hydrodeoxygenation reaction, whereby the oxygen content of the oil reacted with the hydrogen produced by the 2-propanol [225]. Summarily, the optimum process parameters for the CTH of the microalgae oil were temperature (390 ^{o}C), pressure (24 bar), the reaction time of 3 h, and algae oil to 2-propanol ratio (0.08g/g), It could be estimated that the 2-propanol-to-oil ratio was 12.2 liter 2-propanol per liter algae oil, compared to using a gaseous H_2 as hydrogen donor, as found in literature (200-300 liters H_2/liter oil) [25].

4.2.12. CTH Kinetic model

Based on percent conversion, the kinetic parameters (reaction order, activation energy, and pre-exponential factor) were estimated. Reaction at 390-420 ^{o}C was considered to develop the kinetics of CTH of algae oil, with the following elementary assumptions:

(i) isothermal and steady-state conditions are assumed;

(iv) for the sake of simplicity, all of the products were lumped into one product;

(v) the rate of coke and gaseous products formation were not considered, as the amounts produced were considered insignificant compared to that of the liquid products;

(vi) intraparticle mass-transfer resistance was assumed to be negligible, since diffusion was very fast, such that the overall rate was not affected by mass transfer in any fashion; and

[85] the rates of adsorption and desorption of products and reactants were not considered.

The CTH reaction was condensed, as shown in Eq. (4.5).

$$A \xrightarrow{Catalyst} Products \tag{4.5}$$

Since the fatty acid could be monitored easily, the rate law could be written as shown in Eq. (4.6).

$$-r_A = kC_A^n \tag{4.6}$$

Where k and n are the rate constant and reaction order, respectively. Combining the rate law with the mole balance for a batch reactor, Eq. (4.6) could be written as shown in Eq. (4.7).

$$kC_A^n = -\frac{dC_A}{dt} \tag{4.7}$$

Integrating Eq. (7) at the boundary condition (t = 0, C_{A0}; t = t , C_A), the instantaneous concentration of the fatty acid could written as in Eq. (4.8).

$$C_A = \left[C_{A0}^{(1-n)} - tk(1-n)\right]^{\frac{1}{(1-n)}} \tag{4.8}$$

Since conversion data was available, Eq. (8) could be written in terms of conversion, as shown in Eq. (4.9).

$$x = 1 - \frac{\left[C_{A0}^{(1-n)} - tk(1-n)\right]^{\frac{1}{(1-n)}}}{C_{A0}} \tag{4.9}$$

Also, the rate constant is related to the temperature, as proved by Arrhenius equation (Eq. (4.10)). The Arrhenius equation was employed based on the assumption that the rate constant depended on the temperature only. Besides, this equation has been verified empirically to give the temperature behavior of most reaction rate constants within experimental accuracy over fairly large temperature ranges [217].

$$k = Ae^{\left(-\frac{E_a}{RT}\right)} \tag{4.10}$$

With the knowledge of the initial concentration (C_{A0}) of the fatty acid (0.0136 mol/L), the time of reaction, the temperature, the rate constant, order of reaction, and the activation energy of the reaction were estimated by employing POLYMATH software and the Excel Solver facility. This was achieved by using *least square method* (Eq. (4.11)) by minimizing the squared errors of conversion data.

$$f = \sum_{i=1}^{n} \left[\left(X_{pred} \right)_i - \left(X_{exp} \right)_i \right]^2 \tag{4.11}$$

Table B8 and Figure B6-B8 highlight the experimental and estimated conversion of the algae oil. The kinetic parameters could be found from Table 4.7, which also highlighted the statistical parameters.

Table 4.7. Estimated kinetic parameters

Temperature (^oC)	390	405	420
k (s^{-1})	7.12E-05	1.55E-04	2.84E-04
A (s^{-1})	5.85E+09	5.85E+09	5.85E+09
Ea (kJ/mol)	176.6	176.6	176.6
Reaction order, n	0.7681	0.8936	0.9213
R^2	0.9928	0.9993	0.9996
R^2-adj	0.9909	0.9991	0.9995
Rmsd	0.0124	0.0039	0.0030
Variance	0.0014	0.0001	0.0001

The reaction was found to be first order (range from 0.76-0.92), whereas the activation energy was estimated to be 176 kJ/mol, which was lower that obtained from the pyrolysis in the preceding section, probably due to the use of catalyst. This value was obtained from linearizing Eq. (4.10) and plotting lnk against ($1/T$) (Figure B9). The reaction rate constant could be estimated by Eq. (4.12). The activation energy for the CTH is somewhat lower than that obtained from the pyrolysis of the BI.

$$lnk = 22.5 - \frac{21229.3}{T} \tag{4.12}$$

4.2.13. Material Balance for CTH Reaction

To render the work beneficial to the biofuel readership, a scale-up material balance was done by considering processing 1.0 ton of BI (Figure 20). With 1000 kg of BI, 62% of the oil would be extracted as estimated during the oil extraction. To ensure an oil concentration of 0.0136 mol/L as used in this work, a reactor volume of 87 m^3 would be required. It was estimated that the yield for liquid fuel was 42%, while that for the gaseous products was 46%. With the high yield of gaseous product, the process would be sustainable if the gas were used as the source of fuel to power the reactor or used to generate electricity. The material balance also revealed a water yield of 7.8 % that showed the presence of hydrodeoxygenation during the CTH reaction. It was also evident that there was a coke yield of 4.5% that required catalyst regeneration. To fully appreciate the sustainability of CTH reaction with BI as the feedstock, exhaustive technoeconomic analysis must be made, but this is outside the scope of this work.

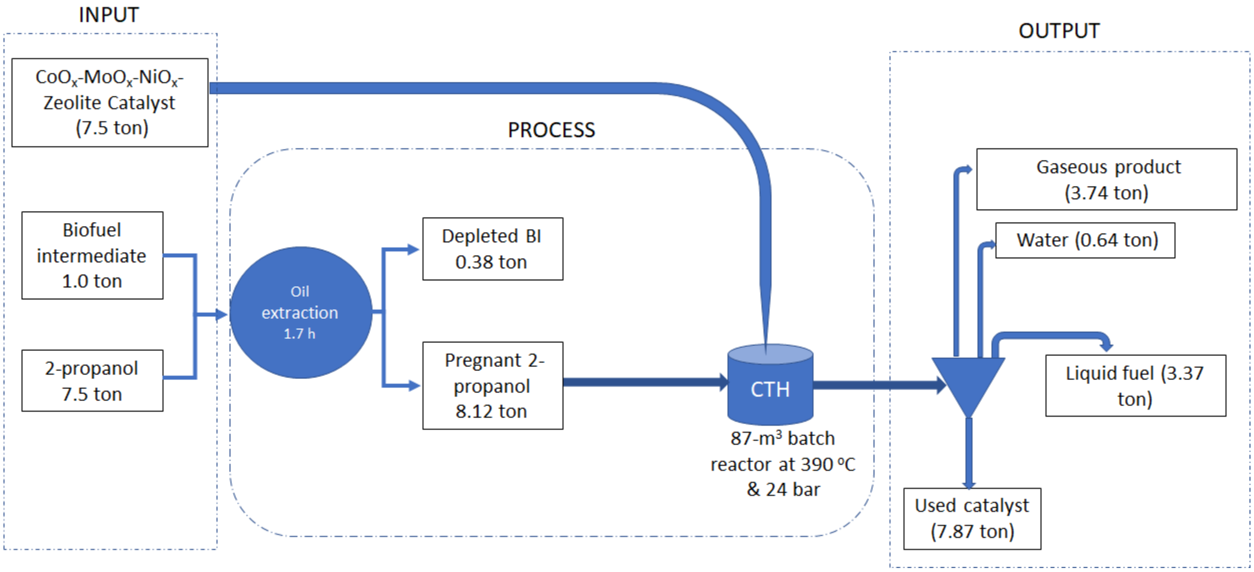
INPUT
CoO_x-MoO_x-NiO_x-Zeolite Catalyst (7.5 ton)
Biofuel intermediate 1.0 ton
2-propanol 7.5 ton
PROCESS
Oil extraction 1.7 h
Depleted BI 0.38 ton
Pregnant 2-propanol 8.12 ton
CTH
87-m^3 batch reactor at 390 °C & 24 bar
OUTPUT
Gaseous product (3.74 ton)
Water (0.64 ton)
Liquid fuel (3.37 ton)
Used catalyst (7.87 ton)

Figure 4.20. Material balance for scale up CTH reaction at 390 °C for 1.0 ton of BI treatment.

4.3. Conclusions

2-propanol was used as both oil extract and an in-situ hydrogen donor, in order to convert oil-laden BI into liquid hydrocarbon fuel over a trimetallic catalyst. BI (from microalgae) with limited usefulness was employed to produce high quality gaseous and liquid high hydrocarbon fuels (jet-fuel range) by employing pyrolysis and catalytic transfer hydrogenation methods. The BI was characterized to evaluate the oil content and the temperature at which thermal decomposition could occur. It was revealed that, above a temperature of 400 ^oC, most of the BI was decomposed. Below a temperature range of 400-700 ^oC, most of the gaseous products from the pyrolysis were oxygenates. However, increasing the temperature above 750 ^oC produced mainly hydrocarbon with significant alkenes, which were not chemically stable, due to their C=C bonds.

Because of the high cost in handling gaseous fuel, the BI was converted to liquid hydrocarbon products via CTH over a NiO_x-CoO_x-MoO_x-zeolite catalyst that produced mainly iso-cyclo alkanes (76%) that are chemically stable with a considerable octane rating. Above 390 ^oC, a significant amount of polyaromatics was produced, rendering the liquid products environmentally unfriendly. It was estimated that 2-propanol-to-oil ratio was 12.2 liter/ liter algae oil compared to using gaseous H_2 as the hydrogen donor, as found in the literature (550 liters H_2/liter oil). This work showed a way to significantly eliminate the issue of handling a huge volume of gaseous hydrogen in hydrogenation reactions.

The trimetallic nature of the NiO_x-CoO_x-MoO_x-zeolite was understandably able to enhance the cyclization and the ring opening of the algae oil, with insignificant coke formation. Despite the production of poly-aromatics in the liquid fuel products, the TGA of showed only a 4% weight increase due to coke formation, which was better than what had been reported in the literature.

Further characterization the catalyst revealed the cubic nature of the zeolite, which slightly lost its crystallinity after one cycle run of the CTH reaction.

4.4. Acknowledgements

The authors are thankful for the support offered by Dr. Cao and his team at The Jefferson Laboratory. The authors are thankful for financial support from the National Science Foundation (NSF) through PFI: AIR Award #1640593 and CAREER Award #CBET-1351413 and Sandia National Laboratories.

CHAPTER 5

TECHNO-ECONOMIC ANALYSIS AND LIFE-CYCLE ASSESSMENT OF JET FUELS PRODUCTION FROM WASTE COOKING OIL VIA CATALYTIC TRANSFER HYDROGENATION

Note: The contents of this chapter have been submitted to be published in the Journal of Renewable Energy

Elena Barbera, Rustem Naurzaliyev, Alexander Asiedu, Alberto Bertucco, Eleazer P. Resurreccion, Sandeep Kumar

This work evaluates the feasibility of renewable jet-fuel production from waste cooking oil (WCO) via the catalytic transfer hydrogenation (CTH), using isopropanol as hydrogen donor. Results were compared to a commercial hydroprocessed renewable jet (HRJ) fuel technology, employing a process simulation-based techno-economic analysis (TEA) and life-cycle assessment (LCA). The two routes were compared in process performance, economic and environmental metrics, and allocation methods. The total capital expenditure (CAPEX) of CTH plant (7.3M$) was significantly lower than that of HRJ ($149.7M$). CTH's annual revenue (153.9M$/year) was close to HRJ's (150.8M$/year), due to similar fuel yields. To be profitable, the liquid fuel could be sold at $3.00/gal ($0.79/L) and at $1.67/gal ($0.44/L) for CTH and HRJ, respectively. The cumulative fossil energy demand (CED) of HRJ was 1.6 times that of CTH, and the total 100-year GWP of CTH was 8% less than HRJ's, with both systems not sequestering CO_2 through co-product offsets. Environmental endpoints based on mass- and energy-allocations were similar to each other, but were remarkably different from market-value allocation. Sensitivity analysis indicated that both systems were driven by transportation factors and not by

process inputs. Finally, trend analysis on CTH’s energy-return-on-investment (EROI) showed that wide improvements could be made in energy efficiency (EROI=10.30-11.30).

5.0. Introduction

The progressive depletion of fossil fuels, along with its environmental impacts, has driven the scientific community to search for sustainable and renewable energy sources. The search has been compelled by the burgeoning global population at 0.9% annual rate, reaching over 9 billion by 2050, resulting in a 29% increase in world energy consumption [226]. One of the highest energy-consuming sectors is transportation. In the U.S., 92% of transportation fuels are petroleum-derived, while only 5% are biofuels obtained from renewable sources [227]. Among transportation fuels, the development of bio-based jet fuels is of tremendous interest. According to the U.S. Energy Information Administration, an increase of approximately 45% in jet fuels consumption is expected by 2040 [227]. About 278 billion liters of jet fuels were consumed by commercial operators in 2016, leading to 781 million tons of CO_2 emissions [228].

While other energy sources (e.g. electricity, fuel cells) are being investigated for road transportation, the aviation sector relies on liquid fuels, with strict quality requirements to power gas-turbine engines [229]. These are kerosene-range hydrocarbons with C_8–C_{16} carbon atoms. These hydrocarbons can be obtained from renewable sources, such as triglycerides. Among the numerous fatty acid sources (mainly animal fats and vegetable oils), waste cooking oil (WCO) is particularly promising. Unlike virgin oils, WCO is not used in food applications and is also a cheaper feedstock. It is largely available in the U.S. and around the globe, with an annual global production of 29 million tons [19]. Moreover, WCO is already largely used in the U.S. for biodiesel production, so a well-developed transportation and supply infrastructure already exists [230].

Several technologies have been investigated for the conversion of fatty acids into jet fuels [229, 231]. These involve oxygen removal from the fatty acids via hydrodeoxygenation (HY) or decarboxylation/decarbonylation reactions using hydrogen. Depending on the catalyst used, one reaction pathway can be favored over another. Most commonly used catalysts are sulfided bimetallic materials such as Ni-Mo or Co-Mo, characterized by their selectivity towards decarboxylation route, or noble metals like Pt or Pd, which favor the HDO pathway [232]. The hydrotreating process for biojet fuels production from triglyceride-based feedstock, known as hydroprocessed renewable jet (HRJ) or hydroprocessed esters of fatty acids (HEFA), is a mature technology and has already been commercialized. For example, Honeywell's UOP, in collaboration with ENI, has successfully commercialized the Ecofining™ process that converts vegetable oils into green jet fuels by deoxygenation [231, 233] as shown in Figure 1A. Accordingly, the distillate products are obtained from a series of two-reaction system with an intermediate separation of by-products. Various feedstock types, such as vegetable oils, animal fats, and greases, can be processed using the UOP-Eni Ecofining. The first reactor, the HDO reactor R1, is fed with the feedstock and hydrogen to produce n-alkanes [234, 235]. The nature of the product is dictated by the feedstock's fatty acid composition, catalyst type, and operating conditions. The by-products are separated from the n-alkanes in a flash drum operated at the reaction pressure. The gaseous stream is a mixture of unreacted hydrogen, CO_2, and CO. The liquid is an immiscible mixture of organic liquid and water. In the second reactor, the hydroisomerization/hydrocracking [164] reactor R2, the liquid product is isomerized and cracked in the presence of hydrogen [231, 233]. This step is necessary to obtain a kerosene boiling range and jet fuel requirements. Light fuels and residual diesel (if any), are the valuable by-products. The latter might be recycled to increase jet fuel production or directly sold to the market.

Despite its maturity level, HRJ has drawbacks associated with the use of hydrogen gas. First, H_2 is poorly miscible with oil at atmospheric conditions; thus, 25-100 bar pressure is required to enhance mass transfer. This results in high capital outlay and high operating costs. Second, storage and transportation of the hydrogen increases cost and creates safety issues, due to its high reactivity and flammability. Third, the production of hydrogen in refineries relies on fossil sources, resulting into large CO_2 emissions.

This study addresses the three issues associated with HRJ by employing catalytic transfer hydrogenation (CTH) as an alternative process to convert WCO into jet fuels (Figure 5.1(B)) [100]. CTH utilizes hydrogen-donating compounds that, in the presence of a catalyst, release H_2 to saturate and reduce triglyceride compounds in oils. We have proven, in our previous investigation, that CTH using isopropanol as hydrogen donor over activated carbon-based catalyst is effective in producing jet/diesel range fuels from waste cooking oil at nearly atmospheric pressure conditions. With this work, we aimed to carry out a detailed, process simulation-based techno-economic analysis (TEA) and life-cycle assessment (LCA) of the proposed CTH process at industrial-scale and to compare its market and environmental performance with that of commercial HRJ process.

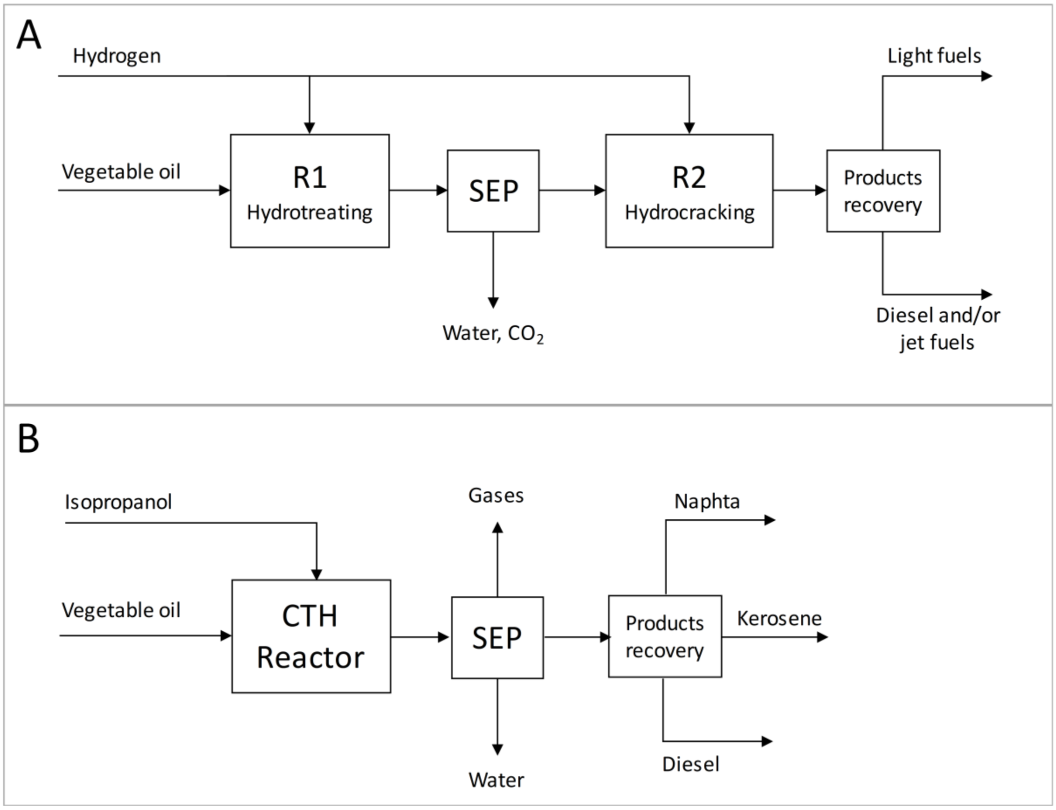
A
Hydrogen
Light fuels
Vegetable oil
R1
Hydrotreating
SEP
R2
Hydrocracking
Products recovery
Water, CO2
Diesel and/or jet fuels
B
Isopropanol
Gases
Naphta
Vegetable oil
CTH Reactor
SEP
Products recovery
Kerosene
Water
Diesel

Figure 5. 1. Block-flow diagram of HRJ (A) and CTH (B) processes for the conversion of triglyceride into biojet fuels.

5.1. Materials and Methods

Process simulations of renewable jet fuels production from WCO by direct hydrogenation (HRJ via pressurized hydrogen) and CTH were performed using Aspen Plus® software v.9. The Peng-Robinson equation of state and NRTL were selected as thermodynamic models. The goal of this study was to perform a comparative TEA and LCA (attributional) between HRJ and CTH process. For the TEA, a basis of 1,000 ton/day WCO feedstock was employed, because this represents the throughput of a small- to medium- scale refinery in the U.S. [236]. The two processes were compared in terms of economic metrics (internal rate of return (IRR) and net present value (NPV)) and environmental impacts (cumulative fossil energy demand (CED) and life cycle greenhouse gas (GHG) emissions). All the assumptions and the methods used in the analysis were described in the succeeding sections. The TEA considered a WCO feed flow rate of 1,000 ton/day, and the LCA adapted a 1 MJ of usable energy produced embodied in liquid biojet fuel.

5.1.1. Waste Cooking Oil Feedstock

The fatty acids composition of the WCO feedstock considered was reported in Table 5.1 [100] . The number of unsaturated bonds in each fatty acid was specified after the length of the carbon chain. Roughly 70 wt% of the oil was composed of unsaturated fatty acids (oleic and linoleic acids), while the remaining compounds were saturated carbon chains.

Table 5.1. Fatty acids composition of waste cooking oil feedstock.

Compound	Formula	wt%
C15:0 Pentadecanoic acid	$C_{15}H_{30}O_2$	17.9
C19:0 Nonadecanoic acid	$C_{16}H_{30}O_2$	11.3
C18:1 Oleic Acid	$C_{18}H_{34}O_2$	18.6
C18:2 Linoleic Acid	$C_{18}H_{32}O_2$	52.3

5.1.2. Hydroprocessed Renewable Jet (HRJ) Process

The process flowsheet for the HRJ process was built in Aspen Plus, based on the UOP commercial process (Section 1), as shown in Figure 5.2. The WCO feed was pumped and heated up to the operating conditions of the HDO reactor R1 (HDOR1) together with H_2, which was fed at 2.6 wt% ratio with respect to WCO [237]. The HDO unit was modeled as a stoichiometric reactor *RStoich.* For each saturated fatty acid, the stoichiometric reactions of decarboxylation, decarbonylation, and hydrodeoxygenation were defined according to:

$$C_nH_{2n}O_2 \rightarrow C_{n-1}H_{2n} + CO_2 \tag{5.1}$$

$$C_nH_{2n}O_2 + H_2 \rightarrow C_{n-1}H_{2n} + CO + H_2O \tag{5.2}$$

$$C_nH_{2n}O_2 + 3H_2 \rightarrow C_nH_{2n+2} + 2H_2O \qquad (5.3)$$

For the unsaturated fatty acids, additional hydrogen was consumed to hydrogenate the double bonds (Table D1). The operating conditions and the fatty acid conversions for the three reactions were taken from the works of Chu et al. [237] and Veriansyah et al. [120], which analyzed the conversion of vegetable oil into fuels at 400 °C, 92 bar, and 2-h reaction time over a nickel-molybdenum catalyst. Accordingly, the extent of reaction was set equal to 0.68 for decarboxylation, 0.03 for decarbonylation, and 0.29 for hydrodeoxygenation, with overall oil conversion equal to 1. The hydrogen consumption associated with the cleavage of triglycerides backbone (3 moles of H_2 for each triglyceride) and the corresponding formation of 1 mole of propane was also considered (Table D2).

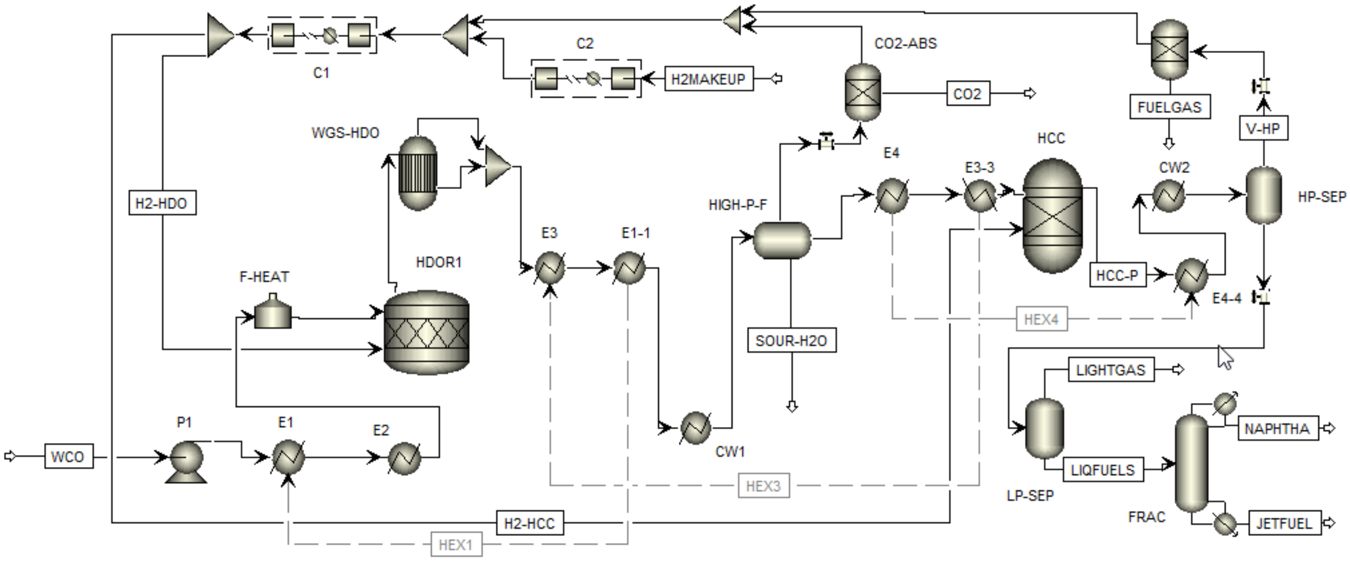
C1
C2
H2MAKEUP
CO2-ABS
CO2
FUELGAS
V-HP
WGS-HDO
HCC
E4
E3-3
CW2
HP-SEP
H2-HDO
HIGH-P-F
E3
E1-1
HDOR1
F-HEAT
HCC-P
E4-4
HEX4
SOUR-H2O
LIGHTGAS
NAPHTHA
P1
E1
E2
CW1
WCO
LIQFUELS
LP-SEP
HEX3
FRAC
JETFUEL
H2-HCC
HEX1

Figure 5.2. Process flowsheet for the HRJ process. Black solid lines indicate material flows while gray dashed lines indicate energy/heat flows.

The gaseous products (CO, CO_2, H_2 and H_2O) might give rise to Water Gas Shift (WGS) and Methanation reactions. However, Veriansyah et al. reported that no methanation was observed over a Ni-Mo catalyst under the experimental conditions investigated. To allow for possible WGS, a *REquil* reactor unit (WGS-HDO) was added to calculate the gas phase equilibrium reaction (Eq.4), which was evaluated at the same operating conditions (400 °C and 92 bar).

$$\mathrm{CO} + \mathrm{H_2O} \rightleftharpoons \mathrm{H_2} + \mathrm{CO_2} \tag{5.4}$$

A high-pressure flash was used to separate the liquid and gaseous products, and products were cooled to 40 °C, which rendered the water and hydrocarbons completely immiscible. Hence, a 3-phase adiabatic flash (HIGH-P-F) was used to achieve complete separation of water, organic liquids, and gases (Table D3).

The organic liquid products were then sent to a hydrocracking unit (HCC) that cracked and isomerized the paraffins, in order to obtain the desired product mixture quality at 350 °C and 90 bar [238, 239]. Because of the complexity of modelling hydrocracking reactions, the reactor was simulated with a *RGibbs* model, considering a total of 358 hydrocarbon components from the Aspen Plus database, including all of the isomers ranging from C1 to C18 carbon atoms. The validity of this approach was verified by checking the product yields (LPG, naphtha, kerosene and diesel ranges) with those reported in the literature [237, 240, 241]. The amount of H_2 required for hydrocracking was evaluated based on the properties of the feed, namely °API gravity and Watson factor (Table D4) that amounted to 84.44 Nm^3 of H_2 per m^3 of oil (Table D5) [241]. Hydrogen is typically fed in large excess to absorb the heat of reaction by direct quench at different stages of the reactor. Therefore, a higher amount of inert hydrogen was required in the reactor, depending on the heat produced. The amount of hydrogen required for quench was estimated through an energy balance to keep the difference between inlet and outlet of reactor in the maximum range of 25 °C (assuming adiabatic operation). This amount of H_2 was set as inert fraction in the *RGibbs* unit, so it was not accounted for in the equilibrium calculation. HCC process input parameters in Aspen Plus are shown in Table D6.

The products from the HCC reactor were separated by means of two flash units in series. The first one operated at high pressure (HP-SEP) to recover the unreacted hydrogen, while the second one operated at low pressure (LP-SEP) to separate C1-C4 gaseous products from the liquid mixture, which was to be sent to an atmospheric fractionation tower to recover the different product fractions. The higher the operating pressure of the LP-SEP unit, the higher the recovery of liquid fuels (Table D10). However, it was preferred to operate the flash at 1 bar, so that a higher amount of propane C_3H_8 (94%) was recovered in the gaseous stream, to be used as additional fuel.

The liquid fuels mixture was then sent to an atmospheric fractionation tower (FRAC) to recover the different product fractions, i.e. naphtha and kerosene. Distillation was modelled as a *RadFrac* unit, operating with 30 ideal stages and reflux ratio of 0.8.

The large excess of H_2 recovered from the HIGH-P-F and HP-SEP flash units was valuable, so that high recovery from the gaseous streams was desired to maximize recycle. The gas mixture separated from the first flash unit was characterized by large amounts of CO and CO_2, while the one recovered after the hydrocracking unit mostly comprised light hydrocarbons such as CH_4, C_2H_6 and C_3H_8. Industrially, the recovery of hydrogen was performed by Pressure Swing Adsorption (PSA), with operating pressures varying between 10-40 bar [240, 242]. As a higher recovery pressure results in lower compression loads required for H_2 recycling, 40 bar was chosen for the simulations. For the purposes of the simulations, the PSA units were modelled by simple SEP blocks, assuming complete H_2 recovery. The H_2 make-up stream was compressed up to 40 bar by means of a 3-stage compressor (C2, compression ratio = 3.14, which considered the final temperature of each stage, not exceeding 225 °C for H_2), with inter-stage cooling at 40 °C. The make-up and recycled H_2 streams were then mixed and compressed up to the final pressure of 92 bar in a second single-stage compressor (C1) and were delivered to the HDO and HCC reactors, respectively.

Finally, pinch analysis was performed, in order to optimize heat integration (Table D7, Figure D1&S3). The optimized heat exchanger networks were displayed in the process flowsheet (Figure 5.2), where integrated heat exchangers were connected by energy streams (dashed lines). Accordingly, the needed external process utilities consisted of a fired heater to achieve 400 °C prior to the HDO reactor, and cooling water to cool the products at 40 °C in units CW1 and CW2. The column reboiler and the condenser duties were also provided by external utilities.

5.2.3. Catalytic Transfer Hydrogenation (CTH) Process

The process flowsheet of the CTH process is shown in Figure 5.3. The simulation was based on the block flow diagram (Figure 1(B)) and on the experimental data obtained in the laboratory using a fixed-bed tubular reactor filled with charcoal catalyst [100]. The WCO feedstock was mixed with isopropanol (ISO-P) at a flowrate of 341.8 ton/day (ISO-P/WCO ratio = 0.3418), and was heated up to the CTH reactor operating temperature (380 °C), found to be the optimal value [100]. The operating pressure was set to 2 bar. The reactor (CTH) was simulated using a *RYield* model. The product yields, defined as mass of product over inlet mass of reagents, were calculated based on the experimental material balance results (Table D19).

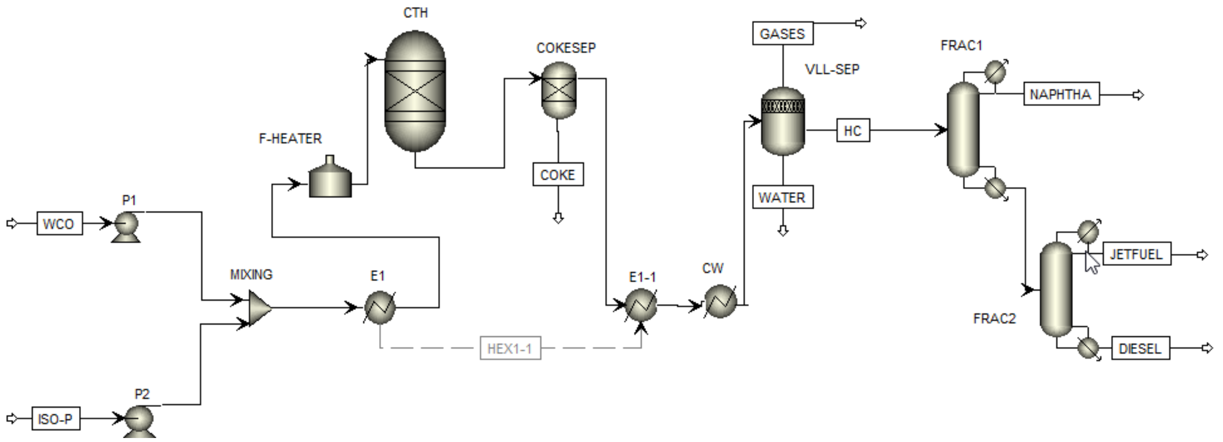

Figure 5.3. Process flowsheet for the CTH process. Black solid lines indicate material flows while gray dashed lines indicate energy/heat flows.

The gaseous products considered were H_2, H_2O, CO, CO_2, CH_4, C_2H_6 and C_3H_8, which were formed either by decarboxylation, decarbonylation, or hydrodeoxygenation reactions, as well as by isopropanol decomposition. Concerning the liquid products, for the sake of simplicity, only three reference components were taken as representatives for the naphtha, kerosene and diesel range hydrocarbons, respectively. Based on the average properties (boiling point and molecular weight) of the experimental products distribution, C_8H_{16}, $C_{12}H_{26}$, and $C_{17}H_{36}$ were selected as the three respective liquid fuel fractions (Table D13-D18).

Because the reaction leads to coke formation, catalyst regeneration was included by simulating the coke removal using a SEP unit. The composition of the outlet stream from the CTH reactor was characterized by a mixture of hydrocarbons (C_8H_{16}, $C_{12}H_{26}$, $C_{17}H_{36}$), water (H_2O), and gaseous products (CO_2, CO, C_1-C_3). The separation of the hydrocarbon mixture from gases and water could be achieved at low temperature, since the solubility of water is inversely dependent on temperature. Accordingly, a 3-phase flash model was used to simulate the required separation (VLL-SEP) at atmospheric pressure after cooling the products to 25 °C. For the correct estimation of the vapor-liquid-liquid equilibrium at low pressure, NRTL was used as the thermodynamic model. The solubility of the incondensable compounds (CO, CO_2 and H_2) was determined from the Henry constants, available in the Aspen Plus database. The validity of the binary interaction parameters of the H_2O-hydrocarbon systems was first verified against experimental data (Table D20-D21). Finally, the three liquid fuel fractions were separated by means of two atmospheric distillation columns in series: the first one (FRAC1) separated the naphtha from the heavier fractions, which were then separated in the second one (FRAC2). The column specifications were, respectively: 10 ideal stages and reflux ratio = 0.2 for the first separation, and 15 ideal stages and reflux ratio = 0.2 for the second one.

Heat integration was also carried out between the cold feed and the hot products, as shown by the energy stream (dashed line) in Figure 3. By analyzing the vaporization range of the WCO-isopropanol feed, the feed outlet temperature from the integrated heat exchanger was set to 300 °C. As most of the WCO vaporized in the range of 300-350 °C (Figure D4), it was preferred to avoid the phase change within the heat exchanger, and to supply the latent heat duty by means of a fired heater. Accordingly, the external utilities were represented by the fired heater required to reach 380 °C and refrigerated cooling water (available at 5 °C) to cool down the products to 25 °C, in addition to the reboiler and condenser duties of the two distillation columns.

5.1.4. Techno-economic Analysis

For a 1,000 ton/day WCO feed flow rate (approximately 270,000 gal/day), the economic and profitability analysis of both HRJ and CTH processes were performed according to the method proposed by Towler et al. [243] for chemical plants. Accordingly, the Fixed Capital Investment (FCI) and the Cost of Manufacturing (COM) were estimated together with the revenues. The FCI consists of the capital expenses of the plant, including construction and engineering costs

(CAPEX), contingency charges, and offsite infrastructure investment (OSBL) (Eq. D1). The CAPEX were estimated based on the Bare Module Cost of each equipment unit, evaluated using the correlations proposed by Guthrie [244]. According to this method, the purchase cost of the equipment was calculated as a function of the size, as well as the construction material and the operating pressure, which became particularly relevant for the HRJ process, characterized by high pressures. Furthermore, the material chosen for HDO and HCC reactors was stainless steel (SS) because of hydrogen gas in compatibility with respect to the normal carbon steel (CS) [245]. Moreover, to account for inflation, all of the costs were referred to the year 2017, using the Chemical Engineering Plant Cost Index (CEPCI).

A rigorous sizing procedure was applied to determine the size of the HDO and HCC reactors for the HRJ process and that of the CTH reactor. A Trickle Bed Reactor (TBR), composed by adiabatic multi-stage beds, was selected as the HDO reactor [246]. Considering the properties of the feed, catalyst hold-up of 60%, and liquid residence time of 2 h, the resulting reactor [245] was determined to have four stages, each of diameter D = 3.048 m and H = 8.39 m, for a total volume of 245 m^3 . The HCC reactor was sized as a multi-stage packed bed reactor, such as those used at commercial level. Taking a typical gas residence time of 1 h, the reactor volume equaled 392.5 m^3 with 5 stages of D = 3.81 m and H = 6.9 m [247]. Finally, a packed bed reactor was also selected for the CTH reactor. The scale-up was based on the experimental value of the weight hourly space velocity (WHSV) of 6.8 h^{-1}. The resulting volume, assuming a 60% catalyst hold-up, was equal to 27.4 m^3. Given the high coke formation, two parallel reactors were considered, in order to allow for a continuous operation when performing catalyst regeneration.

The sieved tray distillation columns were sized according to the Fair Method [248]. In particular, the distillation tower of the HRJ process resulted as having a diameter D = 1.8 m and H = 15.7

m, which allowed operating at 74% of the flooding condition. The diameters and the heights of the columns of the CTH process were (H=17.5 m, D = 1.35 m) and (H = 17.5 m, D = 1.7 m), respectively (approximately 78% of the flooding). In addition, the capital cost, related to the building of an internal H_2 production facility by Steam Methane Reforming (SMR), was considered for the HRJ process [243]. The capital cost of the PSA unit was instead determined using a capacity factor with respect to a similar reference unit [242]. According to the simplified procedure employed, the OSBL were estimated as 50% of the total CAPEX (with reference to atmospheric pressure purchase costs), while contingencies amounted to 15% of the actual CAPEX [243].

The COM considered both direct and indirect manufacturing costs, as well as general expenses related to business administration. Direct manufacturing costs were directly correlated with the production rate and comprised raw materials and utilities or operations expenses (OPEX), as well as staff and operating labor. The OPEX were evaluated based on the results of the process simulations. For the estimation of natural gas utility in the fired heater unit, an efficiency of 80% of the thermal system was assumed. Moreover, the utility used for cooling the CTH reactor was hot oil or molten salts, due to the high operating temperature, i.e. 380 °C. The price of this utility was estimated based on the reference for Hot Oil/Molten Salts for reactor cooling [249]. More specifically, the cost was based on the price of natural gas that would be required to heat the hot oil/molten salts. The number of operators was calculated based on the number of equipment units and was equal to 29 for the HRJ and 26 for the CTH processes. Indirect manufacturing costs and general expenses were instead estimated as percentages of the FCI [241].

The plant was assumed to operate for 8000 h/year, i.e. a stream factor of 0.913 was applied. The economic profitability of the processes was evaluated by means of a discounted cash flow analysis, according to four criteria: discounted payback period (DPBP), net present value (NPV), internal rate of return (IRR), and present value ratio (PVR). The following additional assumptions were made [250-252]: first, the useful life of the plant was taken to equal to 25 years, the first two of which were used for construction and start-up, while full regime production started at Year 3. 70% of the capital was invested in the first year, while the remaining 30% was invested in the second year. Second, the discount rate was taken as a simple interest rate of 8%; hence, it was not based on loan interests or debt ratio. Third, depreciation was evaluated according to the Modified Accelerated Cost Recovery System (MACRS). The depreciation period was seven years, starting at the beginning of the third year and ending at the end of the tenth year. In particular, the double declining balance was applied for the first five years after the plant start-up, after which it was switched to the straight-line method. No salvage value of the plant was assumed. Thus, the total capital to be depreciated equaled the fixed capital investment (FCI). Fourth, the income tax rate was assumed to be 35% of the gross profit. Fifth, the cost of the land was not considered as it was not relevant for the sake of comparison between the profitability of the two processes. Finally, the amount of the annual operators’ salary was taken from U.S. Bureau of Labor Statistics [253].

The revenues were evaluated based on the wholesale prices of the refinery products, which included the production costs and refiner profit, while distribution and transportation costs and taxes were not considered. The wholesale prices, corresponding to the different refinery products (naphtha, kerosene, and diesel), were retrieved from the U.S. Energy Information and Administration [254, 255] and were equal to 0.426 $/L, 0.443 $/L, and 0.440 $/L, respectively, as average prices for 2017. The large amount of fuel gases produced by both the HRJ and CTH process was assumed to be sold at the same price as that of natural gas (0.13 \$/m^3), as their lower heating values (LHV) were comparable to those of natural gas.

5.1.5. Life Cycle Assessment

Goal and Scope

The comparative environmental impacts of HRJ and CTH processes using WCO as feedstock were evaluated in terms of CED and life cycle GHG emissions. It was assumed that one biorefinery was located in any medium-sized U.S. city (population: 100,000-300,000 persons) [256]. A biorefinery serves one division for each U.S. region (e.g. one biorefinery for Division 2 [Mid-Atlantic] of Region 1 [Northeast] which includes New Jersey, New York, and Pennsylvania). WCO were assumed to be collected from restaurants, hotels, casinos, malls, and other food providers operating in these cities. The volume of WCO generated from household sources was insignificant, relative to the food service industry; restaurants still dominate total spent oil output. The states mentioned above are ideal test locations for a WCO-based refinery for the following reasons. First, they are affordable, offering abundant opportunities for business investments. Second, these cities have numerous restaurants that can provide appreciable amount of WCO. They have high average number of restaurants per 1,000 people, compared to the national average of 1.52 for cities whose population is greater than 50,000 [257]. Third, these cities are not as busy as megacities, which cuts transportation costs. Cities were assumed to be located within 150-mile maximum radius from a Metropolitan Statistical Area (MSA) (>1 million population) to ensure a reliable supply of spent oil. Examples of these medium-sized U.S. cities are Pittsburgh (2019 population: 302, 908) serving Division 2, Region 1; Greensboro, North Carolina (2019 population: 292,265) serving Division 5, Region 3; and Fremont, California (2019 population: 238, 281) serving Division 9, Region 4 [256]. Based on the 270,000 gal/day (98.55 Mgal/year continuous operation) TEA basis, the nine biorefineries in the U.S. will require 8.87 x 10^8 gal/yr. The U.S. generates more than enough WCO at 3.8 Mton WCO annually (9.92 x 10^{11} gal/yr) [35], with 2.84 Mton yellow and other grease [258].

The system boundary for the analysis was "well-to-tank" (WTT), in which all associated energy and material flows were determined and quantified for each unit operation: hydrogenation/hydrocracking/separation for HRJ and hydrogenation/separation for CTH. Fuel combustion was excluded in the analysis. The WTT system boundary starts with the acquisition of all raw materials up to distribution of products to end-users (e.g. airports). For ease of analysis, HRJ was modeled as the base case using the UOP-Eni Ecofining^{TM} process. CTH was considered as the alternative case.

Functional Unit

The functional unit (FU) chosen for this analysis was 1 MJ/year embodied energy in liquid biojet fuel (main product) produced from either the HRJ or the CTH process using WCO as feedstock. Such FU was conveniently adapted to provide a quantitative reference with which all calculated materials and energy flows were based. Co-products were light fuels and naphtha from HRJ and naphtha and diesel from CTH.

5.1.5.1. System Boundary

The HRJ process was divided into eight sub-systems which include WCO transport (WT), hydrodeoxygenation (HY), CO and CO_2 flash separation [257], hydroisomerization and hydrocracking [164], high pressure flash [220], low pressure flash (LF), distillation (DT), and fuel transport (FT). Figure 1A represents hydrotreating as HY, separation as FS, hydrocracking as HH, and products recovery as HF, LF, and DT. In the case of CTH, there were six sub-systems identified: WCO transport (WT), catalytic transfer hydrogenation (CH), low pressure flash (LF), distillation 1 (DT1), distillation 2 (DT2), and fuel transport (FT). These sub-systems are represented in Figure 1B as: hydrogenation for CH, and separation for LF, and products recovery for DT1 and DT2. Both HRJ and CTH have identical WT and FT sub-systems.

HRJ Sub-System 1: Waste Cooking Oil Transport (WT). This sub-system involved the systematic collection of WCO from restaurants and food service businesses in cities where a biorefinery was to be established. Additional WCO were to be collected from MSA located within 150-mile maximum radius of the biorefinery to meet the 1,000 ton/day biorefinery requirement used in TEA (approximately 270,000 gallons/day WCO). WCO were transported from sources near the biorefinery or from MSAs using diesel trucks with likeliest truck mileage efficiency of 6.5 miles/gallon [259]. Diesel Class 8 heavy trucks were assumed to travel for six hours in a day at 50 miles/hr. Material input to WT was transportation diesel, while material outputs were combustion products CO_2 and H_2O. The maximum travel distance per truck was 300 miles, and the mileage efficiency was taken to be 6.5 miles/gal [260].

HRJ Sub-System 2: Hydrodeoxygenation (HY). WCO entered the biorefinery as pretreated spent oil suitable for processing. Depending upon the nature of fatty acids, conversion can be decarboxylation, decarbonylation, or hydrodeoxygenation (Table D1). HY was adopted as the general term for hydrotreatment. The chemical reaction was operated at the following conditions: 400 °C, 9.2 MPa and 2 h of residence time [120, 261] . A four-stage HY unit was utilized in this sub-system. Material inputs included pretreated crude oil, H_2 as hydrogenating agent, and nickel-molybdenum (NiMo) catalyst. The output from HY was a mixture of straight-chain alkanes consisting of tetradecane, pentadecane, heptadecane, and nonadecane. Moreover, gases such as CO, CO_2, and propane were generated in addition to water. The amount of total H_2 required and the propane generated were based on stoichiometry, as presented in Table D2. The energy consumption for HY was attributed to: [262] pressurization assuming isentropic compression of H_2 at 85% efficiency and (2) WCO pumping at 95% efficiency. Heat was utilized to raise the oil temperature from 380 to 400 °C, determined as the heat duty to be supplied resulting from heat integration.

HRJ Sub-System 3: CO and CO_2 Flash Separation (FS) Flash separation was performed to separate the gaseous by-products from the output liquid straight chain alkanes. Separation input parameters for FS were as follows: 9.2. MPa, 10 min liquid hold-up [244], adiabatic operation, and vapor-liquid-dirt water phases, employing the Peng-Robinson property method in Aspen Plus modeling. A single vertical-type separation vessel was used. These gases include CO, CO_2, water vapor, propane, and H_2. Along with liquid alkanes, sour water was generated. The energy requirement for this sub-system was attributed to the lowering of product temperature from 231 to 40 °C (after heat integration).

HRJ Sub-System 4: Hydroisomerization and Hydrocracking (HH). The separated liquid straight chain alkanes were isomerized/cracked to get smaller chains of iso-paraffines. Mild conditions were employed in this sub-system: 350 °C and 9.0 MPa at 1-hour HH reaction time. Detailed process input parameters used in Aspen Plus modeling are tabulated in Table D6. The hydroisomerization and hydrocracking unit comprised five stages. The properties of feed oil and hydrogen are presented in Tables D4 and D5, respectively. Material inputs to this sub-system include the alkanes, H_2 for isomerization and cracking, and H_2 for quenching. Output isoparaffins include N-paraffins (C1-C3, C4-C8, C9-C15, C16-C18) and their methylated counterparts (naphtha, jet fuel, and diesel). The compression energy was already accounted for in the HH unit. All input H_2 was previously compressed and then was split into the two reactors, thereby making pressurization energy of this unit to be 0. Direct heat use is also 0 (i.e. reactor is adiabatic) due to heat integration (See Section 1.5 of SI). The heat needed to reach the operating temperature was recovered from other streams.

HRJ Sub-System 5: High Pressure Flash (HF). High-pressure flash was employed to recover H_2 and other gaseous compounds from the liquid products. Herein, the process conditions were: 9 MPa, 10-min liquid hold-up, and no heat duty (adiabatic operation, temperature after cooling was stable at 40 °C). There was one vertical-type HF vessel used. Two material streams were produced in this sub-system: [263] the gaseous stream, consisting of the recovered H_2, CO, CO_2, N-paraffins, and methylated paraffins, and (2) the liquid stream, consisting of naphtha, jet fuel, and diesel. There were residual H_2, CO, and CO_2 present in the output liquid. Like sub-system FS, the energy requirement was cooling energy use, or the latent heat expelled to lower the product temperature from 196 to 40 °C (after heat integration) (exothermic).

HRJ Sub-System 6: Low Pressure Flash (LF). Atmospheric sub-system LF was employed, following HF, to separate the light hydrocarbons to be used as fuel gas and the residual H_2, CO, and CO_2 from the liquid fraction. Process conditions for this sub-system were: 0.10 MPa, 10-min liquid hold-up, and no heat duty (temperature was stable at 24 °C). A horizontal vessel was used. The output liquid was heavy with biojet fuel, diesel, and naphtha, with very little CO_2 left. There was no cooling energy requirement for this sub-system.

HRJ Sub-System 7: Distillation (DT). The final stage of product recovery was atmospheric distillation, to separate the liquid fractions naphtha (C6-C8) from the top and the jet fuels (C9-C15) from the bottom. DT process conditions were as follows: 0.10 MPa, 30 stages, feed input at the 15th stage, 0.80 reflux ratio, 164.8 °C reboiler temperature, and 65.30 °C condenser temperature. The reflux ratio was optimized by sensitivity analysis to maximize the recovery of N-octane (light-key component) in the distillate. The output distillate (naphtha) was heavy in mono-x-methyl (C5-C8) (44 wt%), while the output residue (biojet fuels) was predominantly mono-x-methyl (C9-C15) (38 wt%) and multi-yy-methyl (C9-C15) (57 wt%). The energy use for this sub-system came from two sources: the heating duty at the reboiler and the cooling energy at the condenser; both were function of WCO feed rate.

HRJ Sub-System 8: Fuel Transport (FT). Like WT, FT utilized diesel to transport naphtha and biojet fuel to distribution endpoints (i.e. gate). The designated fuel distributors were assumed to be located within a 150-mile maximum of WCO collection. The trucks were assumed to have a mileage efficiency of 6.5 miles/gallon. The distance hauled was calculated to be 300 miles/truck-day at 6 h per truck per day at 50 miles/hr. Material input to FT was diesel, and material outputs were CO_2 and H_2O.

CTH Sub-System 1: Catalytic Transfer Hydrogenation (CH). The CH was modeled based on the experimental work of Asiedu et al. [100]. Hydrogenation and deoxygenation of WCO was accomplished by means of a hydrogen donor solvent. Herein, gaseous H_2 was replaced by isopropanol. Details on lab-scale reactor geometry and catalyst properties are presented in Table D11, and experimental conversions at different temperatures are shown in Table D12. From these results, an industrial model was built, based on a scale-up of the experimental reactor and the CH reactor material balance at T = 380 ^{o}C; this is presented in Figure D3. The reaction conditions for a CH sub-system were as follows: 380 °C, 2 bar, 6.8 h^{-1} weight hourly space velocity in a continuous fixed-bed plug-flow reactor (PFR). There were 2 PFRs, each with a total capacity of 27.4 m^3, with each one to be operated alternately while the other undergoes catalyst regeneration. The activated carbon catalyst was assumed to be replaced every 90 days. Material input streams consisted of WCO, with isopropanol as the hydrogenating agent. The main liquid fuel product contained C1-C3 gases, naphtha, diesel (heptadecane), and biojet fuels. Gases were also generated in the reaction: CO, CO_2, and H_2, in addition to water and coke. Energy was utilized to pressurize WCO and 2-propoanol to 2 bar and heat was used to raise the feed's temperature from 300 to 380 °C, after heat integration.

CTH Sub-System 2: Low Pressure Flash (LP). Like HRJ, output liquid from the main chemical reaction (CH) was subjected to LP in order to separate gases from main products (naphtha, diesel, biojet fuels). However, unlike HRJ, CTH has three output streams: gas (mainly CO and CO_2), organic liquid (main products), and aqueous liquid (water and residual main products). Conditions were like HRJ's sub-system LF, albeit the condition was exothermic; heat was expelled from the system to cool the reaction products from 50 to 25 °C. The cooling down to 50 °C was achieved by heat integration.

CTH Sub-System 3: Distillation 1 (DT1) and Distillation 2 (DT2). Product recovery involved a series of successive distillations DT1 and DT2, each employing one column. In DT1, naphtha (C6-C8) was recovered from the top, while the heavier fuels (C9-C18) were separated from the residue. The residue was further distilled in DT2 to extract jet fuels as distillate and diesel from the bottom. Process conditions for DT1 were: 0.10 MPa, 10 stages, feed input at the third stage, 0.20 reflux ratio, 220 °C reboiler temperature, and 130 °C condenser temperature. Process conditions for DT2 were: 0.10 MPa, 15 stages, feed input at the ninth stage, 0.20 reflux ratio, 299 °C reboiler temperature, and 212 °C condenser temperature. For both distillation columns, heat was applied to the reboilers and heat was removed from the condensers.

5.1.5.2. Allocation

Allocation is a critical step in LCA, as it directly affects the results of impact assessment. Allocation involves the partitioning of the environmental impacts from the process based on product (materials output) flows [262]. Allocation is not a straightforward division of environmental impacts between products and co-products; thus, protocols set forth by the ISO 14044:2006 guidelines [263] were adapted. For this analysis, mass-, energy- and market-based allocation methods were necessary. In both HRJ and CTH, the products were identified as naphtha/gasoline (C4-C8, e.g. octane C_8H_{18}) and jet fuels (C9-C15, e.g. dodecane $C_{12}H_{26}$) obtained at the very last sub-system (distillation). In some intermediate sub-systems, co-products were generated. For example, the sub-system HF in HRJ produced output liquid (gasoline and jet fuel mixture) that fed into a subsequent LF sub-system. Concurrently, it also generated a co-product output gas mixture consisting of short-chain N-paraffins C1-C3 (e.g. ethane, propane), short-chain N-paraffins C4-C8 (e.g. butane, octane), and mono-x-methyl or multi-yy-methyl C9-C15 (e.g. dodecane, hexadecane or cetane), which can be pressurized and distilled into LPG, naphtha, and jet fuel, respectively. In the case of HRJ, the co-products were as follows: FS = propane; HF = [C1-C3, C4-C8, C9-C15] gaseous hydrocarbons; LF = [C1-C3, C4-C8, C9-C15] gaseous hydrocarbons, [C1-C3 (LPG), C16-C18 (diesel)] liquid hydrocarbons, and liquid CO_2. For CTH, the co-products were as follows: CH = coke; LF = [C1-C3, octane, dodecane, heptadecane] gaseous hydrocarbons, and [C1-C3] (LPG) liquid hydrocarbons. Table 5.2 details the energy- and market-based allocation factors for the HRJ and CTH processes. Thus, the CED and life cycle GHG emissions for each process were apportioned between products and co-products, using mass flows, lower heating values, and unit selling price at prevailing market conditions.

5.1.5.3. Inventory

Life cycle inventory [264] is the most tedious process in LCA, as it involves the acquisition of high-quality data essential to accurate environmental impacts assessment. The development of

HRJ and CTH models in this study entailed data from various sources and methods. The models were created and developed using an Excel spreadsheet with Crystal Ball^{TM} add-in functionality.

Table 5.2. Mass-, energy-, and market-based equivalency (impact) factors used in the impact assessment phase of HRJ and CTH life cycle.

Output[1]	Mass		Energy	Market[5]
HRJ Products	0.8176		0.8109	0.0254
Naphtha	0.2934		0.2993	0.0098
Jet fuel	0.5242		0.5116	0.0156
HRJ Co-products	0.1824		0.1891	0.9746
Propane gas	0.0045		0.0047	0.0675
C1-C3 gas[2]	0.1070		0.1146	0.9043
C4-C8[3]	0.0568		0.0569	0.0022
C9-C15[4]	0.0013		0.0013	0.0000
C1-C3 liquid (LPG)	0.0082		0.0087	0.0004
C16-C18 (diesel)	0.0029		0.0028	0.0001
Liquid CO_2	0.0017		0.0000	0.0000
CTH Products	0.7899		0.7867	0.0167
Naphtha	0.2428		0.2495	0.0056
Jet fuel	0.4200		0.4129	0.0086
Diesel	0.1270		0.1243	0.0026
CTH Co-products	0.2101		0.2133	0.9833
Coke	0.0307		0.0201	0.0006
C1-C3 gas[2]	0.1687		0.1821	0.9823
Octane	0.0061		0.0062	0.0003
Dodecane	0.0001		0.0001	0.0000
C1-C3 liquid (LPG)	0.0046		0.0049	0.0002

[1] Output flow rates obtained from mass balance (tons/day). [2] Represented by ethanegas.
[3] Represented by compressed liquid hexane. [4] Represented by compressed liquid dodecane.
[5] Obtained based on wholesale market price in 2019 US dollars excluding taxes.

This allows certain material inputs and process conditions to contain probability distributions (Table D35) that were subsequently used stochastically for the Monte Carlo simulation, resulting into probabilistic outputs ("endpoints").

The upstream impacts of electricity and selected materials were calculated using U.S. equivalency factors (or European, where U.S. values were not available) and are presented in Table 5.3.

The hydrodeoxygenation LCI were largely based on the experimental results of Veriansyah et al. [120], appropriately scaled up to 1,000 tons/day FU. Gaseous H_2 was stoichiometrically supplied to crude WCO using a nickel-molybdenum (NiMo) catalyst. Pressurization electricity was determined from Aspen, assuming isentropic compression with H_2 (85% efficiency) and continuous pumping of WCO (95% efficiency). LCI data for the rest of the sub-systems were obtained from various literature sources, and detailed technical descriptions were reported in Section 1 of SI. Pressurization electricity, heat, and material flows were determined from Aspen modeling. Compressed hydrogen gas was supplied as the make-up contribution, because part of the non-reacted H_2 is recovered and recycled. As for CTH, large-scale LCI were based on the experimental study by Asiedu et al. [100]. Specifically, isopropanol was supplied in a large quantity (341.8 tons/day) following the scale-up of the CTH reaction of WCO at different temperatures. Pressurization electricity was applied to pump the WCO and isopropanol to 2 bar. The heat needed to increase the feed's temperature from 300 to 380 °C was calculated by Aspen's heat integration. Catalytic transfer hydrogenation output to succeeding sub-systems was based on experimental yields by Asiedu et. al. A full accounting of energy/materials inputs/outputs is presented in Table 5.4.

Table 5.3. Equivalency factors used in modeling HRJ and CTH processes . [265]

Impact	Value	Unit	Notes
Electricity, U.S.			
Energy use	12.5747	MJ/kWh	1.43% from surface coal mining, 1.85% from transportation, and 96.72% from electricity generation. Normal, SD = 1. [265]
Water use	0.00004	m^3/kWh	Hard coal extraction region in the U.S., low-volatile bituminous coal at LHV = 33,412 kJ/kg. Normal, SD = 1.[266]
CO_2 to air	1.0220	kg/kWh	0.94% from surface coal mining, 1.72% from transportation, and 97.34% from electricity generation. Normal, SD = 1. . [265]
SO_2 to air	0.0067	kg/kWh	1.06% from surface coal mining, 1.42% from transportation, and 97.52% from electricity generation. Normal, SD = 1. . [265]
Petro Diesel			
Energy use	51.0996	MJ/kg	47.75% domestic crude production, 45% foreign crude production, 0.27% domestic crude transport, 1.09% foreign crude transport, 5.38% crude refining, 0.51% diesel transport. Normal, SD = 1[267]
Water use	0.0004	m^3/kg	Normal, SD = 1. [267]
CO_2 to air	10.0476	kg/kg	86.54% tailpipe fossil (combustion), 13.46% production. Normal, SD = 1. [267]
SO_2 to air	0.0027	kg/kg	Normal, SD = 1. [267]
H_2, from fossil fuels (RER), as liquid H_2			
Energy use	33.6420	MJ/kg	As oil, crude, in ground. Normal, SD = 1. [268]
Water use	0.0739	m^3/kg	0.000723 m^3 water estimate + 0.0732 m^3 cooling water, unspecified origin. Normal, SD = 1. [268]
CO_2 to air	1.2328	kg/kg	1.23 kg fossil CO_2 – 0.00278 kg biogenic CO_2. Normal, SD = 1. [268]
SO_4^{2-} to water	0.0005	kg/kg	Normal, SD = 1. [268]
Isopropanol			
Energy use	3.2000	MJ/kg	Propylene oxide production via direct hydration demands a split of 50% natural gas, 38% electricity, and 12% steam. All energy used for heat of steam was obtained from natural gas. Lognormal, SD = 1.88. [269]
Water use	0.0271	m^3/kg	0.0032 m^3 water estimate as 10x stoichiometric amount + 0.024 m^3 cooling water. Lognormal, SD = 1.88.
CO_2 to air	0.0990	kg/kg	From wastewater treatment. Lognormal, SD = 1.88. [270]
SO_4^{2-} to water	0.1740	kg/kg	Calculated from mass balance. Lognormal, SD = 2.11.[270]
Carbon black, at plant (RER)			
Energy use	9.8820	MJ/kg	As heat from industrial furnace, >100 kW. Lognormal, SD = 1.24. [271]
Water use	0.0000	m^3/kg	Uniform = 0.00 (minimum), 0.01 (maximum). [270]
CO_2 to air	1.9700	kg/kg	Calculated from mass balance. Lognormal, SD = 1.38. [270]
Cryolite (2 AlF_3 • 3NaF)*			
Energy use	3.2000	MJ/kg	2 MJ/kg natural gas and 1.2 MJ/kg electricity. Normal, SD = 1.
Water use	0.0300	m^3/kg	24 kg/kg + 6 kg/kg cooling water. Normal, SD = 1.
CO_2 to air	0.0000	kg/kg	Uniform = 0.00 (minimum), 0.01 (maximum).
Steel			
Energy use	2.1826	MJ/kg	18.66% coke-making, 9.59% sintering, 67% blast furnace, 4.75% LD steel converter. Cradle-to-casting plate gate (steel plates). Normal, SD = 1. [272]
Water use	0.0003	m^3/kg	Normal, SD = 1. [51
CO_2 to air	1.1586	kg/kg	Normal, SD = 1. [51

* Due to missing production data for Ni-Mo/Al_2O_3 catalyst, the impacts of cryolite production was adapted as a rough estimate on energy use, water use, and CO_2 emissions according to the overall reaction: $12\ HF + Al_2O_3 \bullet 3H_2O + 6\ NaOH \rightarrow 2\ AlF_3 \bullet 3\ NaF + 12\ H_2O$. To produce 1 kg cryolite, these reactants are needed stoichiometrically: 28.580 mol HF, 2.382 mol $Al_2O_3 \bullet 3H_2O$, and 14.290 mol NaOH at 100% assumed yield. Gendorf (2000).

Table 5.4. Global LCI for HRJ and CTH detailing energy/materials inputs/outputs to and from the technosphere/environment based on Table **D36.** Energy and heat are in MJ/day and materials and chemicals are in tons/day.

HRJ			
Energy, chemicals (input from technosphere)		Products, co-products (output to technosphere)	
Electricity	683,059.20	Naphtha	267.80
Heat	512,599.92	Jet fuel	478.37
Diesel	16.53	Propane gas	4.12
WCO	1,000.00	C1-C3 gas	97.64
Ni-Mo/Al_2O_3	3.26	C4-C8	51.81
H_2 (gross)	83.44	C9-C15	1.19
H_2 (net, minus recycle)*	35.20	C1-C3 liquid (LPG)	7.52
Steel	0.0017	C16-C18 (diesel)	2.64
Emissions (output to environment)		Liquid CO_2	1.52
Air		Heat (cooling)	1,207,360.70
CO_2	150.71		
CO	11.42		
H_2	25.75		
Water			
Pure H_2O	18.69		
Sour water (H_2O+CO_2)	37.77		
CTH			
Energy, chemicals (input from technosphere)		Products, co-products (output to technosphere)	
Electricity	158,696.70	Naphtha	232.86
Heat	485,100.00	Jet fuel	402.88
Diesel	14.44	Diesel	122.13
WCO	1,000.00	Coke	29.41
Isopropanol	341.80	C1-C3 gas	161.85
Activated carbon	0.0913	Octane	5.83
Emissions (output to environment)		Dodecane	0.11
Air		C1-C3 liquid (LPG)	4.40
CO_2	210.79	Heat (cooling)	493,849.44
CO	127.90		
H_2	6.85		
Water			
Pure H_2O	16.26		
Sour water (H_2O+CO_2)	72.06		

*Net H_2 requirement is 35.20 tons/day, of which 22.93 tons/day is consumed in the hydrodeoxygenation reactor, 11.34 ton/day in the hydrocracking unit, and 0.93 ton/day are lost in the light gas stream separated by the low-pressure flash.

5.2. Results and discussions

5.2.1. Process Performance

The results of process simulation for the HRJ and CTH systems are summarized in Table 5.5. Aspen simulation resulted in an overall HRJ hydrogen consumption of 35.2 ton/day, of which 22.93 ton/day were consumed in the HY reactor (at hydrogen conversion of 88.2%), 11.34 ton/day in the hydrocracking unit, and 0.93 ton/day was lost in the light gas stream separated by the low-pressure flash. Hydrogen was assumed to be completely recycled without any losses, although, in practice, these may vary between 15-25% for PSA unit. Hence, the amount of hydrogen consumed would be slightly larger than indicated. The overall hydrogen-to-WCO ratio of 3.5% w/w is similar to the ones calculated by Chu et al. (2.6-3% w/w), Han et al. (2-3% w/w), and Pearlson et al. (4% w/w) [240, 250, 261]. Nevertheless, Chu et al. did not consider the amount of hydrogen used for hydrocracking reactions, assuming that it was a factor of the degree of cracking, instead. Pearlson et al. proposed that a 4% w/w overall process ratio is appropriate for maximum jet fuel production, based on data in the literature. The consumption of isopropanol in CTH is equal to its supply (341.8 ton/day), since it was completely decomposed inside the reactor and was, hence, non-recyclable.

Table 5.5. Process performances of HRJ and CTH systems. All specific energy consumption of utilities is scaled to the mass of WCO feed.

Performance parameter	HRJ	CTH	Unit
Waste cooking oil basis rate	1,000	1,000	ton/day
H_2/isopropanol consumption	35.2	341.8	ton/day
Liquid fuels products			
Liquid yield	77	76	%w/w
Naphtha	20	30	%v/v
Kerosene	80	60	%v/v
Diesel	0	10	%v/v
Energy consumption			
Heating energy	0.243	0.298	kWh/kg
Cooling energy	-0.517	-0.365	kWh/kg
Electric energy	0.092	$7.4 \cdot 10^{-5}$	kWh/kg
Maximum pressure	9.2	0.2	MPa
Maximum temperature	400	380	°C

The yield of liquid fuel products obtained from both systems was similar, comparable to previous studies [120, 237, 250, 251] (77 wt% for HRJ and 76 wt% for CTH). The liquid mixture obtained from the conventional HRJ system was characterized by a larger amount of kerosene products, roughly 16% higher than that obtained from CTH. However, CTH produced more naphtha and diesel than HRJ. Both systems produced gaseous by-products. Specifically, about 10% of the WCO feed was converted into light gas (mostly propane) in HRJ, comparable to what has been reported in other studies, ranging between 7% and 10% [237, 240, 249]. This light gas had low LHV because it contained large amount of CO and CO_2. The CTH system produced around 162 ton/day of fuel gas, with LHV of 21.2 MJ/kg. The thermal and electricity comparison between the two systems reflected their relative process conditions: temperature and pressure. The thermal energy (heat) consumptions were comparable between the two systems (513 GJ/day for HRJ, 485 GJ/day for CTH), due to the optimized heat integration network and the similar operating temperatures. CTH's cooling energy requirement was 59% lower than HRJ's due to the latter's combined exothermic effect via flash separation and high-pressure flash. In terms of direct electricity, HRJ consumed more than four times the electricity than CTH did, because of its high operating pressure and the handling of gaseous hydrogen via multi-stage compressors. CTH utilized low electricity because it operates at relatively low pressure and because pumps were employed in place of compressors to transport liquid streams. In general, CTH consumed far less heat and electricity than HRJ, because the number of pieces of equipment necessary in an HRJ reaction was much larger (two reaction systems: HY and HH), whereas only one reactor is used in CTH. Further, CTH does not require the large recycling of gaseous streams, which is beneficial in reactor sizing and operation.

5.2.2. Capital Expenditure

The results of CAPEX and FCI for both HRJ and CTH systems are summarized in Tables 5.6 and 5.7, respectively. A summary of direct manufacturing costs for both systems are reported in Table 5.8. Moreover, the results of COM for HRJ and CTH systems were shown in Tables 5.9 and 5.10, respectively, using direct, fixed, and general costs of manufacturing data (Table D24 and Table D25).

Table 5.6. Total bare module cost in HRJ and CTH jet fuel production processes. For HRJ the cost at atmospheric pressure (base) is reported in addition to the final one.

Equipment Type	HRJ		CTH	
Reaction System	$C_{bm,base}$	C_{bm}	Reaction System	C_{bm}
Hydrodeoxygenation[1]	$ 1,650,989	$ 40,814,774	Hydrodeoxygenation	$ 132,396
Hydrocracking[2]	$ 2,972,309	$ 76,618,490	2nd hydrodeox. regen.	$ 132,396
Steam methane reform.	$ 3,441,561	$ 16,313,000		
Heating[3]	$ 1,450,520	$ 1,675,585	Heating[3]	$ 3,010,654
Compression	$C_{bm,base}$	C_{bm}	Pumps	C_{bm}
Compression 1	$ 448,539	$ 1,704,448	Feed pumping WCO	$ 12,046
Compression 2	$ 1,234,069	$ 4,689,461	Feed pumping ISOP[4]	$ 11,158
Feed pumping WCO	$ 73,966	$ 174,098		
Separation	$C_{bm,base}$	C_{bm}	Separation	C_{bm}
By-P HP separation	$ 74,603	$ 663,506	LP separation	$ 74,603
Product HP separation	$ 53,829	$ 581,562		
Product LP separation	$ 63,636	$ 63,636		
PSA-hydrogen recov.	$ 889,876	$ 2,936,590		
Distillation	$C_{bm,base}$	C_{bm}	Distillation	C_{bm}
Fractionation 1[5]	$ 487,216	$ 487,216	Fractionation 1[5]	$ 387,179
			Fractionation 2[5]	$ 491,028
Heat Exchangers	$C_{bm,base}$	C_{bm}	Heat Exchangers	C_{bm}
Heat exchange 1	$ 104,310	$ 123,010	Heat exchange 1	$ 469,833
Heat exchange 2	$ 157,024	$ 185,174		
Heat exchange 3	$ 387,390	$ 456,232		
Heat exchange 4	$ 159,540	$ 187,891		
Cooling 1[6]	$ 139,372	$ 164,358	Cooling[6]	$ 151,479
Colling 2[6]	$ 144,417	$ 169,854		
Heating[3]	$ 1,450,520	$ 1,672,574	Heating[3]	$ 2,446,909
Total (2017)	$ 15,383,686	$ 149,681,462	Total (2017)	$ 7,319,681

[1]4x5 bed, [2]5x5 bed, [3]Fired heater, [4]Three stages [5]Trays + columns [6]Cooling water

Table 5.7. Fixed capital investment in HRJ and CTH jet fuel production processes.

Fixed Capital Investment	HRJ	CTH
ISBL + Engineering	$ 149,681,462	$ 7,319,681
OSBL (50% total C_{bm} base)	$ 7,691,843	$ 3,659,841
Contingency (15% total C_{bm})	$ 26,942,663	$ 1,097,952
Total	**$ 184,315,968**	**$ 12,077,474**

Table 5.8. Summary of direct manufacturing costs.

	Unit	Value	Reference
Raw Material			
Waste cooking oil	$ ton^{-1}	150.00	
Hydrogen	$ kg^{-1}	1.60	[250, 251]
Isopropanol	$ kg^{-1}	1.30	[252]
Utility			
Electric power	$ kWh^{-1}	0.087	[254]
Natural gas (LHV=38.42 MJ m^{-3})	$ m^{-3}	0.130	[254]
Cooling tower water (30 °C)	$ GJ^{-1}	0.354	[244]
Refrigerated water (5 °C)	$ GJ^{-1}	4.430	[244]
Medium pressure steam (10 bar, 184 °C)	$ GJ^{-1}	6.870	[244]
High pressure steam (41 bar, 254 °C)	$ GJ^{-1}	9.830	[244]
Hot oil	$ GJ^{-1}	*f*(kW)	[249]
Operators			
Salary	$ year^{-2}	60,000.00	[253]

Table 5.9. Total cost of manufacturing in HRJ jet fuel production process.

Raw Material (RM)	**Value**	**Unit**	**$/year**
WCO	1,000	ton/day	50,000,000
Hydrogen	35.2	ton/day	18,773,333
Utilities (UT)	**Value**	**Unit**	**$/year**
Compressor 1	1,196	kW	836,586
Compressor 2 (make-up)	3,191	kW	2,230,902
Feed WCO pump	125	kW	87,540
Cooling water 1	6,197	kW	63,175
Cooling water 2	5,736	kW	58,477
Fired heater (LHV = 38.42 MJ/m^3)	704	kW	85,807
Condenser	2,042	kW	20,815
Reboiler	4,189	kW	828,901
Waste Treatment (WT)	**-**	**-**	**-**
DMC + FMC + GE (Table D24)			**29,251,124**
Total COM (without depreciation)			**102,236,661**

Table 5.10. Total cost of manufacturing in CTH jet fuel production process.

Raw Material (RM)	Value	Unit	$/year
WCO	1,000	ton/day	50,000,000
Isopropanol	341.8	ton/day	148,113,333
Utilities (UT)	**Value**	**Unit**	**$/year**
Hot oil CTH	9,508	kW	2,138,041
Feed WCO pump	2.1	kW	1,458
Feed ISOP pump	1	kW	696
Cooling water 1	3,153	kW	32,140
Fired heater (LHV = 38.42 MJ/m^3)	5,614	kW	683,904
Reboiler 1	5,034	kW	1,425,077
Reboiler 2	1,747	kW	867,511
Condenser 1	1,058	kW	10,788
Condenser 2	1,505	kW	15,348
Waste Treatment (WT)	**-**	**-**	**-**
DMC + FMC + GE (Table D5)			**15,147,753**
Total COM (without depreciation)			**218,436,050**

In both the CTH and the HRJ systems, CAPEX was controlled by their main reaction sub-systems: 91% in HRJ and 45% in CTH, calculated in reference to the bare module cost, assuming a factor of 4.74 to fluid process as single Lang factor, C_{bm} [243]. The heating component in CTH's main reactor cost over 3 M$, about 2% the cost of the heating component in HRJ's main reactor. CTH required pumping, as the solvent was isopropanol, while HRJ required compression, as the solvent was gaseous hydrogen. Gas compression is prohibitively expensive, in the order of M$. Both systems needed infrastructure for separation, although CTH demanded a single low-pressure separator, while HRJ required multiple high- and low-pressure separators, including a PSA hydrogen recovery unit.

The breakdown of CAPEX for the HRJ and CTH systems is shown in Figure 5.4 (top panel). The total cost of the CTH plant (7.3 M$) was significantly lower (around 98%) than the total cost of the HRJ plant ($149.7 M$). This was mainly due to the high operating pressure in HRJ, which increased the bare module cost by about ten times, relative to atmospheric conditions. Together, the cost of the HY and HH reactors in HRJ represented more than three-fourths of the 2017 total CAPEX, or 64% of FCI. This large contribution was attributed to the slow reactions that unavoidably resulted in large reactor volumes and critical operating conditions.

The SMR plant for hydrogen production substantially contributed to the overall capital investment, at about 11%. Fractionation in both the HRJ and the CTH systems operated atmospherically. HRJ's single fractionation column had a negligible contribution to total CAPEX (<1%). But unlike the HRJ, the CTH system consisted of two fractionation columns in series, thereby doubling the cost of distillation. The contribution of these two columns to the total CAPEX was 12%. The CTH main reactor was comparably priced relative to other units, thanks to the low cost of the catalyst employed. In terms of heat exchange, CTH has one integrated heat exchanger, one cooling unit, and one fired-heating element, as opposed to HRJ's four integrated heat exchangers, two cooling units, and one fired-heating element.

The FCI of the two systems, accounting for the offsite and contingency contributions, are 184.3 M$ and 12.1 M$ for HRJ and CTH system, respectively (Table 5.7). The direct manufacturing costs in HRJ and CTH, as summarized in Table 5.8, demonstrated that on a per kg basis, isopropanol and hydrogen's unit costs were relatively similar. However, when mass flow rates and hours of operation were factored in, the total annual cost of isopropanol ballooned to 148.11 M$, in comparison to hydrogen's 18.77 M$, regardless of hydrogen's compression requirement. In fact, isopropanol's cost represented 67.8% of CTH's total COM (without depreciation, Table 5.10). Table 5.9, on the other hand, shows that the driver in HRJ's total COM was WCO, not hydrogen. Hydrogen compression was another significant driver, in conjunction with the cost associated with heating the single reboiler in the HRJ system.

5.2.3. Operations Expenditure

The breakdown of total OPEX (raw materials, utilities) for the two systems is shown in Figure 5.4 (bottom panel). It is worth noting that the OPEX for HRJ amounted to 73 M$/year, while the OPEX for CTH amounted to 203 M$/year. This huge difference was determined by the cost of isopropanol (148 M$/year), around 68% of CTH's total operating cost (COM without depreciation). In general, the feedstock supply represented the major input to both systems. The overall COM, accounting for operating labor, fixed cost of manufacturing, and general expenses, amounted to 102 M$/year and 218 M$/year for the HRJ and CTH systems, respectively.

In terms of revenue, the two systems were very similar, i.e. 150.8 M$/year for HRJ and 153.9 M$/year for CTH (Table 5.11). By comparing the revenues with the total COM, CTH generated a negative gross profit, with most of the income offset by the cost of supplying isopropanol.

Table 5.11. Product incomes and gross profits in HRJ and CTH jet fuel production processes.

	HRJ			CTH		
Fuel Product	Produced	Unit	Income ($/yr)	Produced	Unit	Income ($/yr)
Fuel gas	6,969	Nm^3/hr	9,433,018	12,978	Nm^3/hr	13,497,224
Naphtha	8,041	L/hr	27,405,246	12,042	L/hr	41,038,506
Kerosene	32,166	L/hr	113,969,798	24,084	L/hr	85,333,119
Diesel	-	L/hr	-	4,014	L/hr	13,997,406
Total revenue (R)			150,808,063			153,866,254
Cost of manufacturing (COM_d)			102,236,661			218,436,050
Gross profit (GP)			48,571,402			-64,569,796

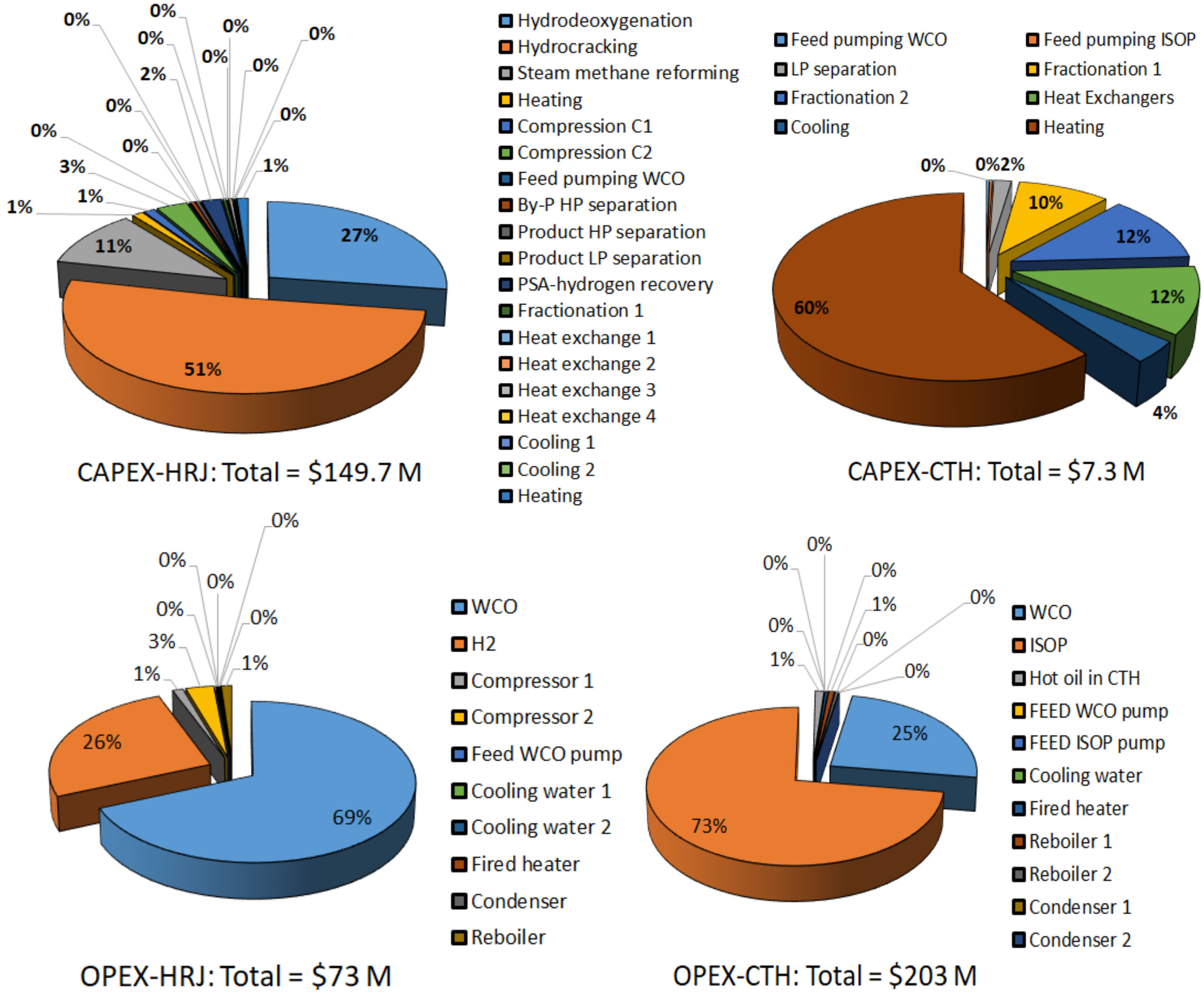

Figure 5.4. Capital expenses of HRJ (above left) and CTH (above right) systems. Operating expenses for raw materials and utilities of HRJ (below left) and CTH (B) systems.

5.2.4. Break-even Analysis

Break-even analysis was performed to ascertain the profitability of CTH and HRJ systems using total CAPEX (CTH=$7.3M, HRJ=$149.7M), annual total COM (without depreciation) (CTH=$218.4M, HRJ=$102.2M), revenues from liquid fuel (CTH=$140.4M, HRJ=$141.4M), revenues from gaseous fuel (CTH=$13.5M, HRJ=$9.4M), and depreciation (use MACRS for 7 years). With these inputs, the net present value (NPV) for both processes under a ten-year debt financing term was evaluated (CTH=-$216.6M, HRJ=$6.4M). Thereafter, the break-even point (i.e. time in years at NPV=0) for the 10-year term was calculated for both systems by setting the NPV=0 and by generating a new annual cumulative NPV profile (0-25 years) with Year 10 as the break-even point. This method was repeated for other break-even points: 5, 15, 20, and 25 years for both CTH and HRJ systems. The results are plotted in Figure 5.5.

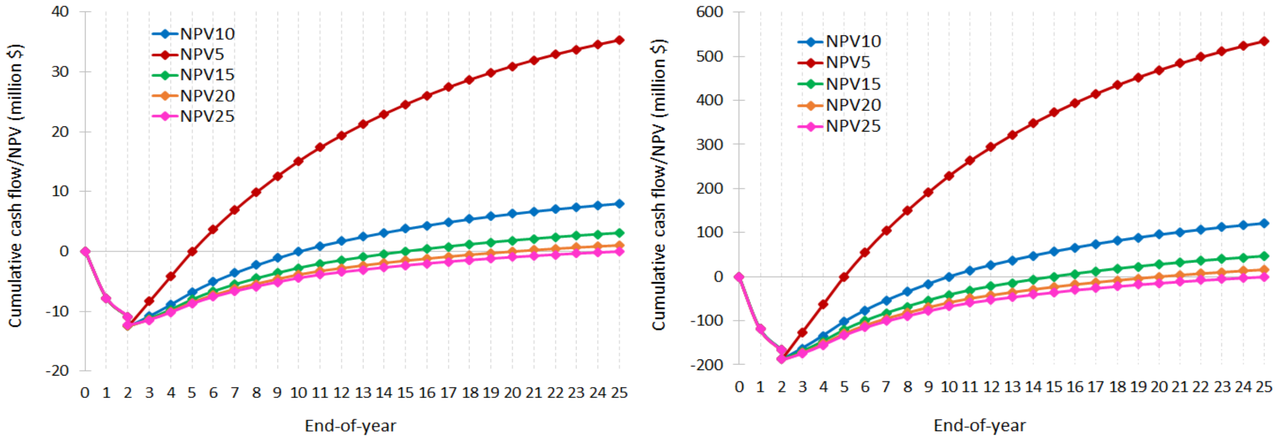

Figure 5.5. Cumulative NPV profiles for CTH (left) and HRJ (right) systems at various debt financing terms showing corresponding break-even points (5, 10, 15, 20, and 25 years).

The 25-year NPV profiles of the CTH (left) and the HRJ (right) systems reveal the general trend in cumulative NPV across all financing terms. The initial dip in NPV from 0-2 years indicates the M$ initial investment. Seventy percent of the initial investment was spent in the first year and the remaining 30% in the second year. At Year 2, the profile vertically dips even further with magnitude corresponding to the working capital. From Year 2 onward, the profile increases until it hits the break-even point. Thus, DPBP coincided from Year 2 to the break-even point. This discounted cash flow analysis revealed that the cumulative cash flow became positive past the break-even point. Depreciation was factored in from Year 4 to Year 11, and the tail end of the profile shows the NPV of each system at the end of its life. For example, CTH's end-of-life NPVs were as follows: 35.29 M$, 8.01 M$, 3.05 M$, 1.04 M$, and 0 M$ for financing term of 5, 10, 15, 20, 25 years, respectively. In both the CTH and the HRJ systems, the salvage value of the project decreased as the financing term increased.

Negative cumulative NPV indicated that any system was deemed unprofitable, while positive cumulative NPV indicated otherwise. For a system to be viable using the break-even analysis, one must understand that the current cumulative NPV at year *n* is a function of revenue, total COM, and depreciation at that year, including the initial investment. The break-even point is the time at which the annual revenue equals the total business costs (total COM, depreciation) progressively achieved by paying a fraction of the initial investment year after year. Typically, the break-even point in most economic analyses determines the amount or the volume of product sales in a year that equals total dollar sales to total dollar COM (i.e. gross profit = $0). In this analysis, however, the break-even point was calculated as the year beyond which total dollar sales exceeded total dollar COM, coinciding with cumulative NPV > $0. There was no set break-even point for which a business model ensured profitability; however, if total COM were higher than expected total sales, the business plan could be re-examined, and alternative strategies must be implemented. This study determined that, if the biojet fuel were sold at $2.99/gal ($0.79/L) and $1.32/gal ($0.35/L) for CTH and HRJ, respectively, it would take 25 years to break even. Since most corporations prefer break-even points to be less than ten years, it would, therefore, be profitable to sell biojet fuel at $3.00/gal ($0.79/L) and $1.67/gal ($0.44/L) for CTH and HRJ, respectively. At these rates, and for a project life of 25 years, the NPV for CTH and HRJ were estimated to be 8 M$ and 121 M$, respectively. It was observed that the biojet fuel selling price for the CTH system was higher than that of HRJ, due the higher operation cost associated with CTH. However, as the break-even point approached five years, the biojet fuel selling price for HRJ ($2.70/gal) and that for CTH ($3.10/gal) converged (12.94% difference) such that, in the long run, CTH fuel would be affordable as a result of its low total CAPEX. It appears that CTH would recover its initial investment faster than HRJ through faster payment of its CAPEX. As capital recovery within five years appears ambitious, maintaining DPBP (8 years after the construction) and an interest rate of 8% for both processes would be ideal.

An IRR analysis was performed for both the CTH and the HRJ systems, covering interest rates from 1-50% for the entire 25-year life. The inputs to this analysis were base case inputs; that is, CTH-NPV was negative and HRJ-NPV was positive at the end of 25 years under a 10-year financing term. The results are presented in Figure 5.6. The IRR is an index of the investment risk, a method used in capital budgeting to estimate the profitability of investments. It refers to the discount rate that makes NPV of all cash flows equal to 0. IRR calculations followed the same method as NPV. As the interest rate increased, HRJ-NPV decreased, while CTH-NPV increased. Since HRJ-based biojet fuel production is a mature technology with low risk, its IRR of 15.91% represents an attractive value for the investment. As of the current market without any subsidies, incentives, or any of the investigated case scenarios from Table D34, CTH's IRR profile seems to suggest that the system is untenable.

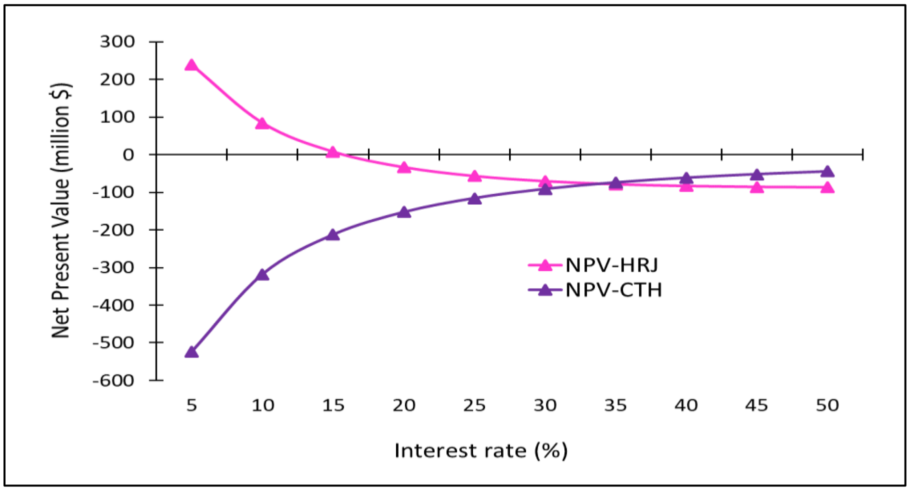

Figure 5.6. IRR profiles for CTH and HRJ systems under 10-year debt financing term.

At the present state, the CTH process, based on the experimental conditions investigated, has the potential to be economically profitable, despite the large input cost associated with isopropanol. Given that the isopropanol cost represents 68% of CTH's total COM, total COM must be reduced by around 30% to even start realizing net profit. This can be done using a combination of two strategies: (1) reduce both isopropanol cost and total direct/fixed/general cost by 60%, and (2) reduce isopropanol cost by 55%. It is highly unlikely that a 60% reduction in staff salaries, plant overhead, and distribution/selling costs can be achieved, because these variables are set by prevailing market conditions and, for an emerging technology such as CTH-based biojet fuel, these costs will be slightly elevated, leaving the latter option to be realistically feasible. It was calculated that, to obtain the same Present Value Ratio of HRJ (a more meaningful index than the NPV when two processes with very different capital investments are compared), the price of the isopropanol should not exceed 0.735 \$ kg^{-1} (i.e., a 43.5% reduction from current cost) (Table D34). Alternatively, at the current market price, the maximum isopropanol inlet was calculated to be 196.54 ton/day (isopropanol/WCO feed ratio of 0.204 by weight) in order to be profitable. However, performances and product yields should be verified, in this scenario.

5.2.5. Environmental Metrics

The results of the inventory analysis described in Section 5.2.5.5 were used in a life cycle impacts assessment, a step in LCA that quantifies the environmental impacts, selects priorities from these environmental impacts, and transforms these priorities into meaningful environmental endpoints (a damage category or a forecast). In this study, two major environmental endpoints were identified: CED and life cycle greenhouse gas. GHG emissions using the Eco-Indicator 99 method [273] and the equivalency factors (damage factors) detailed in Table 5.3. CED represent the cumulative non-renewable fossil energy requirement of the entire process in MJ per 1,000 tons WCO. Life cycle GHG emissions were reported as having 100-year global warming potential (GWP) in kg CO_2 equivalents per 1,000 tons WCO.

Figure 5.7 and Table 5.12 depict the characterization results in the production of biojet fuel from WCO via the CTH and HRJ processes. The left pane demonstrates the environmental endpoints (CED and GWP, positive bar) and the environmental credits (negative bars). The right pane shows the energy distribution of fuel products produced from CTH and HRJ processes, including the energy-return-on-investment (EROI), defined as the ratio of the total energy output from the system to the total energy input into the system.

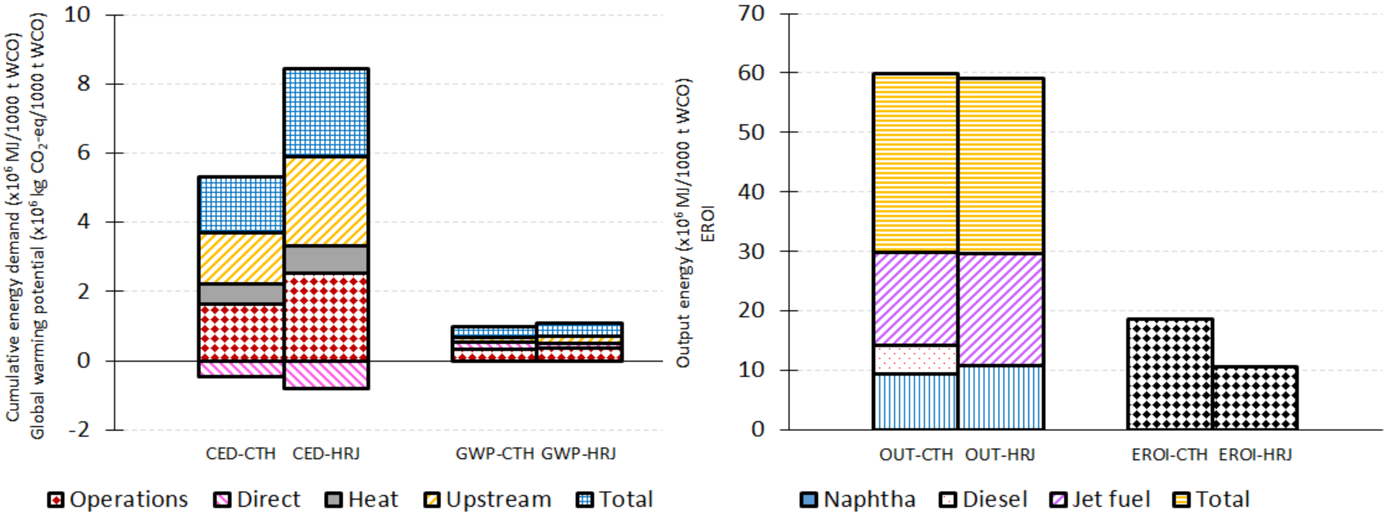

Figure 5.7. Results of characterization in the production of CTH- and HRJ-based biojet fuel from 1,000 tons WCO. Left pane corresponds to environmental endpoints (CED and GWP) and right pane corresponds to distribution of output energy. Energy-return-on-investment (EROI) is included in the right pane.

Table 5.12. Characterization results of Figure 5.7. Cumulative fossil energy demand (CED) and output fuel energy (OUT) are expressed as × 10^6 MJ/1,000 tons WCO and global warming potential (GWP) is expressed as 10^6 kg CO_2-equivalents/1,000 tons WCO.

Input (CED/GWP)	Operations	Direct	Heat	Upstream
CED-CTH	1,625,836	-447,771	583,780	1,489,773
CED-HRJ	2,539,483	-804,010	793,395	2,550,098
GWP-CTH	327,414	192,557	0	134,240
GWP-HRJ	356,414	137,451	0	218,686
Output (Fuel Energy)	**Naphtha**	**Diesel**	**Jet Fuel**	**Total**
OUT-CTH	9,485,084	4,720,114	15,716,052	29,921,250
OUT-HRJ	10,908,355	0	18,660,657	29,569,011

To facilitate analysis, it was important to note that CTH operation includes the pressurization energy required to pump WCO and isopropanol to the CTH reactor at 2-bar pressure, the cooling energy (negative energy) needed to cool reaction products in low-pressure flash unit, the distillation units (by heat integration), and the heat input. On the other hand, HRJ operations involved hydrogen pressurization energy in HY and HH units, assuming isentropic compression (85% efficient) and WCO pumping (95% efficient). It also included cooling energy in the flash separator, a high-pressure flash unit, a distillation column (exothermic conditions), and heat input. From a gross operations perspective, HRJ exhibits 1.6 times the CED of CTH. This was not surprising, given that it has greater upstream fossil energy brought about by the production, pressurization, and delivery of hydrogen. Gaseous hydrogen was primarily produced from stream reforming of natural gas. Isopropanol was the main upstream driver in CED of CTH, albeit of an insufficient amount to cause a higher CED of HRJ.

Direct CED of CTH and HRJ systems were negative; that is, surplus electricity was generated by the system. The energy generated from cooling the reactor was re-captured and utilized as in-process energy. HRJ operated at higher temperature than CTH, enabling larger energy release. It also had more reactor units. Consequently, HRJ's net heat consumption was 26% higher than

CTH's. HRJ's direct heat use comes from heating the oil from 380 to 400 °C plus the heat duty of the distillation column. Although the CTH consisted of two distillation units in series needing heating of WCO from 300 to 380 °C, the combined heat demand was still lower than HRJ's. Total CED was equal to operations CED plus infrastructure CED. The results suggest that the total CED for both systems is equal to their operations CED, due to the minuscule contributions of steel. Reactor steel demand for both systems is between 33-177 kg/yr, annualized over a 30-year period.

The results of operations GWP were consistent with the results of operations CED in both systems, i.e. operations GWP-CTH < operations GWP-HRJ; however, the difference was low, at around 8%. This result considers that the net GHG emissions has two components – direct GHG emissions and upstream GHG emissions. Both CTH and HRJ systems did not sequester CO_2 through co-product offsets because there was no biogenic carbon embodied in the final fuel, unlike jet fuel from algae or switchgrass. While it is true that some WCO are plant-based (olive oil, palm oil, soybean oil, or canola oil), others are animal-derived (butter, lard) or synthetic. In fact, even if this study assumed that all WCO were plant-derived, it is still outside its scope to identify which location produced waste olive oil or canola oil. Thus, this analysis does not consider carbon sequestration. Direct GHG emissions from CTH were higher than direct GHG emissions from HRJ, mainly due to higher CO_2 emissions from CTH reaction. Evidently, there are three moles of carbon in 2-propanol, while gaseous hydrogen has zero carbon. Hence, there is high propensity of some of the carbon from 2-propanol converting to CO_2 during the triglyceride reduction process. However, upstream GHG emissions from CTH were 26% lower than HRJ's, because of the considerable emissions associated with hydrogen production. Total GWP is equal to operations GWP, due to the insignificant GHG emissions associated with steel in the reactors.

Further, both CTH and HRJ systems had no heat offset, i.e. total heat use equals net heat use. The hydrodeoxygenation reaction in HRJ consumed more heat than the CTH reaction.

The conversion of 1,000 tons/day WCO generated approximately 60 x 10^6 MJ usable fuel energy in the form of jet fuel, naphtha, and diesel, from both the CTH and the HRJ systems. As is evident in the right pane of Figure 5.7, the relative magnitudes of these energies were similar, except that the HRJ reaction did not produce a diesel product. HRJ had a slightly lower total energy than CTH despite its higher jet fuel and naphtha production, because HRJ did not produce diesel. The EROI of both systems were calculated using total energy output and total energy input. EROI is the system's energy efficiency measured in terms of energy productivity normalized by energy expenditure. It is used as a decision tool in adapting any process from an energetic standpoint with EROI > 1 to be desirable (i.e. energy break-even =1, total energy output = total energy input). However, different EROIs can be calculated from the same dataset, as a result of dissimilar energy accounting methods [274]. In this study, EROI was evaluated as the ratio of the summation of all energy embodied in the main product and co-products plus surplus electricity (if any), and, the summation of net energy (if any), net heat, upstream energy, and infrastructure energy consumption. Although both energy platforms were energetically favorable, CTH's EROI was 1.8 times higher than HRJ's, attributable to its lower heat and upstream impacts.

Figure 5.8 shows that CTH had lower electricity and heat consumption than HRJ; in fact, CTH's negligible electricity use was credited to pressurization, while the rest of the sub-processes yielded in-process heat. Both systems had comparable direct heat use. Because CO_2 separation, high-pressure separation, and fractionation units in HJR operate at high temperatures, a large amount of heat was expended to the lower product temperature. HRJ's single fractionation unit consumed more than twice the electricity of CTH's.

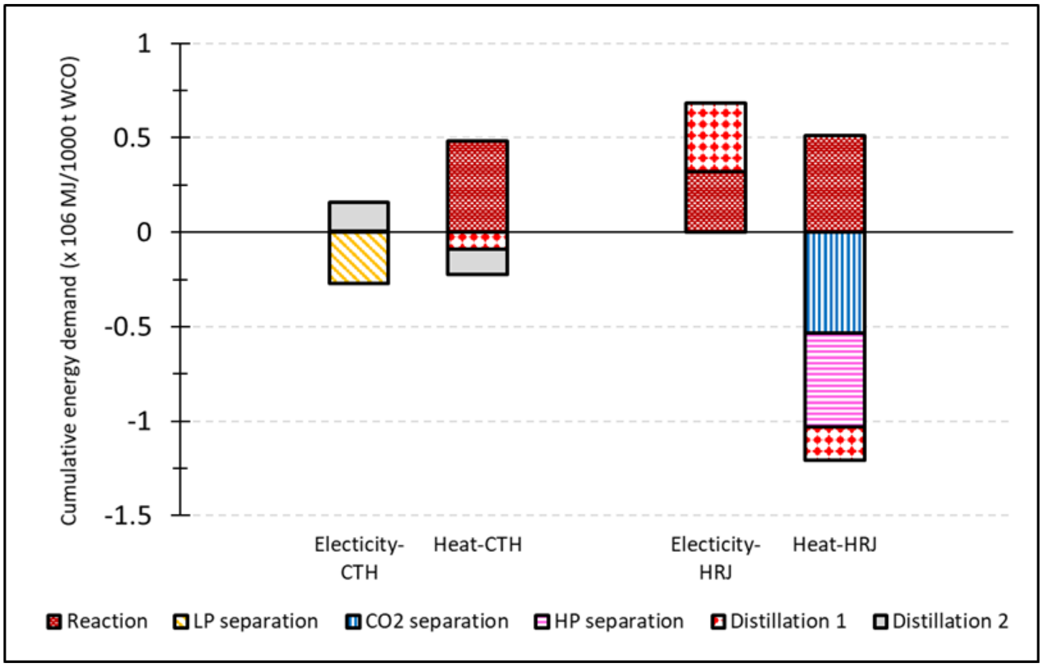

Figure 5.8. Electricity and heat use breakdown among sub-processes in the production of CTH- and HRJ-based biojet fuel from 1,000 tons WCO.

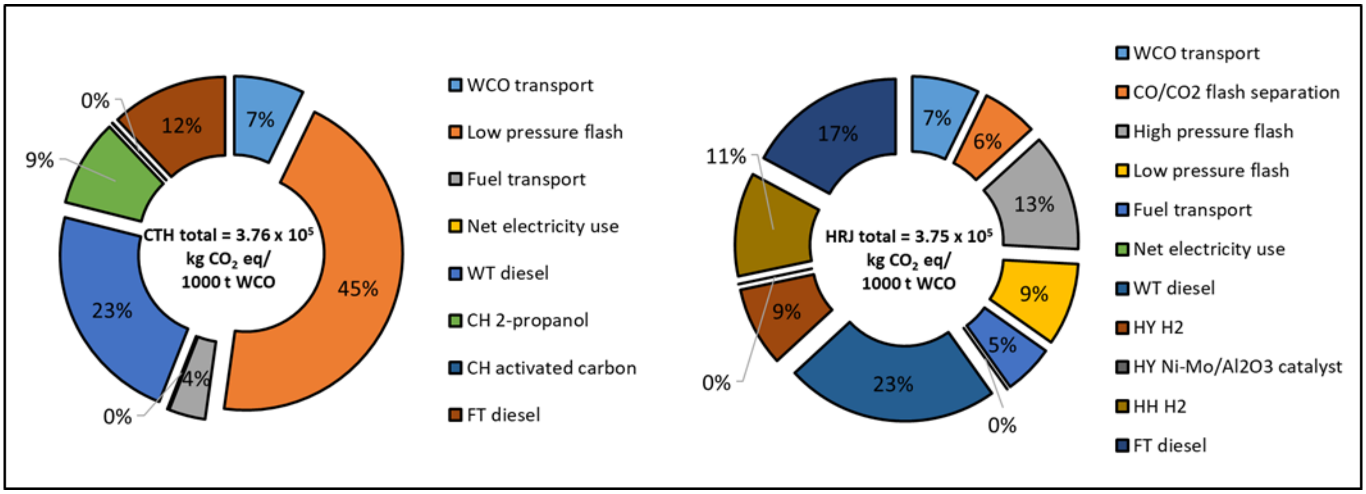

Figure 5.9. GWP breakdown among sub-processes in the production of CTH- and HRJ-based biojet fuel from 1,000 tons WCO.

The relative global warming potential (GWP) contributions reported as kg CO_2 equivalents/1,000 tons WCO of the different sub-processes for CTH and HRJ systems are presented in Figure 5.9. The results indicate that both systems create similar warming within 100 years (CTH=376,403. HRJ=375,420). CTH's GWP is dominated by emissions from low-pressure flash, while HRJ's is driven by WCO transport emissions. This is surprising, given that the CED of HRJ is 1.56 times that of the CED of CTH. A closer look at the GWP breakdown reveals that the main reaction in CTH produces half the GHG emissions of HRJ's main reaction. Nonetheless, the sum of GHG emissions associated with the sub-processes in CTH, except for WCO/fuel transport and diesel emissions, was higher than HRJ's by 33%. Beyond CTH's main reactor, the low-pressure flash generated the most emissions among all of the sub-processes, at 169,390 kg CO_2-eq/1,000 tons WCO. Such a phenomenon is associated with: (1) the atmospheric 3-phase (VLLE) flash unit following CTH that separates gaseous products from the liquid organic fraction and water, and (2) the large temperature differential in cooling the reaction products. The system has neither the provision for recouping this large emission for re-use, nor a method of sequestration. In contrast, emissions associated with low-pressure flash in HRJ were one-fifth that for CTH's, as exhibited by the stable reactor temperature of HRJ at 24 ^oC.

5.2.6. Effect of Allocation Method

The allocation methods were analyzed in the context of understanding the relative effect on CED and GWP (Figure 5.10). For CTH, the CED for main products via mass- and energy-allocations was in the order of millions, while the CED for main products via market-allocation was in the order of thousands. Conversely, the CED for co-products via mass- and energy-allocations were two orders of magnitude greater than the CED for co-products via market-allocation. This was due to mass rates (tons/day) corresponding to energy rates (MJ/day) and the LHVs (MJ/kg) among fuel products, and the fact that the co-products were close to each other (min = 42.791, max = 47.206). Yet, market-allocation was based on price ($/gal) and density (kg/m^3). Hence, the resulting allocation was remarkably different from the mass- and energy-allocations. In the case of CTH, 28.20 M$ was attributed to co-products, of which 28.17 M$ was generated by the sales of gaseous products (C1-C3 gas). Consequently, 98.33% was allocated to co-products, while only 1.67% was allocated to main products. A similar trend was observed in HRJ main products: 2.08 MMJ/1,000 tons WCO and 2.06 MMJ/1,000 tons WCO for mass- and energy-allocations, respectively, while 0.06 MMJ/1,000 tons WCO for market-allocation. In the case of co-products, mass- and energy-allocations were in the order of a hundred thousand, while market-allocation was in the order of millions. A similar trend was observed in GWP. From an environmental life cycle perspective, price and density have more pronounced effects on impact assessment than LHV. Because this analysis pertains to comparing an emerging energy platform to a more established conventional processing, reporting CED and GWP impacts based on the three allocation methods was vital.

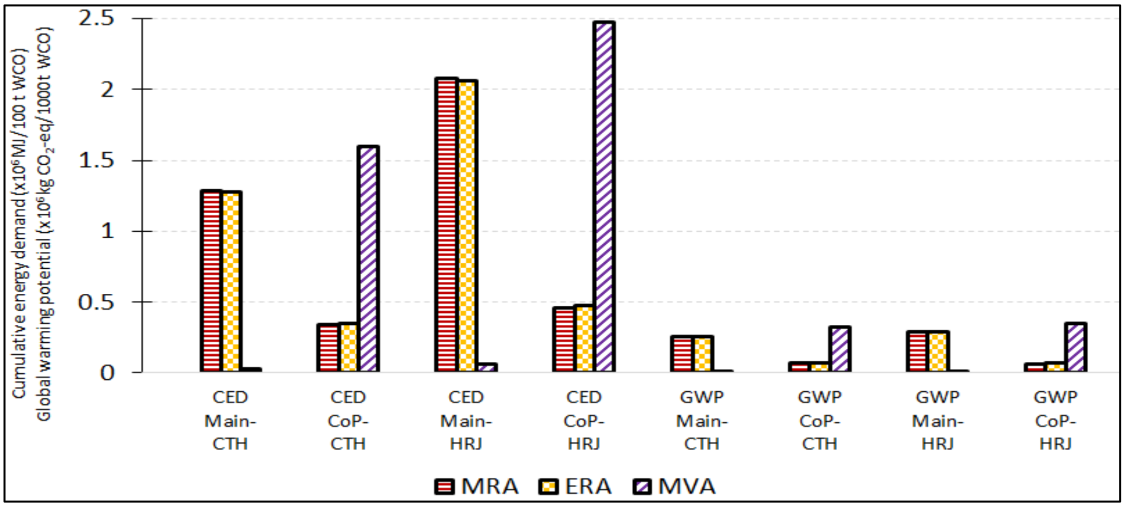

Figure 5.10. Analysis of CED and GWP in the production of CTH- and HRJ-based biojet fuel from 1,000 tons WCO using mass rate (MRA), energy rate (ERA), and market value (MVA) allocations.

5.2.7. Sensitivity

The construction of the CTH and HRJ models required the incorporation of materials and process inputs with distributions (“assumptions”) obtained from this study’s experimental results and from various literature sources (Table D35). The models also applied the equivalency factors in Table 5.3 during life cycle impacts assessment. These factors contain distributions. When analyzing a model, it is useful to know which input variables have the greatest impact on the model’s result (endpoint or forecast). The goal is to determine the driver of a forecast, while ignoring inconsequential inputs.

The tornado plots presented in Figure 5.11 are the result of independently testing each input variable one at a time against the target forecast, CED and GWP for CTH. The Monte Carlo simulation of the models utilized assumptions and generated several charts that depicted the relationships between the assumptions and the target. It is evident that CED and GWP of CTH were dependent on transportation – hauling of WCO/fuels and not on process parameters. For example, a 9% increase in truck mileage efficiency from the 5.50 mi/gal base case to the 6.05 mi/gal resulted in a 2.4% decrease in CED, from the median value of 0.0835 MJ/MJ WCO. The results revealed that, as the truck mileage efficiency increased, CED and GWP decreased; whereas, as distance hauled increased, both CED and GWP increased.

Of special case is the GHG emissions associated with the electricity equivalency factor (U.S. grid). The base case is 1.0220 kg/kWh and SD = 1. A 125% decrease in electricity equivalency factor resulted in a 68% increase in GWP (0.015 to 0.047 kg CO_2 eq/MJ WCO). Similarly, a 51% decrease in electricity equivalency factor caused a negligible increase in GWP (0.015 to 0.016 kg CO_2 eq/MJ WCO).

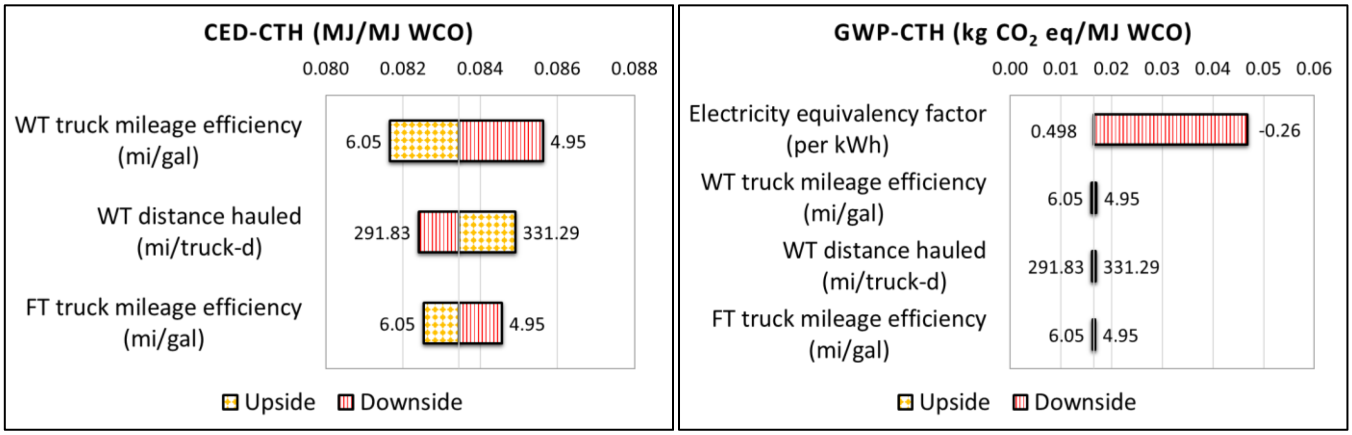

Figure 5.11. Tornado plots depicting drivers in CED and GWP of CTH. Dotted bars indicate +5-10% change in assumption from base case and lined bars indicate -5-10% change in assumption from base case. Bar labels show the test range for each input variable. Tornado method used is percentiles of the variables and test range is between 10% to 90%. Explained variation in forecast is cumulative.

Results of the sensitivity analysis highlighted two key findings: (1) fossil energy consumption and GWP are highly sensitive to externalities associated with transportation of WCO and fuels, and (2) the relative contributions of surface coal mining, transportation, and electricity generation to GWP are insignificant because the combined effects of these processes tend to amplify GHG emissions. The first finding has an advantage and a disadvantage. The advantage relates to the minimal influence of CTH's reaction chemistry on the environment, which allows any research and development to further enhance energy and emissions performance. The CTH-based biofuel plant did not require reconfigurations of the main reactor to cut costs, increase profits, and improve sustainability, other than those that were detailed in this analysis. Because the CED and GWP drivers are transportation-related and not process-related, the disadvantage would be the effect of diesel fuel used in heavy trucks on the circular bioeconomy, to the extent that diesel's volatile market creates a gap between any gain or loss incurred by the plant. Such a disadvantage would have a more pronounced impact on the TEA aspect than the environmental outcome.

Given the knowledge that the environmental impacts of CTH are driven by externalities, it is essential to examine the CTH model regarding variations in truck mileage efficiency and in distance hauled. There are two types of variations: uncertainty and variability. Uncertainty is the lack of pertinent information about the driver, while variability is the characteristic spread of the driver in a set of observations or population. Truck mileage efficiency has variability [259, 260], while distance hauled has uncertainty. The current state of the trucking industry in the U.S. has been essentially stable and, therefore, emphasis must be placed on distance traveled, which is a function of the study's scope. This analysis determined that the most optimal hauling distance is 300 mi/truck-d (6 h per truck per day at 50 miles/hr), obtained from the four-region, nine-division scheme (Section 5.2.5.1).

To capture CTH's energy outlook as a function of distance hauled and truck mileage efficiency across all regions using the process conditions and reaction chemistry described herein, a trend analysis on CTH's EROI was made on a single CTH-based biojet fuel plant. This plant was assumed to transition from HRJ to CTH in one year. The results are presented in Figure 5.12. HRJ's median EROI of 10.5 lay within the 25% certainty band (range: 10.4-10.6). In other words, HRJ will have a 25% probability of enhancing EROI to 10.6, from the median value of 10.5. It also has a 90% chance of improving EROI to 11.30, from the median value of 10.5. Clearly, the latitude on improvement (or deterioration) of energy efficiency through optimization in the HRJ system is limited (EROI=10.30-11.30). In contrast, the range by which CTH's EROI could be improved is quite wide, from 18.6 to a maximum of 25. This finding is significant, considering that, on a per volume WCO basis, CTH yields statistically equivalent biofuel energy as HRJ, expends half the fossil energy as HRJ, and creates 92% GWP of HRJ's. Despite isopropanol's high cost in the TEA (Section 5.3.3), it only accounts for 57% of CTH's total CED and, surprisingly, around 9% of CTH's total GWP.

The contributions between the CTH's main reaction system versus the HRJ's on EROI projections are evident in their individual CED. While isopropanol's CED represents 99% of CTH's main reaction system (activated carbon's CED is merely 1% of CTH's main reaction system and is assumed to be regenerated and replaced every 90 days), CTH reaction constitutes half the CED of HY and HH reactions combined. More importantly, isopropanol's CED in producing CTH biojet fuel is less than hydrogen's CED in producing HRJ biojet fuel by a factor of 0.5. Clearly, the environmental opportunities in using an alcohol-based solvent remarkably outweigh any cost barrier.

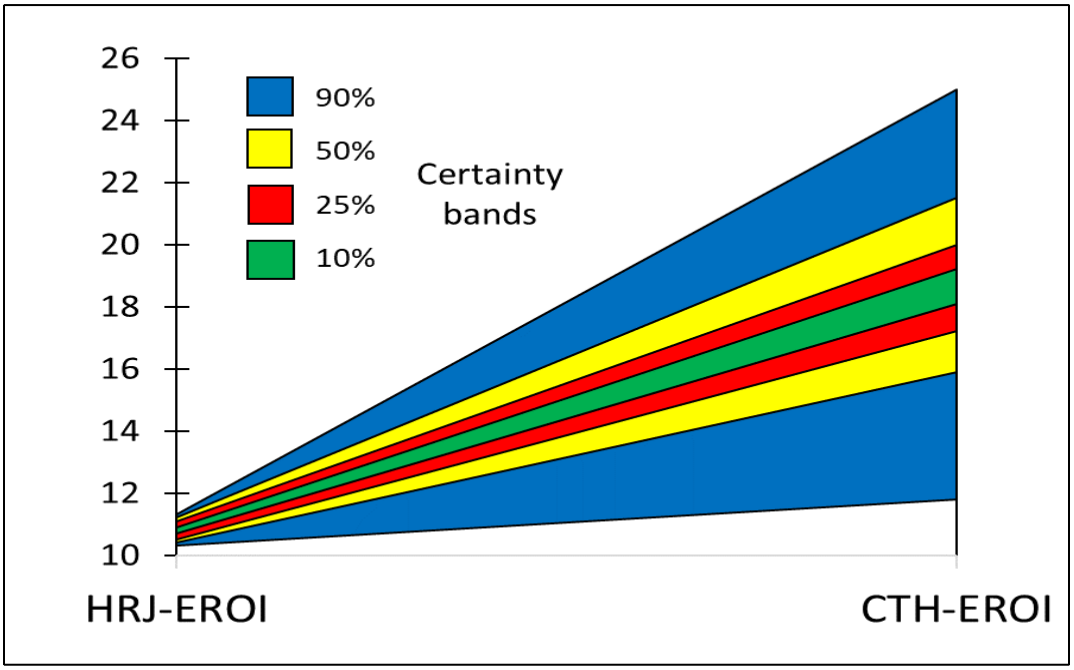

Figure 5.12. Trend chart showcasing the shift in EROI from HRJ to EROI at median EROI values (HRJ-EROI=10.5, CTH-EROI=18.6.

5.3. Conclusions

This study analyzed the techno-economic and environmental life-cycle implications of biojet fuel production from WCO via the CTH process. The results, then, were compared to the conventional HRJ process. The TEA demonstrates that the CTH process, based on experimental conditions, has the potential to be economically profitable despite the large input cost associated with isopropanol.

The LCA results reveal that the environmental opportunities in using an alcohol-based solvent remarkably outweigh any cost barriers. The latitude on the improvement (or the deterioration) of energy efficiency through optimization of CTH's process parameters are wide. Despite isopropanol's restrictive cost, CTH outperforms HRJ, regardless of the allocation method employed. The fossil energy consumption and the GWP are highly sensitive to externalities associated with transportation of WCO and fuels, and the relative contributions of surface coal mining, transportation, and electricity generation to GWP are insignificant because the combined effects of these processes tend to amplify GHG emissions.

5.4. Acknowledgements

This research did not receive any specific grant from funding agencies in the public, commercial, or not-for-profit sectors.

CHAPTER 6

RECOMMENDATION FOR FUTURE WORK

The purpose of this study was to explore the potential hydrogen-donating capacity of 2-propanol to reduce waste oil. However, the quantity of 2-propanol employed in all of the reactions was comparatively significant. Moreover, the catalyst employed in all the reaction was not exhaustively explored, as far as preparations and characterization were concerned.

In Chapter Two, 2-propanol was used the react with waste cooking oil by considering four reaction parameters: temperature, oil flow rate, WHSV, and pressure. Finally, the kinetics of the reaction were ascertained, in order to estimate reaction order, activation energy, and kinetic rate constant. As all but the temperature was kept constant, it is worthwhile to run optimization to assess the effect of the rest of the three parameters on the results. To minimize the volume of the 2-propanol used, it would be advisable to use aqueous 2-propanol, which might reduce the potential cost of production. Not much work has been done on the kinetics of catalyst deactivation. With a detailed assessment of catalyst deactivation study, stakeholders would be risk-free as they embark upon commercial scale CTH reactions.

Chapter Three employed a commercial catalyst doped with transition metals, which catalyzed the reaction between waste cooking oil and 2-propanol. Optimization of the reaction was studied by varying temperature, WHSV, pressure, and oil-2-propanol ratio. The percent of transition metal employed remained constant. It would be important to optimize the percent of transition metal used to dope the zeolite. As the modified catalyst could be amenable to deactivation, a thorough study could be undertaken to assess the catalyst deactivation kinetics. Also, it would be worthwhile to use aqueous 2-propanol at different concentrations to reduce the amount of 2-propanol per liter of oil used.

Chapter Four, on the other hand, explored the possibility of using oil-laden biofuel intermediate from flash hydrolyzed algae. The purpose was to utilize 2-propanol as oil extract and hydrogen donor in CTH reaction of the oil. It was observed that a considerable amount of 2-propanol was used in the CTH, leading to the production of branched and cyclo-alkanes. However, a significant level of gaseous products was produced, rendering the process unsustainable. It was proposed that process optimization could be employed to find the best oil-to-2-propanol ratio that would produce significant branched and cyclo-alkanes and low gaseous products. In addition, it is well-advised to optimize the amount catalyst, the percent metal precursors for doping.

Finally, Chapter Five thoroughly treated the technoeconomic and the environmental performance of the CTH reaction of waste cooking oil and 2-propanol. Results were compared to HRJ and it was concluded that HRJ, economically, performed better than CTH, due to significant amount of 2-propanol utilization. To reduce the operational cost, future work should focus on researching different hydrogen donors that are recyclable. Or, with the proposed exploration of aqueous 2-propanol, if viable, a thorough assessment of technoeconomic and environmental performance of CTH should be performed.

REFERENCES

[1] P. Zareh, A.A. Zare, B. Ghobadian, Comparative assessment of performance and emission characteristics of castor, coconut and waste cooking based biodiesel as fuel in a diesel engine, Energy 139 (2017) 883-894.
[2] E. U.S. Energy Information Administration, Annual Energy Outlook 2019 with Projections to 2050, 2019. file:///C:/Users/asiea/OneDrive/Documents/Reseach-Summer-2019/Dessertation/aeo2019.pdf. (Accessed August 10 2019).
[3] M. Balakrishnan, E.R. Sacia, S. Sreekumar, G. Gunbas, A.A. Gokhale, C.D. Scown, F.D. Toste, A.T. Bell, Novel pathways for fuels and lubricants from biomass optimized using life-cycle greenhouse gas assessment, Proceedings of the National Academy of Sciences of the United States of America 112(25) (2015) 7645-7649.
[4] ASTMD6751-12, Standard Specification for Biodiesel Fuel Blend Stock (B100) for Middle Distillate Fuels, ASTM International, West Conshohocken, PA, 2012.
[5] E. Committee on Propulsion and Energy Systems to Reduce Commercial Aviation Carbon Emissions; Aeronautics and Space Engineering Board; Division on Engineering and Physical Sciences; National Academies of Sciences, and Medicine, Sustainable Alternative Jet Fuels, Commercial Aircraft Propulsion and Energy Systems Research: Reducing Global Carbon Emissions,The National Academic Press, Washington D.C., 2016, pp. 72-108.

[6] I.E. Agency(IEA), World Energy Model, 2016. http://www.worldenergyoutlook.org/media/weowebsite/2016/WEM_Documentation_WEO2016.pdf. (Accessed March 29 2017).
[7] U.S.E.I. Administration(EIA), Annual Energy Outlook, 2017. https://www.eia.gov/outlooks/aeo/pdf/0383(2017).pdf. (Accessed April 1 2017).
[8] A.T.A.G. (ATAG), Aviation Benefits Beyond Borders, 2016. http://www.atag.org/component/downloads/downloads/346.html. (Accessed April 1 2017).
[9] X. Wu, P. Jiang, F. Jin, J. Liu, Y. Zhang, L. Zhu, T. Xia, K. Shao, T. Wang, Q. Li, Production of jet fuel range biofuels by catalytic transformation of triglycerides based oils, Fuel 188 (2017) 205-211.
[10] A. Talebian-Kiakalaieh, N.A.S. Amin, H. Mazaheri, A review on novel processes of biodiesel production from waste cooking oil, Applied Energy 104 (2013) 683-710.
[11] D. Pimentel, A. Marklein, M.A. Toth, M.N. Karpoff, G.S. Paul, R. McCormack, J. Kyriazis, T. Krueger, Food Versus Biofuels: Environmental and Economic Costs, Human Ecology 37(1) (2009) 1.
[12] S. Srinivasan, The food v. fuel debate: A nuanced view of incentive structures, Renewable Energy 34(4) (2009) 950-954.
[13] K.-R. Hwang, I.-H. Choi, H.-Y. Choi, J.-S. Han, K.-H. Lee, J.-S. Lee, Bio fuel production from crude Jatropha oil; addition effect of formic acid as an in-situ hydrogen source, Fuel 174 (2016) 107-113.
[14] J. Wang, P. Bi, Y. Zhang, H. Xue, P. Jiang, X. Wu, J. Liu, T. Wang, Q. Li, Preparation of jet fuel range hydrocarbons by catalytic transformation of bio-oil derived from fast pyrolysis of straw stalk, Energy 86 (2015) 488-499.
[15] I.-H. Choi, K.-R. Hwang, J.-S. Han, K.-H. Lee, J.S. Yun, J.-S. Lee, The direct production of jet-fuel from non-edible oil in a single-step process, Fuel 158 (2015) 98-104.
[16] J. Fu, C. Yang, J. Wu, J. Zhuang, Z. Hou, X. Lu, Direct production of aviation fuels from microalgae lipids in water, Fuel 139 (2015) 678-683.

[17] S.S. Lam, R.K. Liew, A. Jusoh, C.T. Chong, F.N. Ani, H.A. Chase, Progress in waste oil to sustainable energy, with emphasis on pyrolysis techniques, Renewable and Sustainable Energy Reviews 53 (2016) 741-753.

[18] H. Li, J. Zhao, Y. Huang, Z. Jiang, X. Yang, Z. Yang, Q. Chen, Investigation on the potential of waste cooking oil as a grinding aid in Portland cement, Journal of Environmental Management 184, Part 3 (2016) 545-551.

[19] K. Nanou, T. Roukas, Waste cooking oil: A new substrate for carotene production by Blakeslea trispora in submerged fermentation, Bioresource Technology 203 (2016) 198-203.

[20] Z.-X. Xu, P. Liu, G.-S. Xu, Q. Liu, Z.-X. He, Q. Wang, Bio-fuel oil characteristic from catalytic cracking of hydrogenated palm oil, Energy 133(Supplement C) (2017) 666-675.

[21] S. Senthur Prabu, M.A. Asokan, R. Roy, S. Francis, M.K. Sreelekh, Performance, combustion and emission characteristics of diesel engine fuelled with waste cooking oil bio-diesel/diesel blends with additives, Energy 122 (2017) 638-648.

[22] C.D. Mandolesi de Araújo, C.C. de Andrade, E. de Souza e Silva, F.A. Dupas, Biodiesel production from used cooking oil: A review, Renewable and Sustainable Energy Reviews 27(Supplement C) (2013) 445-452.

[23] A. Tangy, I.N. Pulidindi, N. Perkas, A. Gedanken, Continuous flow through a microwave oven for the large-scale production of biodiesel from waste cooking oil, Bioresource Technology 224 (2017) 333-341.

[24] D. Kubička, L. Kaluža, Deoxygenation of vegetable oils over sulfided Ni, Mo and NiMo catalysts, Applied Catalysis A: General 372(2) (2010) 199-208.

[25] K.-C. Ho, C.-L. Chen, P.-X. Hsiao, M.-S. Wu, C.-C. Huang, J.-S. Chang, Biodiesel Production from Waste Cooking Oil by Two-step Catalytic Conversion, Energy Procedia 61 (2014) 1302-1305.

[26] V. Itthibenchapong, A. Srifa, R. Kaewmeesri, P. Kidkhunthod, K. Faungnawakij, Deoxygenation of palm kernel oil to jet fuel-like hydrocarbons using Ni-MoS2/γ-Al2O3 catalysts, Energy Conversion and Management 134 (2017) 188-196.

[27] C. Detoni, F. Bertella, M.M.V.M. Souza, S.B.C. Pergher, D.A.G. Aranda, Palladium supported on clays to catalytic deoxygenation of soybean fatty acids, Applied Clay Science 95 (2014) 388-395.

[28] M. Herskowitz, M.V. Landau, Y. Reizner, D. Berger, A commercially-viable, one-step process for production of green diesel from soybean oil on Pt/SAPO-11, Fuel 111 (2013) 157-164.

[29] S.K. Kim, S. Brand, H.-s. Lee, Y. Kim, J. Kim, Production of renewable diesel by hydrotreatment of soybean oil: Effect of reaction parameters, Chemical Engineering Journal 228 (2013) 114-123.

[30] L. Li, Z. Ding, K. Li, J. Xu, F. Liu, S. Liu, S. Yu, C. Xie, X. Ge, Liquid hydrocarbon fuels from catalytic cracking of waste cooking oils using ultrastable zeolite USY as catalyst, Journal of Analytical and Applied Pyrolysis 117 (2016) 268-272.

[31] S. Bai, C. Chen, R. Luo, A. Chen, D. Li, Synthesis of MoO3/reduced graphene oxide hybrids and mechanism of enhancing H2S sensing performances, Sensors and Actuators B: Chemical 216 (2015) 113-120.

[32] Rogelio Sotelo-Boyás, F. Trejo-Zárraga, F.d.J. Hernández-Loyo, Chapter 8. Hydroconversion of Triglycerides into Green Liquid Fuel, First ed., IntechOpen Limited, London, UK. , 2012.

[33] M. Elsherif, Z.A. Manan, M.Z. Kamsah, State-of-the-art of hydrogen management in refinery and industrial process plants, Journal of Natural Gas Science and Engineering 24(Supplement C) (2015) 346-356.
[34] J.-G. Na, B.E. Yi, J.K. Han, Y.-K. Oh, J.-H. Park, T.S. Jung, S.S. Han, H.C. Yoon, J.-N. Kim, H. Lee, C.H. Ko, Deoxygenation of microalgal oil into hydrocarbon with precious metal catalysts: Optimization of reaction conditions and supports, Energy 47(1) (2012) 25-30.
[35] H. Zhang, H. Lin, Y. Zheng, The role of cobalt and nickel in deoxygenation of vegetable oils, Applied Catalysis B: Environmental 160-161(Supplement C) (2014) 415-422.
[36] D. Kubička, J. Horáček, M. Setnička, R. Bulánek, A. Zukal, I. Kubičková, Effect of support-active phase interactions on the catalyst activity and selectivity in deoxygenation of triglycerides, Applied Catalysis B: Environmental 145(Supplement C) (2014) 101-107.
[37] L. Chen, F. Zhang, G. Li, X. Li, Effect of Zn/Al ratio of Ni/ZnO-Al2O3 catalysts on the catalytic deoxygenation of oleic acid into alkane, Applied Catalysis A: General 529(Supplement C) (2017) 175-184.
[38] E. Agyenim-Boateng, S. Huang, J. Sheng, G. Yuan, Z. Wang, J. Zhou, A. Feng, Influence of laser peening on the hydrogen embrittlement resistance of 316L stainless steel, Surface and Coatings Technology 328(Supplement C) (2017) 44-53.
[39] T. Zhang, W. Zhao, Q. Deng, W. Jiang, Y. Wang, Y. Wang, W. Jiang, Effect of microstructure inhomogeneity on hydrogen embrittlement susceptibility of X80 welding HAZ under pressurized gaseous hydrogen, International Journal of Hydrogen Energy 42(39) (2017) 25102-25113.
[40] R. Bandyopadhyay, S. Upadhyayula, Thermodynamic analysis of diesel hydrotreating reactions, Fuel 214 (2018) 314-321.
[41] Y. Xiang, X. Li, C. Lu, L. Ma, Q. Zhang, Water-improved heterogeneous transfer hydrogenation using methanol as hydrogen donor over Pd-based catalyst, Applied Catalysis A: General 375(2) (2010) 289-294.
[42] Y. Zeng, Z. Wang, W. Lin, W. Song, In situ hydrodeoxygenation of phenol with liquid hydrogen donor over three supported noble-metal catalysts, Chemical Engineering Journal 320(Supplement C) (2017) 55-62.
[43] H. Shafaghat, P.S. Rezaei, W.M.A.W. Daud, Using decalin and tetralin as hydrogen source for transfer hydrogenation of renewable lignin-derived phenolics over activated carbon supported Pd and Pt catalysts, Journal of the Taiwan Institute of Chemical Engineers 65(Supplement C) (2016) 91-100.
[44] Z. Huang, S. Ding, Z. Li, H. Lin, F. Li, L. Li, Z. Zhong, C. Gao, C. Chen, Y. Li, Catalytic conversion of stearic acid to fuel oil in a hydrogen donor, International Journal of Hydrogen Energy 41(37) (2016) 16402-16414.
[45] L.O. Alemán-Vázquez, J.L.C. Domínguez, J.L. García-Gutiérrez, Effect of Tetralin, Decalin and Naphthalene as Hydrogen Donors in the Upgrading of Heavy Oils, Procedia Engineering 42(Supplement C) (2012) 532-539.
[46] A. Koriakin, S. Moon, D.-W. Kim, C.-H. Lee, Liquefaction of oil palm empty fruit bunch using sub- and supercritical tetralin, n-dodecane, and their mixture, Fuel 208(Supplement C) (2017) 184-192.
[47] D. He, I.T. Horváth, Application of silica-supported Shvo's catalysts for transfer hydrogenation of levulinic acid with formic acid, Journal of Organometallic Chemistry 847(Supplement C) (2017) 263-269.

[48] Z. Fu, Z. Wang, W. Lin, W. Song, S. Li, High efficient conversion of furfural to 2-methylfuran over Ni-Cu/Al2O3 catalyst with formic acid as a hydrogen donor, Applied Catalysis A: General 547(Supplement C) (2017) 248-255.
[49] A. Hart, C. Lewis, T. White, M. Greaves, J. Wood, Effect of cyclohexane as hydrogen-donor in ultradispersed catalytic upgrading of heavy oil, Fuel Processing Technology 138(Supplement C) (2015) 724-733.
[50] Y. Yan, L. Shi, Q. Liu, X. Shi, T. Wang, Q. Zhou, Z. Liu, W. Han, M. Li, Coke and radicals formation on a sulfided NiMo/γ-Al2O3 catalyst during hydroprocessing of an atmospheric residue in hydrogen donor media, Fuel Processing Technology 159(Supplement C) (2017) 404-411.
[51] M.V. Domínguez-Barroso, C. Herrera, M.A. Larrubia, L.J. Alemany, Diesel oil-like hydrocarbon production from vegetable oil in a single process over Pt–Ni/Al2O3 and Pd/C combined catalysts, Fuel Processing Technology 148(Supplement C) (2016) 110-116.
[52] A.E. Díaz-Álvarez, P. Crochet, V. Cadierno, Ruthenium-catalyzed reduction of allylic alcohols using glycerol as solvent and hydrogen donor, Catalysis Communications 13(1) (2011) 91-96.
[53] A. Wolfson, C. Dlugy, Y. Shotland, D. Tavor, Glycerol as solvent and hydrogen donor in transfer hydrogenation–dehydrogenation reactions, Tetrahedron Letters 50(43) (2009) 5951-5953.
[54] Y. Kamiya, S. Nagae, Relative reactivity of hydrogen donor solvent in coal liquefaction, Fuel 64(9) (1985) 1242-1245.
[55] K.M. Isa, T.A.T. Abdullah, U.F.M. Ali, Hydrogen donor solvents in liquefaction of biomass: A review, Renewable and Sustainable Energy Reviews (2017).
[56] A.S. Amarasekara, M.A. Hasan, Pd/C catalyzed conversion of levulinic acid to γ-valerolactone using alcohol as a hydrogen donor under microwave conditions, Catalysis Communications 60 (2015) 5-7.
[57] Intratec, Solutions, Chemical Pricing Data Store, 2017. https://www.intratec.us/indexes-and-pricing-data/chemicals-pricing-data-store. (Accessed 04/05/2018 2018).
[58] J. Eichman, A. Townsend, M. Melaina, Economic Assessment of Hydrogen Technologies Participating in California Electricity Markets National Renewable Energy Laboratory, Colorado, USA, February 2016.
[59] Califonia, Fuel, Cell, Partnership, Cost to Refill, 2018. https://cafcp.org/content/cost-refill. (Accessed 04/05/2018 2018).
[60] D. Sladkovskiy, L.I. Godina, K.V. Semikin, E.V. Sladkovskaya, D.A. Smirnova, D.Y. Murzin, Process design and techno-economical analysis of hydrogen production by aqueous phase reforming of sorbitol, Chemical Engineering Research and Design.
[61] F. Alonso, P. Riente, M. Yus, Transfer hydrogenation of olefins catalysed by nickel nanoparticles, Tetrahedron 65(51) (2009) 10637-10643.
[62] J.H. Northrop, L.H. Ashe, R.R. Morgan, A Fermentation Process for the Production of Acetone and Ethyl Alcohol, Journal of Industrial & Engineering Chemistry 11(8) (1919) 723-727.
[63] Y. Duan, M. Xu, X. Zhou, X. Huai, A structured packed-bed reactor designed for exothermic hydrogenation of acetone, Particuology 17 (2014) 125-130.
[64] J. Guo, X. Huai, X. Li, M. Xu, Performance analysis of Isopropanol–Acetone–Hydrogen chemical heat pump, Applied Energy 93 (2012) 261-267.

[65] D. Sun, Y. Yamada, S. Sato, Efficient production of propylene in the catalytic conversion of glycerol, Applied Catalysis B: Environmental 174-175 (2015) 13-20.
[66] Y. Xu, K.T. Chuang, A.R. Sanger, Design of a Process for Production of Isopropyl Alcohol by Hydration of Propylene in a Catalytic Distillation Column, Chemical Engineering Research and Design 80(6) (2002) 686-694.
[67] B.H. Bui, R.S. Zhu, M.C. Lin, Thermal decomposition of iso-propanol: First-principles prediction of total and product-branching rate constants, The Journal of Chemical Physics 117(24) (2002) 11188-11195.
[68] J.P. Ford, J.G. Immer, H.H. Lamb, Palladium Catalysts for Fatty Acid Deoxygenation: Influence of the Support and Fatty Acid Chain Length on Decarboxylation Kinetics, Topics in Catalysis 55(3) (2012) 175-184.
[69] M.R. Riazi, D. Charamonti, Biofuel Production and Processing Technology, First edition ed., Taylor & Francis Group, LLC, Boca Raton, Florida, USA, 2017.
[70] J.E.S. Seymour Lowell, Martin A. Thomas, Matthias Thommes, Characterization of Porous Solids and Powders: Surface Area, Pore Size and Density, 4th edition ed., Springer, The Netherlands, 2006.
[71] M. Toba, Y. Abe, H. Kuramochi, M. Osako, T. Mochizuki, Y. Yoshimura, Hydrodeoxygenation of waste vegetable oil over sulfide catalysts, Catalysis Today 164(1) (2011) 533-537.
[72] H. Zhang, H. Lin, W. Wang, Y. Zheng, P. Hu, Hydroprocessing of waste cooking oil over a dispersed nano catalyst: Kinetics study and temperature effect, Applied Catalysis B: Environmental 150-151(Supplement C) (2014) 238-248.
[73] S. Bezergianni, A. Dimitriadis, L.P. Chrysikou, Quality and sustainability comparison of one- vs. two-step catalytic hydroprocessing of waste cooking oil, Fuel 118(Supplement C) (2014) 300-307.
[74] G.A. Alsultan, N. Asikin-Mijan, H.V. Lee, A.S. Albazzaz, Y.H. Taufiq-Yap, Deoxygenation of waste cooking to renewable diesel over walnut shell-derived nanorode activated carbon supported CaO-La2O3 catalyst, Energy Conversion and Management 151(Supplement C) (2017) 311-323.
[75] J. Esmaeili, F. Rahimpour, Regeneration of spent nickel catalyst from hydrogenation process of edible oils: Heat treatment with hydrogen injection, International Journal of Hydrogen Energy 42(38) (2017) 24197-24204.
[76] S. Popov, S. Kumar, Rapid Hydrothermal Deoxygenation of Oleic Acid over Activated Carbon in a Continuous Flow Process, Energy & Fuels 29(5) (2015) 3377-3384.
[77] A.N. Kay Lup, F. Abnisa, W.M.A.W. Daud, M.K. Aroua, A review on reaction mechanisms of metal-catalyzed deoxygenation process in bio-oil model compounds, Applied Catalysis A: General 541(Supplement C) (2017) 87-106.
[78] L. Hermida, A.Z. Abdullah, A.R. Mohamed, Deoxygenation of fatty acid to produce diesel-like hydrocarbons: A review of process conditions, reaction kinetics and mechanism, Renewable and Sustainable Energy Reviews 42(Supplement C) (2015) 1223-1233.
[79] L.N. Silva, I.C.P. Fortes, F.P. de Sousa, V.M.D. Pasa, Biokerosene and green diesel from macauba oils via catalytic deoxygenation over Pd/C, Fuel 164(Supplement C) (2016) 329-338.
[80] S.K. Kim, J.Y. Han, S.-A. Hong, Y.-W. Lee, J. Kim, Supercritical CO2-purification of waste cooking oil for high-yield diesel-like hydrocarbons via catalytic hydrodeoxygenation, Fuel 111(Supplement C) (2013) 510-518.

[81] S.K. Kim, J.Y. Han, H.-s. Lee, T. Yum, Y. Kim, J. Kim, Production of renewable diesel via catalytic deoxygenation of natural triglycerides: Comprehensive understanding of reaction intermediates and hydrocarbons, Applied Energy 116 (2014) 199-205.
[82] S. Bezergianni, A. Dimitriadis, T. Sfetsas, A. Kalogianni, Hydrotreating of waste cooking oil for biodiesel production. Part II: Effect of temperature on hydrocarbon composition, Bioresource Technology 101(19) (2010) 7658-7660.
[83] ASTMD1655-19, Standard Specification for Aviation Turbine Fuels, ASTM International, West Conshohocken, PA, 2016, p. 5.
[84] ASTMD1319-18, Standard Test Method for Hydrocarbon Types in Liquid Petroleum Products by Fluorescent Indicator Adsorption, ASTM International, West Conshohocken, PA, USA., 2018.
[85] A.T. Madsen, E.H. Ahmed, C.H. Christensen, R. Fehrmann, A. Riisager, Hydrodeoxygenation of waste fat for diesel production: Study on model feed with Pt/alumina catalyst, Fuel 90(11) (2011) 3433-3438.
[86] U.S.D.o. Commerce., NIST Chemistry WebBook, 2017. https://webbook.nist.gov/cgi/cbook.cgi?ID=C57114&Units=SI&Mask=4#Thermo-Phase. (Accessed April 20, 2017 2017).
[87] F.O. Rice, R.E. Vollrath, The Thermal Decomposition of Acetone in the Gaseous State, Proceedings of the National Academy of Sciences of the United States of America 15(9) (1929) 702-705.
[88] H.S. Fogler, Elements of Chemical Reaction Engineering, 3rd ed., Prentice-Hall of India Private Limited, New Delhi, India, 2004.
[89] D.C. Montgomery, G.C. Runger., Applied Statistics and Probabiltiy for Engineers, 6th Edition ed., Willey, USA, 2014.
[90] A.K. Sinha, M. Anand, B.S. Rana, R. Kumar, S.A. Farooqui, M.G. Sibi, R. Kumar, R.K. Joshi, Development of Hydroprocessing Route to Transportation Fuels from Non-Edible Plant-Oils, Catalysis Surveys from Asia 17(1) (2013) 1-13.
[91] M. Anand, A.K. Sinha, Temperature-dependent reaction pathways for the anomalous hydrocracking of triglycerides in the presence of sulfided Co–Mo-catalyst, Bioresource Technology 126(Supplement C) (2012) 148-155.
[92] M. Anand, S.A. Farooqui, R. Kumar, R. Joshi, R. Kumar, M.G. Sibi, H. Singh, A.K. Sinha, Kinetics, thermodynamics and mechanisms for hydroprocessing of renewable oils, Applied Catalysis A: General 516 (2016) 144-152.
[93] M. Anand, S.A. Farooqui, R. Kumar, R. Joshi, R. Kumar, M.G. Sibi, H. Singh, A.K. Sinha, Kinetics, thermodynamics and mechanisms for hydroprocessing of renewable oils, Applied Catalysis A: General 516(Supplement C) (2016) 144-152.
[94] M. Snåre, I. Kubičková, P. Mäki-Arvela, K. Eränen, J. Wärnå, D.Y. Murzin, Production of diesel fuel from renewable feeds: Kinetics of ethyl stearate decarboxylation, Chemical Engineering Journal 134(1) (2007) 29-34.
[95] Y. Li, C. Zhang, Y. Liu, S. Tang, G. Chen, R. Zhang, X. Tang, Coke formation on the surface of Ni/HZSM-5 and Ni-Cu/HZSM-5 catalysts during bio-oil hydrodeoxygenation, Fuel 189(Supplement C) (2017) 23-31.
[96] M. Guisnet, L. Costa, F.R. Ribeiro, Prevention of zeolite deactivation by coking, Journal of Molecular Catalysis A: Chemical 305(1) (2009) 69-83.
[97] M. Guisnet, P. Magnoux, Organic chemistry of coke formation, Applied Catalysis A: General 212(1) (2001) 83-96.

[98] F. Wang, J. Xu, J. Jiang, P. Liu, F. Li, J. Ye, M. Zhou, Hydrotreatment of vegetable oil for green diesel over activated carbon supported molybdenum carbide catalyst, Fuel 216 (2018) 738-746.
[99] E.W. Qian, N. Chen, S. Gong, Role of support in deoxygenation and isomerization of methyl stearate over nickel–molybdenum catalysts, Journal of Molecular Catalysis A: Chemical 387 (2014) 76-85.
[100] A. Asiedu, E. Barbera, R. Naurzaliyev, A. Bertucco, S. Kumar, Waste cooking oil to jet-diesel fuel range using 2-propanol via catalytic transfer hydrogenation reactions, Biofuels (2019) 1-14.
[101] M.J.A. Romero, A. Pizzi, G. Toscano, G. Busca, B. Bosio, E. Arato, Deoxygenation of waste cooking oil and non-edible oil for the production of liquid hydrocarbon biofuels, Waste Management 47 (2016) 62-68.
[102] Z. Li, Z. Huang, S. Ding, F. Li, Z. Wang, H. Lin, C. Chen, Catalytic conversion of waste cooking oil to fuel oil: Catalyst design and effect of solvent, Energy 157 (2018) 270-277.
[103] S. Ding, Z. Li, F. Li, Z. Wang, J. Li, T. Zhao, H. Lin, C. Chen, Catalytic hydrogenation of stearic acid over reduced NiMo catalysts: Structure–activity relationship and effect of the hydrogen-donor, Applied Catalysis A: General 566 (2018) 146-154.
[104] H. Wang, L. Zhang, G. Li, K. Rogers, H. Lin, P. Seers, T. Ledan, S. Ng, Y. Zheng, Application of uniform design experimental method in waste cooking oil (WCO) co-hydroprocessing parameter optimization and reaction route investigation, Fuel 210(Supplement C) (2017) 390-397.
[105] H. Wang, G. Li, K. Rogers, H. Lin, Y. Zheng, S. Ng, Hydrotreating of waste cooking oil over supported CoMoS catalyst – Catalyst deactivation mechanism study, Molecular Catalysis 443 (2017) 228-240.
[106] H. Wang, H. Lin, Y. Zheng, S. Ng, H. Brown, Y. Xia, Kaolin-based catalyst as a triglyceride FCC upgrading catalyst with high deoxygenation, mild cracking, and low dehydrogenation performances, Catalysis Today 319 (2019) 164-171.
[107] J. Sani, A.M. Sokoto, A.D. Tambuwal, N.A. Garba, Effect of NiO/SiO2 on thermo-chemical conversion of waste cooking oil to hydrocarbons, Heliyon 3(5) (2017) e00304.
[108] E. Santillan-Jimenez, R. Loe, M. Garrett, T. Morgan, M. Crocker, Effect of Cu promotion on cracking and methanation during the Ni-catalyzed deoxygenation of waste lipids and hemp seed oil to fuel-like hydrocarbons, Catalysis Today 302 (2018) 261-271.
[109] T. Li, J. Cheng, R. Huang, J. Zhou, K. Cen, Conversion of waste cooking oil to jet biofuel with nickel-based mesoporous zeolite Y catalyst, Bioresource Technology 197(Supplement C) (2015) 289-294.
[110] I.-H. Choi, K.-R. Hwang, J.-S. Han, K.-H. Lee, J.S. Yun, J.-S. Lee, The direct production of jet-fuel from non-edible oil in a single-step process, Fuel 158(Supplement C) (2015) 98-104.
[111] M. Herskowitz, M.V. Landau, Y. Reizner, D. Berger, A commercially-viable, one-step process for production of green diesel from soybean oil on Pt/SAPO-11, Fuel 111(Supplement C) (2013) 157-164.
[112] M. Elsherif, Z.A. Manan, M.Z. Kamsah, State-of-the-art of hydrogen management in refinery and industrial process plants, Journal of Natural Gas Science and Engineering 24 (2015) 346-356.
[113] Y. Zeng, Z. Wang, W. Lin, W. Song, In situ hydrodeoxygenation of phenol with liquid hydrogen donor over three supported noble-metal catalysts, Chemical Engineering Journal 320 (2017) 55-62.

[114] K.M. Isa, T.A.T. Abdullah, U.F.M. Ali, Hydrogen donor solvents in liquefaction of biomass: A review, Renewable and Sustainable Energy Reviews 81(Part 1) (2018) 1259-1268.
[115] D.A. Sladkovskiy, L.I. Godina, K.V. Semikin, E.V. Sladkovskaya, D.A. Smirnova, D.Y. Murzin, Process design and techno-economical analysis of hydrogen production by aqueous phase reforming of sorbitol, Chemical Engineering Research and Design 134 (2018) 104-116.
[116] R. Tiwari, B.S. Rana, R. Kumar, D. Verma, R. Kumar, R.K. Joshi, M.O. Garg, A.K. Sinha, Hydrotreating and hydrocracking catalysts for processing of waste soya-oil and refinery-oil mixtures, Catalysis Communications 12(6) (2011) 559-562.
[117] O.İ. Şenol, T.R. Viljava, A.O.I. Krause, Hydrodeoxygenation of methyl esters on sulphided NiMo/γ-Al2O3 and CoMo/γ-Al2O3 catalysts, Catalysis Today 100(3) (2005) 331-335.
[118] H. Ge, X. Li, G. Wang, Z. Qin, Z. LÜ, J. Wang, Presulfidation of CoMo and NiMoP Catalysts by Ammonium Thiosulfate, Chinese Journal of Catalysis 31(1) (2010) 18-20.
[119] M. Shahinuzzaman, Z. Yaakob, Y. Ahmed, Non-sulphide zeolite catalyst for bio-jet-fuel conversion, Renewable and Sustainable Energy Reviews 77 (2017) 1375-1384.
[120] B. Veriansyah, J.Y. Han, S.K. Kim, S.-A. Hong, Y.J. Kim, J.S. Lim, Y.-W. Shu, S.-G. Oh, J. Kim, Production of renewable diesel by hydroprocessing of soybean oil: Effect of catalysts, Fuel 94(Supplement C) (2012) 578-585.
[121] A. Guzman, J.E. Torres, L.P. Prada, M.L. Nuñez, Hydroprocessing of crude palm oil at pilot plant scale, Catalysis Today 156(1) (2010) 38-43.
[122] W. Kiatkittipong, S. Phimsen, K. Kiatkittipong, S. Wongsakulphasatch, N. Laosiripojana, S. Assabumrungrat, Diesel-like hydrocarbon production from hydroprocessing of relevant refining palm oil, Fuel Processing Technology 116 (2013) 16-26.
[123] O.V. Kikhtyanin, A.E. Rubanov, A.B. Ayupov, G.V. Echevsky, Hydroconversion of sunflower oil on Pd/SAPO-31 catalyst, Fuel 89(10) (2010) 3085-3092.
[124] J. Hancsók, M. Krár, S. Magyar, L. Boda, A. Holló, D. Kalló, Investigation of the production of high cetane number bio gas oil from pre-hydrogenated vegetable oils over Pt/HZSM-22/Al2O3, Microporous and Mesoporous Materials 101(1) (2007) 148-152.
[125] A. Sonthalia, N. Kumar, Hydroprocessed vegetable oil as a fuel for transportation sector: A review, Journal of the Energy Institute (2017).
[126] A.K. Singh, K. Kondamudi, R. Yadav, S. Upadhyayula, A. Sakthivel, Uniform Mesoporous Silicoaluminophosphate Derived by Vapor Phase Treatment: Its Catalytic and Kinetic Studies in Hydroisomerization of 1-Octene, The Journal of Physical Chemistry C 118(48) (2014) 27961-27972.
[127] M. Ameen, M.T. Azizan, S. Yusup, A. Ramli, M. Yasir, Catalytic hydrodeoxygenation of triglycerides: An approach to clean diesel fuel production, Renewable and Sustainable Energy Reviews 80(Supplement C) (2017) 1072-1088.
[128] D. Verma, B.S. Rana, R. Kumar, M.G. Sibi, A.K. Sinha, Diesel and aviation kerosene with desired aromatics from hydroprocessing of jatropha oil over hydrogenation catalysts supported on hierarchical mesoporous SAPO-11, Applied Catalysis A: General 490(Supplement C) (2015) 108-116.
[129] M.Y. Smirnova, O.V. Kikhtyanin, M.Y. Smirnov, A.V. Kalinkin, A.I. Titkov, A.B. Ayupov, D.Y. Ermakov, Effect of calcination temperature on the properties of Pt/SAPO-31 catalyst in one-stage transformation of sunflower oil to green diesel, Applied Catalysis A: General 505 (2015) 524-531.

[130] C. Wang, Q. Liu, X. Liu, L. Yan, C. Luo, L. Wang, B. Wang, Z. Tian, Influence of reaction conditions on one-step hydrotreatment of lipids in the production of iso-alkanes over Pt/SAPO-11, Chinese Journal of Catalysis 34(6) (2013) 1128-1138.
[131] X. Li, Y. Chen, Y. Hao, X. Zhang, J. Du, A. Zhang, Optimization of aviation kerosene from one-step hydrotreatment of catalytic Jatropha oil over SDBS-Pt/SAPO-11 by response surface methodology, Renewable Energy 139 (2019) 551-559.
[132] Q. Liu, H. Zuo, T. Wang, L. Ma, Q. Zhang, One-step hydrodeoxygenation of palm oil to isomerized hydrocarbon fuels over Ni supported on nano-sized SAPO-11 catalysts, Applied Catalysis A: General 468(Supplement C) (2013) 68-74.
[133] P. Zhang, H. Liu, Y. Yue, H. Zhu, X. Bao, Direct synthesis of hierarchical SAPO-11 molecular sieve with enhanced hydroisomerization performance, Fuel Processing Technology 179 (2018) 72-85.
[134] A.K. Sinha, S. Sivasanker, Hydroisomerization of n-hexane over Pt–SAPO-11 and Pt–SAPO-31 molecular sieves, Catalysis Today 49(1) (1999) 293-302.
[135] T. Blasco, A. Chica, A. Corma, W.J. Murphy, J. Agúndez-Rodríguez, J. Pérez-Pariente, Changing the Si distribution in SAPO-11 by synthesis with surfactants improves the hydroisomerization/dewaxing properties, Journal of Catalysis 242(1) (2006) 153-161.
[136] M. Rabaev, M.V. Landau, R. Vidruk-Nehemya, A. Goldbourt, M. Herskowitz, Improvement of hydrothermal stability of Pt/SAPO-11 catalyst in hydrodeoxygenation–isomerization–aromatization of vegetable oil, Journal of Catalysis 332(Supplement C) (2015) 164-176.
[137] S. Gopal, P.G. Smirniotis, Factors affecting isomer yield for n-heptane hydroisomerization over as-synthesized and dealuminated zeolite catalysts loaded with platinum, Journal of Catalysis 225(2) (2004) 278-287.
[138] W. Zhang, P.G. Smirniotis, Effect of Zeolite Structure and Acidity on the Product Selectivity and Reaction Mechanism forn-Octane Hydroisomerization and Hydrocracking, Journal of Catalysis 182(2) (1999) 400-416.
[139] S. Thongkumkoon, W. Kiatkittipong, U.W. Hartley, N. Laosiripojana, P. Daorattanachai, Catalytic activity of trimetallic sulfided Re-Ni-Mo/γ-Al2O3 toward deoxygenation of palm feedstocks, Renewable Energy 140 (2019) 111-123.
[140] A.G. Bhavani, W.Y. Kim, J.Y. Kim, J.S. Lee, Improved activity and coke resistance by promoters of nanosized trimetallic catalysts for autothermal carbon dioxide reforming of methane, Applied Catalysis A: General 450 (2013) 63-72.
[141] H. Wu, G. Pantaleo, V. La Parola, A.M. Venezia, X. Collard, C. Aprile, L.F. Liotta, Bi- and trimetallic Ni catalysts over Al2O3 and Al2O3-MOx (M=Ce or Mg) oxides for methane dry reforming: Au and Pt additive effects, Applied Catalysis B: Environmental 156-157 (2014) 350-361.
[142] G. Sharma, D. Kumar, A. Kumar, A.a.H. Al-Muhtaseb, D. Pathania, M. Naushad, G.T. Mola, Revolution from monometallic to trimetallic nanoparticle composites, various synthesis methods and their applications: A review, Materials Science and Engineering: C 71 (2017) 1216-1230.
[143] M.K. Rath, K.-T. Lee, Superior electrochemical performance of non-precious Co-Ni-Mo alloy catalyst-impregnated Sr2FeMoO6-δ as an electrode material for symmetric solid oxide fuel cells, Electrochimica Acta 212 (2016) 678-685.

[144] A.N. Kay Lup, F. Abnisa, W.M.A. Wan Daud, M.K. Aroua, A review on reactivity and stability of heterogeneous metal catalysts for deoxygenation of bio-oil model compounds, Journal of Industrial and Engineering Chemistry 56(Supplement C) (2017) 1-34.
[145] ASTMD445-18, Standard Test Method for Kinematic Viscosity of Transparent and Opaque Liquids (and Calculation of Dynamic Viscosity), ASTM International, PA, USA, 2017.
[146] A. D3242-11, Standard Test Method for Acidity in Aviation Turbine Fuel, ASTM International, , West Conshohocken, PA, USA., 2017.
[147] A. D1298-12b, Standard Test Method for Density, Relative Density, or API Gravity of Crude Petroleum and Liquid Petroleum Products by Hydrometer Method, ASTM International, West Conshohocken, PA, USA., 2017.
[148] ASTMD5972-16, Standard Test Method for Freezing Point of Aviation Fuels (Automatic Phase Transition Method), ASTM International, West Conshohocken, PA, USA., 2016, p. 6.
[149] A. D445-18, Standard Test Method for Kinematic Viscosity of Transparent and Opaque Liquids (and Calculation of Dynamic Viscosity), ASTM International, West Conshohocken, PA, USA, 2018.
[150] ASTMD4529-17, Standard Test Method for Estimation of Net Heat of Combustion of Aviation Fuels, ASTM International, West Conshohocken, PA, 2017.
[151] J. Li, J. Liu, X. Sun, Y. Liu, The mathematical prediction model for the oxidative stability of vegetable oils by the main fatty acids composition and thermogravimetric analysis, LWT 96 (2018) 51-57.
[152] Q.-V. Bach, W.-H. Chen, Pyrolysis characteristics and kinetics of microalgae via thermogravimetric analysis (TGA): A state-of-the-art review, Bioresource Technology 246 (2017) 88-100.
[153] C. Gai, Y. Zhang, W.-T. Chen, P. Zhang, Y. Dong, Thermogravimetric and kinetic analysis of thermal decomposition characteristics of low-lipid microalgae, Bioresource Technology 150 (2013) 139-148.
[154] R. Font, M.D. Rey, Kinetics of olive oil pyrolysis, Journal of Analytical and Applied Pyrolysis 103 (2013) 181-188.
[155] R. Mutschler, E. Moioli, W. Luo, N. Gallandat, A. Züttel, CO2 hydrogenation reaction over pristine Fe, Co, Ni, Cu and Al2O3 supported Ru: Comparison and determination of the activation energies, Journal of Catalysis 366 (2018) 139-149.
[156] O.B. Ayodele, W.M.A.W. Daud, Optimization of catalytic hydrodeoxygenation of oleic acid into biofuel using fluoroplatinum oxalate zeolite supported catalyst, Journal of the Taiwan Institute of Chemical Engineers 47 (2015) 113-124.
[157] N. Asikin-Mijan, H.V. Lee, Y.H. Taufiq-Yap, G. Abdulkrem-Alsultan, M.S. Mastuli, H.C. Ong, Optimization study of SiO2-Al2O3 supported bifunctional acid–base NiO-CaO for renewable fuel production using response surface methodology, Energy Conversion and Management 141 (2017) 325-338.
[158] Z.-y. Jing, T.-q. Zhang, J.-w. Shang, M.-l. Zhai, H. Yang, C.-z. Qiao, X.-q. Ma, Influence of Cu and Mo components of γ-Al2O3 supported nickel catalysts on hydrodeoxygenation of fatty acid methyl esters to fuel-like hydrocarbons, Journal of Fuel Chemistry and Technology 46(4) (2018) 427-440.
[159] M.-G. Lee, J.-W. Park, S.-K. Kam, C.-H. Lee, Synthesis of Na-A zeolite from Jeju Island scoria using fusion/hydrothermal method, Chemosphere 207 (2018) 203-208.
[160] Y. Yu, G. Xiong, C. Li, F.-S. Xiao, Characterization of aluminosilicate zeolites by UV Raman spectroscopy, Microporous and Mesoporous Materials 46(1) (2001) 23-34.

[161] P.J. Reeve, H.J. Fallowfield, Natural and surfactant modified zeolites: A review of their applications for water remediation with a focus on surfactant desorption and toxicity towards microorganisms, Journal of Environmental Management 205 (2018) 253-261.
[162] E.B.G. Johnson, S.E. Arshad, Hydrothermally synthesized zeolites based on kaolinite: A review, Applied Clay Science 97-98 (2014) 215-221.
[163] O.B. Ayodele, H.F. Abbas, W.M.A.W. Daud, Catalytic upgrading of oleic acid into biofuel using Mo modified zeolite supported Ni oxalate catalyst functionalized with fluoride ion, Energy Conversion and Management 88 (2014) 1111-1119.
[164] J. Van Aelst, M. Haouas, E. Gobechiya, K. Houthoofd, A. Philippaerts, S.P. Sree, C.E.A. Kirschhock, P. Jacobs, J.A. Martens, B.F. Sels, F. Taulelle, Hierarchization of USY Zeolite by NH4OH. A Postsynthetic Process Investigated by NMR and XRD, The Journal of Physical Chemistry C 118(39) (2014) 22573-22582.
[165] A.K. Aboul-Gheit, M.S. El-Masry, A.E. Awadallah, Oxygen free conversion of natural gas to useful hydrocarbons and hydrogen over monometallic Mo and bimetallic Mo–Fe, Mo–Co or Mo–Ni/HZSM-5 catalysts prepared by mechanical mixing, Fuel Processing Technology 102 (2012) 24-29.
[166] S.R. Dhage, M.S. Hassan, O.B. Yang, Low temperature fabrication of hexagon shaped h-MoO3 nanorods and its phase transformation, Materials Chemistry and Physics 114(2) (2009) 511-514.
[167] A. Soultati, I. Kostis, P. Argitis, D. Dimotikali, S. Kennou, S. Gardelis, T. Speliotis, A.G. Kontos, D. Davazoglou, M. Vasilopoulou, Dehydration of molybdenum oxide hole extraction layers via microwave annealing for the improvement of efficiency and lifetime in organic solar cells, Journal of Materials Chemistry C 4(32) (2016) 7683-7694.
[168] M.M.Y.A. Alsaif, M.R. Field, B.J. Murdoch, T. Daeneke, K. Latham, A.F. Chrimes, A.S. Zoolfakar, S.P. Russo, J.Z. Ou, K. Kalantar-zadeh, Substoichiometric two-dimensional molybdenum oxide flakes: a plasmonic gas sensing platform, Nanoscale 6(21) (2014) 12780-12791.
[169] H. Mahandra, R. Singh, B. Gupta, Development of a hydrometallurgical route for the recovery of molybdenum from spent hydrodesulphurization catalyst using Cyphos IL 104, Journal of Industrial and Engineering Chemistry (2018).
[170] X. Liu, D. Wu, W. Ji, W. Hou, Uniform MoO2@carbon hollow nanospheres with superior lithium-ion storage properties, Journal of Materials Chemistry A 3(3) (2015) 968-972.
[171] L. Sharma, H.S. Khushwaha, A. Mathur, A. Halder, Role of molybdenum in Ni-MoO2 catalysts supported on reduced graphene oxide for temperature dependent hydrogen evolution reaction, Journal of Solid State Chemistry 265 (2018) 208-217.
[172] N.A. Stepashkin, M.K. Chernenko, V.D. Khripun, N.S. Ivanov, N.G. Sukhodolov, Electrochemical properties of Langmuir-Blodgett films containing cobalt hexacyanoferrate nanoparticles, Thin Solid Films 661 (2018) 1-6.
[173] A.K. Sharma, D. Sameerah, D. Charu, V. Utkarshaa, S. Ankur, Extraction of nickel nanoparticles from electroplating waste and their application in production of bio-diesel from biowaste, International Journal of Chemical Engineering and Applications 6(3) (2015) 156-159.
[174] S. Yedurkar, C. Maurya, P. Mahanwar, Biosynthesis of Zinc Oxide Nanoparticles Using Ixora Coccinea Leaf Extract¡ªA Green Approach, Open Journal of Synthesis Theory and Applications Vol.05No.01 (2016) 14.

[175] S. Zavareh, Z. Farrokhzad, F. Darvishi, Modification of zeolite 4A for use as an adsorbent for glyphosate and as an antibacterial agent for water, Ecotoxicology and Environmental Safety 155 (2018) 1-8.
[176] X. Guo, A. Navrotsky, Hydration dynamics in zeolite A – An X-ray diffraction and infrared spectroscopic study, Microporous and Mesoporous Materials 268 (2018) 197-201.
[177] Y. Zhou, W. Chen, P. Wang, Y. Zhang, EMT-type zeolite for deep purification of trace polar-oxygenated compounds from light olefins, Microporous and Mesoporous Materials 271 (2018) 273-283.
[178] A. Ates, Effect of alkali-treatment on the characteristics of natural zeolites with different compositions, Journal of Colloid and Interface Science 523 (2018) 266-281.
[179] A.I. McNab, A.J. McCue, D. Dionisi, J.A. Anderson, Quantification and qualification by in-situ FTIR of species formed on supported-cobalt catalysts during the Fischer-Tropsch reaction, Journal of Catalysis 353 (2017) 286-294.
[180] M.A.T. J.E.S. Seymour Lowell, Matthias Thommes Characterization of Porous Solids and Powders: Surface Area, Pore Size and Density, 4th edition ed., Springer, The Netherlands, 2006.
[181] H.S. Fogler, Elements of Chemical Reaction Engineering, 2nd ed., Prentice Hall International, New Jessy, USA, 1992.
[182] E. Epelde, A.T. Aguayo, M. Olazar, J. Bilbao, A.G. Gayubo, Kinetic Model for the Transformation of 1-Butene on a K-Modified HZSM-5 Catalyst, Industrial & Engineering Chemistry Research 53(26) (2014) 10599-10607.
[183] E.-M. Ryymin, M.L. Honkela, T.-R. Viljava, A.O.I. Krause, Insight to sulfur species in the hydrodeoxygenation of aliphatic esters over sulfided NiMo/γ-Al2O3 catalyst, Applied Catalysis A: General 358(1) (2009) 42-48.
[184] P. Arora, H. Ojagh, J. Woo, E. Lind Grennfelt, L. Olsson, D. Creaser, Investigating the effect of Fe as a poison for catalytic HDO over sulfided NiMo alumina catalysts, Applied Catalysis B: Environmental 227 (2018) 240-251.
[185] H. Ojagh, D. Creaser, S. Tamm, P. Arora, S. Nyström, E. Lind Grennfelt, L. Olsson, Effect of Dimethyl Disulfide on Activity of NiMo Based Catalysts Used in Hydrodeoxygenation of Oleic Acid, Industrial & Engineering Chemistry Research 56(19) (2017) 5547-5557.
[186] J.M. Anthonykutty, J. Linnekoski, A. Harlin, J. Lehtonen, Hydrotreating reactions of tall oils over commercial NiMo catalyst, Energy Science & Engineering 3(4) (2015) 286-299.
[187] J. Hu, W.B. Li, R.F. Liu, Highly efficient copper-doped manganese oxide nanorod catalysts derived from CuMnO hierarchical nanowire for catalytic combustion of VOCs, Catalysis Today 314 (2018) 147-153.
[188] J. Cheng, Y. Zhang, T. Wang, H. Xu, P. Norris, W.-P. Pan, Emission of volatile organic compounds (VOCs) during coal combustion at different heating rates, Fuel 225 (2018) 554-562.
[189] S.K. Kim, J.Y. Han, H.-s. Lee, T. Yum, Y. Kim, J. Kim, Production of renewable diesel via catalytic deoxygenation of natural triglycerides: Comprehensive understanding of reaction intermediates and hydrocarbons, Applied Energy 116(Supplement C) (2014) 199-205.
[190] S. Bilgiç-Keleş, N. Şahin-Yeşilçubuk, A. Barla-Demirkoz, M. Karakaş, Response surface optimization and modelling for supercritical carbon dioxide extraction of Echium vulgare seed oil, The Journal of Supercritical Fluids 143 (2019) 365-369.
[191] ASTMD7566-19, Standard Specification for Aviation Turbine Fuel Containing Synthesized Hydrocarbons, ASTM International, PA, USA, 2016, p. 6.
[192] J. Ancheyta, Processes and Reactors for Upgrading of Heavy Petroleum, Taylor & Francis Group, CRC Press, Florida, USA, 2013.

[193] U.S.E.I.A. (USEIA), Transportation Sector Energy Consumption, 2019. https://www.eia.gov/totalenergy/data/browser/?tbl=T02.05#/?f=A&start=1949&end=2018&charted=3-4-7. (Accessed May 12, 2019 2019).
[194] U.S.E.I.A. (USEIA), Annual Energy Outlook 2019, 2019. https://www.eia.gov/outlooks/aeo/data/browser/#/?id=7-AEO2019&region=0-0&cases=ref2019&start=2017&end=2050&f=A&linechart=ref2019-d111618a.5-7-AEO2019~~~ref2019-d111618a.14-7-AEO2019~ref2019-d111618a.71-7-AEO2019&ctype=linechart&sid=ref2019-d111618a.71-7-AEO2019~ref2019-d111618a.14-7-AEO2019&sourcekey=0. (Accessed May 13, 2019 2019).
[195] Statista, Transportation & Logistics, 2019. https://www.statista.com/statistics/655057/fuel-consumption-of-airlines-worldwide/. (Accessed May 14, 2019 2019).
[196] W. Tian, R. Liu, W. Wang, Z. Yin, X. Yi, Effect of operating conditions on hydrothermal liquefaction of Spirulina over Ni/TiO2 catalyst, Bioresource Technology 263 (2018) 569-575.
[197] F. Liu, P. Lane, J.C. Hewson, V. Stavila, M.B. Tran-Gyamfi, M. Hamel, T.W. Lane, R.W. Davis, Development of a closed-loop process for fusel alcohol production and nutrient recycling from microalgae biomass, Bioresource Technology (2019).
[198] B. Zhu, G. Chen, X. Cao, D. Wei, Molecular characterization of CO2 sequestration and assimilation in microalgae and its biotechnological applications, Bioresource Technology 244 (2017) 1207-1215.
[199] C. Song, J. Liu, M. Xie, Y. Qiu, G. Chen, Y. Qi, Y. Kitamura, Intensification of a novel absorption-microalgae hybrid CO2 utilization process via fed-batch mode optimization, International Journal of Greenhouse Gas Control 82 (2019) 1-7.
[200] T.C.d. Assis, M.L. Calijuri, P.P. Assemany, A.S.A.d.P. Pereira, M.A. Martins, Using atmospheric emissions as CO2 source in the cultivation of microalgae: Productivity and economic viability, Journal of Cleaner Production 215 (2019) 1160-1169.
[201] W.Y. Cheah, P.L. Show, J.-S. Chang, T.C. Ling, J.C. Juan, Biosequestration of atmospheric CO2 and flue gas-containing CO2 by microalgae, Bioresource Technology 184 (2015) 190-201.
[202] A. Xia, Z. Hu, Q. Liao, Y. Huang, X. Zhu, W. Ye, Y. Sun, Enhancement of CO2 transfer and microalgae growth by perforated inverted arc trough internals in a flat-plate photobioreactor, Bioresource Technology 269 (2018) 292-299.
[203] S.A. Razzak, S.A.M. Ali, M.M. Hossain, H. deLasa, Biological CO2 fixation with production of microalgae in wastewater – A review, Renewable and Sustainable Energy Reviews 76 (2017) 379-390.
[204] I. Durán, F. Rubiera, C. Pevida, Microalgae: Potential precursors of CO2 adsorbents, Journal of CO2 Utilization 26 (2018) 454-464.
[205] C. Sepulveda, C. Gómez, N. El Bahraoui, G. Acién, Comparative evaluation of microalgae strains for CO2 capture purposes, Journal of CO2 Utilization 30 (2019) 158-167.
[206] Y. Guo, Z. Yuan, J. Xu, Z. Wang, T. Yuan, W. Zhou, J. Xu, C. Liang, H. Xu, S. Liu, Metabolic acclimation mechanism in microalgae developed for CO2 capture from industrial flue gas, Algal Research 26 (2017) 225-233.
[207] H.-Y. Wang, D. Bluck, B.J. Van Wie, Conversion of microalgae to jet fuel: Process design and simulation, Bioresource Technology 167 (2014) 349-357.
[208] J. Cheng, Z. Zhang, X. Zhang, Z. Fan, J. Liu, J. Zhou, Continuous hydroprocessing of microalgae biodiesel to jet fuel range hydrocarbons promoted by Ni/hierarchical mesoporous Y zeolite catalyst, International Journal of Hydrogen Energy 44(23) (2019) 11765-11773.

[209] J.K. Bwapwa, A. Anandraj, C. Trois, Possibilities for conversion of microalgae oil into aviation fuel: A review, Renewable and Sustainable Energy Reviews 80 (2017) 1345-1354.
[210] J. Cheng, Z. Zhang, X. Zhang, J. Liu, J. Zhou, K. Cen, Hydrodeoxygenation and hydrocracking of microalgae biodiesel to produce jet biofuel over H3PW12O40-Ni/hierarchical mesoporous zeolite Y catalyst, Fuel 245 (2019) 384-391.
[211] M.L. Menegazzo, G.G. Fonseca, Biomass recovery and lipid extraction processes for microalgae biofuels production: A review, Renewable and Sustainable Energy Reviews 107 (2019) 87-107.
[212] D. López Barreiro, W. Prins, F. Ronsse, W. Brilman, Hydrothermal liquefaction (HTL) of microalgae for biofuel production: State of the art review and future prospects, Biomass and Bioenergy 53 (2013) 113-127.
[213] F. Wanignon Ferdinand, L. Van de Steene, K. Kamenan Blaise, T. Siaka, Prediction of pyrolysis oils higher heating value with gas chromatography–mass spectrometry, Fuel 96 (2012) 141-145.
[214] X. Yuan, J. Wang, G. Zeng, H. Huang, X. Pei, H. Li, Z. Liu, M. Cong, Comparative studies of thermochemical liquefaction characteristics of microalgae using different organic solvents, Energy 36(11) (2011) 6406-6412.
[215] A. Teymouri, K.J. Adams, T. Dong, S. Kumar, Evaluation of lipid extractability after flash hydrolysis of algae, Fuel 224 (2018) 23-31.
[216] J.L. Garcia-Moscoso, W. Obeid, S. Kumar, P.G. Hatcher, Flash hydrolysis of microalgae (Scenedesmus sp.) for protein extraction and production of biofuels intermediates, The Journal of Supercritical Fluids 82 (2013) 183-190.
[217] A. Asiedu, S. Kumar, Kinetics and Optimization of Catalytic Transfer Hydrogenation of WCO Using 2-propanol as H-donor over NiOx-MoOx-CoOx/Zeolite, Industrial & Engineering Chemistry Research (2019).
[218] N.T.T. Tran, Y. Uemura, S. Chowdhury, A. Ramli, Vapor-phase hydrodeoxygenation of guaiacol on Al-MCM-41 supported Ni and Co catalysts, Applied Catalysis A: General 512 (2016) 93-100.
[219] P.M. Mortensen, H.W.P. de Carvalho, J.-D. Grunwaldt, P.A. Jensen, A.D. Jensen, Activity and stability of Mo2C/ZrO2 as catalyst for hydrodeoxygenation of mixtures of phenol and 1-octanol, Journal of Catalysis 328 (2015) 208-215.
[220] K. Azizi, A. Moshfegh Haghighi, M. Keshavarz Moraveji, M. Olazar, G. Lopez, Co-pyrolysis of binary and ternary mixtures of microalgae, wood and waste tires through TGA, Renewable Energy 142 (2019) 264-271.
[221] M. González-Cabrera, A. Domínguez-Vidal, M.J. Ayora-Cañada, Hyperspectral FTIR imaging of olive fruit for understanding ripening processes, Postharvest Biology and Technology 145 (2018) 74-82.
[222] J. Wang, X. Ma, Z. Yu, X. Peng, Y. Lin, Studies on thermal decomposition behaviors of demineralized low-lipid microalgae by TG-FTIR, Thermochimica Acta 660 (2018) 101-109.
[223] Y. Zhang, X. Kong, Z. Wang, Y. Sun, S. Zhu, L. Li, P. Lv, Optimization of enzymatic hydrolysis for effective lipid extraction from microalgae Scenedesmus sp, Renewable Energy 125 (2018) 1049-1057.
[224] M.A. Kassim, K. Kirtania, D. De La Cruz, N. Cura, S.C. Srivatsa, S. Bhattacharya, Thermogravimetric analysis and kinetic characterization of lipid-extracted Tetraselmis suecica and Chlorella sp, Algal Research 6 (2014) 39-45.

[225] D. Valencia, L. Díaz, L.F. Ramírez-Verduzco, M.A. Amezcua-Allieri, J. Aburto, MoO3-based catalysts supported on SiO2 and their performance in hydrodeoxygenation, Materials Letters 251 (2019) 226-229.
[226] I.-I.E. Agency:, WEO 2018 Special Report Outlook for Producer Economies 2018. https://webstore.iea.org/world-energy-outlook-2018 (Accessed December 20 2018).
[227] E.-U.S.E.I. Administration, Annual Energy Outlook 2019 with projections to 2050, 2019. https://www.eia.gov/outlooks/aeo/pdf/aeo2019.pdf (Accessed August 22 2019).
[228] A.T.A.G. (ATAG), Aviation Benefits Beyond Borders 2016. (Accessed Agust 25 2019).
[229] L.T. Wei-Cheng Wang, Jennifer Markham, Yanan Zhang, Eric Tan, Liaw Batan, Ethan Warner, and Mary Biddy Review of biojet fuel conversion technologies, 2016. https://www.nrel.gov/docs/fy16osti/66291.pdf. (Accessed August 21 2019).
[230] M.G. Kulkarni, A.K. Dalai, Waste Cooking OilAn Economical Source for Biodiesel: A Review, Industrial & Engineering Chemistry Research 45(9) (2006) 2901-2913.
[231] G. Liu, B. Yan, G. Chen, Technical review on jet fuel production, Renewable and Sustainable Energy Reviews 25(Supplement C) (2013) 59-70.
[232] S. Popov, S. Kumar, Renewable fuels via catalytic hydrodeoxygenation of lipid-based feedstocks, Biofuels 4(2) (2013) 219-239.
[233] T.N. Kalnes, M.M. McCall, D.R. Shonnard, Chapter 18 Renewable Diesel and Jet-Fuel Production from Fats and Oils, Thermochemical Conversion of Biomass to Liquid Fuels and Chemicals, The Royal Society of Chemistry2010, pp. 468-495.
[234] J.A.K. Michael J. McCall, Alakananda Bhattacharyya, Tom N. Kalnes, Timothy A. Brandvold, Production of aviation fuel from renewable feedstock, 2011.
[235] T.L.M. John A Petri, Production of diesel fuel from biorenewable feedstocks, 2009.
[236] O.J. Guerra, G.A.C. Le Roux, Improvements in Petroleum Refinery Planning: 2. Case Studies, Industrial & Engineering Chemistry Research 50(23) (2011) 13419-13426.
[237] P.L. Chu, C. Vanderghem, H.L. MacLean, B.A. Saville, Process modeling of hydrodeoxygenation to produce renewable jet fuel and other hydrocarbon fuels, Fuel 196(Supplement C) (2017) 298-305.
[238] M. Rigutto, Cracking and Hydrocracking, Zeolites and Catalysis2010, pp. 547-584.
[239] G. Valavarasu, M. Bhaskar, K.S. Balaraman, Mild Hydrocracking—A Review of the Process, Catalysts, Reactions, Kinetics, and Advantages, Petroleum Science and Technology 21(7-8) (2003) 1185-1205.
[240] J. Han, A. Elgowainy, H. Cai, M.Q. Wang, Life-cycle analysis of bio-based aviation fuels, Bioresource Technology 150 (2013) 447-456.
[241] G.E.H. James H. Gary, Mark J. Kaiser, Petroleum Refining: Technology and Economics, Fifth Edition 5th Edition, Fifth Edition ed., CRC Press2007.
[242] S. Peramanu, B.G. Cox, B.B. Pruden, Economics of hydrogen recovery processes for the purification of hydroprocessor purge and off-gases, International Journal of Hydrogen Energy 24(5) (1999) 405-424.
[243] R.S. Gavin Towler, Chemical engineering design: Principles, practice and economics of plant and process design, Second Edition ed., Butterworth-Heinemann, MA, USA, 2012.
[244] R.C.B. Richard Turton, Wallace B. Whiting, Joseph A. Shaeiwitz, Debangsu Bhattacharyya, Analysis, Synthesis and Design of Chemical Processes, Fourth Edition ed., Prentice-Hall, Michigan, USA 2012.

[245] B.P.S. C. San Marchi, Technical reference for hydrogen compatibility of materials, 2012. https://energy.sandia.gov/wp-content//gallery/uploads/SAND2012_7321.pdf. (Accessed July 15 2019).
[246] V.V. Ranade, R.V. Chaudhari, P.R. Gunjal, Chapter 3 - Reaction Engineering of Trickle Bed Reactors, in: V.V. Ranade, R.V. Chaudhari, P.R. Gunjal (Eds.), Trickle Bed Reactors, Elsevier, Amsterdam, 2011, pp. 77-116.
[247] G.E.W. Ruppel, Catalytic Fixed-Bed Reactors, Ullmann's Encyclopedia of Industrial Chemistry2012.
[248] C.C. Herron Jr., B.K. Kruelskie, J.R. Fair, Hydrodynamics and mass transfer on three-phase distillation trays, AIChE Journal 34(8) (1988) 1267-1274.
[249] P.T.V. Gael D. Ulrich, How to Estimate Utility Costs 2006. https://www.chemengonline.com/how-to-estimate-utility-costs/?printmode=1.
[250] M. Pearlson, C. Wollersheim, J. Hileman, A techno-economic review of hydroprocessed renewable esters and fatty acids for jet fuel production, Biofuels, Bioproducts and Biorefining 7(1) (2013) 89-96.
[251] F. Mueller-Langer, E. Tzimas, K. Martin, S. Peteves, Techno-Economic Assessment of Hydrogen Production Processes for the Hydrogen Economy for the Short and Medium Term, International Journal of Hydrogen Energy 32 (2007) 3797-3810.
[252] I. Independent Chemical Information Services, 2018. https://www.icis.com. (Accessed March 06 2018).
[253] B. U.S. Bureau of Labor Statistics, 2018. https://www.bls.gov/home.htm. (Accessed March 15 2018).
[254] E. U.S. Energy Information Administration. https://www.eia.gov/. (Accessed March 06 2018).
[255] A. Radich, Biodiesel Peerformance, Costs, and Use. http://large.stanford.edu/courses/2011/ph240/garcia1/docs/biodiesel.pdf. (Accessed April 20 2006).
[256] W.p. review, The 200 largest cities in the United States by population 2019”, (2019), 2019. http://worldpopulationreview.com/us-cities/. (Accessed April 4 2019).
[257] A. Miller, Determining the rate of used cooking oil output by the restaurant industry in the Salt Lake Valley, UT, 2007. https://pdfs.semanticscholar.org/df64/5451e44cf04e4e6946020554b922cd182797.pdf
[258] L.A. Nelson, T.A. Foglia, W.N. Marmer, Lipase-Catalyzed Production of Biodiesel, J. Am. Oil Chem. Soc. 73(8) (1996) 1191.
[259] R. T. E, Commercial medium- and heavy-duty truck fuel efficiency technology study - Report #1, 2015. https://www.nhtsa.gov/sites/nhtsa.dot.gov/files/812146-commercialmdhd-truckfuelefficiencytechstudy-v2.pdf
[260] GEOTAB, The state of fuel economy in trucking. https://www.geotab.com/truck-mpg-benchmark/. (Accessed August 15 2019).
[261] P.L. Chu, C. Vanderghem, H.L. MacLean, B.A. Saville, Process modeling of hydrodeoxygenation to produce renewable jet fuel and other hydrocarbon fuels, Fuel 196 (2017) 298-305.
[262] C.H. M. Brander; R. Tipper, G. Davis, Consequential and AttributionalApproaches to LCA: a Guide to Policy Makers withSpecific Reference to Greenhouse Gas LCA ofBiofuels, 2008. http://www.globalbioenergy.org/uploads/media/0804_Ecometrica_-_Consequential_and_attributional_approaches_to_LCA.pdf (Accessed August 24 2019).

[263] I. 14044, Environmental management — Life cycle assessment — Requirements and guidelines, Geneva, Switzerland, 2006.
[264] R.C.R. Santos, A. Valentini, C.L. Lima, J.M. Filho, A.C. Oliveira, Modifications of an HY zeolite for n-octane hydroconversion, Applied Catalysis A: General 403(1) (2011) 65-74.
[265] M.B. Spielmann, Christian; Dones, Roberto ; Tuchschmid, Matthias Transport services, Data v2.0, ecoinvent report No. 14., 2007. https://db.ecoinvent.org/reports/14_Transport.pdf. (Accessed August 20 2019).
[266] R.B. Dones, Christian; Bolliger, Rita; Burger, Bastian; Heck,Thomas; Röder, Alexander; Emmenegger, Mireille Faist; Frischknecht, Rolf; Jungbluth, Niels; Tuchschmid, Matthias Life Cycle Inventories of Energy Systems: Results for Current Systems in Switzerland and other UCTE Countries 2007. http://ecolo.org/documents/documents_in_english/Life-cycle-analysis-PSI-05.pdf. (Accessed August 22 2019).
[267] J.C. Sheehan, Vince; Duffield, James ; Graboski, Michael: Shapouri, Housein An Overview of Biodiesel andPetroleum Diesel Life Cycles, 1998. https://www.nrel.gov/docs/legosti/fy98/24772.pdf.
[268] H. Roland, Life Cycle Inventories of Packaging and Graphical Paper. Final report ecoinvent data v2.0 No. 11. , Swiss Centre for Life Cycle Inventories, Dübendorf, CH (2007).
[269] A.J. Papa, Propanols, Ullmann's Encyclopedia of Industrial Chemistry, Wiley InterScience2000.
[270] H.-J.H. Althaus, Roland ; Osses, Maggie ; Primas, Alex: Hellweg, Stefanie; Jungbluth, Niels ; Chudacoff, Mike Life Cycle Inventories of Chemicals, Data v2.0, ecoinvent report No. 8, 2007. https://db.ecoinvent.org/reports/08_Chemicals.pdf. (Accessed 2019 August 15).
[271] M.K. Voll, Peter Carbon, 6. Carbon Black, Ullmann's Encyclopedia of Industrial Chemistry, Wiley InterScience2010.
[272] P.A. Renzulli, Notarnicola, Bruno ; Tassielli, Giuseppe; Arcese, Gabriella; Capua, Rosa Di Life Cycle Assessment of Steel Produced in an Italian Integrated Steel Mill Sustainability 2016, 8(8), 719; https://doi.org/10.3390/su8080719 (2016).
[273] H.-J.B. Althaus, Christian; Doka, Gabor; Dones, Roberto; Frischknecht, Rolf; Hellweg, Stefanie; Humbert, Sébastien; Jungbluth, Niels; Köllner, Thomas; Loerincik, Yves; Margni, Manuele; Nemecek, Thomas Implementation of Life Cycle Impact Assessment Methods, Data v2.2, Ecoinvent report no. 3, 2010. https://www.ecoinvent.org/files/201007_hischier_weidema_implementation_of_lcia_methods.pdf. (Accessed August 25 2019).
[274] Y. Zhang, Practical ambiguities during calculation of energy ratios and their impacts on life cycle assessment calculations, Energy Policy v. 57 (2013) pp. 630-633-2013 v.57.

APPPENDIX A

Waste Cooking Oil to Jet-Diesel Fuel Range Using 2-Propanol via Catalytic Transfer Hydrogenation Reactions: Supplementary documents

List of Figures

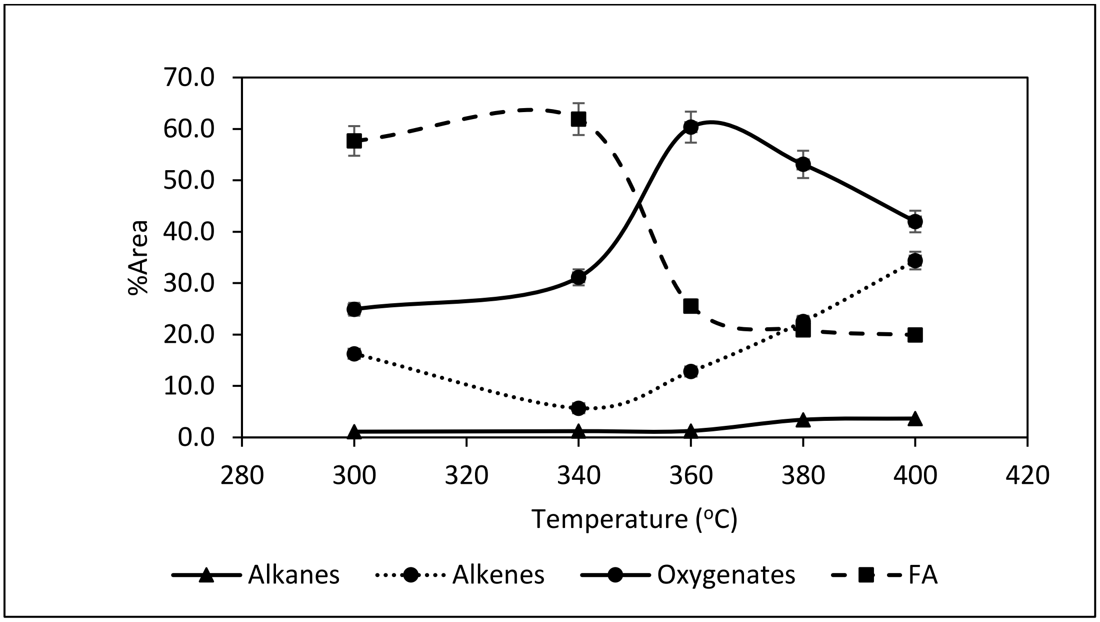

Figure A1. Heating WCO in the tubular reactor without 2-propanol and catalyst as a control experiment for CTH.

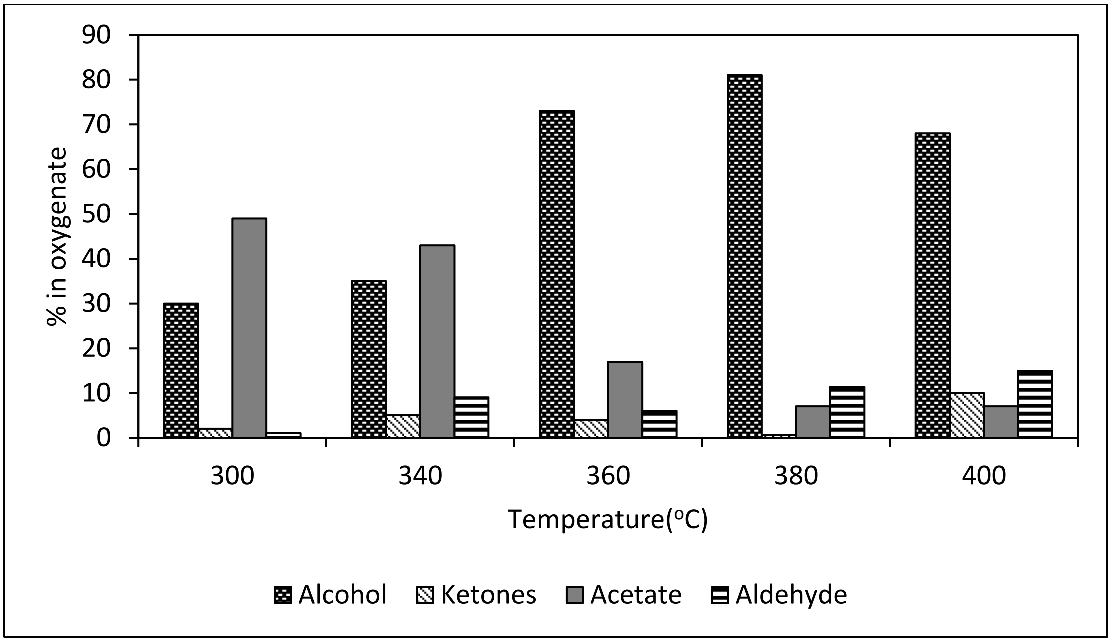

Figure A2. Heating WCO in the tubular reactor without 2-propanol and catalyst as a control experiment for CTH. Resulting oxygenates in the product at different reaction temperatures.

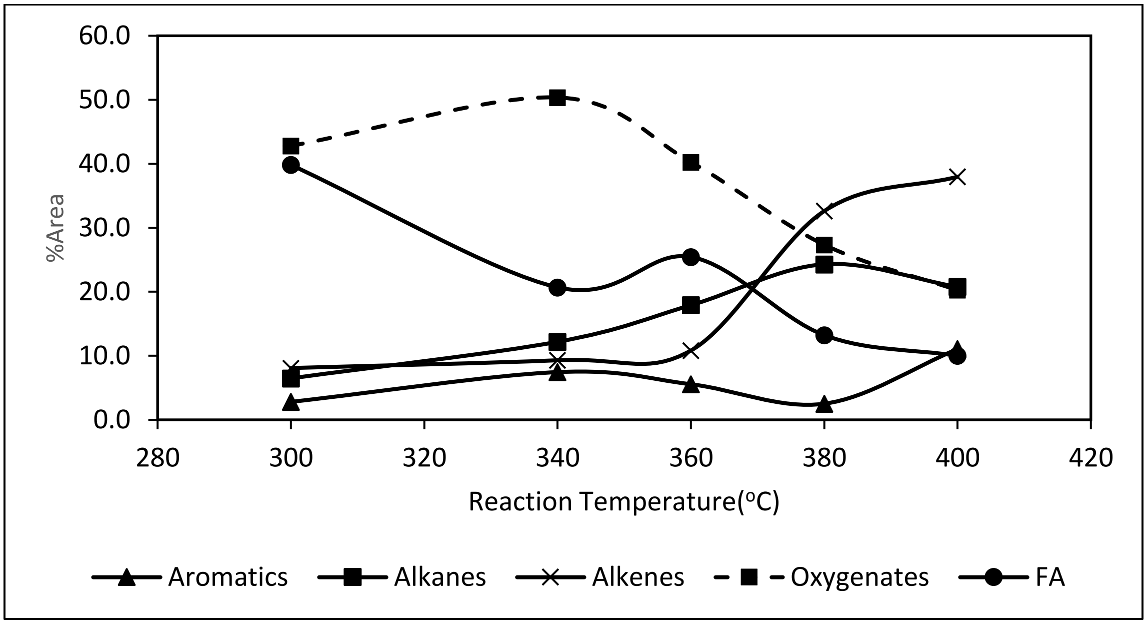

Figure A3. Heating WCO over catalyst in the tubular reactor without 2-propanol as a control experiment for CTH.

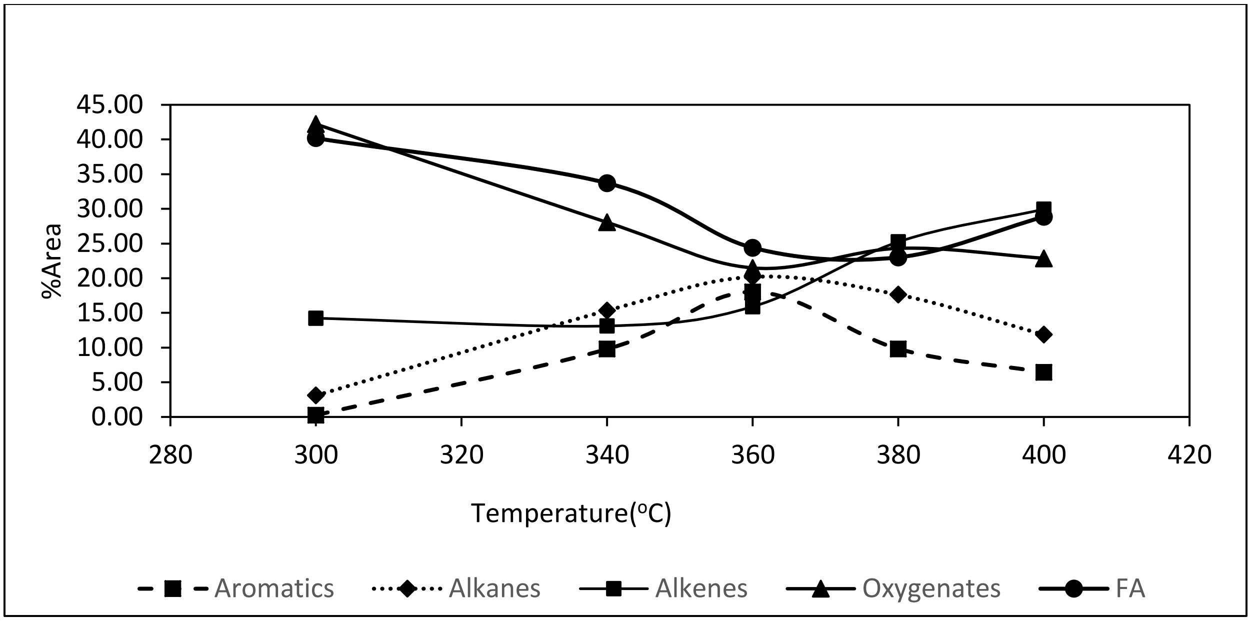

Figure A4. Deoxygenation of WCO with 2-propanol and without a catalyst as a control experiment for CTH. Resulting oxygenates in the product at different reaction temperatures.

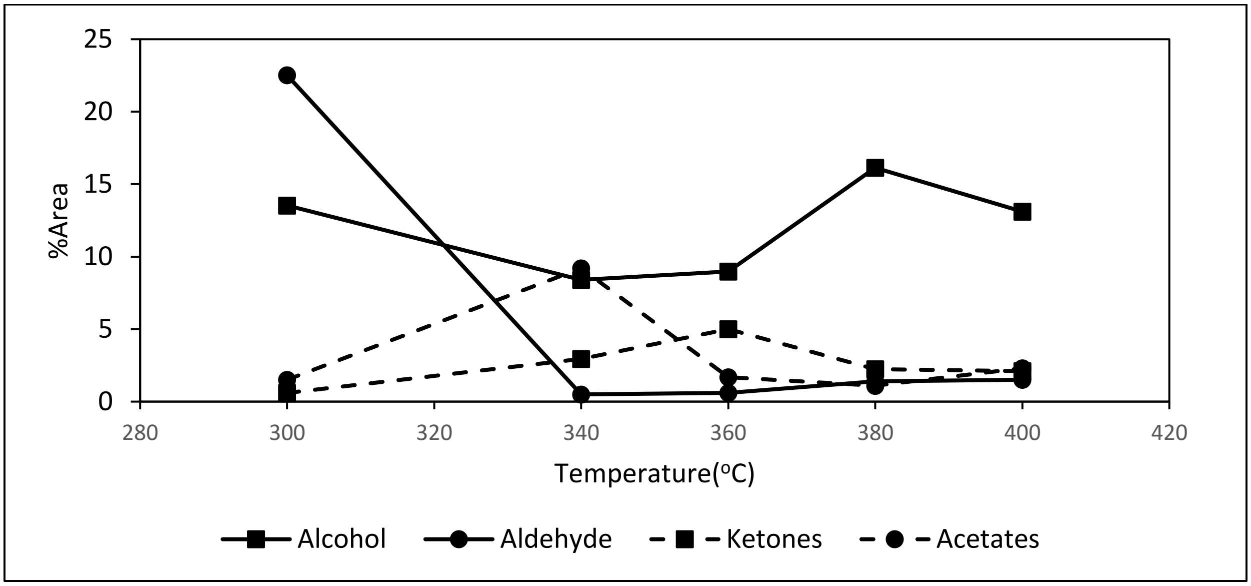

Figure A5. Deoxygenation of WCO with 2-propanol and without a catalyst as a control for CTH. Resulting oxygenates in the product at different reaction temperatures.

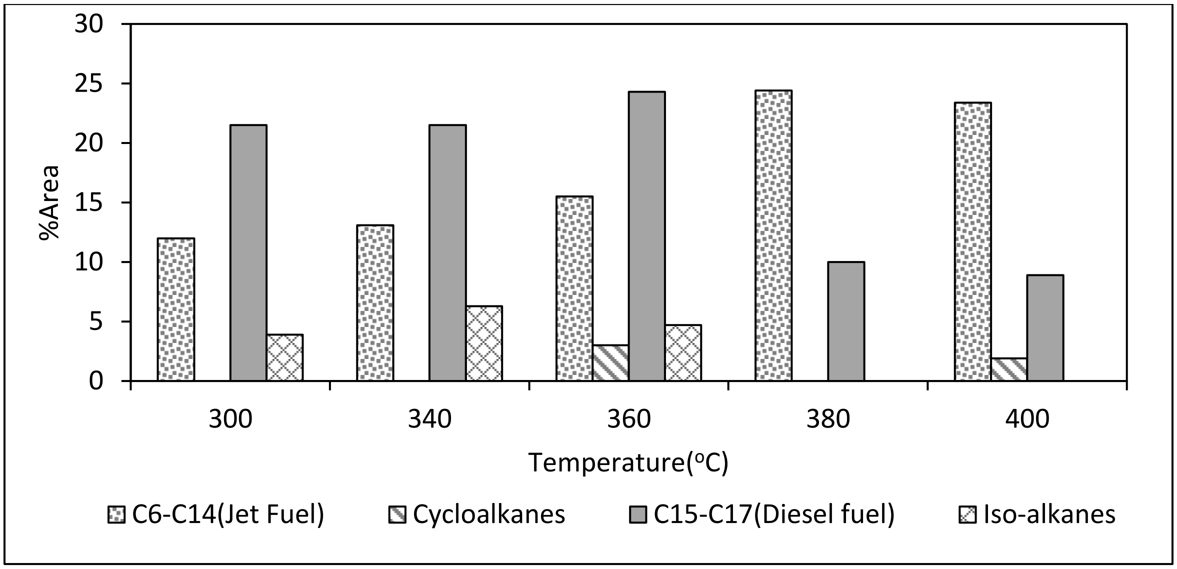

Figure A6. Alkanes composition in the liquid fuel from CTH at different reaction temperatures.

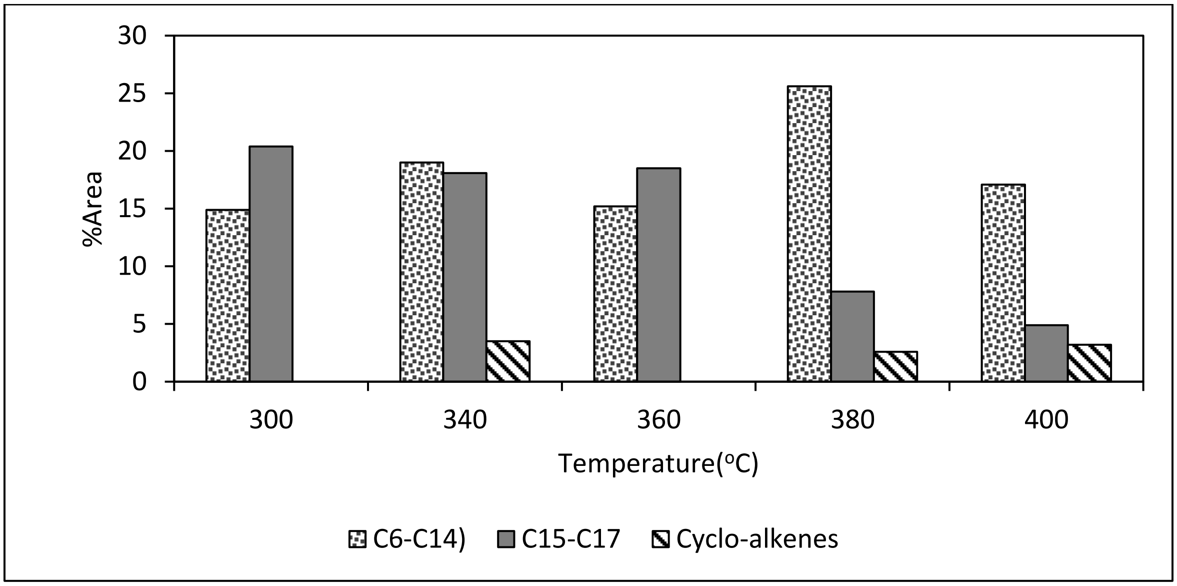

Figure A7. Alkenes composition in the liquid fuel from CTH of WCO at different reaction temperatures.

Table of Values

Table A1. Gas Composition Obtained from CTH Using 2-propanol as H-donor at 380 ^oC

Gas	H_2	CO	CO_2	CH_4	C_2H_6	C_3H_8
Volume (%)	21	26	22	10	10	11

Table A2. Main Chemical compositions of LHC using 2-propanol as H-donor @ 400 ^{o}C

Composition	%Area	Composition	%Area
Short Chain n-alkane(C_6-C_{14})	**23.4**	**Short Chain n-alkene(C_6-C_{14})**	**17.1**
Heptane(C_7H_{14})	3.5	2-Hexene, (E)-(C_6H_{12})	0.6
Octane(C_8H_{18})	4.4	2-Hexene, (Z)-(C_6H_{12})	0.4
Nonane(C_9H_{20})	3.0	1,3,5-Hexatriene, (Z)-(C_6H_8)	0.2
Decane($C_{10}H_{22}$)	2.4	1-Heptene(C_7H_{14})	2.2
Indane(C_9H_{10})	1.8	2-Heptene(C_7H_{14})	1.4
Undecane($C_{11}H_{24}$)	2.1	1-Octene (C_8H_{16})	2.0
Tridecane($C_{13}H_{28}$)	2.0	2-Octene(C_8H_{16})	1.0
Tetradecane($C_{14}H_{30}$)	1.5	2-Octene, (Z)-(C_8H_{16})	0.5
Pentane, 2,4-dimethyl(C_7H_{16})	2.6	2,4-Octadiene(C_8H_{14})	0.5
Cyclo-alkanes	**1.9**	1-Nonene(C_9H_{18})	1.5
Cyclopentane, methyl-(C_6H_{12})	0.2	2-Nonene, (E)-(C_9H_{18})	0.5
Cyclohexane, methyl-(C_7H_{14})	0.3	1-Decene($C_{10}H_{20}$)	1.3
Cyclopentane, ethyl-(C_7H_{14})	0.3	trans-3-Decene($C_{10}H_{20}$)	0.5
Cyclopropane, 1-ethyl-2-heptyl-($C_{12}H_{24}$)	1.0	1-Undecene($C_{11}H_{22}$)	0.5
Long Chain alkanes(C15-C17)	**8.9**	1-Dodecene($C_{12}H_{24}$)	2.2
Hexadecane ($C_{16}H_{34}$)	4.8	1-Tetradecene($C_{14}H_{28}$)	1.9
Heptadecane($C_{17}H_{36}$)	3.0	**Cyclo-alkenes**	**3.2**
Aromatics-32.9%	**32.9**	1,3-Cyclopentadiene, 1-methyl-(C_6H_8)	0.2
Benzene(C_6H_6)	1.8	Cyclopentene, 3-methyl-(C_6H_{10})	0.8
Toluene(C_7H_8)	4.6	Cyclohexene(C_6H_{10})	0.5
Ethylbenzene(C_8H_{10})	3.7	Cyclobutane, (1-methylethylidene)-(C_7H_{12})	0.3
o-Xylene(C_8H_{10})	1.8	1-Ethylcyclopentene(C_7H_{12})	0.6
p-Xylene(C_8H_{10})	3.7	Cyclohexene, 1-methyl-(C_7H_{12})	0.4
Benzene, propyl-(C_9H_{12})	1.4	Cyclooctene(C_8H_{14})	0.3
Benzene, 1-ethyl-2-methyl-(C_9H_{12})	3.6	1-Propylcyclopentene(C_8H_{14})	0.2
Benzene, 1-ethyl-4-methyl-(C_9H_{12})	0.5	**Oxygenates-7.7%**	**7.7**
Benzene, n-butyl-($C_{10}H_{14}$)	1.6	2-Pentanone($C_5H_{10}O$)	0.6
Benzene, 1-methyl-2-propyl-($C_{10}H_{14}$)	1.4	2-Hexanone($C_6H_{12}O$)	0.6
Benzene, pentyl-($C_{11}H_{16}$)	2.9	2-Heptanone($C_7H_{14}O$)	0.9
Naphthalene, 2-methyl-($C_{11}H_{10}$)	1.8	Phenol(C_6H_6O)	0.5
Naphthalene, 1-methyl-($C_{11}H_{10}$)	1.6	2-Octanone($C_8H_{16}O$)	1.6
Naphthalene, 1-ethyl-($C_{12}H_{12}$)	1.1	Phenol, 2-ethyl-($C_8H_{10}O$)	0.4
Fluorene(C13H10)	1.0	2-Nonadecanone($C_{19}H_{38}O$)	2.0
9H-Fluorene, 1-methyl-(C14H12)	0.3	2-Nonadecanone($C_{19}H_{38}O$)	1.2
Pyrene(C16H10)	0.4		
Long Chain alkenes(C_{15}-C_{17})	**4.9**		
1-Pentadecene($C_{15}H_{30}$)	2.6		
8-Heptadecene($C_{17}H_{34}$)	1.3		
3-Heptadecene, (Z)-($C_{17}H_{34}$)	0.8		
9-Tricosene, (Z)-($C_{23}H_{46}$)	0.2		

Table A3. Main Chemical compositions of LHC using 2-propanol as H-donor @ 380 ^{o}C

Composition	%Area	Composition	%Area
Short Chain n-alkane(C6-C14)	**24.4**	**Short chain alkenes(C6-C14)-28.5%**	**25.6**
n-Hexane(C_6H_{12})	2.1	1-Heptene (C_7H_{14})	2.9
Heptane (C_7H_{16})	3.2	2-Heptene, (E)-(C_7H_{14})	1.2
Octane(C_8H_{18})	3.6	2-Heptene(C_7H_{14})	0.4
Nonane(C_9H_{20})	2.8	1-Octene (C_8H_{16})	2.6
Undecane($C_{11}H_{24}$)	1.6	2-Octene, (E)-(C_8H_{16})	1.7
Indane(C_9H_{10})	0.8	Cyclooctene(C_8H_{14})	0.4
Undecane($C_{11}H_{24}$)	2.2	2,4-Octadiene(C_8H_{14})	0.5
Dodecane($C_{12}H_{26}$)	3.9	1-Nonene(C_9H_{18})	2.1
Tridecane($C_{13}H_{28}$)	2.4	1-Decene($C_{10}H_{20}$)	1.5
Tetradecane($C_{14}H_{30}$)	1.8	2-Decene, (Z)-($C_{10}H_{20}$)	0.4
Aromatics	**20.0**	1-Undecene($C_{11}H_{22}$)	4.8
Benzene(C_6H_6)	0.8	2-Undecene, (E)- ($C_{11}H_{22}$)	1.4
Toluene(C_7H_8)	3.2	1-Dodecene($C_{12}H_{24}$)	3.2
Ethylbenzene(C_8H_{10})	1.7	1-Tetradecene($C_{14}H_{28}$)	2.7
p-Xylene(C_8H_{10})	2.9	**Cyclo-alkenes**	**2.6**
Benzene, propyl-(C_9H_{12})	1.0	Cyclopentene, 3-methyl-(C_6H_{10})	0.7
Benzene, 1-ethyl-3-methyl-(C_9H_{12})	1.1	Cyclohexene(C_6H_{10})	0.7
Benzene, 1-ethyl-4-methyl-(C_9H_{12})	0.3	Cyclohexane, methyl-(C_7H_{14})	0.3
Benzene, 1-ethyl-2-methyl-(C_9H_{12})	1.3	1-Ethylcyclopentene(C_7H_{12})	0.4
Benzene, n-butyl-($C_{10}H_{14}$)	1.3	Cyclohexene, 1-methyl-(C_7H_{12})	0.5
Benzene, 1-methyl-2-propyl-($C_{10}H_{14}$)	0.9	**Oxygenates**	**9.7**
Benzene, pentyl-($C_{11}H_{16}$)	2.8	2-Pentanone($C_5H_{10}O$)	0.6
Naphthalene, 2-methyl-($C_{11}H_{10}$)	1.5	2-Hexanone($C_6H_{12}O$)	0.6
Benzene, hexyl-($C_{12}H_{18}$)	1.1	2-Heptanone($C_7H_{14}O$)	1.0
Long Chain alkanes(C15-C17)	**10.0**	Phenol(C_6H_6O)	0.4
Pentadecane($C_{15}H_{32}$)	5.6	2-Octanone($C_8H_{16}O$)	1.4
Hexadecane ($C_{16}H_{34}$)	1.1	2-Heptadecanone($C_{17}H_{34}O$)	3.0
Heptadecane($C_{17}H_{36}$)	3.3	2-Nonadecanone($C_{19}H_{38}O$)	1.6
Long-chain alkenes(C15-C23)	**7.8**	Fatty acid	1.1
1-Pentadecene($C_{15}H_{30}$)	3.5		
8-Heptadecene ($C_{17}H_{34}$)	2.1		
1-Heptadecene($C_{17}H_{34}$)	1.1		
9-Tricosene, (Z)-($C_{23}H_{46}$)	1.1		

Table A4. Main Chemical compositions of LHC using 2-propanol as H-donor @ 360 ^{o}C

Composition	**%Area**	**Composition**	**%Area**
Short Chain n-alkane(C6-C14)	**15.5**	**Short-chain alkenes**	**15.2**
n-Hexane(C_6H_{14})	1.4	1-Hexene(C_6H_{12})	0.8
Heptane (C_7H_{16})	2.3	1-Heptene (C_7H_{14})	2.0
Nonane(C_9H_{20})	2.6	2-Heptene, (E)-(C_7H_{14})	0.6
Undecane($C_{11}H_{24}$)	1.8	1-Octene (C_8H_{16})	1.8
Dodecane($C_{12}H_{26}$)	2.5	2-Octene, (E)-(C_8H_{16})	1.7
Tridecane($C_{13}H_{28}$)	2.3	1-Nonene(C_9H_{18})	1.3
Tridecane($C_{13}H_{28}$)	2.6	2-Nonene, (E)-(C_9H_{18})	0.7
i-alkanes-4.7%		1-Decene($C_{10}H_{20}$)	0.9
Hexane, 2,4-dimethyl-(C_8H_{18})	3.1	2-Undecene, (E)- ($C_{11}H_{22}$)	1.3
Octane, 2,4,6-trimethyl-($C_{11}H_{24}$)	1.6	1-Dodecene($C_{12}H_{24}$)	1.9
cyclo-alkanes-3%		1-Tetradecene($C_{14}H_{28}$)	2.1
Cyclopropane, nonyl-($C_{12}H_{24}$)	2.5	**Long-chain alkenes -18.6%**	
Cyclopropane, octyl-($C_{11}H_{22}$)	0.5	1-Pentadecene($C_{15}H_{30}$)	2.0
Aromatics-2.7%		1-Pentadecene($C_{15}H_{30}$)	1.8
Toluene(C_7H_8)	0.9	8-Heptadecene ($C_{17}H_{34}$)	3.7
Benzene, pentyl-($C_{11}H_{16}$)	1.3	3-Heptadecene, (Z)-($C_{17}H_{34}$)	5.3
Benzene, propyl-(C_9H_{12})	0.5	1-Heptadecene ($C_{17}H_{34}$)	2.2
Long-chain alkanes(C15-C24)-25%		9-Tricosene, (Z)-($C_{23}H_{46}$)	2.8
Pentadecane($C_{15}H_{32}$)	10.1	9-Tricosene, (Z)-($C_{23}H_{46}$)	0.7
Hexadecane ($C_{16}H_{34}$)	2.3	**Oxygenates-15.4%**	
Heptadecane($C_{17}H_{36}$)	10.8	2-Heptanone($C_7H_{14}O$)	0.5
Tetracosane($C_{24}H_{50}$)	1.1	2-Octanone($C_8H_{16}O$)	0.6
Benzene, n-butyl-($C_{10}H_{14}$)	0.7	2-Heptadecanone($C_{17}H_{34}O$)	4.7
		2-Nonadecanone($C_{19}H_{38}O$)	3.3
		9-Octadecen-1-ol, (Z)-($C_{18}H_{36}O$)	6.4

Table A5. Main Chemical compositions of LHC using 2-propanol as H-donor @ 340 ^{o}C

Short-Chain n-alkanes	**13.1**	**Short-chain alkenes**	**19.0**
n-Hexane(C_6H_{14})	1.4	1-Heptene (C_7H_{14})	1.8
Heptane (C_7H_{16})	2.3	2-Heptene, (E)-(C7H14)	0.4
Nonane(C_9H_{20})	2.4	1-Octene (C_8H_{16})	1.8
Dodecane($C_{12}H_{26}$)	2.2	2-Octene, (E)-(C_8H_{16})	1.7
Tridecane($C_{13}H_{28}$)	4.8	1-Nonene(C_9H_{18})	1.2
Aromatics	**3.6**	2-Nonene, (E)-(C9H18)	0.7
Toluene(C_7H_8)	0.8	1-Decene($C_{10}H_{20}$)	1.0
o-Xylene(C_8H_{10})	1.1	2-Undecene, (E)- ($C_{11}H_{22}$)	2.4
Benzene, n-butyl-($C_{10}H_{14}$)	0.7	1-Dodecene($C_{12}H_{24}$)	1.9
Benzene, pentyl-($C_{11}H_{16}$)	1.2	1-Tetradecene($C_{14}H_{28}$)	1.8
i-alkanes	**6.3**	1-Tetradecene($C_{14}H_{28}$)	2.3
Hexane, 2,4-dimethyl-(C_8H_{18})	2.9	7-Tetradecene($C_{14}H_{28}$)	2.1
Octane, 2,4,6-trimethyl-($C_{11}H_{24}$)	1.5	**Long-chain alkenes**	**18.1**
Octane, 2,4,6-trimethyl-($C_{11}H_{24}$)	1.9	1-Pentadecene($C_{15}H^{30}$)	5.2
cycloalkanes	**3.5**	8-Heptadecene ($C_{17}H_{34}$)	4.7
Cyclobutane, butyl-(C_8H18)	1.1	9-Eicosene, (E)-($C_{20}H_{40}$)	6.0
Cyclopropane, nonyl-($C_{12}H_{24}$)	2.4	1-Octadecene($C_{18}H_{36}$)	2.2
Long-chain alkanes(C15-C24)	**21.5**	**Oxygenates**	**14.9**
Pentadecane($C_{15}H_{32}$)	9.7	2-Octanone($C_8H_{16}O$)	0.5
Hexadecane (C16H34)	2.2	2-Heptadecanone($C_{17}H_{34}O$)	5.4
Heptadecane($C_{17}H_{36}$)	8.4	2-Nonadecanone(C_{19}H38O)	4.0
Tetracosane($C_{24}H_{50}$)	1.2	9-Octadecen-1-ol, (Z)-($C_{18}H_{36}O$)	0.7
		n-Tetracosanol-1($C_{24}H_{50}O$)	0.7
		9-Octadecen-1-ol, (Z)-($C_{18}H_{36}O$)	1.2
		9-Octadecen-1-ol, (Z)-($C_{18}H_{36}O$)	2.3

Table A6. Main Chemical compositions of LHC using 2-propanol as H-donor @ 300 ^{o}C

Short-Chain n-alkanes (C7-C13)	**11**	**short-chain alkenes(C6-C14)**	**14.8**
Heptane (C_7H_{16})	2.1	1-Hexene(C_6H_{12})	1.0
n-Hexane(C6H14)	2.0	1-Heptene (C_7H_{14})	2.0
Nonane(C_9H_{20})	2.3	2-Heptene, (E)-(C_7H_{14})	0.4
Undecane(C11H24)	1.2	1-Octene (C_8H_{16})	1.9
Dodecane(C12H26)	1.6	2-Octene, (E)-(C_8H_{16})	2.0
Tridecane($C_{13}H_{28}$)	1.8	1-Nonene(C_9H_{18})	1.1
i-alkanes	3.9	2-Nonene, (E)-(C_9H_{18})	0.7
Hexane, 2,4-dimethyl-(C_8H_{18})	2.9	1-Dodecene($C_{12}H_{24}$)	2.3
Octane, 2,4,6-trimethyl-($C_{11}H_{24}$)	1.1	2-Undecene, (E)- ($C_{11}H_{22}$)	1.5
Aromatics	**1.6**	1-Tetradecene($C_{14}H_{28}$)	2.0
o-Xylene(C_8H_{10})	0.9	**Long-chain alkenes (C16-C23)**	**20.5**
Benzene, n-butyl-($C_{10}H_{14}$)	0.7	Cetene($C_{16}H_{32}$)	1.3
Long-chain n-alkanes (C16-C17)	**20.4**	1-Pentadecene($C_{15}H_{30}$)	1.6
Hexadecane ($C_{16}H_{34}$)	4.7	9-Eicosene, (E)-($C_{20}H_{40}$)	2.1
Pentadecane($C_{15}H_{32}$)	8.6	8-Heptadecene ($C_{17}H_{34}$)	12.8
Heptadecane($C_{17}H_{36}$)	7.2	1-Heptadecene($C_{17}H_{34}$)	1.7
		9-Tricosene, (Z)-($C_{23}H_{46}$)	0.9
		oxygenates	**27.7**
		2-Pentadecanone($C_{15}H_{30}O$)	4.1
		2-Nonadecanone($C_{19}H_{38}O$)	3.0
		9-Octadecen-1-ol, (Z)-($C_{18}H_{36}O$)	0.8
		9-Octadecen-1-ol, (Z)-($C_{18}H_{36}O$)	1.3
		Fatty acid	18.6

Material balance, kinetics & scale-up

Table A7. CTH product composition at 380 °C modified. The products chosen as representatives for each fraction are highlighted in grey

Component	MW (g/mol)	T_b (°C)	Product	%area
C_6H_{14}	86.18	68.73	Naphta	2.1
C_6H_6	78.11	80.09	Naphta	0.8
C_7H_{14}	98.19	93.64	Naphta	4.3
C_7H_{14}	98.19	97.95	Naphta	0.4
C_7H_{16}	100.20	98.43	Naphta	3.2
C_8H_{18}	114.23	109.43	Naphta	3.6
C_7H_8	100.19	109.70	Naphta	3.2
C_8H_{16}	112.22	121.26	Naphta	4.3
C_8H_{10}	106.17	136.2	Naphta	1.7
C_8H_{10}	106.17	138.36	Naphta	2.9
C_8H_{14}	110.10	143.00	Naphta	0.9
C_9H18	126.24	146.87	Naphta	2.1
C_9H_{20}	128.26	150.82	Naphta	2.8
C_9H_{12}	120.19	159.24	Naphta	3.7
$C_{11}H_{24}$	156.31	169.77	Naphta	2.2
TOTAL NAPHTA %				**38.00**
$C_{10}H_{20}$	140.27	170.60	Kerosene	1.9
C_9H_{12}	118.00	177.97	Kerosene	0.8
$C_{10}H_{14}$	134.22	183.31	Kerosene	2.2
$C_{11}H_{22}$	154.30	192.67	Kerosene	6.2
$C_{11}H_{24}$	156.31	195.93	Kerosene	1.6
$C_{11}H_{16}$	148.25	205.46	Kerosene	2.8
$C_{12}H_{24}$	168.32	213.00	Kerosene	3.2
$C_{12}H_{18}$	162.20	215.90	Kerosene	1.1
$C_{12}H_{26}$	170.34	216.32	Kerosene	3.9
$C_{13}H_{28}$	184.37	235.47	Kerosene	2.4
$C_{11}H_{10}$	142.10	244.68	Kerosene	1.5
$C_{14}H_{28}$	196.38	251.10	Kerosene	2.7
$C_{14}H_{30}$	198.30	253.57	Kerosene	1.8
$C_{15}H_{30}$	210.40	268.46	Kerosene	3.5
$C_{15}H_{32}$	212.42	270.69	Kerosene	5.6
TOTAL KEROSENE %				**41.20**
$C_{16}H_{34}$	226.45	286.86	Diesel	1.1
$C_{17}H_{34}$	238.46	292.40	Diesel	2.1
$C_{17}H_{34}$	238.46	300.33	Diesel	1.1
$C_{17}H_{36}$	240.47	302.15	Diesel	3.3
$C_{23}H_{46}$	322.62	384.66	Diesel	1.1
TOTAL DIESEL %				**8.70**

Table A8. Data for regression of kinetic equation

Molar fraction y_O^{in}	0.0603*
Concentration C_O^{in} (mol/m^3)	2.22
Flow rate F_{H2} (mol/hr)	0.1569
Flow rate F_O (mol/hr)	0.0331
$R_{H_2}^{in}$	4.742
Pressure (Pa)	200000
R gas constant (J/mol K)	8.314
Temperature (K) (380°C)	653
Total concentration (mol/m^3)	36.84
Catalytic bed length (m)	0.14
Internal diameter of reactor(m)	0.014

$$* \; y_O^{in} = \frac{F_{oil}}{F_{CH4} + F_{CO} + F_{H2} + F_{C2H4}}$$

CH_4, CO, C_2H_4 are from the assumption that 2-propanol decompose as shown in Eq.(A2).

$$C_3H_7OH \rightarrow C_3H_6O + H_2 \rightarrow CH_4 + CO + H_2 + 0.5\, C_2H_4 \qquad \text{(A2)}$$

Weight of catalyst required

For n-order reaction the weight, w, of catalyst required is given by

$$w\left(1 - {}^{\overline{\alpha}}\!/_{2}\, w\right) = \frac{v_o}{k}\left(\frac{(1-x)^{1-n}-1}{n-1}\right) = \text{b} \qquad \text{[A3][88]}$$

$$\Longrightarrow w = \frac{1 \pm \sqrt{1-2\overline{\alpha}b}}{\overline{\alpha}}$$

Where $\overline{\alpha} = \frac{\overline{\beta}}{A_c P_o (1-\varepsilon)\rho_c}$

$$\overline{\beta} = \frac{G(1-\varepsilon)}{\overline{\rho} D_p \varepsilon^3}\left[\frac{150(1-\varepsilon)\mu}{D_p} + 1.75G\right]$$

G= superficial mass velocity = $\frac{(volumetric\ flowrate)(fluid\ density)}{(cross\text{-}sectional\ area\ of\ reactor)}$

k = reaction rate constant @ 380°C = 0.00022 s^{-1}

n = order of reaction = 2

D_p = average particle size of the catalyst = 1.63 mm

ε = porosity of catalyst = 0.51

x = % conversion of WCO = 0.99

A_c = reactor cross-sectional area, m^2

P_o = entry pressure of the feed, 2 bars

μ = viscosity of feed, 180 mPa.s

ρ_c = average density of the catalyst, 980 kg/m^3

ρ =density of the feed @ 380°C = 27 kg/m^3

(evaluated using Peng-Robinson equation of state)

v_o = volumetric flowrate, m^3/s

Processing 60 barrels of WCO per day requires 24 barrels of 2-propanol. This scale up amounts to a scale factor of 13248. This factor leads to catalyst weight of 73 kg at operation pressure of 2 bars (Table A9& Table A10)

Table A9. Effect of catalyst particle size on the amount of catalyst required to process 60 barrels of WCO

Particle size, mm	Catalyst weight, kg
0.50	6.9
0.70	13.0
1.00	27.5
1.50	62.0
1.63	**73.0**
2.00	110.0
2.50	172.0

Table A10. Effect of reaction on the amount of catalyst required to process 60 barrels of WCO

Pressure, bar	Catalyst weight, kg
1	36.6
2	**73.0**
3	110.0
4	147.0
5	183.0
10	367.0
15	550.0

APPENDIX B

SUPPORTING INFORMATION

Kinetics and Optimization of Catalytic Transfer Hydrogenation of Wco Using 2-Propanol as H-Donor Over NiO_X-MoO_X-CoO_X/zeolite

WCO Characterization

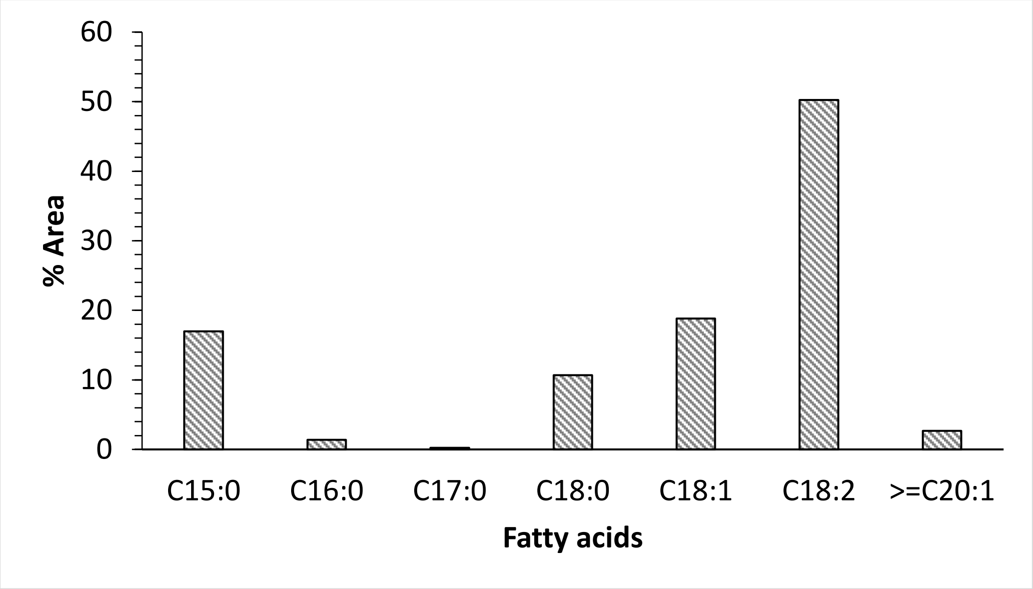

Figure B1. Fatty acid composition depicting 72% level of unsaturation.

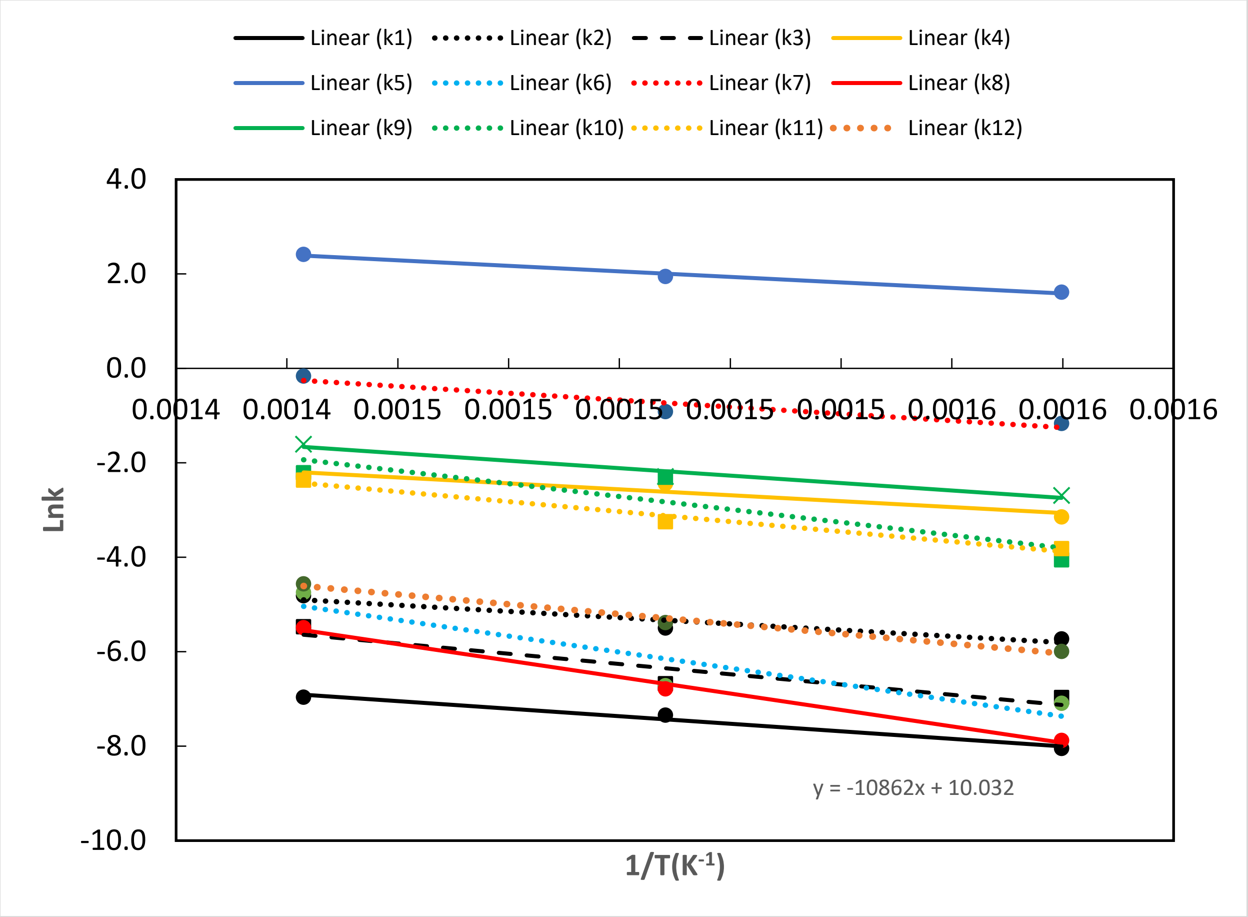

Figure B2. Fitting of rate constants at different temperatures.

Design of Experiment

Table B1. Coded and Real Values of Factorial Design of CTH of WCO.

Experimental	Coded Values				Real values			
Runs	A	B	C	D	A	B	C	D
1	-1	-1	0	-1	340	2	1.0	2
2	-1	0	1	1	340	10	2.5	12
3	-1	-1	-1	-1	340	2	0.8	2
4	1	-1	1	0	400	2	2.5	6
5	-1	0	0	-1	340	10	1.0	2
6	-1	1	-1	0	340	20	0.8	6
7	1	1	-1	-1	400	20	0.8	2
8	1	0	-1	0	400	10	0.8	6
9	0	0	0	0	370	10	1.0	6
10	-1	1	0	1	340	20	1.0	12
11	0	-1	1	-1	370	2	2.5	2
12	1	0	0	1	400	10	1.0	12
13	1	1	0	-1	400	20	1.0	2
14	1	-1	0	1	400	2	1.0	12
15	1	1	1	1	400	20	2.5	12
16	-1	0	-1	1	340	10	0.8	12
17	0	-1	-1	1	370	2	0.8	12
18	0	1	1	-1	370	20	2.5	2
19	-1	0	1	-1	340	10	2.5	2
20	0	1	-1	1	370	20	0.8	12
21	0	0	-1	-1	370	10	0.8	2
22	0	1	0	0	370	20	1.0	6
23	0	-1	-1	0	370	2	0.8	6
24	0	-1	1	1	370	2	2.5	12
25	-1	1	1	0	340	20	2.5	6

WCO Characterization Continues

Table B2. Equations Used to Model TGA of WCO.

Decomposition mechanism	Model equation f(α)	Integrated model equation G(α)
Zero order	1	α
First order	1-α	-ln(1-α)
Second order	$(1-\alpha)^2$	$(1-\alpha)^{-1}-1$
Third order	$(1-\alpha)^3$	$[(1-\alpha)^{-2}-1]/2$

Universal Equation

$$ln\left[\frac{G(\alpha)}{(T-T_o)}\right] = ln\left(\frac{A}{\beta}\right) - \frac{E_a}{RT} \qquad \text{(B1)}$$

A is the pre-exponential factor in seconds.

α is the fractional decomposition of WCO

T is the arbitrary temperature in Kelvin

T_o is the initial temperature at which TGA begins

E_a is the activation energy in kJ/mol

β is the heating rate in °C/min

R = 8.314 J/(mol K)

Table B3. Zero-Order Model.

Time (s)	Temp (°C)	% mass remaining	conversion	(G(α))	T(K)	1/T (1/K)	f(T, α)
4403	374.41	80.14	0.2000	0.2000	647.41	0.001545	-7.47704
4507	382.93	69.92	0.3030	0.3030	655.93	0.001525	-7.08544
4592	390.01	60.26	0.4002	0.4002	663.01	0.001508	-6.82649
4667	396.38	50.27	0.5008	0.5008	669.38	0.001494	-6.61938
4741	402.45	40.31	0.6012	0.6012	675.45	0.00148	-6.45278
4821	408.83	30.49	0.7001	0.7001	681.83	0.001467	-6.31704
4919	417.38	20.55	0.8002	0.8002	690.38	0.001448	-6.20519

Table B4. First-Order Model.

Time (s)	Temp (°C)	% mass remaining	Fractional decomposition	(G(α))	T(K)	1/T (1/K)	f(T, α)
4403	374.41	80.14	0.20000	0.2231	647.41	0.001545	-7.36754
4505	382.81	70.13	0.30084	0.3579	655.81	0.001525	-6.91866
4592	390.01	60.26	0.40024	0.5112	663.01	0.001508	-6.58174
4667	396.38	50.27	0.50084	0.6948	669.38	0.001494	-6.292
4741	402.45	40.31	0.6012	0.9193	675.45	0.00148	-6.0281
4821	408.83	30.49	0.70012	1.2044	681.83	0.001467	-5.77458
4919	417.38	20.55	0.80024	1.6106	690.38	0.001448	-5.50572

Table B5. 2nd-Order Model.

Time(s)	T (°C)	% mass remaining	Fractional decomposition	(G(α))	T(K)	1/T (1/K)	f(T, α)
4403	374.41	80.14	0.200	0.2500	647.41	0.00155	-7.25389
4505	382.81	70.13	0.301	0.4303	655.81	0.00153	-6.73439
4592	390.01	60.26	0.400	0.6673	663.01	0.00151	-6.31526
4667	396.38	50.27	0.501	1.0034	669.38	0.00149	-5.92455
4741	402.45	40.31	0.601	1.5075	675.45	0.00148	-5.53348
4821	408.83	30.49	0.700	2.3347	681.83	0.00147	-5.11267
4919	417.38	20.55	0.800	4.0060	690.38	0.00145	-4.59455

Table B6. 3rd-Order Model.

Time(s)	Temp(°C)	%rem	Fractional decomposition	(G(α))	T(K)	1/T(1/K)	f(T, α)
4403	374.41	80.14	0.200	0.2812	647.41	0.00155	-7.13611
4505	382.81	70.13	0.301	0.5229	655.81	0.00153	-6.53953
4592	390.01	60.26	0.400	0.8900	663.01	0.00151	-6.02733
4667	396.38	50.27	0.501	1.5067	669.38	0.00149	-5.51796
4741	402.45	40.31	0.601	2.6438	675.45	0.00148	-4.97172
4821	408.83	30.49	0.700	5.0600	681.83	0.00147	-4.33917
4919	417.38	20.55	0.800	12.0300	690.38	0.00145	-3.49494

Table B7. Results for Four Different Models.

Reaction order	Slope	Intercept	Activation energy (kJ/mol)	Pre-exponential factor(s^{-1})	R-Squared
0	-13325	13.212	110.8	45574.03157	0.9686
1	-19508	22.819	162.2	677617379.9	0.9958
2	**-27712**	**35.515**	**230.4**	**2.21201E+14**	**0.9989**
3	-37748	51.012	313.8	1.18864E+21	0.9903

Kinetics Model

Table B8. Experimental Data at 360 °C and 14 bar for Kinetic Modeling.

τ	C9	C8	C7	C6	C5	C4	C3	C2	C1
0.0	0.00	0.00	0.00	0.00	0.00	0.00	0.00	0.00	100.00
36.2	0.00	0.25	0.18	0.07	0.46	0.09	12.90	1.70	84.29
180.4	0.42	1.53	3.05	8.24	0.62	0.38	30.45	2.82	52.51
360.1	0.81	4.69	2.89	26.27	1.12	0.18	30.53	7.68	25.86
630.1	6.50	4.48	7.03	41.38	0.56	0.28	25.64	6.87	7.30
900.1	6.57	6.41	12.52	50.54	0.59	0.10	12.46	8.91	1.93
1224.0	15.65	3.56	11.97	57.83	0.28	0.04	2.82	7.07	1.14
1566.0	13.38	4.80	16.82	52.96	0.33	0.01	2.88	8.78	0.16
1800.0	19.32	1.79	13.37	57.81	0.28	0.06	0.96	6.39	0.08

C_1 = WCO; C_2 = oxygenates; C_3 = long-chain alkanes; C_4 = long-chain alkenes; C_5 = short-chain alkenes (C6-C14); C_6 = short-chain alkanes (C6-C14); C_7 = iso-alkanes; C_8 = cyclo-alkanes, C_9 = aromatics

Table B9. Experimental Data at 390 °C and 14 bar for Kinetic Modeling.

τ(s)	C9	C8	C7	C6	C5	C4	C3	C2	C1
0.0	0.0	0.0	0.0	0.0	0.0	0.0	0.0	0.0	100.0
36	0.0	0.3	0.5	1.6	0.6	0.3	13.6	1.2	82.1
180	1.8	4.6	3.9	15.2	0.7	0.5	34.1	8.9	30.4
360	5.0	5.1	11.4	34.5	0.6	0.2	22.0	8.7	12.6
630	13.7	5.6	18.9	43.2	0.5	0.1	5.8	11.0	1.2
900	16.6	2.9	24.6	43.9	0.4	0.0	2.6	9.0	0.4
1260	25.6	3.3	24.4	34.0	0.2	0.0	0.4	12.5	0.0
1530	29.2	2.8	28.4	31.3	0.2	0.0	0.1	8.1	0.0
1800	27.6	1.0	29.0	30.5	0.3	0.0	0.0	11.8	0.0

C_1 = WCO; C_2 = oxygenates; C_3 = long-chain alkanes; C_4 = long-chain alkenes; C_5 = short-chain alkenes (C6-C14); C_6 = short-chain alkanes (C6-C14); C_7 = iso-alkanes; C_8 = cyclo-alkanes, C_9 = aromatics

Table B10. Experimental Data at 390 °C and 14 bar for Kinetic Modeling.

τ	C_9	C_8	C_7	C_6	C_5	C_4	C_3	C_2	C_1
0	0.00	0.00	0.00	0.00	0.00	0.00	0.00	0.00	100.00
36	0.14	1.08	0.78	8.58	0.75	0.33	26.57	3.52	58.33
180	5.37	4.41	7.48	45.88	0.97	0.18	16.98	7.94	10.85
360	20.05	7.20	20.70	44.05	0.39	0.02	1.37	5.93	0.30
630	33.37	4.38	28.16	27.92	0.25	0.00	0.08	5.89	0.03
900	41.11	1.81	30.39	19.89	0.30	0.00	0.00	6.51	0.00
1260	46.19	0.57	34.52	10.11	0.15	0.00	0.00	8.43	0.00
1530	50.88	0.53	37.27	5.14	0.06	0.00	0.00	6.16	0.00
1800	50.84	0.60	39.22	3.86	0.05	0.00	0.00	5.53	0.00

C_1 = WCO; C_2 = oxygenates; C_3 = long-chain alkanes; C_4 = long-chain alkenes; C_5 = short-chain alkenes (C6-C14); C_6 = short-chain alkanes (C6-C14); C_7 = iso-alkanes; C_8 = cyclo-alkanes, C_9 = aromatics

Optimization

Table B11. Experimental (Y_{exp}) and Calculated (Y_{cal}) Values of Alkanes.

Run	A	B	C	D	Yexp	Ycal
1	340	2	1.0	2	16.8	17.5
2	340	10	2.5	12	27.6	27.4
3	340	2	0.8	2	18.1	17.7
4	400	2	2.5	6	18.4	18.8
5	340	10	1.0	2	30.7	30.9
6	340	20	0.8	6	19.3	19.4
7	400	20	0.8	2	55.2	56.2
8	400	10	0.8	6	65.1	64.6
9	370	10	1.0	6	73.7	74.4
10	340	20	1.0	12	6.2	6.4
11	370	2	2.5	2	17.5	17.4
12	400	10	1.0	12	46.9	47.5
13	400	20	1.0	2	57.8	57.5
14	400	2	1.0	12	27.9	27.6
15	400	20	2.5	12	50.4	50.5
16	340	10	0.8	12	14.3	14.3
17	370	2	0.8	12	33.6	34.0
18	370	20	2.5	2	49.1	49.1
19	340	10	2.5	2	14.9	15.0
20	370	20	0.8	12	39.3	39.5
21	370	10	0.8	2	65.8	66.0
22	370	20	1.0	6	65.6	65.0
23	370	2	0.8	6	53.8	54.1
24	370	2	2.5	12	32.5	32.7
25	340	20	2.5	6	27.6	28.2

Table B12. Comparison between the current study the previous work.

	Parameters	**Published**	**Current study**
	Catalyst	Activated Carbon	Mo-Ni-Co-Zeolite
PRODUCTS	Alkanes (%)	32.0	77.0
	Alkenes (%)	37.0	3.8
	Aromatics (%)	16.0	12.3
	Oxygenates (%)	6.7	0.0
	Gaseous products (%)	30.0	6.7
OTHER	Liquid Yield (%)	72.0	80.0
	Conversion (%)	100.0	100.0
	Activation energy (kJ/mol)	53.0	84.0
VARIBLES	WCO/2-propanol (mL/mL)	2.5	1.6
	WHSV (h^{-1})	6.7	6.7
	Temperature (^{o}C)	380.0	384.0
	Pressure (Bar)	2.0	14.7

Table B13. ANOVA Test for Polynomial Model.

Coefficient	**Estimated**	**SE**	**tstat**	**P-value**
β0	-3429.8000	47.6650	-71.9580	6.55E-15
β1	18.5090	0.2785	66.4660	1.45E-14
β2	-8.4322	1.5280	-5.5185	0.000255
β3	39.8190	7.5916	5.2452	0.000376
β4	-5.7728	2.5265	-2.2849	0.045407
β5	0.0339	0.0045	7.5689	1.91E-05
β6	-0.0871	0.0117	-7.4535	2.18E-05
β7	0.0283	0.0075	3.7734	0.003641
β8	0.7349	0.0273	26.967	1.14E-10
β9	0.8729	0.2107	4.1426	0.002004
β10	1.6505	0.0501	32.9280	1.57E-11
β11	-0.0248	0.0004	-58.8040	4.91E-14
β12	-0.1893	0.0064	-29.3980	4.84E-11
β13	-8.9783	1.4649	-6.1288	0.000111
β14	-0.51732	0.0220	-23.4670	4.47E-10
β15	-0.0024	0.0006	-4.2254	0.001757

APPENDIX C

Catalytic Transfer Hydrogenation and Characterization of Flash Hydrolyzed Microalgae into Hydrocarbon Fuels Production (Jet Fuel, & Diesel): Supplementary Documents

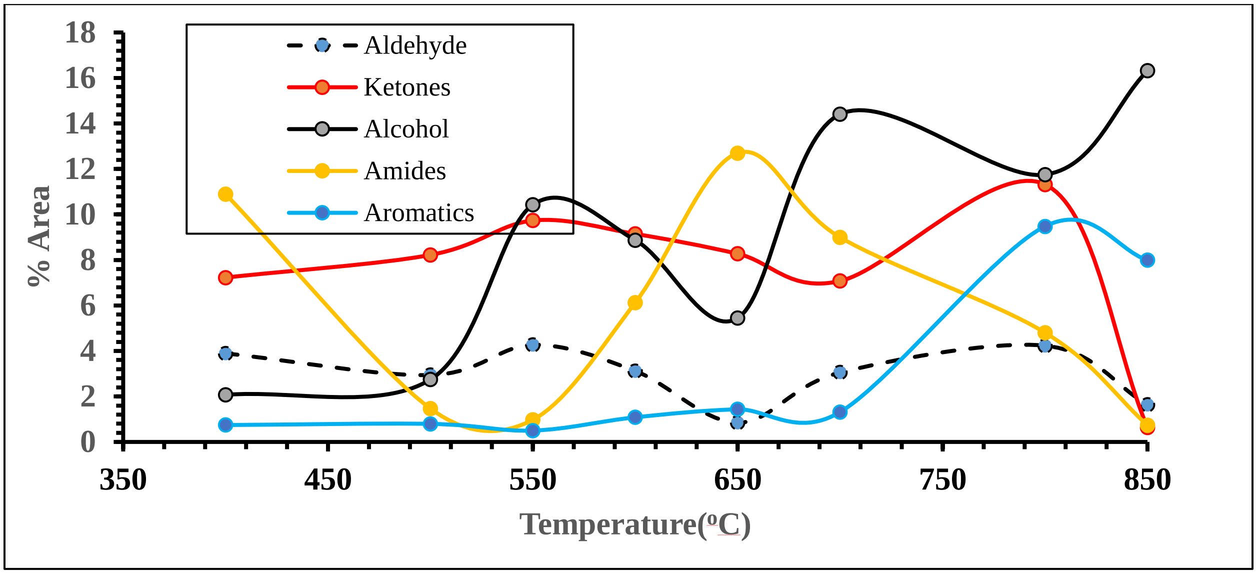

Figure C1. Other compounds formed during the pyrolysis of the BI.

Determination of Activation Energy of BI Thermal Decomposition

The activation energy of BI decomposition was determined by using two isothermal methods: the Flynn-Wall-Ozawa (FWO) and Kissinger-Akahira-Sunose (KAS)

$$ln\beta = ln\left[\frac{AE_a}{Rg(\alpha)}\right] - 5.331 - 1.052\,\frac{E_a}{RT} \qquad \text{(C1)}$$

$$ln\left[\frac{\beta}{T^2}\right] = ln\left[\frac{AR}{E_a g(\alpha)}\right] - \frac{E_a}{RT} \qquad \text{(C2)}$$

$$g(\alpha) = \frac{(1-\alpha)^{1-n}-1}{n-1} \qquad \text{(C3)}$$

A is the pre-exponential factor in second.

α is the fractional decomposition of BI

T is the arbitrary temperature in Kelvin

E$_a$ is the activation energy in kJ/mol

β is the heating rate in °C/min

R = 8.314 J/molK

n is the order of reaction.

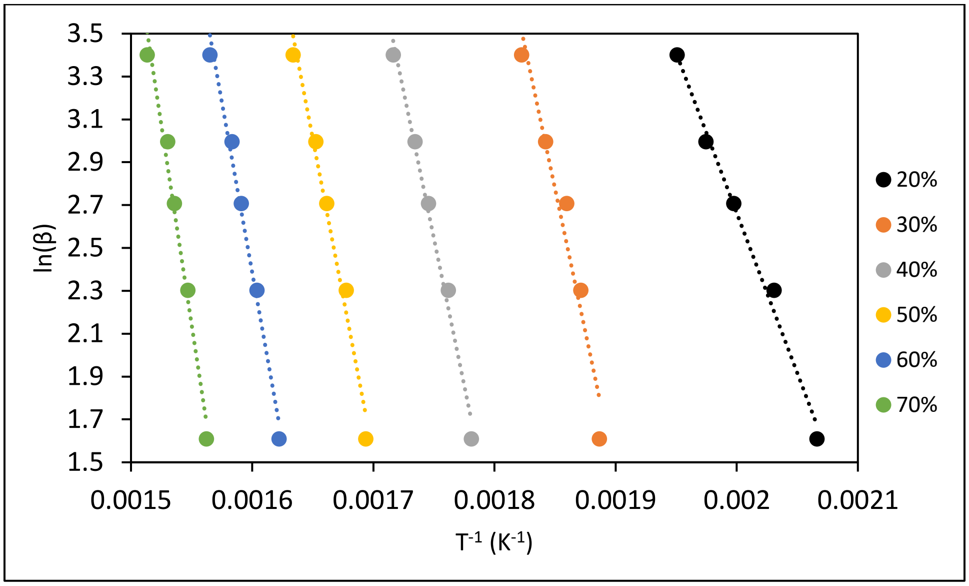

Figure C2. A plot to determine the activation energy using FWO equation.

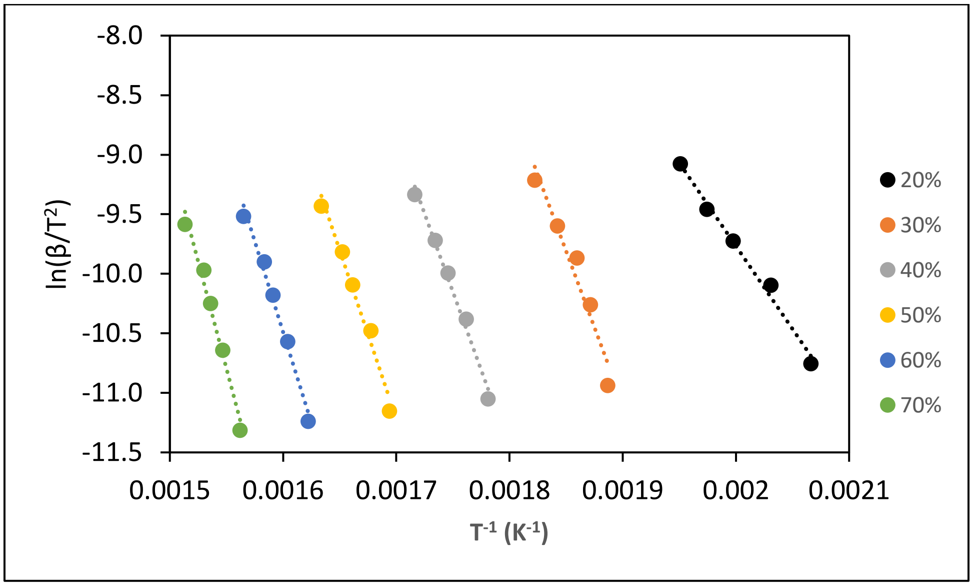

Figure C3. A Determination of activation energy using KAS equation.

Table C1. Activation energy obtained using Eq. (C1), FWO

Conversion (%)	slope	intercept	R-squared	Ea, kJ/mol
20.0	-14941	32.545	0.9913	118.1
30.0	-26667	52.110	0.9499	210.8
40.0	-27405	50.504	0.9890	216.6
50.0	-29466	51.631	0.9814	232.9
60.0	-31722	53.141	0.9871	250.7
70.0	-37254	59.888	0.9820	294.4

Table C2. Activation energy obtained using Eq. (C2), KAS.

Conversion (%)	slope	intercept	R-squared	Ea, kJ/mol
20.0	-13945	18.124	0.9900	115.9
30.0	-25588	37.529	0.9458	212.7
40.0	-26561	35.806	0.9879	220.8
50.0	-28264	36.834	0.9797	234.9
60.0	-30467	38.258	0.9860	253.3
70.0	-35954	44.933	0.9807	298.9

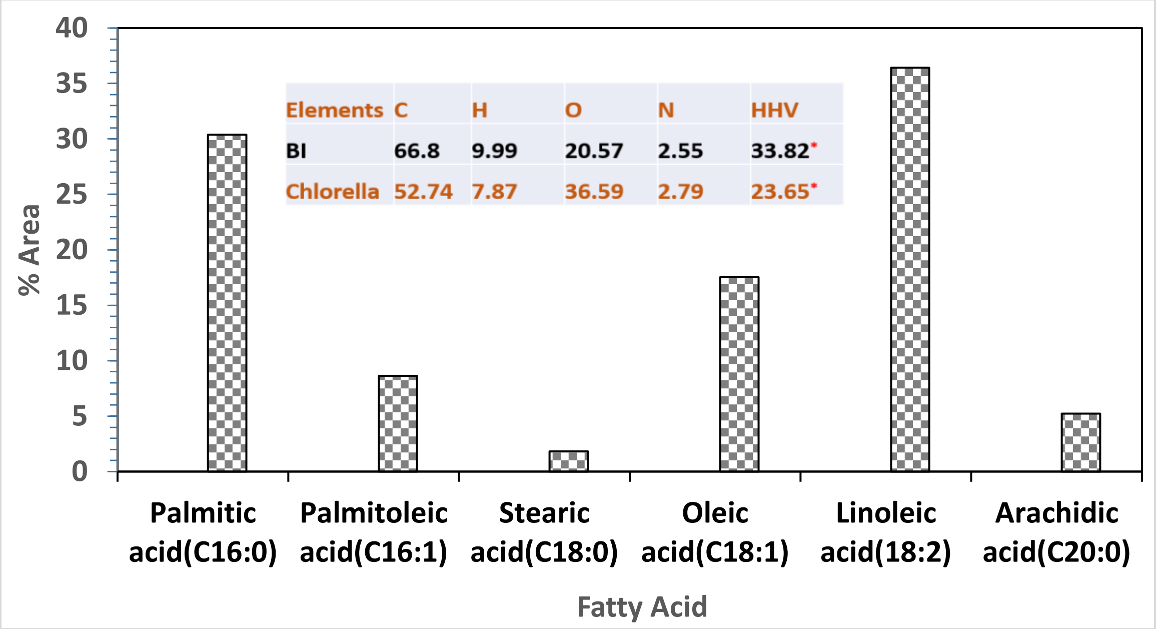

Elements	C	H	O	N	HHV
BI	66.8	9.99	20.57	2.55	33.82*
Chlorella	52.74	7.87	36.59	2.79	23.65*

Figure C4. Fatty Acid profile of the oil extracted (*Calculated from HHV = 33.5[C]+142.3[H]-15.4[O]+14.5[N], MJ/kg)

Table C3. CTH Reaction in1 hour

Compounds	%Area
Tridecane	6.89
Carbonic acid, decyl vinyl ester	4.18
Diethylene glycol dibenzoate	19.23
Heptadecanoic acid, TMS derivative	2.96
4-Tripropylsilyloxypentadecane	1.23
1-Phenazinecarboxylic acid, 6-[1-[(1-oxooctyl)oxy]ethyl]-, (.+-.)-	1.53
Cyclononasiloxane, octadecamethyl-	1.61
n-Octadecanoic acid, pentamethyldisilyl ester	3.05
1-Phenanthrenecarboxaldehyde, 1,2,3,4,4a,9,10,10a-octahydro-1,4a-dimethyl-7-(1-methylethyl)-, [1R-(1.alpha.,4a.beta.,10a.alpha.	7.34
Heptasiloxane, 1,1,3,3,5,5,7,7,9,9,11,11,13,13-tetradecamethyl-	2.48
1-O-Heptadecylglycerol, bis-trimethylsilyl ether	1.9
Nordazepam, TMS derivative	3
Cycloheptasiloxane, tetradecamethyl-	5.38
Triphenylphosphine oxide	15.56
Heptasiloxane, hexadecamethyl-	1.95
Silane, triethyl(2-phenylethoxy)-	1.75
Diisooctyl phthalate	6.16
3-Tripropylsilyloxypentadecane	3.17
3-Isopropoxy-1,1,1,5,5,5-hexamethyl-3-(trimethylsiloxy)trisiloxane	4.93
Tris(tert-butyldimethylsilyloxy)arsane	5.7

Table C4. CTH Reaction in 2 hours

Compounds	%Area
Bicyclo[2.1.0]pentane, 1,4-dimethyl-	1.73
Hexane, 2,3-dimethyl-	0.71
Heptane, 4-methyl-	3.54
Hexanal	1.93
2-Hexene, 4,4,5-trimethyl-	1.65
2,4-Dimethyl-1-heptene	0.9
Cyclohexane, 1,2,4-trimethyl-	0.94
Octane, 4-methyl-	1.73
Cyclohexane, 1,2,4-trimethyl-	0.59
Cyclopentane, 1-hexyl-3-methyl-	3.92
7-Hexadecene, (Z)-	1.49
Nonanoic acid, 9-oxo-, methyl ester	4.73
Hexadecanoic acid, methyl ester	19.98
1,2-Benzenedicarboxylic acid, butyl cyclohexyl ester	1.81
9,12-Octadecadienoic acid (Z,Z)-, methyl ester	8.12
9-Octadecenoic acid, methyl ester, (E)-	38.47
Methyl stearate	7.76

Table C5. CTH Reaction in 3 hours

Compounds	**%Area**
Hexane, 3-methyl-	1.63
Cyclopropane, trimethylmethylene-	6.53
2-Octene, 2,6-dimethyl-	1.13
Hexane, 2,3-dimethyl-	1.97
Heptane, 4-methyl-	11.48
Hexane, 2,4-dimethyl-	0.86
Cyclopentane, 1-methyl-3-(2-methylpropyl)-	0.89
Hexane, 2,4-dimethyl-	1.26
Heptane, 2,4-dimethyl-	4.49
2-Hexene, 4,4,5-trimethyl-	4.25
2,4-Dimethyl-1-heptene	1.87
2,3-Dimethyl-3-heptene	1.32
Cyclohexane, 1,2,4-trimethyl-, (1.alpha.,2.beta.,4.beta.)-	2.71
4-Undecene, 7-methyl-	1.28
Octane, 4-methyl-	7.06
Cyclohexane, 1,2,4-trimethyl-	1.9
Cyclohexane, 1,2,4-trimethyl-	1.52
Cyclopentane, 1-hexyl-3-methyl-	14.89
trans-2-Methyl-3-octene	2.02
Nonane	0.8
2-n-Butyl furan	0.91
Hexane, 2,4,4-trimethyl-	1.27
5,7-Dimethyloctahydrocoumarin	0.63
Cyclooctane, 1,5-dimethyl-	1.03
1-Octene, 3,7-dimethyl-	1.21
Pentane, 2,2,3,3-tetramethyl-	1.49
Bicyclo[2.2.1]heptane, 2,2,3-trimethyl-	1.29
Heptane, 2,5,5-trimethyl-	1.63
Heptane, 2,5,5-trimethyl-	1.42
1,5-Hexadiene-3,4-diol, 3,4-dimethyl-	0.69
Decane, 4-methyl-	1.36
Cyclopentane, 1,2-dibutyl-	0.9
Cyclooctane, 1-methyl-3-propyl-	1.26
Cyclopentane, 1,2-dibutyl-	1.77
5-Octadecene, (E)-	3.22
Cyclohexane, 1,4-dimethyl-2-(2-methylpropyl)-, (1.alpha.,2.beta.,4.alpha.)-	1.17
Octane, 2,3,6,7-tetramethyl-	0.37
cis,cis,cis-1-Isobutyl-2,5-dimethylcyclohexane	2.1
Nonanoic acid, 9-oxo-, methyl ester	0.75

Table C5. CTH Reaction in 3 hours Cont.

Hexadecane	0.39
Hexadecanoic acid, methyl ester	0.95
Dibutyl phthalate	2.31
9-Octadecenoic acid, methyl ester, (E)-	2.02

Table C6**.** CTH Reaction in 4 hours

Compounds	%Area
Hexane, 3-methyl-	1.27
1-Hexene, 2-methyl-	1.97
.alpha.-Pyrrolidone, 5-acetoxymethyl-	0.6
Acetic acid, 1,4-dimethylpent-4-enyl ester	7.79
Cyclopentane, 1,2,4-trimethyl-	0.55
1-Octene, 3,3-dimethyl-	1.08
Hexane, 2,3-dimethyl-	2.2
Heptane, 4-methyl-	13.21
Heptane, 3-methyl-	1.07
Hexane, 2,4-dimethyl-	1.75
Hexane, 2,3,4-trimethyl-	4.86
Ethanone, 1-(1-methylcyclopentyl)-	3.9
2,4-Dimethyl-1-heptene	1.41
2,3-Dimethyl-3-heptene	1.7
Cyclohexane, 1,3,5-trimethyl-	2.35
Decane, 1-chloro-	1.62
Octane, 4-methyl-	7.08
Cyclohexane, 1,2,4-trimethyl-	1.93
Cyclohexane, 1,2,4-trimethyl-	1.49
Cyclopentane, 1-hexyl-3-methyl-	16.93
Nonane	0.6
Pentane, 2,2,3,3-tetramethyl-	1.2
Pentane, 2,2,3,3-tetramethyl-	1.49
Mesitylene	0.65
Octane, 3,3-dimethyl-	1.46
Heptane, 2,5,5-trimethyl-	1.26
Nonane, 2,3-dimethyl-	1.42
Cyclopentane, 1,2-dibutyl-	1.09
Cyclopentane, 1,2-dibutyl-	2.25
5-Octadecene, (E)-	3.92
Cyclohexane, 1,4-dimethyl-2-(2-methylpropyl)-, (1.alpha.,2.beta.,4.alpha.)-	1.05
Dibutyl phthalate	8.85

Table C7. Reaction in 5 hours

Compounds	%Area
Hexane, 3-methyl-	1.99
2,2-Dimethylglutaric anhydride	3.65
cis-3-Methylcyclohexanol	8.2
Benzeneacetic acid, cyclopentyl ester	1.17
Hexane, 2,3-dimethyl-	2.04
Heptane, 4-methyl-	13.53
Hexane, 2,4-dimethyl-	1.39
Hexane, 2,4-dimethyl-	2.36
Hexane, 2,3,3-trimethyl-	4.94
2,3-Dimethyl-2-heptene	3.03
Cyclohexane, 1,2,4-trimethyl-	2.33
o-Xylene	3
Octane, 4-methyl-	9.54
Cyclohexane, 1,2,4-trimethyl-	1.86
Cyclohexane, 1,2,4-trimethyl-	1.6
Cyclopentane, 1-hexyl-3-methyl-	20.25
Nonane	1.05
1-Hexene, 3,5,5-trimethyl-	1.92
Mesitylene	1.25
Heptane, 5-ethyl-2-methyl-	0.96
Nonane, 2,3-dimethyl-	1.03
Nonane, 2,3-dimethyl-	1.43
Cyclopentane, 1,2-dibutyl-	3.96
5-Tetradecene, (E)-	2.56
Undecane	0.91
Pentadecane	2.82
Heptadecane	1.23

Kinetics of CTH of Algae Oil

Table C8. Experimental and Calculated Conversion of Algae Oil

	Conversion					
	T = 390 °C		T = 405 °C		T = 420 °C	
Time (s)	X_{exp}	X_{ca}l	X_{exp}	X_{ca}l	X_{exp}	X_{cal}
0	0.0000	0.0000	0.0000	0.0000	0.0000	0.0000
3600	0.4996	0.5308	0.6126	0.6044	0.7800	0.7818
7200	0.8689	0.8127	0.8413	0.8586	0.9694	0.9613
10800	0.9051	0.9418	0.9649	0.9555	0.9787	0.9948
14400	0.9790	0.9883	0.9970	0.9881	0.9998	0.9995
18000	0.9996	0.9991	0.9989	0.9974	1.0000	1.0000

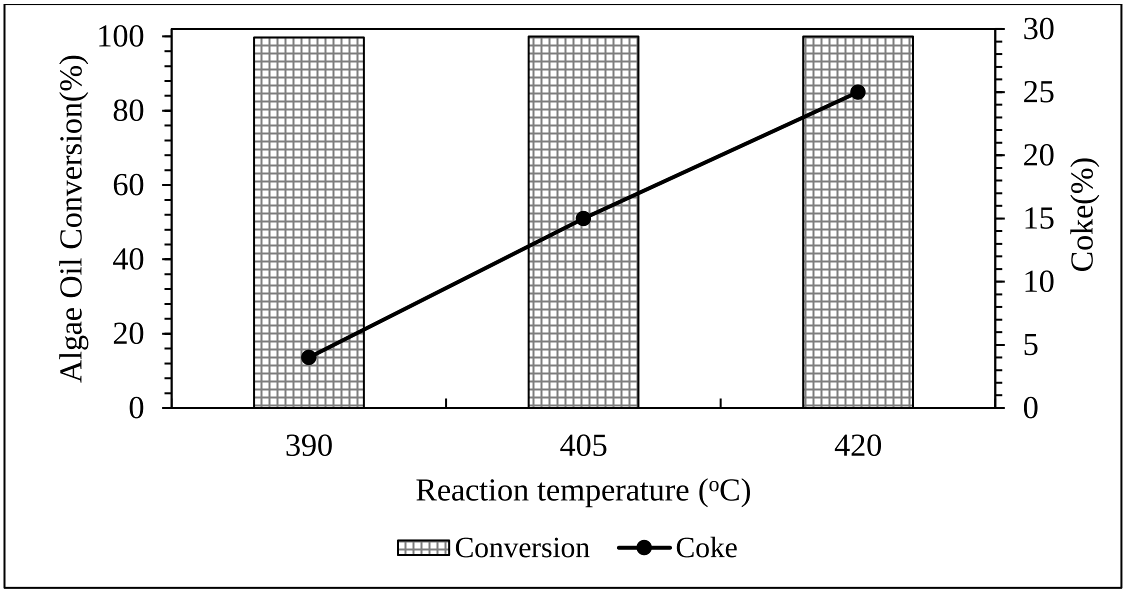

Figure C5. Variation of reaction temperature with percent conversion and coke formation.

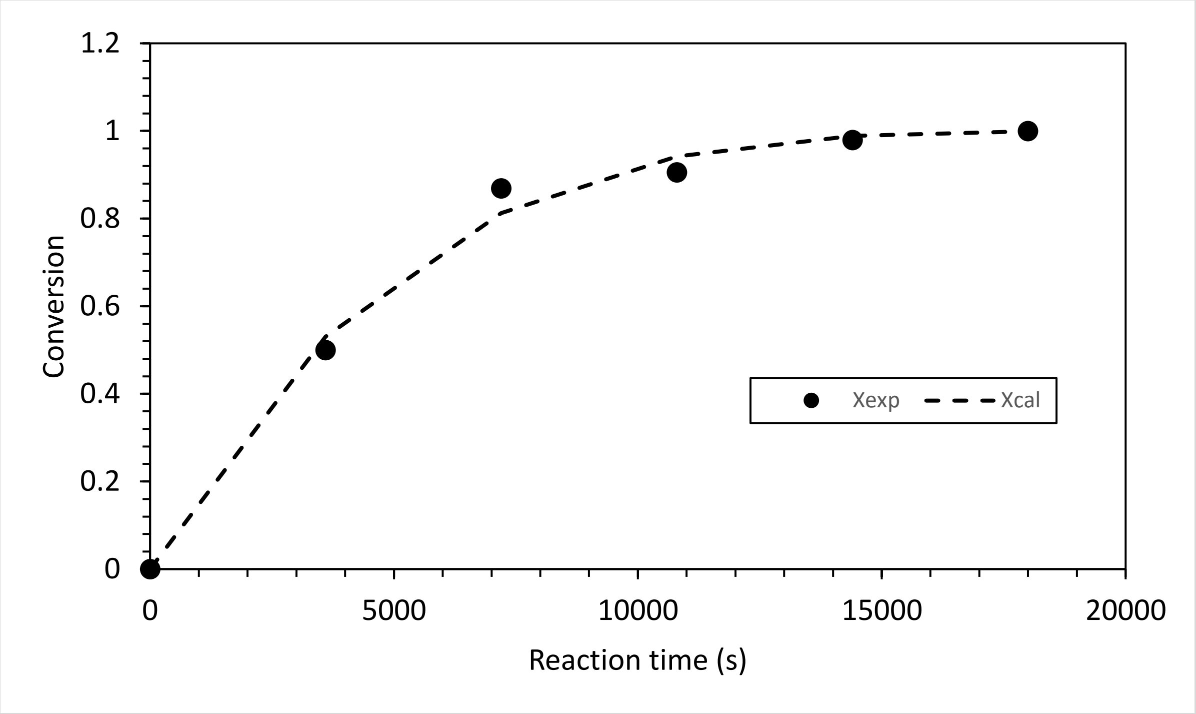

Figure C6. Curve fitting for conversion data at 390 ^{o}C

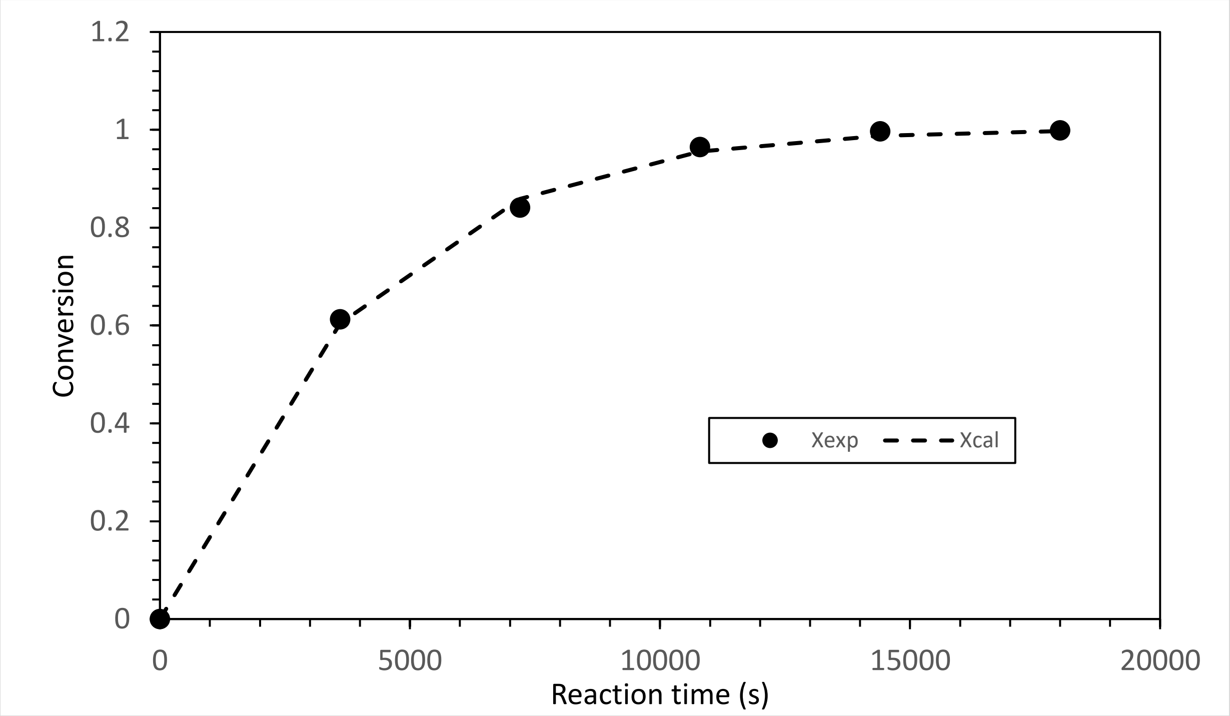

Figure C7. Curve fitting for conversion data at 405 ^{o}C

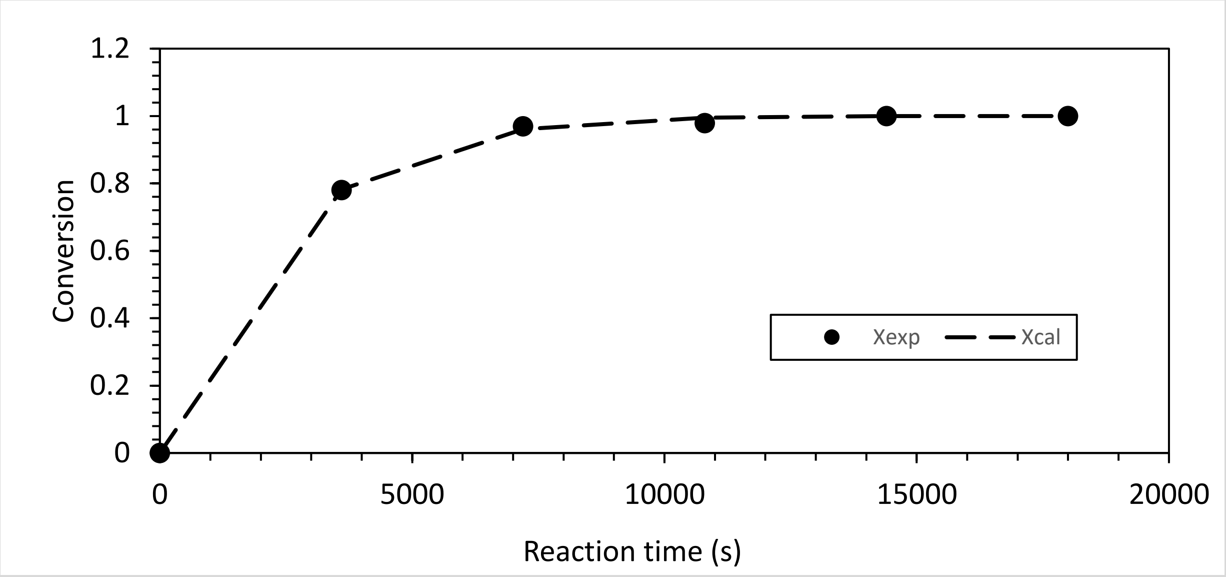

Figure C8. Curve fitting for conversion data at 420 °C

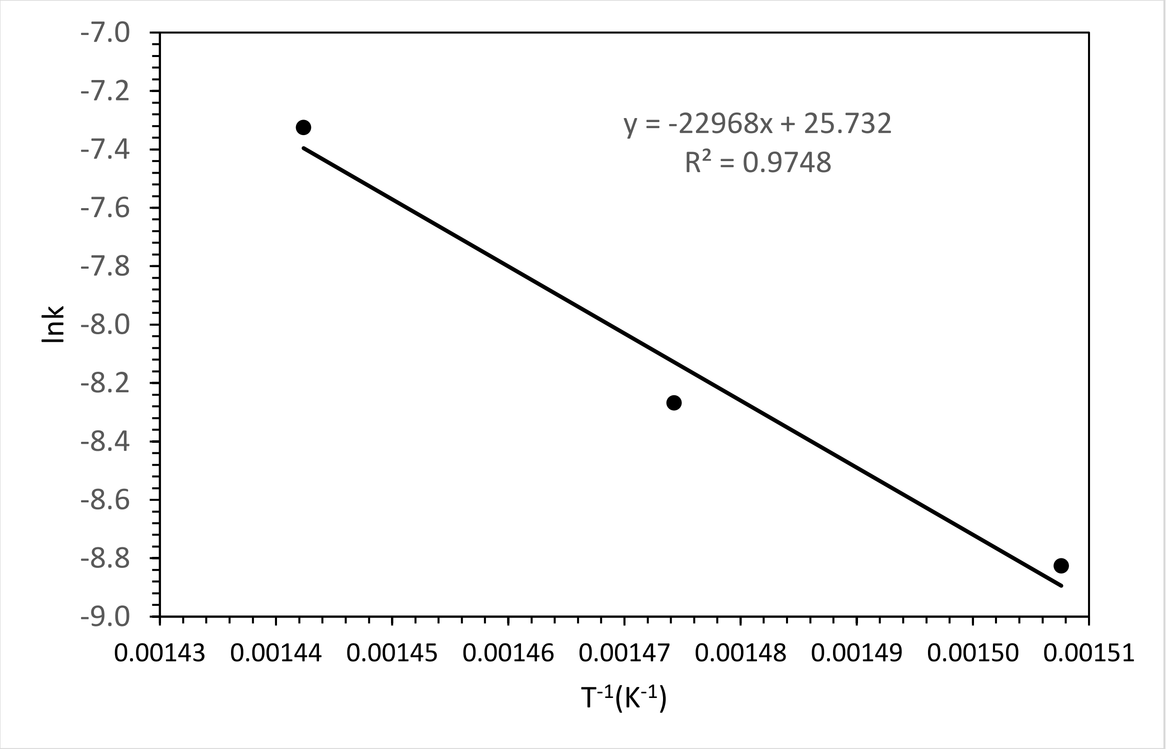

Figure C9. Arrhenius plot for the estimation of activation energy and pre-exponential factor

APPENDIX D

Techno-economic Analysis and Life-cycle Assessment of Jet Fuels Production from Waste Cooking Oil via Catalytic Transfer Hydrogenation: Supplementary Documents

Table D1. HDO Reactions Stoichiometry.

Reactions	
R.1	$C18{:}1 + H_2 \rightarrow C_{17}H_{36} + CO_2$
R.2	$C18{:}1 + 2\,H_2 \rightarrow C_{17}H_{36} + CO + H_2O$
R.3	$C18{:}1 + 4\,H_2 \rightarrow C_{18}H_{38} + 2\,H_2O$
R.4	$C18{:}2 + 2\,H_2 \rightarrow C_{17}H_{36} + CO_2$
R.5	$C18{:}2 + 3\,H_2 \rightarrow C_{17}H_{36} + CO + H_2O$
R.6	$C18{:}2 + 5\,H_2 \rightarrow C_{18}H_{38} + 2\,H_2O$
R.7	$C15{:}0 \rightarrow C_{14}H_{30} + CO_2$
R.8	$C15{:}0 + H_2 \rightarrow C_{14}H_{30} + CO + H_2O$
R.9	$C15{:}0 + 3\,H_2 \rightarrow C_{15}H_{32} + 2\,H_2O$
R.10	$C19{:}0 \rightarrow C_{18}H_{38} + CO_2$
R.11	$C19{:}0 + H_2 \rightarrow C_{18}H_{38} + CO + H_2O$
R.12	$C19{:}0 + 3\,H_2 \rightarrow C_{19}H_{40} + 2\,H_2O$
R.13	$CO + H_2O \leftrightarrow CO_2 + H_2$

Table D2. Material balance for the triglyceride cleavage.

Triglyceride Scission	Mole (kmol/day)	Mass (ton/day)
Fatty acids formed	3.64	1000
Propane formed	1.21	53.45
Hydrogen consumed	3.64	7.33

Table D3. HDO by-products separation reactor input parameters in Aspen Plus.

Process Inputs By-P-SEP	Value
Pressure (MPa)	9.2
Duty Q (adiabatic operation) (kW)	0
Valid phases	Vapor-Liquid-Dirty Water
Aspen model used	Flash
Property method	Peng-Robinson

Table D4. Property of feed oil to the hydrocracking unit in comparison to conventional VGO.

Feed property	Stream HC-MIX	VGO
°API gravity	63	22.3
SG specific gravity	0.72	0.92
TBP (°C)	270-340	450-570
Watson factor, *Kw*	13	10

Table D5. Hydrogen requirement for the hydrocracking reaction.

HCC Variable	Value	Unit
Hydrogen / Oil	500	scf/bbl
Hydrogen / Oil	84.44	Nm^3/m^3
Oil fed	63	m^3/hr
H_2 density (STD)	0.0887	kg/m^3
STD Volume H_2	5320	m^3/hr
Mass H_2	471.9	kg/hr

Table D6. HCC reactor input parameters in Aspen Plus.

Process Inputs	Value
Pressure (MPa)	9.0
Duty Q (adiabatic operation) (kW)	0
Hydrogen consumption (kg/hr)	472
Inert fraction of hydrogen	0.64
Products included	All components from C1-C18 (including isomers)
Aspen model used	RGibbs
Property method	Peng-Robinson

Table D7. Stream properties for the heat integration analysis.

Hydrodeoxygenation	T_{in} (°C)	T_{out} (°C)	Flow rate (ton/day)	mCp (kJ/C-hr)	Energy (kW)
Preheat H_2	157	400	26	15,815	1,068
Preheat WCO	25	400	1,000	105,332	10,972
Heat production HDO	157(H_2) / 400(WCO)	400	1,026	-	-5,235
Heat production HDO (Preheat of H_2)	400	400	1,026		-4,168
Heat production WGS	-	-	1,026	-	137
Cooling HDO	400	40	1,026	128,929	-12,893
Hydrocracking	T_{in} (°C)	T_{out} (°C)	Flow rate (ton/day)	mC_p (kJ/C-hr)	Energy (kW)
Preheat HCC	59	350	911	114,964	9,293
Cooling HCC	350	40	931	124,702	-10,738

Table D8. Temperatures of cold streams, hot streams, and total duty required in HEx-integrated heat exchangers.

	Hot Stream		Cold Stream		
Integrated HEx	T_{in} (°C)	T_{out} (°C)	T_{in} (°C)	T_{out} (°C)	Duty (kW)
E1	363	240	25	219	5,046.8
E2	400	400	219	380	5,228.5
E3	400	359	300	350	1,867.4
E4	372	196	59	300	7,425.6

Table D9. Utilities duty and process stream properties.

Utility	T_{in} (°C)	T_{out} (°C)	Duty (kW)
Cooling water – HDO effluent	259	40	-6,196.6
Cooling water – HCC effluent	196	40	-5,735.7
Fired heater - HDO	380	400	704.4

Table D10. Propane recovery at different pressure of flash.

Parameter	0.1 MPa	1 MPa	2 MPa	3 MPa	4 MPa
Light fuel kg/hr	5174	1817	972	583	370
Liquid distillates kg/hr	32114	35470	36315	36704	36918
Propane in light fuel kg/hr	1233	319	133	70	41
Propane in liquid distillates kg/hr	296	1209	1396	1458	1488
Propane recovery	94%	77%	53%	26%	

Table D11. Reactor geometry and catalyst properties.

Reactor	Value	Catalyst	Value
Diameter internal (cm)	1.4	Mass (g)	5.5
Length pipe (cm)	36	Volume (cm^3)	18.7
Bed length (cm)	14	Porosity (%)	0.51
Volume pipe (cm^3)	55.39	Density (g/cm^3)	0.98
ε_{gas} Void fraction	0.132	Particle size (mm)	0.85-2.4
Bed volume (cm^3)	21.54		

Table D12. Experimental conversion at different temperatures.

Reactor Temperature (°C)	300	340	360	380	400
Experimental oil conversion X	0.866	0.972	0.971	0.989	0.997

Table D13. Total naphtha composition.

Component	MW	TB	Product	% Area
C_6H_{14}	86.1772	68.73	Naphtha	2.1
C_6H_6 (AR)	78.1136	80.09	Naphtha	0.8
C_7H_{14}	98.1882	93.64	Naphtha	4.3
C_7H_{14} (E4)	98.1882	97.95	Naphtha	0.4
C_7H_{16}	100.204	98.43	Naphtha	3.2
C_8H_{18}	114.231	109.43	Naphtha	3.6
C_7H_8	100.189	109.70	Naphtha	3.2
C_8H_{16}	112.215	121.26	Naphtha	4.3
C_8H_{10} (Ethyl Benzene)	106.167	136.2	Naphtha	1.7
C_8H_{10} (p-xylene)	106.167	138.36	Naphtha	2.9
C_8H_{14}	110.10	143.00	Naphtha	0.9
C_9H_{18}	126.242	146.87	Naphtha	2.1
C_9H_{20}	128.258	150.82	Naphtha	2.8
C_9H_{12}	120.194	159.24	Naphtha	3.7
$C_{11}H_{24}$	156.312	169.77	Naphtha	2.2
Total naphtha (%)				38.00

Table D14. Total kerosene composition.

Component	MW	TB	Product	% Area
$C_{10}H_{20}$ (Alkene)	140.269	170.6	Kerosene	1.9
C_9H_{12} (AR)	118	177.97	Kerosene	0.8
$C_{10}H_{14}$ (AR)	134.221	183.30	Kerosene	2.2
$C_{11}H_{22}$ (Alkene)	154.296	192.67	Kerosene	6.2
$C_{11}H_{24}$ (Alkane)	156.312	195.93	Kerosene	1.6
$C_{11}H_{16}$ (AR)	148.248	205.46	Kerosene	2.8
$C_{12}H_{24}$ (Alkene)	168.323	213.00	Kerosene	3.2
$C_{12}H_{18}$ (AR)	162.2	215.9	Kerosene	1.1
$C_{12}H_{26}$ (Alkane)	170.338	216.32	Kerosene	3.9
C_13H_{28} (Alkane)	184.365	235.47	Kerosene	2.4
$C_{11}H_{10}$ (AR)	142.1	244.68	Kerosene	1.5
$C_{14}H_{28}$ (Alkene)	196.376	251.1	Kerosene	2.7
$C_{14}H_{30}$ (Alkane)	198.3	253.57	Kerosene	1.8
$C_{15}H_{30}$ (Alkene)	210.403	268.46	Kerosene	3.5
$C_{15}H_{32}$ (Alkane)	212.419	270.68	Kerosene	5.6
Total kerosene (%)				41.2

Table D15. Total diesel composition.

Component	MW	TB	Product	% Area
$C_{16}H_{34}$	226.446	286.86	Diesel	1.1
$C_{17}H_{34}$	238.457	292.39	Diesel	2.1
$C_{17}H_{34}$	238.457	300.33	Diesel	1.1
$C_{17}H_{36}$	240.473	302.15	Diesel	3.3
$C_{23}H_{46}$	322.618	384.66	Diesel	1.1
Total diesel (%)				8.70

Table D16. Composition of gas phase.

Component	H_2	CO	CO_2	CH_4	C_2H_6	C_3H_8
Volume (%)	21	26	22	10	10	11

Table D17. Composition of liquid product: experimental and normalized molar percentage.

Composition	Experimental	Normalized	Unit
Kerosene	41.2	46.9	% mol
Naphtha	38.0	43.2	% mol
Diesel	8.7	9.9	% mol

Table D18. Aromatics, alkanes, and alkenes in kerosene. Product characterization of liquid: average molecular weight MW and boiling point,T_b.

Kerosene Composition	Mol %	Product	MW (g/mol) Average	T_b (°C) Average
Alkenes	42.5	Naphtha	111.1	122.8
Alkanes	37.1	Kerosene	173.0	224.2
Aromatics	20.4	Diesel	248.3	308.1

Table D19. Yield of product components.

Product	Component	Yield Y_i
COKE	C	0.0219
WATER	H_2O	0.0572
LIQUID	C_8H_{16}	0.1779
	$C_{12}H_{26}$	0.3003
	$C_{17}H_{36}$	0.0910
GAS	H_2	0.0055
	CO	0.0954
	CO_2	0.1268
	CH_4	0.0210
	C_2H_6	0.0394
	C_3H_8	0.0635
	Total	1.0000

Table D20. Binary parameters of NRTL model.

Binary Parameter	$C_{17}H_{36}$- H_2O	$C_{12}H_{26}$- H_2O	C_8H_{16}- H_2O
Aij	28.2178	23.4291	0
Aji	-5.44545	-6.08871	0
Bij	-3920.97	-2638.14	2844.22
Bji	3588.23	3794.11	1431.52
C	0.2	0.2	0.2

Table D21. Verification of NRTL model: calculated and experimental values (% w/w), where W = water (H_2O) and HC =hydrocarbon.

	EXP-P	EXP-T	EXP	EXP	NRTL	NRTL	Relative Error	Relative Error
	P (Pa)	T (°C)	HC in W	W in HC	HC in W	W in HC	HC in W	W in HC
$C_{16}H_{34}$	101,000	298.1	-	6.8E-04	-	6.8E-04	-	0.00
	101,000	313.1	-	1.3E-03	-	1.3E-03	-	0.00
	101,000	298.2	3.0E-09	7.4E-04	4.90E-08	6.8E-04	0.94	0.09
$C_{12}H_{26}$	101,000	298.1	-	6.1E-04	-	6.1E-04	-	0.01
	101,000	313.1	-	1.2E-03	-	1.2E-03	-	0.00
	101,325	293.2	-	5.0E-04	-	4.8E-04	-	0.03
	101,325	303.2	-	6.0E-04	-	7.7E-04	-	0.22
C_6H_{12}	101,325	293.1	1.0E-05	-	9.71E-06	-	0.03	
	101,000	298.0	1.1E-05	-	1.14E-05	-	0.06	

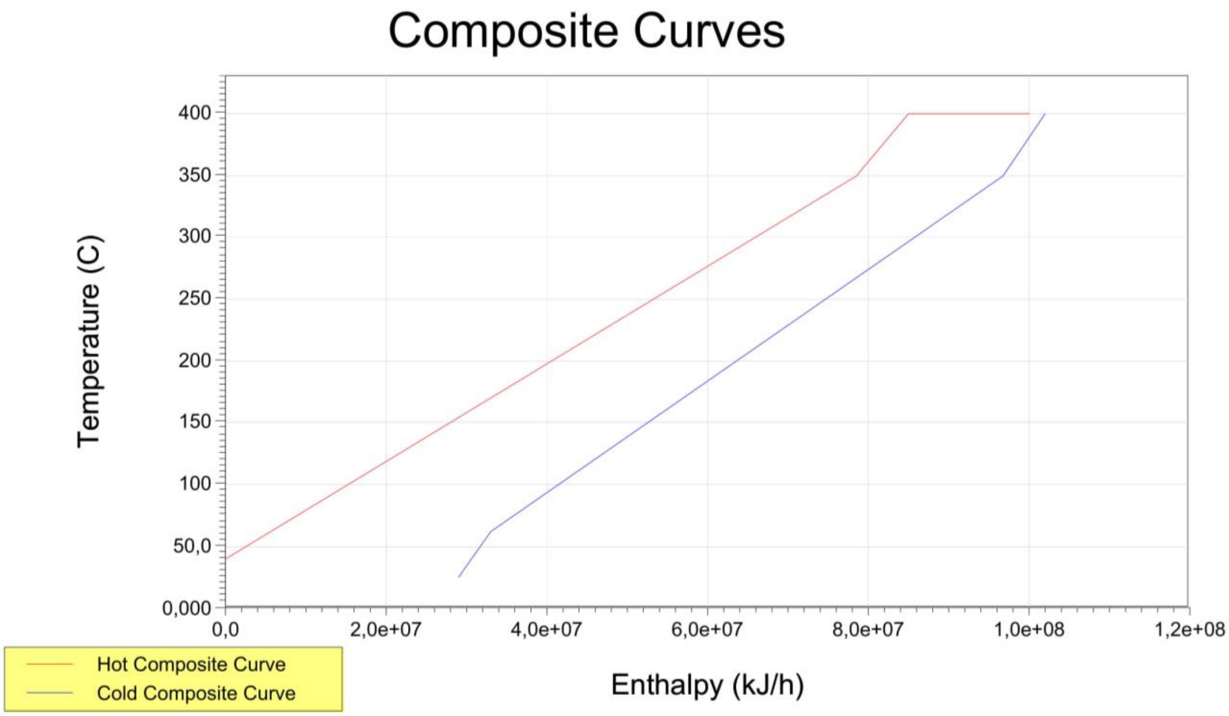

Figure D1. Composite curves of streams shown in Table D7.

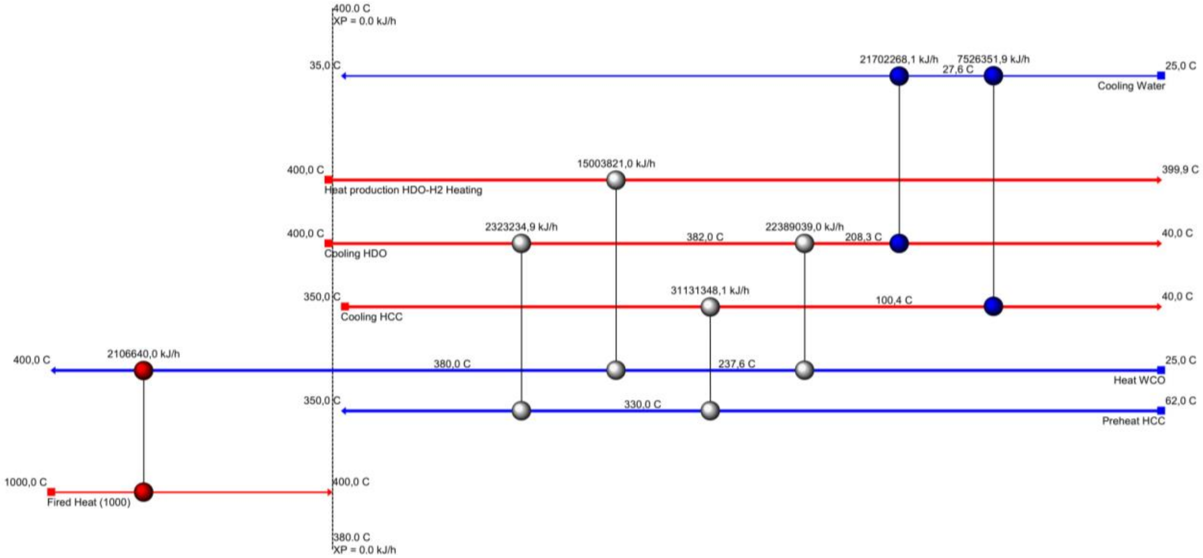
400.0 C
XP = 0.0 kJ/h
35,0 C
21702268,1 kJ/h
7526351,9 kJ/h
27,6 C
25,0 C
Cooling Water
400,0 C
15003821,0 kJ/h
399,9 C
Heat production HDO-H2 Heating
400,0 C
2323234,9 kJ/h
382,0 C
22389039,0 kJ/h
208,3 C
40,0 C
Cooling HDO
350,0 C
31131348,1 kJ/h
100,4 C
40,0 C
Cooling HCC
400,0 C
2106640,0 kJ/h
380,0 C
237,6 C
25,0 C
Heat WCO
350,0 C
330,0 C
62,0 C
Preheat HCC
1000,0 C
Fired Heat (1000)
400,0 C
380.0 C
XP = 0.0 kJ/h

Figure D2. Heat integration network (HEN).

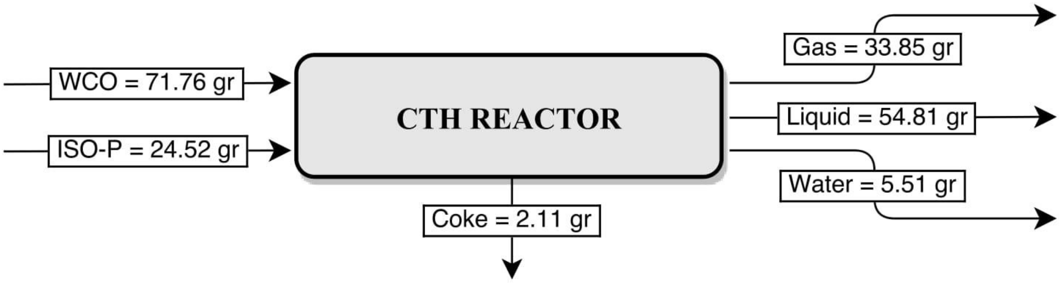
WCO = 71.76 gr
ISO-P = 24.52 gr
CTH REACTOR
Gas = 33.85 gr
Liquid = 54.81 gr
Water = 5.51 gr
Coke = 2.11 gr

Figure D3. Experimental mass balance of CTH reactor at T = 380 ºC

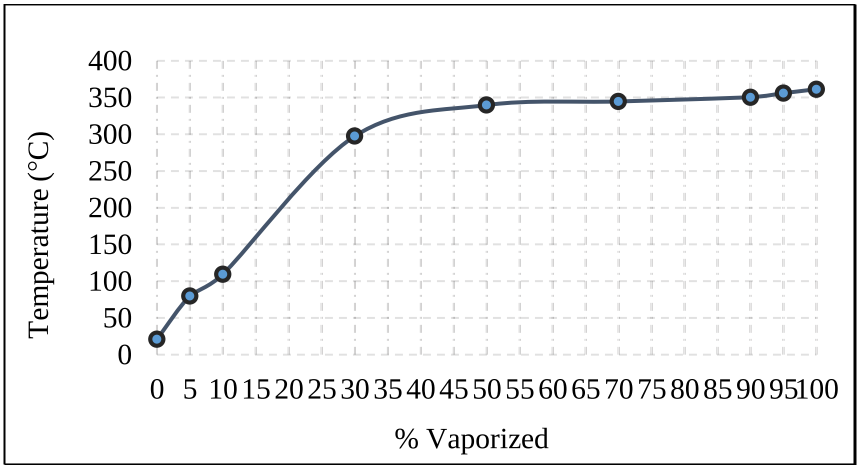

Figure D4. Mixture boiling point range of feed stream.

Fixed Capital Investment (FCI)

The fixed capital investment is the total cost of designing, constructing, and installing a plant and the associated modifications needed to prepare the plant site. The fixed capital investment is made up of:

1. The inside battery limits (ISBL) investment, i.e. the cost of the plant;
2. The modifications and improvements that must be made to the site infrastructure, known as the offsite or OSBL investment;
3. Engineering and construction costs;
4. Contingency charges.

$$\mathrm{FCI} = \mathrm{ISBL} + \mathrm{OSBL} + \mathrm{ENG} + \mathrm{CONT} \qquad \text{(D1)}$$

For the calculation of the C_{bm} of equipment, first the purchase costs (C_p) of single units are obtained from the cost-curves method which can be found in Turton et al. [242]. This cost-curves of equipment are expressed as a function of the type and the size of the corresponding unit.

Additionally, the cost of purchase is affected by inflation along with time; hence, the Chemical Engineering Plant Cost Index (CEPCI) is applied, according to Eq. D2.

$$Price_{t2} = Price_{t1}\left(\frac{CEPCI_{at\ time\ t2}}{CEPCI_{at\ time\ t1}}\right) \qquad \text{(D2)}$$

Specifically, the investment cost is based on the capacity S of hydrogen production, expressed as MMscft/day, as shown in Eq. D3. The amount of hydrogen required for the conventional process is 0.39 Mm^3/day, i.e. 13.804 MMscf/day. The values of a (1.759) and n (0.79) are on 2006-year basis; thus, the inflation rate is corrected by CEPCI reference, as indicated in Eq. D2.

$$C_{SMR} = aS^n \qquad (D3)$$

The cost of the PSA unit employed in the conventional process is based on at similar process unit for hydrogen recovery from flue gases, built in Canada in 1999. This reference unit has a different capacity; therefore, the purchase cost (C_p) is estimated using a capacity factor with a cost exponent (γ), according to Eq. D4. The reference unit considered is the amount of gas to be treated, in m^3/s. As a rough estimation, the exponent factor is assumed as 1, because the main part of the cost in the equipment will be based on the packing of adsorbent, the amount of which will be linearly proportional to the feed rate. It is specified that this method will slightly overestimate the cost, since generally the exponent factor is lower than 1.

$$C_p = \left(\frac{Capacity}{Capacity_{ref}}\right)^{\gamma} C_{p-ref} \tag{D4}$$

Results of equipment bare module costs C_{bm} are summarized in Table D22 for conventional and CTH processes, divided in groups by their function. Thus, the total bare module costs of these processes can be calculated. It is worth specifying that the CTH process conditions are the same as the base conditions, i.e. no special material is required, and the process operating pressure is atmospheric.

Table D22. Total bare module cost for HRJ (conventional) and CTH jet fuel production processes.

Equipment Type	**HRJ**		**CTH**	
Reaction System	**C_{bm} @base**	**C_{bm}**	**Reaction System**	**C_{bm}**
Hydrodeoxygenation[1]	$ 1,650,989	$ 40,814,774	Hydrodeoxygenation	$ 132,396
Hydrocracking[2]	$ 2,972,309	$ 76,618,490	2nd hydrodeox. Regen.	$ 132,396
Steam methane reform.	$ 3,441,561	$ 16,313,000		
Heating[3]	$ 1,450,520	$ 1,675,585	Heating[3]	$ 3,010,654
Compression	**C_{bm} @base**	**C_{bm}**	**Pumps**	**C_{bm}**
Compression 1	$ 448,539	$ 1,704,448	Feed pumping WCO	$ 12,046
Compression 2	$ 1,234,069	$ 4,689,461	Feed pumping ISOP[4]	$ 11,158
Feed pumping WCO	$ 73,966	$ 174,098		
Separation	**C_{bm} @base**	**C_{bm}**	**Separation**	**C_{bm}**
By-P HP separation	$ 74,603	$ 663,506	LP separation	$ 74,603
Product HP separation	$ 53,829	$ 581,562		
Product LP separation	$ 63,636	$ 63,636		
PSA-hydrogen recov.	$ 889,876	$ 2,936,590		
Distillation	**C_{bm} @base**	**C_{bm}**	**Distillation**	**C_{bm}**
Fractionation 1[5]	$ 487,216	$ 487,216	Fractionation 1[5]	$ 387,179
			Fractionation 2[5]	$ 491,028
Heat Exchangers	**C_{bm} @base**	**C_{bm}**	**Heat Exchangers**	**C_{bm}**
Heat exchange 1	$ 104,310	$ 123,010	Heat exchange 1	$ 469,833
Heat exchange 2	$ 157,024	$ 185,174		
Heat exchange 3	$ 387,390	$ 456,232		
Heat exchange 4	$ 159,540	$ 187,891		
Cooling 1[6]	$ 139,372	$ 164,358	Cooling[6]	$ 151,479
Colling 2[6]	$ 144,417	$ 169,854		
Heating[3]	$ 1,450,520	$ 1,672,574	Heating[3]	$ 2,446,909
Total (2017)	**$ 15,383,686**	**$ 149,681,462**	**Total (2017)**	**$ 7,319,681**

[1]4x5 bed, [2]5x5 bed, [3]Fired heater, [4]Three stages [5]Trays + columns [6]Cooling water

Finally, the fixed capital investment FCI of the two processes is reported in Table D23.

Table D23. Fixed Capital Investment for HRJ (conventional) and CTH jet fuel production process.

Fixed Capital Investment	HRJ	CTH
ISBL + Engineering	$ 149,681,462	$ 7,319,681
OSBL (50% total C_{bm} base)	$ 7,691,843	$ 3,659,841
Contingency (15% total C_{bm})	$ 26,942,663	$ 1,097,952
Total	**$ 184,315,968**	**$ 12,077,474**

Cost of Manufacturing (COM)

The cost of manufacturing (COM) for conventional and CTH processes are estimated as the sum of Direct Manufacturing (DMC), Fixed Manufacturing Cost (FMC), and General Expenses (GE) as follows:

$$\mathrm{COM} = \mathrm{DMC} + \mathrm{FMC} + \mathrm{GE} \tag{D5}$$

Direct manufacturing costs represent operating expenses and vary with the throughput. Therefore, these expenses comprise the costs of raw materials (RM), utilities (UT), staff and operating labor, maintenance, miscellaneous supplies and patent with royalties.

Table D24 and Table D25 summarize the results of the calculation of direct and fixed manufacturing and of general expenses for the conventional and CTH processes, respectively. Total manufacturing costs are estimated by the sum of single factors for FMC, DMC and GE, based on heuristic values for petroleum industry because of similarity with petroleum refining [241]. In particular, the maintenance, local taxes and insurance are assumed to be 5.5% and 1.5% of fixed capital investment respectively. The distribution and selling costs are assumed equal to zero, since the product price will be defined at the “gate” of the plant, i.e. not a user selling price.

Table D24. Direct (without RM+UT+WT), fixed, and general costs of manufacturing for HRJ process.

Direct (without RM+UT+WT) (DMC)		**$/year**
Total staff and operators	29	1,740,000
Maintenance and repairs	5.5% FCI	10,137,378
Miscellaneous supply	0.15% FCI	276,474
Patent and royalties	0.94 $\$/m^3$ of feed	355,151
Fixed (without depreciation) (FMC)		**$/year**
Local taxes and insurance	1.5% FCI	2,764,740
Plant overhead	60% (staff + maintenance)	7,126,427
Depreciation	-	-
General Expenses (GE)		**$/year**
Administration costs	15% (staff + maintenance)	1,781,607
Distribution and selling costs	Product based on "gate" prices	-
Research and development	5% COM	5,069,347
Total		**29,251,124**

Table D25. Direct (without RM+UT+WT), fixed, and general costs of manufacturing for CTH jet fuel production process.

Direct (without RM+UT+WT) (DMC)		**\$/year**
Total staff and operators	25	1,500,000
Maintenance and repairs	5.5% FCI	664,261
Miscellaneous supply	0.15% FCI	18,116
Patent and royalties	0.94 \$/m^3 of feed	355,151
Fixed (without depreciation) (FMC)		**\$/year**
Local taxes and insurance	1.5% FCI	181,162
Plant overhead	60% (staff + maintenance)	1,298,557
Depreciation	-	-
General Expenses (GE)		**\$/year**
Administration costs	15% (staff + maintenance)	324,639
Distribution and selling costs	Product based on "gate" prices	-
Research and development	5% COM	10,805,866
Total		**15,147,753**

The number of operators per shift was determined by Eq. D6 and multiplied by 4.5 to cover all shifts in the year. N_{eq} is the total number of equipment from Table D26. The number of all staff (clerical, engineers, technicians etc.) is estimated assuming a modern plant staff for refinery, as detailed in Table D26. The average labor wage for staff and operators in a chemical plant is 60,000 \$/year, as reported in the Bureau of Labor Statistics for 2016 [253].

$$N_{op} = \left(6.29 + 0.23N_{eq}\right)^{0.5} \qquad \text{(D6)}$$

Table D26. Staff and operators in a HRJ (conventional) and CTH jet fuel production processes. The number of staff is taken from a modern refinery.

Staff	N per shift	Conventional	CTH
Refinery manager		1	1
Operations manager		1	1
Maintenance manager		1	1
Engineers		3	3
Operators	4.5 shift per roll	15	11
Lab personnel		2	2
Technicians		2	2
Clerical personnel		4	4
Total		29	25

Accordingly, the total manufacturing cost of conventional and CTH processes are calculated and summarized in Table D27 and Table D28. It is specified that in this study the waste treatment costs (WT) were not analyzed.

Table D27. Total cost of manufacturing (COM) for HRJ (conventional) jet fuel production process.

Raw Material (RM)	**Value**	**Unit**	**$/year**
WCO	1,000	ton/day	50,000,000
Hydrogen	35.2	ton/day	18,773,333
Utilities (UT)	**Value**	**Unit**	**$/year**
Compressor 1	1,196	kW	836,586
Compressor 2 (make-up)	3,191	kW	2,230,902
Feed WCO pump	125	kW	87,540
Cooling water 1	6,197	kW	63,175
Cooling water 2	5,736	kW	58,477
Fired heater (LHV = 38.42 MJ/m^3)	704	kW	85,807
Condenser	2,042	kW	20,815
Reboiler	4,189	kW	828,901
Waste Treatment (WT)	**-**	**-**	**-**
DMC + FMC + GE (Table D24)			**29,251,124**
Total COM (without depreciation)			**102,236,661**

Table D28. Total cost of manufacturing (COM) for CTH jet fuel production process.

Raw Material (RM)	**Value**	**Unit**	**$/year**
WCO	1,000	ton/day	50,000,000
Isopropanol	341.8	ton/day	148,113,333
Utilities (UT)	**Value**	**Unit**	**$/year**
Hot oil CTH	9,508	kW	2,138,041
Feed WCO pump	2.1	kW	1,458
Feed ISOP pump	1	kW	696
Cooling water 1	3,153	kW	32,140
Fired heater (LHV = 38.42 MJ/m^3)	5,614	kW	683,904
Reboiler 1	5,034	kW	1,425,077
Reboiler 2	1,747	kW	867,511
Condenser 1	1,058	kW	10,788
Condenser 2	1,505	kW	15,348
Waste Treatment (WT)	**-**	**-**	**-**
DMC + FMC + GE (Table D25)			**15,147,753**
Total COM (without depreciation)			**218,436,050**

Products Profile and Gross Profit

Products Profile and Revenues

The gross income from refinery products sales was calculated considering prices at the refinery gate, which includes the cost of production and refiner profit. They do not account for the costs for distribution, transportation, retail mark-up and taxes. The gate prices for gasoline and diesel were calculated subtracting the average percentage of taxes (TAX%) and distribution and market (D&M) price from the corresponding average retail price of 2017. In this way, only wholesale price is accounted for the revenues of gasoline and diesel. The kerosene price is instead already defined at refinery gate, since U.S Energy Information and Administration provide prices of distillates in the refinery [254]. The average prices of these fuels for 2017 are summarized in Table D29.

Table D29. Gate prices of products: gasoline, jet fuel, and diesel. naphtha prices are taken as surrogate for gasoline price, respectively.

Product Gate Price	Average (2017)
Gasoline (naphtha)	0.426 $/L
JET-F (kerosene)	0.443 $/L
Diesel	0.440 $/L

The volumetric flowrates of each product

It is noted that the specific gravity SG of naphtha, kerosene, and diesel can be calculated from the definition of °API (Eq. D7). The average values of °API gravity for naphtha, kerosene, and diesel based on respective temperature ranges are shown in Table D30.

$$°API = \frac{141.5}{SG} - 131.5 \tag{D7}$$

Table D30. Specific gravity of products.

Fuel Products	API°	SG
Naphtha (80-170°C)	62	0.731
Kerosene (170-270°C)	42	0.815
Diesel (270-380°C)	38	0.835

Finally, the product revenues calculated from the amount and unitary price of respective fractions are summarized in Table D31.

Table D31. Product incomes for HRJ (conventional) and CTH jet fuel production process.

	HRJ			CTH		
Fuel Product	Produced	Unit	Income ($/yr)	Produced	Unit	Income ($/yr)
Fuel gas	6,969	Nm^3/hr	9,433,018	12,978	Nm^3/hr	13,497,224
Naphtha	8,041	L/hr	27,405,246	12,042	L/hr	41,038,506
Kerosene	32,166	L/hr	113,969,798	24,084	L/hr	85,333,119
Diesel	-	L/hr	-	4,014	L/hr	13,997,406
Total revenue			150,808,063			153,866,254

Gross Profit (GP)

The GP is defined as the difference between revenues from the products and the cost of manufacturing without depreciation (COM_d). The estimation of the gross profit GP without depreciation for conventional and CTH are reported in Table D32.

Table D32. Gross profit for HRJ (conventional) and CTH jet fuel production processes.

Economic Parameter	HRJ ($/year)	CTH ($/yr)
Revenues (R)	150,808,063	153,866,254
Cost of manufacturing (COM_d)	102,236,661	218,436,050
Gross Profit (GP)	48,571,402	-64,569,796

Economic Model and Profitability Analysis

Economic Model

The assumptions used are summarized in Table D33. In this study, similar values are adopted as those of other authors from the U.S. that have recently worked on the profitability of similar processes [21-22].

Table D33. Economic model assumptions.

Interest/discount rate	8%
Plant life	25 years
Income tax rate	35%
Working capital	15% of ISBL + OSBL
Depreciation method	MACRS
Depreciation period	7 years
Construction + Start-up period	2 years
Construction plant 1st/2nd year	70%/30%
Plant salvage value	No value
Land cost	not included
Operating hours per year (91.3%)	8,000 hours

The cash flow (CF) is defined as the amount of money transferred at given time. Therefore, it depends on the FCI distributed over the time of construction, the working capital (WC), the net profit, and the depreciation allowance d. Accordingly, the CF after the plant was started up is determined by the net profit (Eq. D8)) plus the depreciation allowance as reported in Eq.D9:

$$\text{After Tax Profit or Net profit} = (\text{GP} - d_k)(1 - t) \tag{D8}$$

$$\text{CF} = \text{Net profit} + \text{depreciation allowance} = (\text{GP} - d_k)(1 - t) + d_k \tag{D9}$$

where d_k is the value of depreciation at year k, GP the gross profit and t is the tax rate.

The MACRS method for the depreciation uses following equations Eq. D10:

$$\text{MACRS} = \begin{cases} d_k^{DDB} = \dfrac{2}{n}\left(\text{FCI} - \displaystyle\sum_{1}^{k-1} d_j\right) \\ d_k^{SL} = \dfrac{\left(\text{FCI} - \sum_{1}^{k-1} d_j\right)}{n}, \text{when } d_k^{DDB} < d_k^{SL} \end{cases} \tag{D10}$$

where n is the depreciation period. For MACRS method, the depreciation starts with the double declining balance d^{DDB}, and changed to the straight line d^{SL} for the remaining period, when the latter value is bigger than d^{DDB}.

The Annualized Cash Flow (ACF) of each year is discounted back to the year 0 as given in Eq. D11, with an interest rate equal to 8%.

$$\mathrm{ACF_k} = \frac{\mathrm{CF_k}}{(1+\mathrm{i})^{\mathrm{k}}} \qquad \text{(D11)}$$

The three discounted profitability criteria are time, cash and interest rate, i.e. Net Present Value (NPV), Internal Rate of Return (IRR), Discounted Pay Back Period (DPBP), and Present Value Ratio (PVR), evaluated **by** Eq. D12-Eq. D15.

$$\mathrm{NPV} = \sum_{1}^{\text{plant life}} \frac{\mathrm{CF_k}}{(1+\mathrm{i})^{\mathrm{k}}} \qquad \text{(D12)}$$

$$\sum_{1}^{\text{Plant life}} \frac{\mathrm{CF_k}}{(1+\mathrm{IRR})^{\mathrm{k}}} = 0 \qquad \text{(D13)}$$

$$\sum_{1}^{2} \frac{\mathrm{FCI_k}}{(1+\mathrm{i})^{\mathrm{k}}} = \sum_{3}^{\mathrm{DPBP}-3} \frac{\mathrm{CF_k}}{(1+\mathrm{i})^{\mathrm{k}}} \qquad \text{(D14)}$$

$$\mathrm{PVR} = \frac{\text{present value of all positive CF}}{\text{present value of all negative CF}} \qquad \text{(D15)}$$

The internal rate of return (IRR) is the value of interest rate in Eq. D13, when the net present value NPV is set to zero. The Eq. D14 assumes that the completion of construction lasts 2 years hence the DBPB starts from the 3rd year, as reported in Table D33. The DPBP can be also estimated from the working capital cost WC, i.e. it is the time when the cumulative cash flows equal the amount of WC. The Present Value Ratio (PVR) in Eq. D15 is ratio between all positive cash flows and all negative ones. When the difference of investments of two projects is very large, it might be useful to compare this term rather than NPV.

Hydroprocessed Renewable Jet Fuels Profitability Analysis

With the assumptions from Table D33, the cumulative cash flow diagram for the conventional process can be generated.

Catalytic Transfer Hydrogenation Profitability Analysis

The profitability analysis for CTH process was evaluated and different cases are considered. Specifically, the isopropanol price and its feed rate are analyzed in order to have, first, a profitable process at the end of the project life (NPV > 0) and secondly, to compete with conventional process. Accordingly, the values of DPBP and PRV for HRJ are used as objective functions.

Moreover, a possible government incentive tax credit ($/L) is discussed and calculated as a revenue from each liter of kerosene produced, according to Table D34.

The results of profitability analysis are summarized in Table D34 for all the cases listed below.

1. Price of isopropanol ($/kg) to have NPV = 0. This is a measure of the maximum price that project could pay for isopropanol and still break even by the end of the project.
2. Price of isopropanol ($/kg) to have CTH NPV = HRJ NPV.
3. Price of isopropanol ($/kg) to have CTH DPBP = HRJ DPBP.
4. Price of isopropanol ($/kg) to have CTH PVR = HRJ PVR.
5. Amount of isopropanol (ton/day) to have NPV = 0. This is a measure of the maximum feed rate to reach profitable condition at the end of the project life.
6. Amount of isopropanol (ton/day) to have CTH NPV = HRJ NPV.
7. Amount of isopropanol (ton/day) to have CTH DPBP = HRJ DPBP.
8. Amount of isopropanol (ton/day) to have CTH PVR = HRJ PVR.

9. Incentive tax for kerosene jet fuel ($/L) to have NPV = 0. This is the minimum incentive to reach a profit at the end of the project.
10. Incentive tax for kerosene jet fuel ($/L) to have CTH NPV = HRJ NPV.
11. Incentive tax for kerosene jet fuel ($/L) to have CTH DPBP = HRJ DPBP.
12. Incentive tax for kerosene jet fuel ($/L) to have CTH PVR = HRJ PVR.

Table D34. Profitability analysis of CTH: isopropanol price, feed, and incentive tax credit analysis.

Case	**Isopropanol Price**	**Price**	**Unit**
1	Profitable NPV>0	0.748	$/kg
2	CTH SAME NPV as Conventional	0.556	$/kg
3	CTH SAME DPBP as Conventional	0.735	$/kg
4	CTH SAME PVR as Conventional	0.735	$/kg
Case	**Isopropanol Feed**	**Feed**	**Unit**
5	Profitable NPV>0	196.535	ton/day
6	CTH SAME NPV as Conventional	146.145	ton/day
7	CTH SAME DPBP as Conventional	193.206	ton/day
8	CTH SAME PVR as Conventional	193.210	ton/day
Case	**Incentive Tax Credit for Kerosene**	**Tax Credit**	**Unit**
9	Profitable NPV>0	0.344	$/L
10	CTH SAME NPV as Conventional	0.463	$/L
11	CTH SAME DPBP as Conventional	0.352	$/L
12	CTH SAME PVR as Conventional	0.352	$/L

Table D35. Triangular probability distributions of materials and process conditions.

Parameter	Value
Distance hauled (miles/truck-d)	Min = 280, Likeliest = 300, Max = 350
Mileage efficiency (miles/gal)[258]	Min = 4.5, Likeliest = 5.5, Max = 6.5
HY temperature (°C)	Min = 395, Likeliest = 400, Max = 405
HY pressure (bar)	Min = 85, Likeliest = 92, Max = 100
HY reaction time (hr)	Min = 1, Likeliest = 2, Max = 3
WCO linoleic acid fraction	Min = 0.48, Likeliest = 0.52, Max = 0.55
WCO oleic acid fraction	Min = 0.15, Likeliest = 0.19, Max = 0.22
WCO pentadecanoic acid fraction	Min = 0.16, Likeliest = 0.18, Max = 0.20
WCO nonadecanoic acid fraction	Min = 0.09, Likeliest = 0.11, Max = 0.15
FS pressure (MPa)	Min = 9, Likeliest = 9.2, Max = 9.5
FS liquid hold-up time (min)[241]	Min = 9.9, Likeliest = 10, Max = 10.5
HH temperature (°C)	Min = 330, Likeliest = 350, Max = 370
HH pressure (MPa)	Min = 8.5, Likeliest = 9, Max = 9.5
HH reaction time (hr)	Min = 0.8, Likeliest = 1, Max = 1.2
HF pressure (MPa)	Min = 8.5, Likeliest = 9, Max = 9.5
HF liquid hold-up time (min)[241]	Min = 9.9, Likeliest = 10, Max = 10.5
LF pressure (MPa)	Min = 0.09, Likeliest = 0.10, Max = 0.11
LF liquid hold-up time (min)[241]	Min = 9.9, Likeliest = 10, Max = 10.5
DT pressure (MPa)	Min = 0.09, Likeliest = 0.10, Max = 0.11
DT number of stages	Min = 27, Likeliest = 30, Max = 33
DT reboiler temperature (°C)	Min = 160, Likeliest = 164.8, Max = 170
DT condenser temperature (°C)	Min = 60, Likeliest = 65.3, Max = 70
CH temperature (°C)[97]	Min = 370, Likeliest = 380, Max = 390
CH pressure (bar)[97]	Min = 1.5, Likeliest = 2, Max = 2.5
Weight hourly space velocity (1/hr)[97]	Min = 6.5, Likeliest = 6.8, Max = 7
DT1 pressure (MPa)	Min = 0.09, Likeliest = 0.10, Max = 0.11
DT1 number of stages	Min = 9.9, Likeliest = 10, Max = 10.5
DT1 reboiler temperature (°C)	Min = 200, Likeliest = 220, Max = 240
DT1 condenser temperature (°C)	Min = 120, Likeliest = 130, Max = 140
DT2 pressure (MPa)	Min = 0.09, Likeliest = 0.10, Max = 0.11
DT12 number of stages	Min = 13, Likeliest = 15, Max = 17
DT2 reboiler temperature (°C)	Min = 280, Likeliest = 299, Max = 320
DT2 condenser temperature (°C)	Min = 200, Likeliest = 212, Max = 225

Table D36. Sub-system life cycle inventory for HRJ and CTH. Energy and heat are in MJ/day and materials and chemicals are in tons/day.

Energy/Materials	Input	Output
HRJ		
Waste cooking oil transport		
Diesel	9.47	
CO_2		27.15
H_2O		10.65
Hydrodeoxygenation		
Electricity	321,091.20	
Heat	512,599.92	
WCO	1,000.00	
H_2 (gross)	26.08	
H_2 (net, minus recyle)*	35.20	
Ni-Mo/Al_2O_3	3.26	
CO and CO_2 flash separation		
Heat (Cooling)		535,384.56
CO		3.36
CO_2		22.48
H_2O		0.10
Propane gas		4.12
H_2		2.34
Sour water (H_2O + CO_2)		37.77
Hydroisomerization and hydrocraking		
H_2	33.96	
High pressure flash		
Heat (Cooling)		495,567.98
H_2	23.40	
H_2		22.47
CO		7.31
CO_2		47.45
C1-C3 gas		54.22
C4-C8		8.88
C9-C15		0.29
Low pressure flash		
H_2		0.94
CO		0.75
CO_2		33.37
C1-C3 gas		43.42
C4-C8		42.93
C9-C15		0.90
C1-C3 liquid (LPG)		7.52
C16-C18 (diesel)		2.64
Liquid CO_2		1.52
Distillation		
Electricity	361,968.00	
Heat (Cooling)		176,408.16
Naphtha		267.80
Jet fuel		478.37
Fuel transport		

Table D36. Sub-system life cycle inventory for HRJ and CTH. Energy and heat are in MJ/day and materials and chemicals are in tons/day cont.

Diesel	7.06	
CO_2		20.26
H_2O		7.94
Infrastructure		
Steel	0.0017	
CTH		
Waste cooking oil transport		
Diesel	9.47	
CO_2		27.15
H_2O		10.65
Catalytic transfer hydrogenation		
Electricity	266.30	
Heat	485,100.00	
WCO	1,000.00	
2-propanol	341.80	
Activated carbon	0.0913	
Coke		29.41
Low pressure flash		
Heat (Cooling)		272,377.44
H_2		6.85
CO		127.90
CO_2		169.39
H_2O		0.02
C1-C3 gas		161.85
Octane		5.83
Dodecane		0.11
Acidic water (H_2O + CO_2 + CO)		72.06
C1-C3 liquid (LPG)		4.40
Distillation 1		
Electricity	7,542.40	
Heat (Cooling)		91,416.00
Naphtha		229.59
Jet fuel		3.40
Distillation 2		
Electricity	150,888.00	
Heat (Cooling)		130,056.00
Naphtha		3.27
Jet fuel		399.48
Diesel		122.13
Fuel transport		
Diesel	4.97	
CO_2		14.25
H_2O		5.59

*Net H_2 requirement is 35.20 tons/day, of which 22.93 tons/day is consumed in the hydrodeoxygenation reactor, 11.34 ton/day in the hydrocracking unit, and 0.93 ton/day are lost in the light gas stream separated by the low-pressure flash.

APPENDIX E

ANALYTICAL METHODS EMPLOYED IN THIS STUDY

GAS CHROMATOGRAPHY SPECTROMETRIC ANALYSIS

Shimadzu GCMS-QP2010SE and Gas chromatography GC2010 plus was employed in the analysis of fuel liquid. This instrument has a high level of sensitivity as it employs quadrupole ion focusing facility with mass-to-charge ratio of 1000. To ensure accuracy of the analysis and the safety of the instrument, the following routine precautions were maintained.

1. Helium gas (99.995%) was used as carrier gas with supply pressure of 700-800 kPa was applied.
2. To start the instrument, the carrier gas was turned on from the main valve on the gas cylinder to register ~700-800 kPa.
3. It was ensured that the breaker controlling the instrument was on all the time.
4. The GC was turned on, followed by the computer and its monitor.
5. The MS was turned on, making sure the LED in the upper left corner was lit.
6. Method File was created by clicking “file” and “Method” in the menu bar.
7. Figure E1 highlights the real-time analysis program when the system is completely turned on.
8. To ensure proper operation of the instrument, system check was performed to eliminate leaks, overuse of parts, increase sensitivity, etc.
9. The system was tuned in by clicking “Auto tuning” icon in the Assistant Bar.
10. After tuning the system, the tuning file was saved.

11. Corrective measures were performed after tuning. For example, looking and fixing leaks, changing ferrule, cleaning the ion source, etc.
12. It was made sure that the column was baked for 30 minutes at 300 °C to eliminate contaminants after the column had been used for a long time. This was done by disconnecting the column and the mass spectrum (MS) and allowed helium gas to flow through column.
13. When there was a column change, moisture was eliminated allowing helium gas to flow through at 110°C for few minutes.

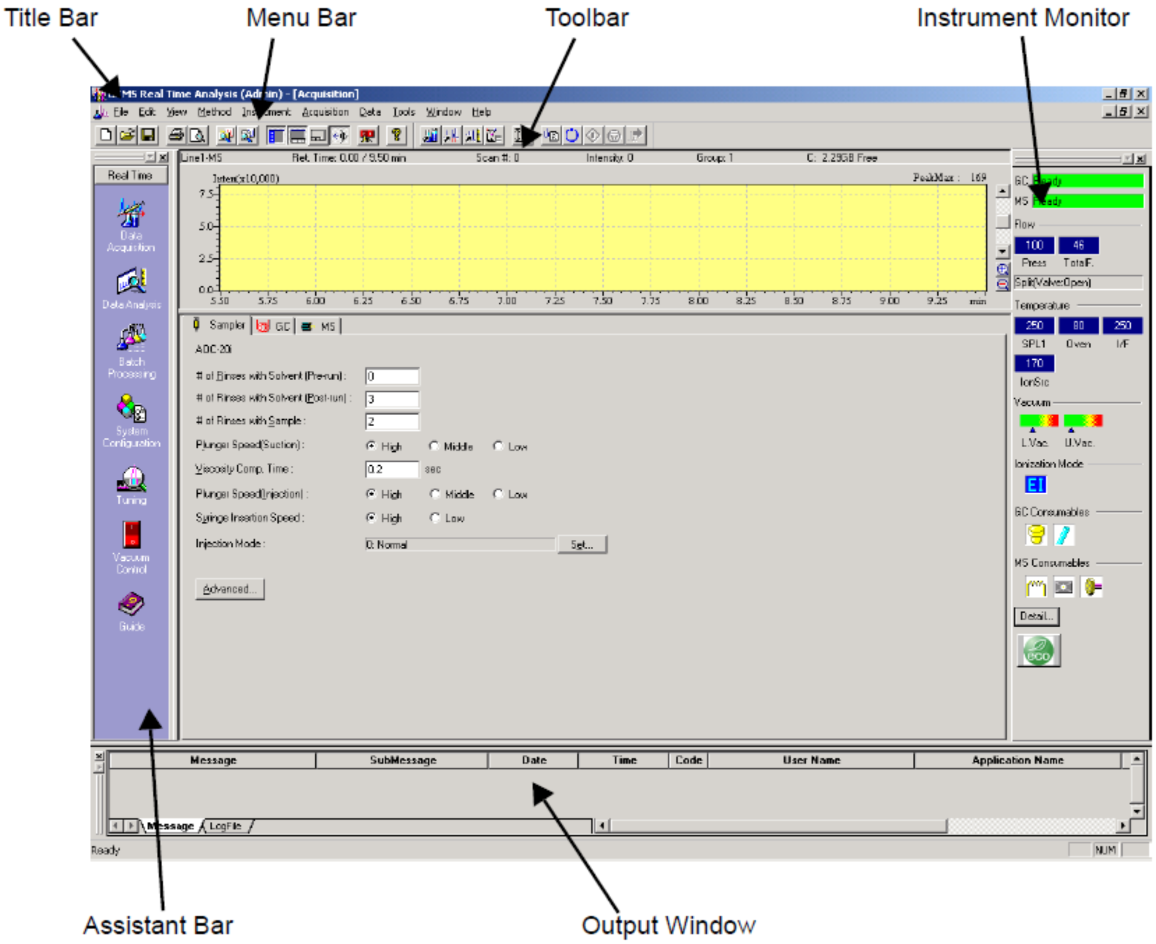
Title Bar
Menu Bar
Toolbar
Instrument Monitor
GCMS Real Time Analysis (Admin) - [Acquisition]
File Edit View Method Instrument Acquisition Data Tools Window Help
Real Time
Data Acquisition
Data Analysis
Batch Processing
System Configuration
Tuning
Vacuum Control
Guide
Inten(x10,000)
PeakMax : 169
7.5
5.0
2.5
0.0
5.50
5.75
6.00
6.25
6.50
6.75
7.00
7.25
7.50
7.75
8.00
8.25
8.50
8.75
9.00
9.25
min
Sampler
GC
MS
Set...
Advanced...
Flow
Temperature
Vacuum
L.Vac.
U.Vac.
Ionization Mode
GC Consumables
MS Consumables
Detail...
eco
Message
SubMessage
Date
Time
Code
User Name
Application Name
Message
LogFile
Ready
NUM
Assistant Bar
Output Window

Line1-MS Ret. Time: 0.00 / 9.50 min Scan #: 0 Intensity: 0 Group: 1 C: 2.29GB Free

ADC-20i

# of Rinses with Solvent (Pre-run) : 0

# of Rinses with Solvent (Post-run) : 3

# of Rinses with Sample : 2

Plunger Speed(Suction) : ● High ○ Middle ○ Low

Viscosity Comp. Time : 0.2 sec

Plunger Speed(Injection) : ● High ○ Middle ○ Low

Syringe Insertion Speed : ● High ○ Low

Injection Mode : 0: Normal

GC Ready

MS Ready

100 Press

46 TotalF.

Split(Valve:Open)

250 SPL1

80 Oven

250 I/F

170 IonSrc

EI

Figure E1. "GCMS Real Time Analysis" Program

E1. SELECTION OF THE RIGHT INJECTION PORT.

Since the GCMS has two different sample injection port (one for GC and the other for pyrolysis), the correct injection port must be selected by the follow procedure.

1. Click on "System configuration" icon.
2. Add or remove the available module as shown in Figure E2.
3. Select Analytical Line #1 for GC while Analytical Line #2 for pyrolysis
4. For GC, select AOC 20i, and for pyrolysis select PY.
5. Select MS for both GC and pyrolysis.

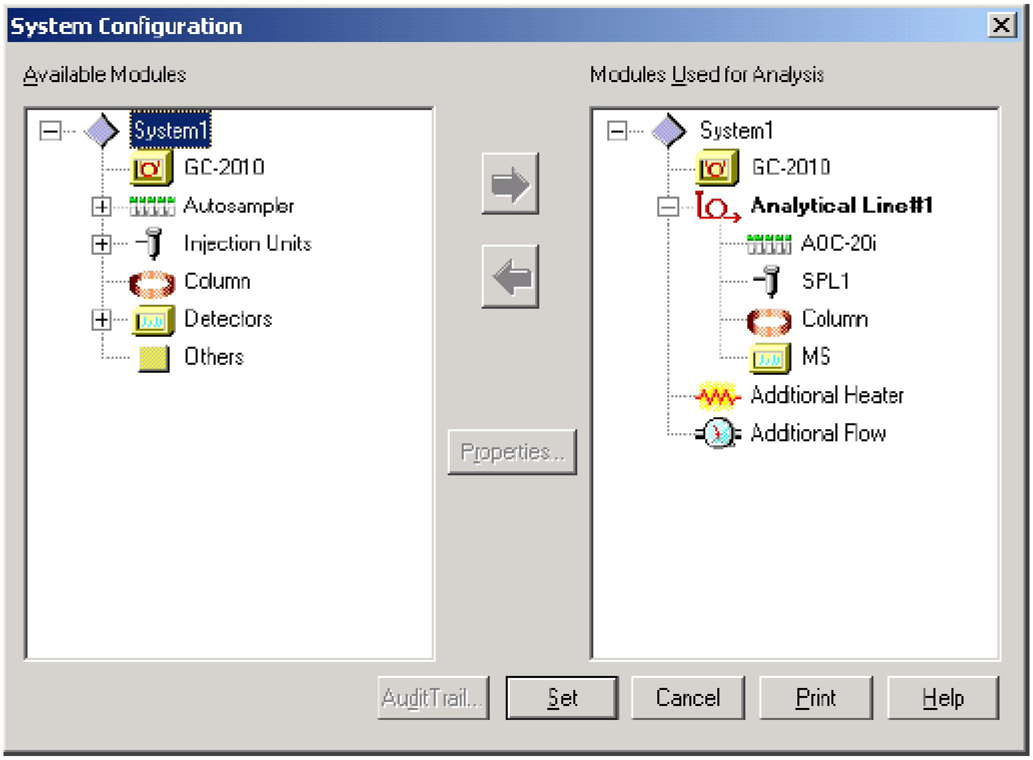
System Configuration
Available Modules
System1
GC-2010
Autosampler
Injection Units
Column
Detectors
Others
Modules Used for Analysis
System1
GC-2010
Analytical Line#1
AOC-20i
SPL1
Column
MS
Addtional Heater
Addtional Flow
Propeties...
AuditTrail...
Set
Cancel
Print
Help

Figure E2. "System Configuration" dialogue box.

E2. DATA ACQUISITION

This section deals with the setting the instrument parameters to run samples (liquid fuel products). The following procedure elucidate the advanced setting the instrument parameters.

1. Select View and click the Instrument parameters.
2. Click on the GC tab as shown in Figure E3.
3. Set the temperature program and carrier gas flow parameters.
4. Repeat the procedure to set the MS parameters.

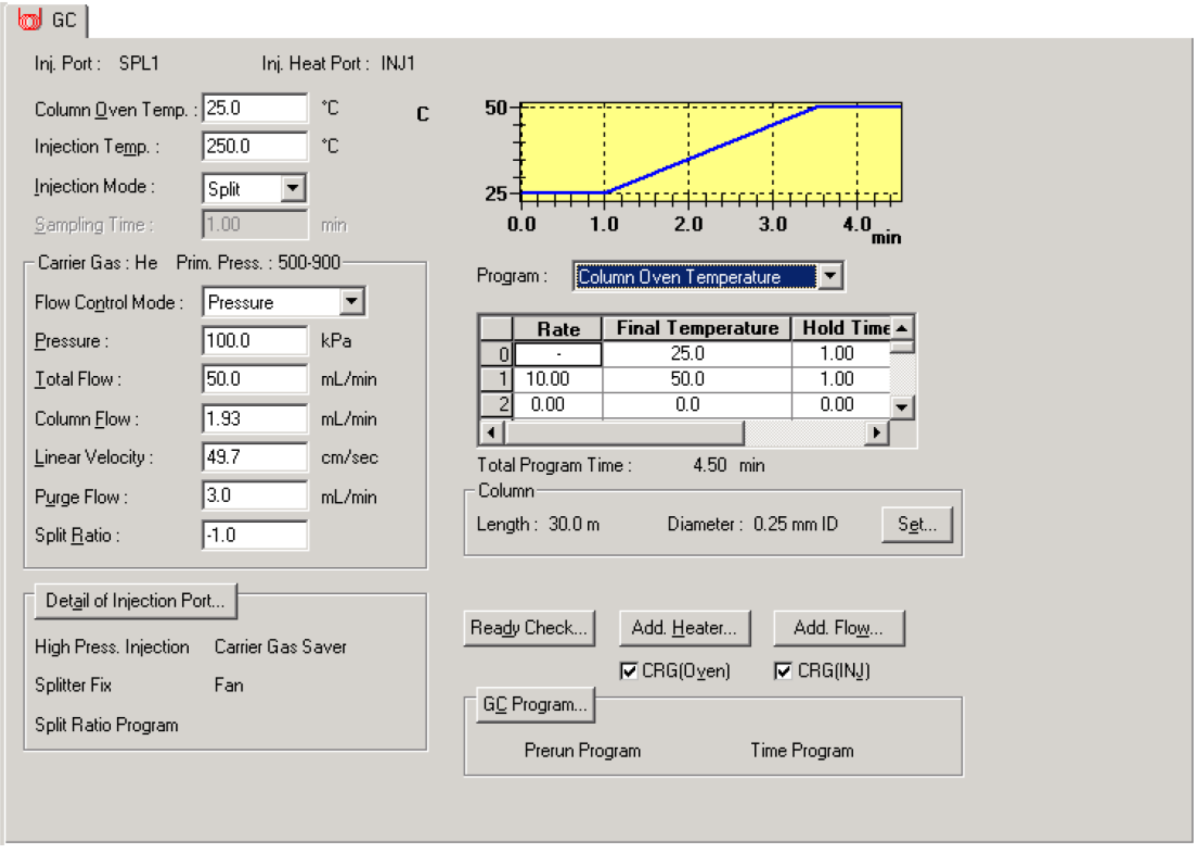
GC
C
50
25
0.0
1.0
2.0
3.0
4.0
min
Detail of Injection Port...
High Press. Injection
Carrier Gas Saver
Splitter Fix
Fan
Split Ratio Program
Set...
Ready Check...
Add. Heater...
Add. Flow...
GC Program...
Prerun Program
Time Program

Inj. Port : SPL1
Inj. Heat Port : INJ1
Column Oven Temp. : 25.0 °C
Injection Temp. : 250.0 °C
Injection Mode : Split
Sampling Time : 1.00 min
Carrier Gas : He
Prim. Press. : 500-900
Flow Control Mode : Pressure
Pressure : 100.0 kPa
Total Flow : 50.0 mL/min
Column Flow : 1.93 mL/min
Linear Velocity : 49.7 cm/sec
Purge Flow : 3.0 mL/min
Split Ratio : -1.0

Program : Column Oven Temperature

	Rate	Final Temperature	Hold Time
0	-	25.0	1.00
1	10.00	50.0	1.00
2	0.00	0.0	0.00

Total Program Time : 4.50 min

Column
Length : 30.0 m
Diameter : 0.25 mm ID

☑ CRG(Oven)
☑ CRG(INJ)

Figure E3. GC Parameters Tab.

E3. LIQUID FUEL ANALYSIS

E3.1. Parameter setting

1. The final temperature for the column was set to 250 ^{o}C
2. 40 ^{o}C was assigned to the oven temperature.
3. Injection temperature was set to 250 ^{o}C.
4. The ramp temperature was set to 20 ^{o}C/min.
5. The split ratio was selected between 100-200 as the component’s concentration varied for different samples.
6. The column pressure was set to 45 kPa, which automatically changed the linear velocity to nearly 36 cm/s.
7. The column purge flow was set to 0.5.
8. MS ion source was set to 225 ^{o}C and solvent cut time was set to 0.5 less than the start time.
9. The scan speed of the MS was set to 666.

E3.2. Sample preparation

1. 0.1 mL liquid sample was pipetted into a 2-mLvial
2. The sample was diluted with hexane (99.99%) to prepare 10 ppm solution
3. 2 mL of the hexane was used as blank.
4. The samples were placed in the auto sampler and analyzed.

E4. PYROLYSIS ANALYSIS

Since the pyrolysis unit has its own column that connects the MS, the GC column should be replaced by that of the pyrolysis. To run the pyro-GCMS, the following procedure was followed.

1. Connect the pyrolysis column to the MS-Pyrolysis interface.
2. Open the pyrolysis program and set the necessary parameters as shown in Figure E4
3. In the menu bar of the GC Click “Acquisition” and select “download parameter.”
4. On the menu bar, select the “Instrument”, the “sample inlet unit”, and “line 2.”
5. Also, select “download parameter” in the “instrument.”
6. Load the 1.0 mg sample into the crucible and place it in the pyrolysis unit.
7. Click “sample login” icon in the assistant bar and enter the necessary parameters.
8. Click the “download” icon.
9. Click “start” button on the Acquisition software.
10. Click “start” in the pyrolysis software and press the sample holder of the pyrolysis unit to release the sample.
11. Quickly click the “start” button on the pyrolysis software and allow it run.

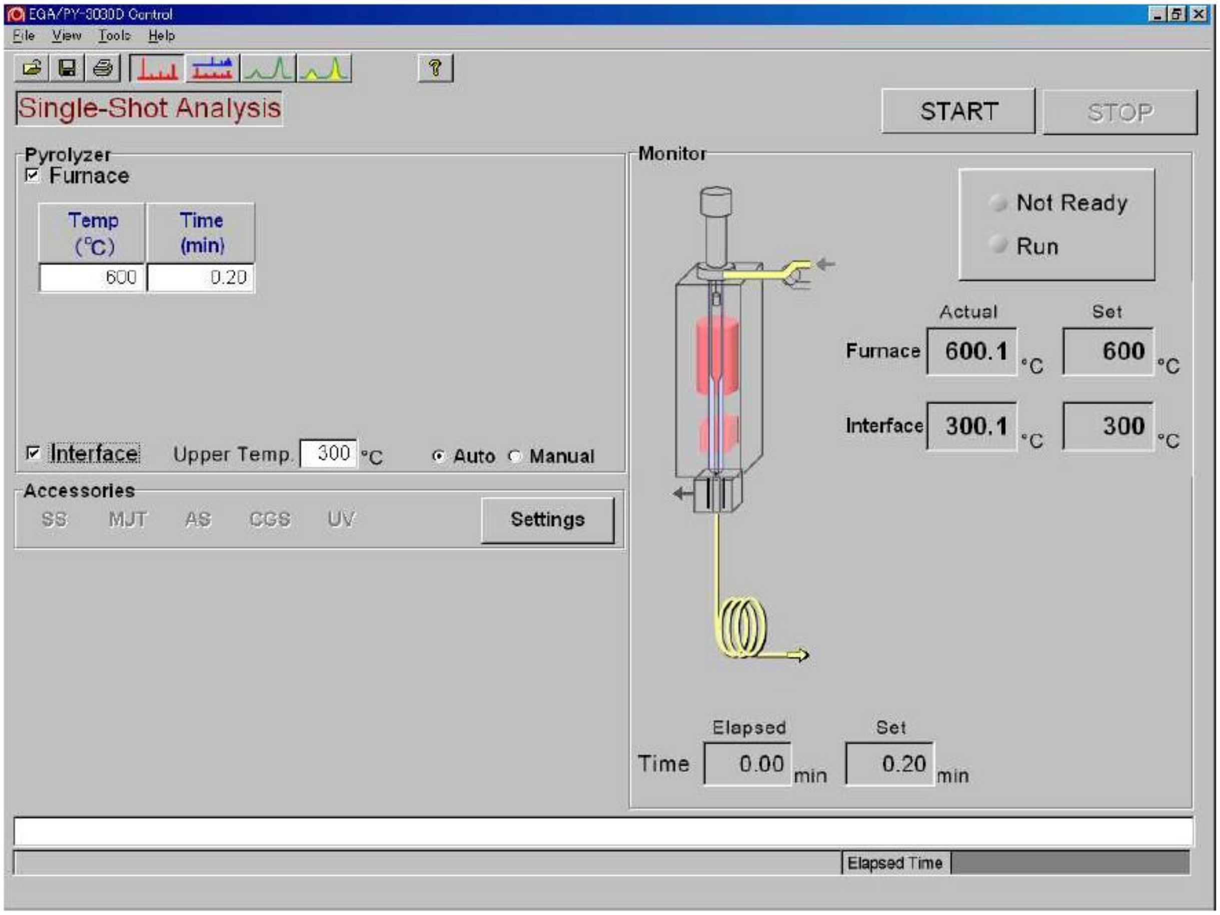

EGA/PY-3030D Control
File
View
Tools
Help
START
STOP
Settings
Elapsed Time

Single-Shot Analysis

Pyrolyzer

☑ Furnace

Temp (°C)	Time (min)
600	0.20

☑ Interface Upper Temp. 300 °C ● Auto ○ Manual

Accessories

SS MJT AS CGS UV

Monitor

○ Not Ready

○ Run

	Actual	Set
Furnace	600.1 °C	600 °C
Interface	300.1 °C	300 °C

	Elapsed	Set
Time	0.00 min	0.20 min

Figure E4. Pyrolysis control software

VITA

EDUCATION

Doctor of Philosophy, Civil and Environmental Engineering December 2019

Old Dominion University, Norfolk VA

Cumulative GPA: 3.39/4.0

Dissertation: Catalytic Transfer Hydrogenation of Lipids

Master of Science, Environmental Engineering December 2015

Old Dominion University, Norfolk Virginia, USA

Cumulative GPA: 3.53

Thesis: Technoeconomic Analysis of Protein Concentrate Produced by Flash Hydrolysis of Microalgae

Master of Science, Chemical Engineering June 2008

Kwame Nkrumah University of Science & Technology, Kumasi, Ghana

Cumulative GPA: 3.52/4.0

Thesis: Life Cycle assessment of Margarine Production from Palm oil in Ghana

Bachelor of Science, Metallurgical Engineering March 2003

Kwame Nkrumah University of Science & Technology, Kumasi, Ghana

Cumulative GPA: 3.37/4.0

Thesis: Aluminum Extraction form Bauxite fine

JOURNAL PUBLICATION (Ph.D.)

1. **Asiedu, A.; Kumar, S.***;* Ch. 12: Liquid Hydrocarbon Biofuels from Lipids. In Biofuels Production and Processing Technology, M.R. Riazi, David Chiaramonti, Eds. CRC Press, Oct. 13, 2017. ISBN 9781498778930 - CAT# K29842
2. **Asiedu, A.**; **Barbera, E.; Naurzaliyev, R.; Bertucco, A.; Kumar, S.**; Waste *Cooking Oil to Jet-diesel fuel Range Using 2-propanol via Catalytic Transfer*

Hydrogenation Reactions in *Biofuels.* Ref.: Ms. No. TBFU2018-0150R1. Jan. 14, 2019.

3. ***Asiedu, A.; Kumar, S.;*** Kinetics and Optimization of Catalytic Transfer Hydrogenation of WCO Using 2-propanol as H-donor over NiOx-MoOx-CoOx/Zeolite, *Ind. Eng. Chem. Res. (2019).* DOI: 10.1021/acs.iecr.9b00648.

4. ***Asiedu, A.; Davis, A.; Kumar, S.;*** Catalytic transfer hydrogenation and characterization of flash hydrolyzed microalgae into hydrocarbon fuels production (jet fuel), *Fuel 261 (2020) 116440.* https://doi.org/10.1016/j.fuel.2019.116440

5. **Barbera, E.; Naurzaliyev, R; Asiedu, A.; Bertucco, A.; Resurreccion, E.; Kumar, S**.; Techno-Economic Analysis and Life-Cycle Assessment of Jet Fuels Production from Waste Cooking Oil Via Catalytic Transfer Hydrogenation. *Journal of Renewable Energy*, **2019** (Under Review)

Journal Publication (M.S.)

1. **Asiedu, A.; Stuart, B.; Resurreccion, E. P.; Kumar, S.** “Techno-economic analysis of protein concentrate produced by flash hydrolysis of microalgae." *Environmental Progress & Sustainable Energy*, DOI: 10.1002/ep.12722 (Sept. **2017**).